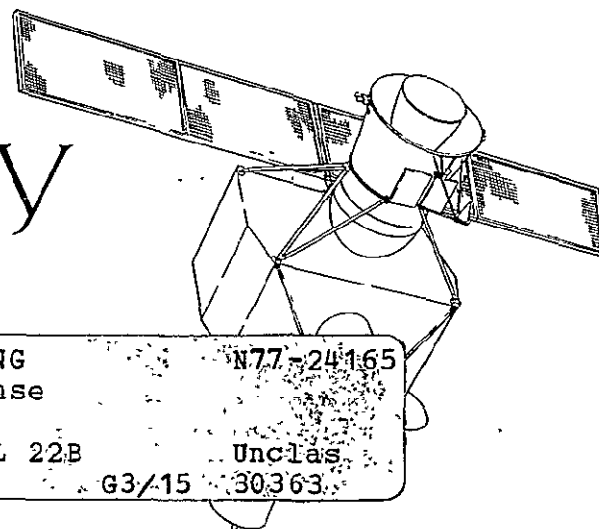


NASA CR-152509

26818-6003-RU-00

FINAL TECHNICAL REPORT

SEVERE STORMS OBSERVING SATELLITE STUDY



(NASA-CR-152509) SEVERE STORMS OBSERVING
SATELLITE STUDY Final Report (TRW Defense
and Space Systems Group) 224 p
HC A10/MF A0-1

N77-24165

CSCL 22B

Unclass

G3/15

30363

Contract No. NAS5-20811

For

NATIONAL AERONAUTICS AND SPACE ADMINISTRATION
Goddard Space Flight Center
Greenbelt, Maryland 20771

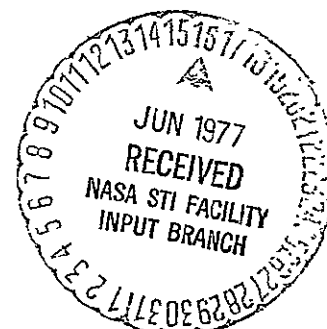
30 JUNE 1976



TRW

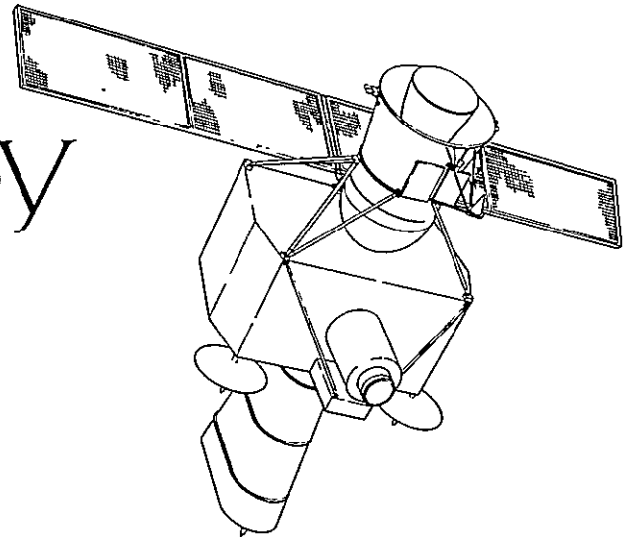
DEFENSE AND SPACE SYSTEMS GROUP

ONE SPACE PARK • REDONDO BEACH, CALIFORNIA 90278



FINAL TECHNICAL REPORT

SEVERE STORMS OBSERVING SATELLITE STUDY



Contract No. NAS5-20811

For

NATIONAL AERONAUTICS AND SPACE ADMINISTRATION
Goddard Space Flight Center
Greenbelt, Maryland 20771

30 JUNE 1976



TRW
DEFENSE AND SPACE SYSTEMS GROUP

ONE SPACE PARK • REDONDO BEACH, CALIFORNIA 90278

Report No. 26818-6003-RU-00

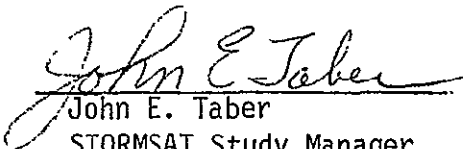
Final Technical Report

SEVERE STORMS OBSERVING SATELLITE STUDY

30 June 1976

Prepared by: R. P. Iwens
D. A. Stern

Approved by:


John E. Taber

STORMSAT Study Manager
TRW Defense and Space Systems Group

Contract No. NAS5-20811

TRW Defense and Space Systems Group
One Space Park
Redondo Beach, California 90278

Prepared for:

National Aeronautics and Space Administration
Goddard Space Flight Center
Greenbelt, Maryland 20771

Contracting Officer: J. W. Pohl

Study Manager: J. Over

Contributors to the STORMSAT System Study

G. E. Bernier	Design, Analysis and Simulation Department
R. J. Chan	Digital Systems Department
W. W. Fleming	Design, Analysis and Simulation Department
R. F. Hofstadter	Design, Analysis and Simulation Department
A. Y. Hung	Data Systems Department
R. P. Iwens	Design, Analysis and Simulation Department
D. P. Lindert	Advanced Digital Processor Department
J. L. Palmer	Design, Analysis and Simulation Department
P. E. Romo	Science and Application Satellite Systems
D. A. Stern	Digital Systems Department
J. E. Taber	Science and Application Satellite Systems
Y. Wakamiya	Design, Analysis and Simulation Department
D. S. Webber	Electro-Optical Sensors Department
J. G. Zaremba	Electromechanical Equipment Department

SUMMARY

This Final Technical Report presents the results of Phase III of the Stormsat System Study. It also summarizes the study results obtained under Phase II of the contract, which is the phase following program redirection to confine the Stormsat System Study to performance of the Stormsat mission using the Multi-Mission Modular Spacecraft (MMS).

Phases I and II of the study were primarily concerned with spacecraft attitude determination and control. Under Phase I, an ACS tradeoff study was conducted among three different attitude control system concepts namely: independent three-axis control, pitch momentum bias control, and dual spin attitude control. The studies conducted in Phase II were concerned with attitude determination and control system design and performance evaluation using MMS type hardware as the baseline.

The baseline Stormsat system in this study was defined to carry the Advanced Atmospheric Sounder and Imaging Radiometer (AASIR) as the only payload and the spacecraft was assumed to consist of a minimally redundant MMS bus and perform no north-south stationkeeping. The preliminary mass properties and power budget used in the study are based on these assumptions.

Under Phase III of the contract, a variety of study topics have been addressed which are primarily characterized by being mission-unique aspects of Stormsat. Three alternate Advanced Atmospheric Sounder and Imaging Radiometer (AASIR) gimbal configurations were studied and a baseline gimbaling concept was selected. The baseline gimbal consists of a bearing about the 18-inch diameter section of the AASIR and a linkage and direct-driven ball-screw type actuator mechanism to provide the angular motion. The orientation of the AASIR is controlled by a tight servo loop (20 rad/second bandwidth) using a two phase, delta-connected, brushless DC motor. It is recommended that the servo control system be implemented by a dedicated microprocessor which receives command inputs from the flight computer.

The baseline Stormsat system was a hydrazine gas reaction control system (RCS) for momentum removal, i.e., unloading of the reaction wheels. Unloading takes place during AASIR frame retrace time so that pointing performance is not affected. As a possible alternate scheme, magnetic

torquing (at synchronous altitude) for momentum removal was also investigated. Magnetic unloading would take place continuously, never interfere with the payload attitude stability requirements, and require no consumables, i.e., propellant. The study showed that this approach to momentum unloading is feasible if three solar-array-mounted, air-coils (one per panel) are used in conjunction with the MMS standard roll and yaw torquer bars. A total weight-optimized design yielded three coils of 7.4 pounds each with a power consumption of 21 watts per coil. The design considered weight-power tradeoffs and accounted for the array weight increase corresponding to a 43 watt increase in required array power.

The impact of flying the Microwave Atmospheric Sounding Radiometer (MASR), in addition to the AASIR on Stormsat was assessed. The general conclusion is the the dynamic interaction between the spacecraft, the MASR scanning reflector antenna, and the AASIR poses a number of significant operational problems. To fly both the AASIR and MASR one must be willing to accept a more complicated spacecraft attitude control system and be willing to sacrifice some performance with regard to AASIR pointing stability and MASR scan efficiency, i.e., give the MASR more time for turn-around and line stepping.

Depending on the users' ultimate demands on AASIR image stability with respect to consistent repeatable motion, north-south stationkeeping may eventually be required for Stormsat to curb the amplitude of the figure-eight type motion of the AASIR image over a 24-hour period. For this reason north-south stationkeeping policies for Stormsat were examined. The propellant requirement amounts to about 50 pounds per year. To control the orbit inclination to ± 0.1 degree requires a stationkeeping maneuver every 39 days. The maneuver (which requires spacecraft reorientation) would last about 6 minutes and imaging must be suspended since pointing stability specifications cannot be met during this period.

Attitude determination and attitude control software requirements were also established assuming that the NASA Standard Space Computer, NSSC-1, is used. Total memory requirement was established as 3805 words of program memory and 1311 words of read/write memory. Computation time per minor cycle (400 mseconds) during normal on-orbit operations is 46.3 mseconds when no star data are being processed; with star data processing and update computations the computation time is 247.5 mseconds.

During Phase III the on-board data handling system was addressed and a straightforward microprocessor based conceptual design developed. The data handling hardware includes a memory used to buffer the sinusoidally varying AASIR data as well as take advantage of the duty cycle of the scanning mirror. Assuming a charge-coupled device (CCD) memory, the total power and weight for the on-board hardware is approximately 10 watts and 3 pounds, exclusive of power supplies.

A straightforward communications system was also designed during this phase using space-qualified hardware. Since this portion of the study included a separate visible spectrum instrument (VSI), a QPSK modulation format was chosen with the I and Q channels being modulated by AASIR and VSI data, respectively. Spacecraft equipment for this design includes a 10-watt transmitter and a 20-inch S-band parabolic dish resulting in full earth coverage. With the 30-foot STDN ground station antenna and a 10^{-6} BER a 3.9 dB margin results.

Lastly, a conceptual design for the ground data processing was formulated. The structure suggested is a framework on which to add the varying tools that will be used by investigators. The objective is to allow the addition of diverse applications modules, written in high level languages, with minimal integration requirements. The conceptual design includes a high speed mini-computer (SEL 32/55), several large discs (up to 300 Mbytes), dual color displays (COMTAL 8000 series), a video disc for viewing visible and IR imaging (motion pictures), assorted peripherals, and an optional 10^{12} bit memory (terabit).

An overall Stormsat System summary within the scope of this study is presented in Section 2 of the report. The MMS is briefly described, the assumed sensor payload characteristics defined, and summary descriptions of the on-board attitude reference system, attitude control system, and on-board data handling and communications system are provided. The main conclusion is that the baseline Stormsat System has the capability to support the AASIR by providing a space platform that can meet the desired attitude accuracy and pointing stability.

TABLE OF CONTENTS

	<u>Page</u>
1. INTRODUCTION	1-1
1.1 History of Contract	1-1
1.2 Organization of Reports	1-7
2. SYSTEM SUMMARY	2-1
2.1 MMS/Stormsat Configuration	2-1
2.1.1 Multi-Mission Modular Spacecraft	2-1
2.1.2 Stormsat Configuration Considerations	2-5
2.2 Payload Description	2-13
2.2.1 AASIR Instrument	2-13
2.2.2 Visible Spectrum Instrument (VSI)	2-18
2.2.3 MASR Instrument	2-21
2.3 Stormsat Pointing Performance Requirements	2-24
2.4 On-Board Attitude Reference System	2-26
2.5 Attitude Control System	2-35
2.5.1 ACS Functional Operating Modes	2-35
2.5.2 Normal On-Orbit Attitude Control	2-38
2.5.3 Dynamic Interaction with Stepping Payloads	2-48
2.5.4 Estimated Performance Summary	2-49
2.6 ACS and ARS Software Requirements	2-51
2.6.1 NASA Standard Space Computer (NSSC-1) Characteristics	2-51
2.6.2 ARS Algorithm Software Requirements	2-51
2.6.3 Attitude Control Software Requirements	2-58
2.6.4 Typical Normal On-Orbit Requirements	2-62
2.7 On-Board Data Handling, Communications, and Ground Data Processing	2-64
2.7.1 On-Board Data Handling	2-64
2.7.2 Communications	2-65
2.7.3 Ground Data Processing	2-66
3. AASIR GIMBAL DRIVE	3-1
3.1 AASIR Gimbaling Concepts	3-1
3.1.1 Background and Basic Functional Requirements	3-1
3.1.2 Direct Drive Gimbal	3-1

TABLE OF CONTENTS (CONTINUED)

	<u>Page</u>
3.1.3 Three Point Suspension Gimbal	3-6
3.1.4 Linear Ball Screw Actuator Driven Gimbal	3-12
3.2 Conceptual Design Ranking	3-19
3.3 Preliminary Gimbal Servo Design	3-22
3.3.1 Gimbal Drive Model	3-22
3.3.2 Performance Requirements	3-26
3.3.3 Controller Design	3-28
3.3.4 Recommendations for Further Study	3-38
4. ON-BOARD DATA HANDLING	4-1
4.1 Introduction	4-1
4.2 AASIR Data Handling Requirements	4-1
4.3 Design Considerations	4-1
4.4 Minor Frame Design	4-2
4.5 Data Rates and Buffer Sizing	4-4
4.6 Timing Derivation	4-6
4.7 Hardware Implementation	4-8
4.7.1 Analog Circuits	4-8
4.7.2 Digital Formatter and Buffer Memory	4-8
4.7.3 Micro-Controller	4-10
4.7.4 Technology	4-10
5. TELECOMMUNICATIONS	5-1
5.1 Introduction	5-1
5.2 Description	5-1
5.3 Link Performance Analysis	5-5
5.4 Hardware Characteristics	5-7
5.5 Trades	5-13
5.5.1 Configuration	5-13
5.5.2 Antenna Versus Transmitter Power	5-16
5.5.3 RF Modulation	5-18
6. GROUND DATA PROCESSING	6-1
6.1 Introduction	6-1
6.2 Background	6-1

TABLE OF CONTENTS (CONTINUED)

	<u>Page</u>
6.3 Discussion	6-2
6.4 Translation of Observation Requirements into Functional Needs	6-8
6.5 Stormsat Data Handling System Overview	6-9
6.6 SSRP Conceptual Design	6-13
7. MOMENTUM UNLOADING USING MAGNETIC TORQUING	7-1
7.1 Summary and Introduction	7-1
7.2 System Concept	7-5
7.2.1 Solar Disturbance	7-5
7.2.2 Geomagnetic Field at Synchronous Altitude	7-9
7.3 Array Mounted Coil Sizing	7-19
7.3.1 Coil for 400 Watt Array	7-19
7.3.2 Minimum Total Weight Design	7-24
7.4 Effects of Generated Magnetic Fields	7-28
7.4.1 Magnetometer Considerations	7-28
7.4.2 Payload and Star Tracker Considerations	7-30
7.5 Conclusions	7-32
8. NORTH-SOUTH STATIONKEEPING ANALYSIS	8-1
8.1 Nominal Requirements	8-1
8.2 Use of 0.2 Pound Thrusters	8-3
8.3 Use of 5 Pound Thrusters	8-5
8.4 Stationkeeping Disturbance Torques	8-8
8.5 Recommended Stationkeeping Policy	8-13
9. Microwave Atmospheric Sounding Radiometer (MASR)	9-1
9.1 Requirements for Spacecraft pointing and Payload Control	9-1
9.2 System Parameters	9-5
9.3 Dynamic Equations	9-7
9.4 MASR and Spacecraft Control	9-13
9.4.1 Spacecraft Control	9-13
9.4.2 Stepping Control of the MASR	9-15
9.4.3 Line Scanning Control of the MASR	9-18

TABLE OF CONTENTS (CONTINUED)

	<u>Page</u>
9.5 Analysis and Simulation Results	9-21
9.5.1 MASR Stepping	9-22
9.5.2 MASR Scan Reversal	9-33
9.5.3 Additional Topics	9-33
9.6 Summary and Conclusions	9-38
REFERENCES	R-1

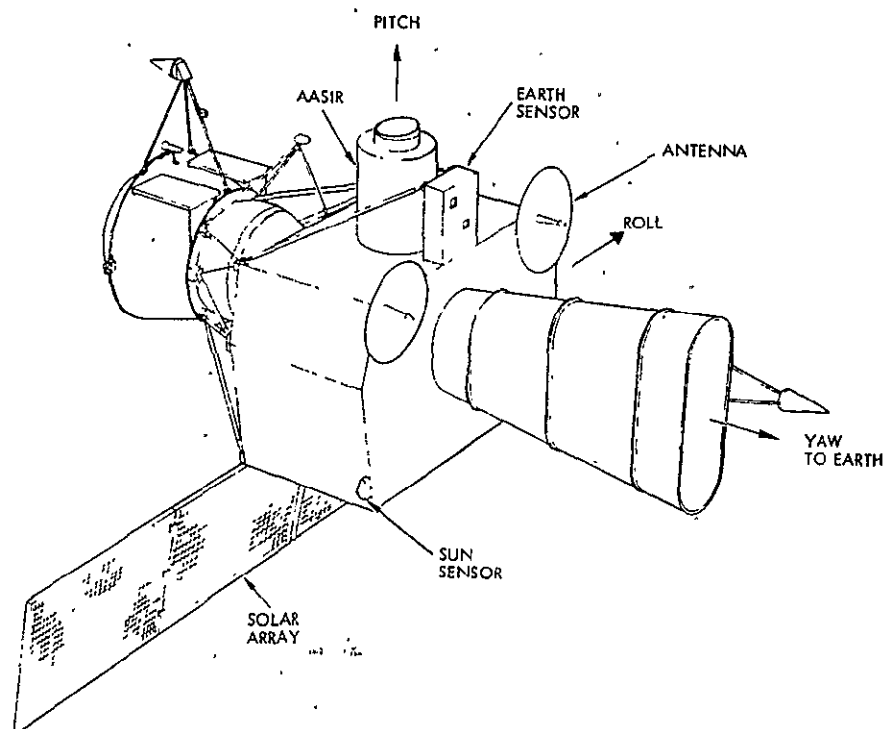
1. INTRODUCTION

The geosynchronous, earth pointing, Severe Storms Observing Satellite, StormSat, provides a major tool in understanding and predicting tornados, hurricanes, and other severe storms. The StormSat System Phase A Study is an important part of the StormSat project because it has demonstrated the capability of spacecraft systems to support the Advanced Atmospheric Sounder and Imaging Radiometer (AASIR). Particular emphasis in the study has been on attitude control, since accurate and stable pointing of the AASIR is of prime importance for a successful StormSat mission. Additional emphasis has been on methods of handling the collected data.

1.1 History of Contract

The Stormsat System Phase A Study was awarded to TRW by NASA Goddard Space Flight Center (GSFC) in January 1975. The original statement of work called for the study and subsequent design of a mission-optimized spacecraft to support the Advanced Atmospheric Sounder and Imaging Radiometer in a geosynchronous orbit. Pointing and control was considered the most difficult design task and therefore Phase I called for tradeoffs among three different attitude control system concepts, namely: independent three-axis control, pitch momentum bias control, and dual spin attitude control. Based on the results obtained in this phase, TRW recommended an independent three-axis stabilized spacecraft and identified it as the baseline system for Stormsat to be investigated in the second phase of the study. The results of Phase I were presented to NASA in a briefing at GSFC on April 24, 1975, and were also documented in an Interim Technical Report entitled "Stormsat ACS Tradeoff Study", Reference 1.

Figure 1-1 shows a drawing of the recommended three-axis stabilized spacecraft configuration. It uses four small reaction wheels of 1.3 ft-lb-sec each in a skewed pyramidal configuration for normal on-orbit attitude control. A three-axis gyro reference assembly, updated by earth horizon sensors and digital sun sensors, provides on-board attitude reference data. The main tradeoff criterion used in the selection of this system was the ability to meet the StormSat pointing performance specifications at competitive system weight, volume, power, reliability and cost. Associated technical risk, system complexity and spacecraft growth capability (flexibility) were also considered.



MASS PROPERTIES

$$I_x = .98 \text{ slug-ft}^2 \text{ (ROLL)}$$

$$I_y = 101 \text{ slug-ft}^2 \text{ (PITCH)}$$

$$I_z = .95 \text{ slug-ft}^2 \text{ (YAW)}$$

$$m = 766 \text{ lb}$$

Figure 1-1. Mission Optimized Three-Axis Stabilized StormSat

The three investigated ACS concepts ranked fairly close with respect to their suitability for the StormSat mission and the selection of the independent three-axis concept as the baseline system was not a clear-cut choice under all circumstances. The various AASIR scan methods under consideration at the time by the AASIR study contractor, Santa Barbara Research Center (SBRC), heavily influenced the suitability of the dual spin system for StormSat. For a one-axis AASIR the choice was clear-cut, however, since the dual spin system had problems meeting the performance requirements because of the uncompensated N-S AASIR mirror scan, which in this case was constrained to occur about an axis perpendicular to the spin axis. With respect to technical risk, system flexibility, and spacecraft growth capability the independent three-axis system was under all circumstances the most favorable configuration, and after accounting for all tradeoff factors involved, it was selected as the baseline system. Pending NASA approval of this recommendation, the statement of work called for a subsequent preliminary design of the entire spacecraft with particular emphasis on the attitude control and data handling subsystems.

After completion of Phase I, at the end of May 1975, the Severe Storms Observing Satellite Study was redirected by NASA/GSFC. The consensus of the redirection was to eliminate any further consideration of mission optimization and instead study how to accomplish the mission using the then evolving Low Cost Modular Spacecraft, later to be adopted as the NASA standard Multi-Mission Modular Spacecraft (MMS). This report therefore provides no justification for the choice of the MMS but only summarizes key aspects of its use once the choice had been through considerations outside the scope of this study. The MMS is an independent three-axis stabilized vehicle using 4 reaction wheels (3 orthogonal plus 1 skewed) in conjunction with a stellar-inertial attitude reference system to provide accurate and stable spacecraft attitude control. As the name implies, the MMS is composed of a set of standard modules: ACS, Communications and Data Handling (CDH), and Power; the optional Propulsion module comes in at least two standard versions, known as SPS-I and SPS-II. In addition, the MMS can accommodate "mission peculiar equipment" of which the payload is usually the dominant component; the payload for Stormsat is, of course, AASIR. A detailed description of the MMS can be found in Reference 3. Figure 1-2 shows one possible configuration of the MMS for the Stormsat mission.

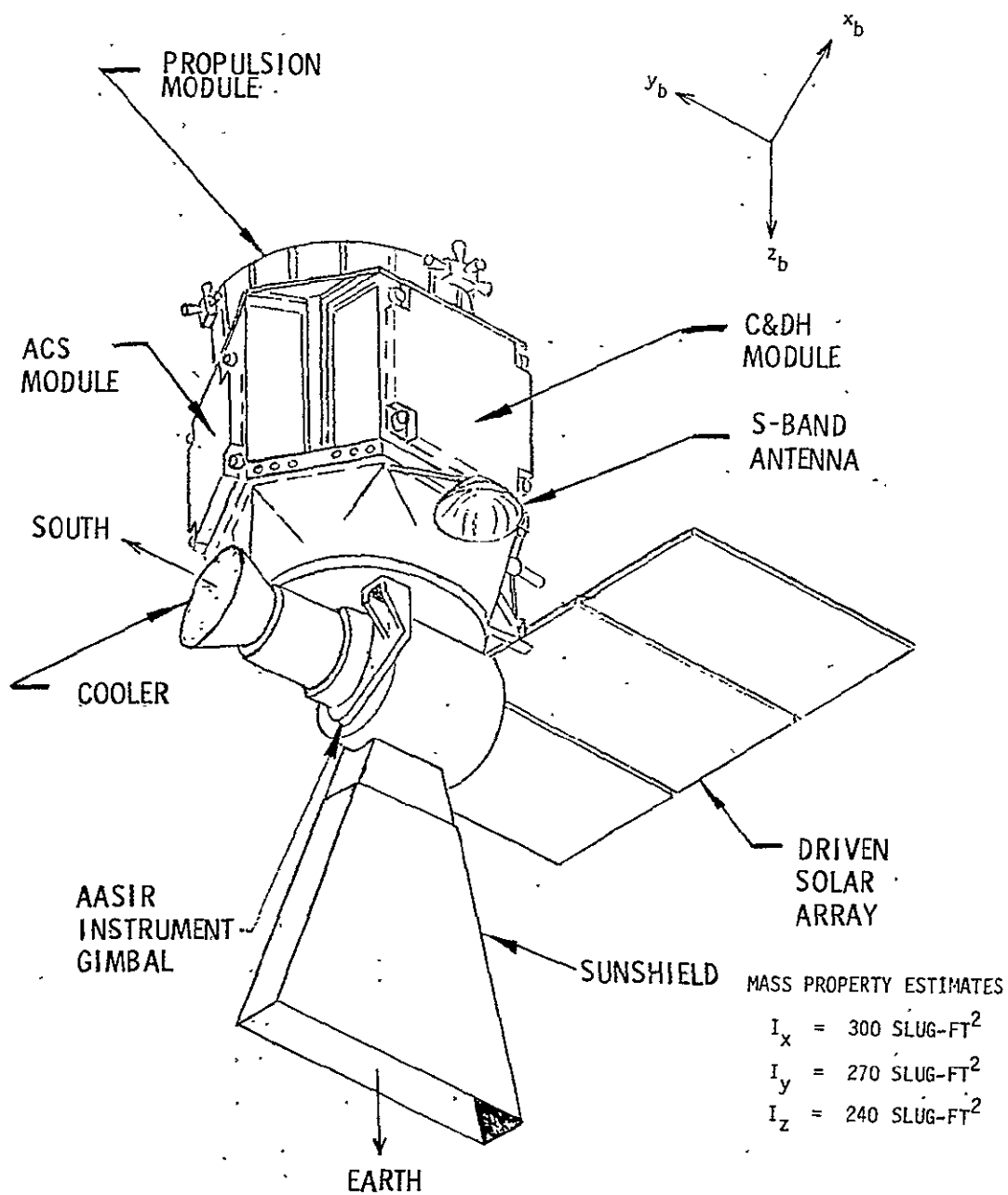


Figure 1-2. A Possible MMS StormSat Configuration

The contract redirection specified that the remaining work was to be divided into two separate, distinct phases. Under the first of these phases, which in view of the entire study was called Phase II, the stellar inertial attitude reference and the attitude control subsystems of the MMS were to be evaluated and achievable performance analyzed in view of the Stormsat mission requirements. The MMS system was to be used in conjunction with a 1 degree of freedom AASIR (providing only the resonant line scan internally) mounted on a single gimballed platform to provide the orthogonal scanning direction. The time line of the stepping motions to be provided by the gimballed platform were also specified at that time. The redirection postponed specific instructions for the last phase of the contract until after the completion of Phase II described above. In general, the last phase was to study mission unique aspects, but it specifically excluded the conceptual design of the complete spacecraft.

The results of Phase II were presented to NASA in a briefing at GSFC on November 13, 1975, and were also documented in an Interim Technical Report, "StormSat ACS Design Study, Phase II," Reference 2. The report provides a detailed account of study activities and results obtained under Phase II. In particular, the following topics were addressed:

- Orbital configuration and module orientation of the MMS for the StormSat mission.
- AASIR gimbaling feasibility.
- Stellar-inertial attitude reference system design and performance evaluation, including tradeoffs between the use of gimballed and strapdown star trackers.
- Detailed ACS design and performance analysis addressing tradeoffs between torque control, momentum control, and speed-biased control.
- Solutions to the dynamic interaction problem created by a stepping gimballed AASIR.

These topics were studied using both analysis and extensive simulation where required.

After the successful completion of Phase II, TRW was directed in December 1975 to study the following mission unique aspects under Phase III of the contract.

- Alternate AASIR gimbal configurations and a preliminary gimbal servo design for the identified baseline gimbal system.
- Impact of flying an additional payload on StormSat: The Microwave Atmospheric Sounding Radiometer (MASR).
- Feasibility of using magnetic torquing (at synchronous altitude) for momentum unloading.
- North-south stationkeeping policy.
- Attitude control and attitude reference system software requirements for the NASA Standard Spacecraft Computer (NSSC).
- On-board payload data handling, communications (RF down link), and ground data processing.

It was reiterated that a conceptual design of the complete spacecraft was to be excluded from the study.

In February 1976 the AASIR scan pattern was undergoing design changes (basically a 1.5 times speed-up) with potentially significant impacts on the data handling subsystem and the dynamic interaction between the AASIR and the spacecraft. Because of this and the possible addition of the MASR as a second payload, it became necessary to establish a strawman baseline system for StormSat and uncouple the remaining study tasks from the volatile nature of the AASIR development. Since most of the ACS related tasks had either already been completed in Phase II, or were nearing completion under Phase III, TRW was directed in March 1976 to let the strawman for the data handling task be based on the latest AASIR scan pattern (1.5 times speeded up scan) while the ACS strawman system would continue to assume the previous baseline pattern. This minor inconsistency is not critical since the actual final AASIR scan pattern could not have been defined at that time anyway. Moreover, this study attempted to treat the topics parametrically and address other system options where possible. The direction provided by NASA also established that the MASR was not a

part of the baseline spacecraft system, but that an additional VISSR type instrument, collecting only lower-resolution visible-spectrum data, was to be a part of the baseline system only as far as the data handling study tasks were concerned.

1.2 Organization of Reports

The purpose of the Final Report is to document the results of Phase III of the Stormsat study. Detailed accounts of the results of Phase I and II were presented in the previously cited interim technical reports, References 1 and 2. However, in order to provide a total overview of the study, Section 2 contains a system summary in which previous and current study results are summarized in an orderly fashion.

The remaining sections provide a detailed account of the study activities and results obtained under Phase III. Section 3 presents the mechanical design of the AASIR gimbal drive mechanism together with a preliminary gimbal servo design. Sections 4, 5, and 6 are concerned with on-board data handling, data downlink communications, and ground data handling. Section 7 investigates magnetic unloading at synchronous altitude, Section 8 examines north-south stationkeeping, and Section 9 studies the feasibility and impact of flying the MASR as an additional payload on Stormsat. The software sizing for the attitude reference and control system is presented with the system summary in Section 2.6 because the mechanics of conducting this task requires little discussion and merely the underlying assumptions and obtained results need be presented.

2. SYSTEM SUMMARY

This section provides a StormSat system summary within the scope of the study. It presents the results obtained under Phases II and III of the StormSat System Study following redirection to the MMS system. Detailed documentation of the Phase II results was presented in an interim technical report, Reference 2, and the Phase III results are presented in detail in subsequent sections of this report.

2.1 MMS/StormSat Configurations

The StormSat mission will be performed using the Multi-Mission Modular Spacecraft (MMS). The MMS is a concept that has been developed by NASA Goddard Space Flight Center (GSFC) over the past six years. It was originally known as the Low Cost Modular Spacecraft and Reference 3 provides an excellent description of its projected characteristics and capabilities. The brief discussion that follows is entirely based on Reference 3, and the illustrations of the MMS in Figures 2-1 through 2-3 are those of Reference 3.

2.1.1 Multi-Mission Modular Spacecraft

The MMS is an independent three-axis stabilized vehicle using three or four reaction wheels in conjunction with a stellar-inertial attitude reference system to provide accurate and stable spacecraft attitude control. As the name implies, the MMS is composed of a set of standard modules: ACS module, Communications and Data Handling (CDH) module and Power module. The propulsion module is optional and comes in two standard versions known as SPS-I and SPS-II. The baseline configuration contains the above mentioned three subsystem modules supported by a module support structure (MSS), as shown in Figure 2-1. A transition adapter and a vehicle adapter complete the structural elements of the system. Mission Unique and adapted items include the solar array, the solar array drive, the solar drive deployment mechanisms, a set of deployable TDRSS antennas and booms, and a mission adapter and payload (see Figures 2-2 and 2-3). The three spacecraft modules are physically the same size. As shown in Figure 2-2, they measure 18 inches deep, 48 inches high, and 48 inches wide.

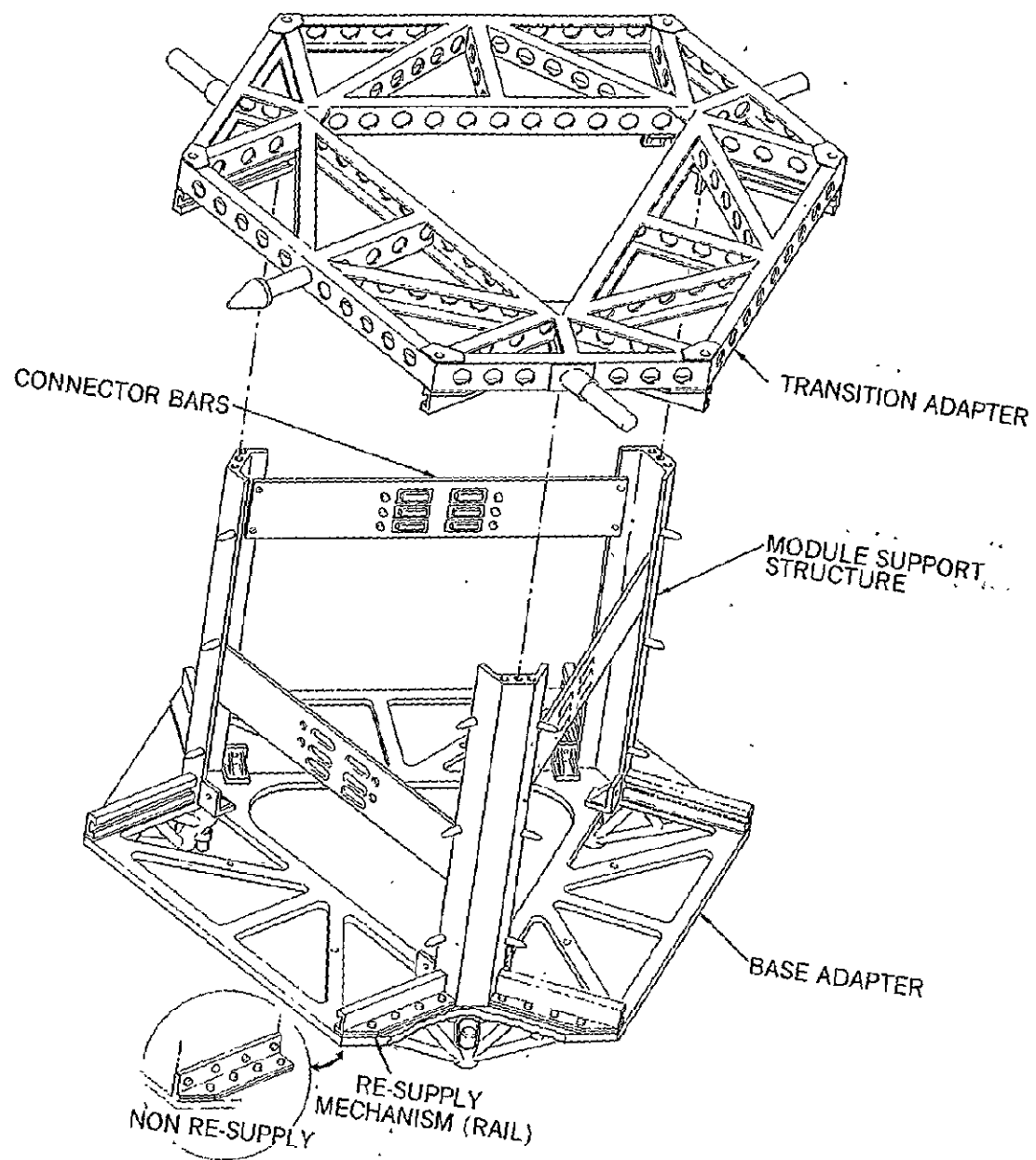


Figure 2-1. Module Support Structure .
(Taken from Reference 3)

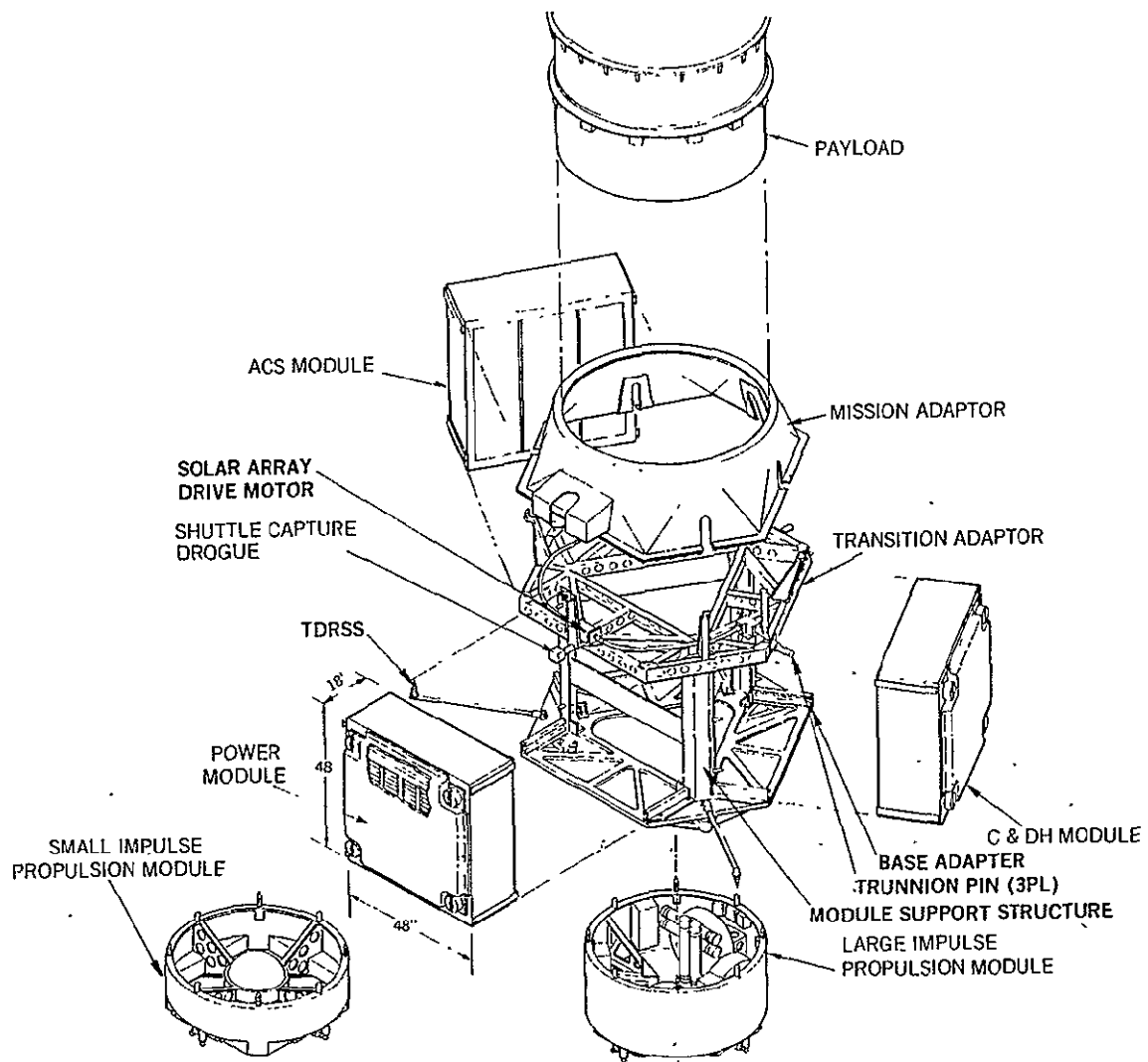


Figure 2-2. Multi-Mission Modular Spacecraft (Exploded View)
(Taken from Reference 3)

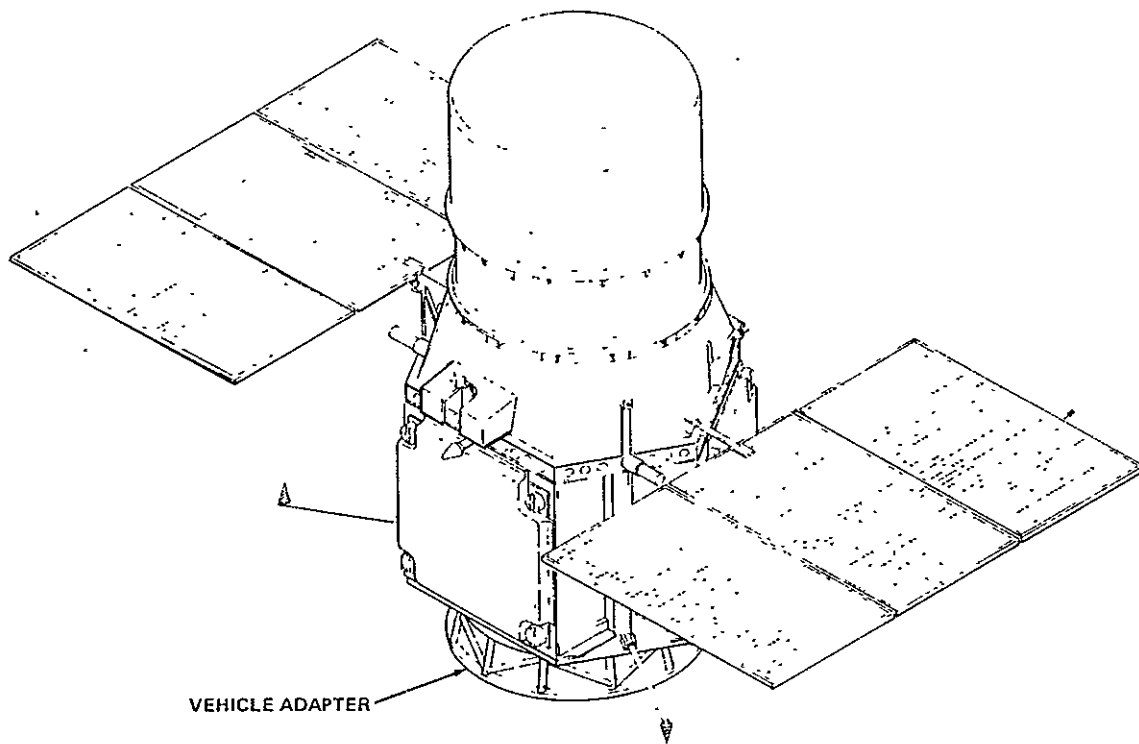


Figure 2-3. Multi-Mission Modular Spacecraft
(Taken from Reference 3)

Alignment between the attitude control subsystem and the payload reference axis is maintained by the transition adapter during orbit operations. The transition adapter has other unique features which allow a shuttle orbiter capture, docking, retrieval and servicing by a manipulator system. The transition adapter also supports the solar array launch restraint and deployment mechanism and the solar array drive motors. The communication antennas are attached to the spacecraft to suit the mission. Optional attachment points include the area above the separation interface on the base adapter and also the transition adapter. The antennas and boom assembly can be folded into the recess formed by the adjacent edges of the modules. Total spacecraft weight without payload is 1235 pounds for the baseline configuration and 1590 pounds for the fully redundant configuration.

Key features of the MMS are listed below. Potential users will find they can:

- (1) Select the level of redundancy from non-redundant to fully redundant based upon their own cost/weight/reliability tradeoffs.
- (2) Alter the solar array size and orientation along with battery capacity.
- (3) Alter the control system software to meet the unique requirements of their mission.
- (4) Add an Actuation Module with large reaction wheels or CMG's and magnetic torquer bars to handle very large payloads without impacting the spacecraft design.
- (5) Add propulsion systems for reaction control, orbit adjust and orbit transfer, as required.
- (6) Modify the spacecraft for on-orbit servicing.

2.1.2 StormSat Configuration Considerations

Figures 2-4 and 2-5 show a total of four spacecraft configurations of the MMS for the StormSat mission. All spacecraft are shown in their northern hemisphere summer orientations when the sun is north of the equator. The ACS module must be oriented such that the lines of sight of the star trackers do not suffer sun interference, while at the same time the direct sun exposure of the power module should be minimized for thermal reasons. Figure 2-6 shows the planned layout of the equipment of the ACS module. In particular the arrangement of the star trackers should be noted.

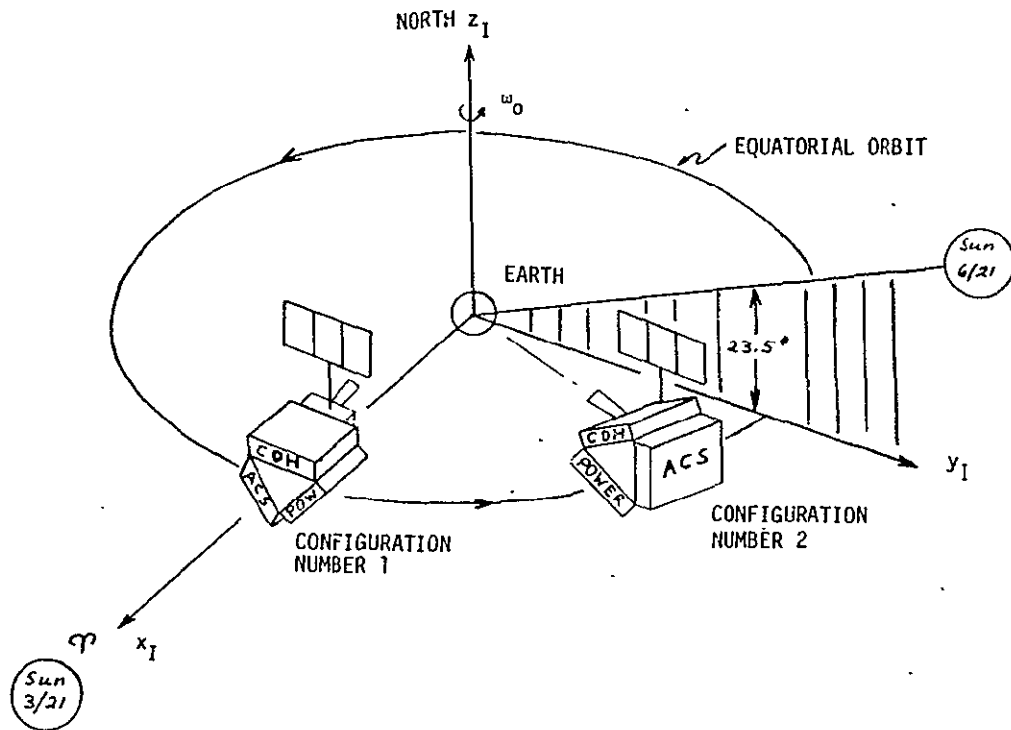


Figure 2-4. Configurations Numbers 1 and 2 in NH Summer Orientation

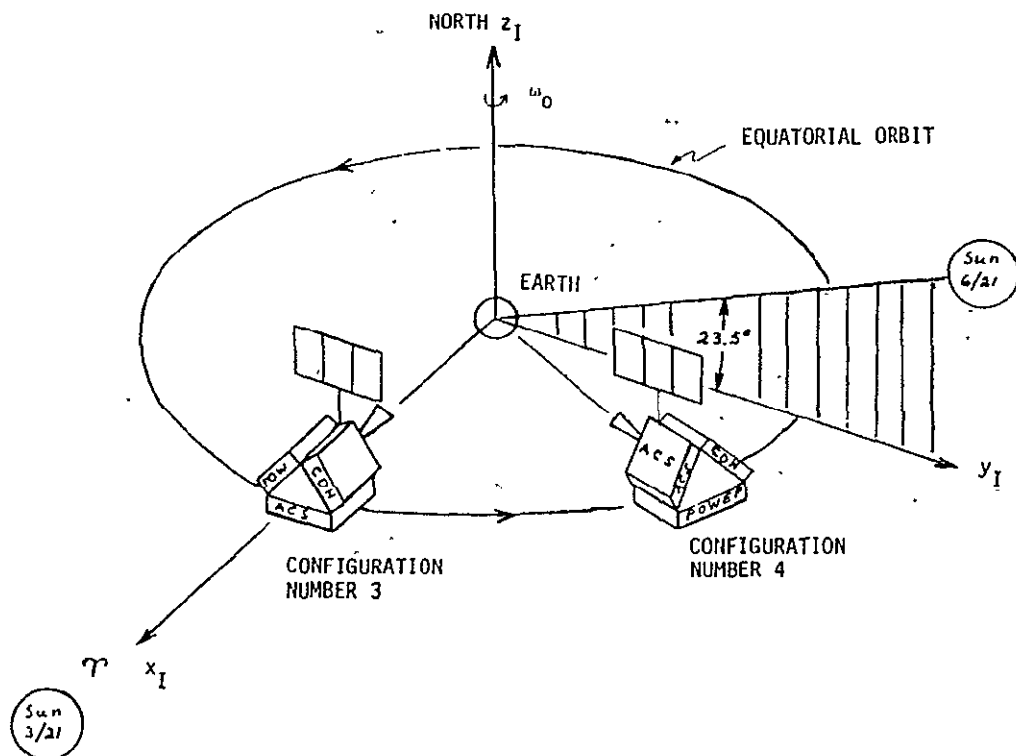
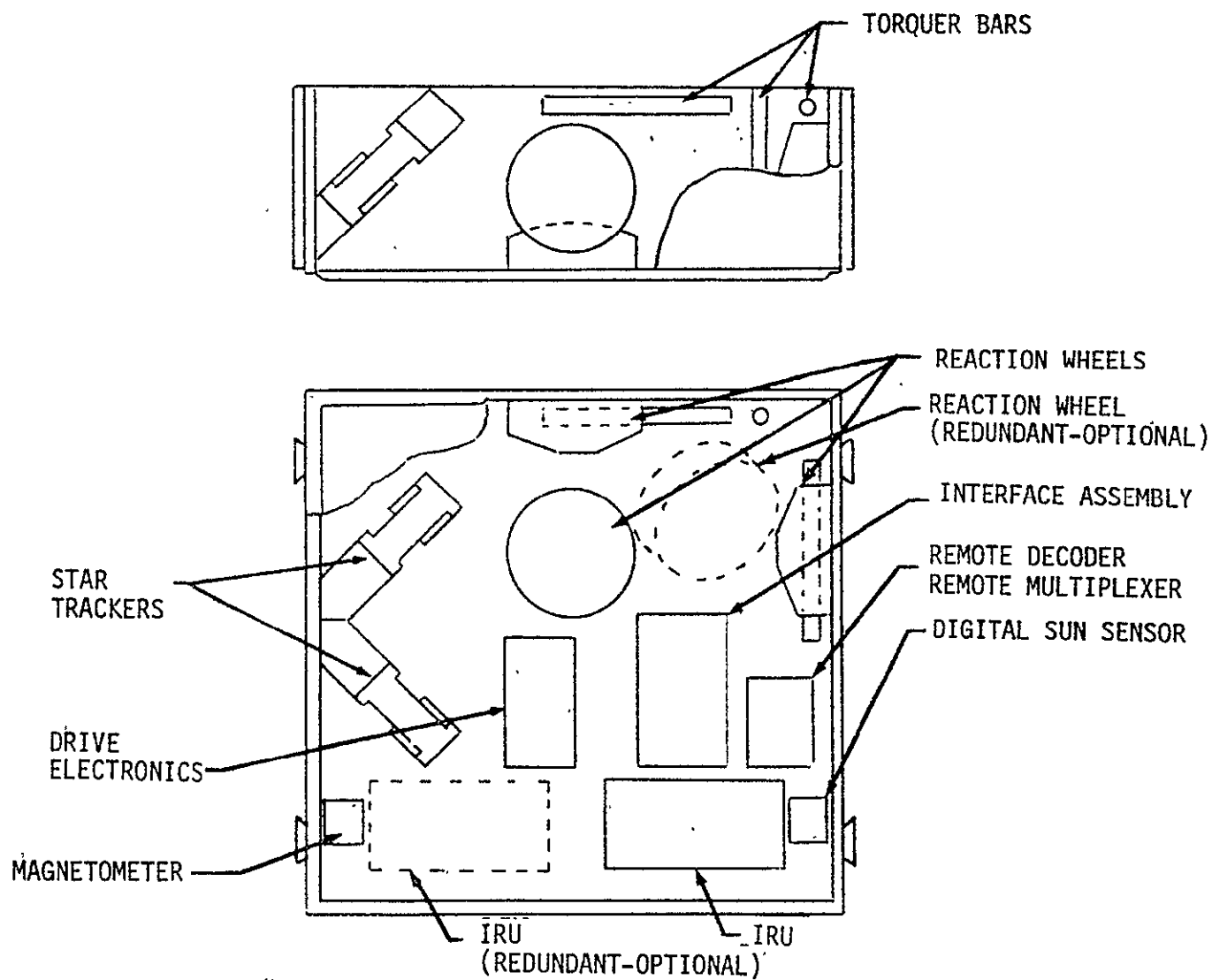


Figure 2-5. Configurations Numbers 3 and 4 in NH Summer Orientation



(from NASA Document X-700-75-140, see Reference 3)

Figure 2-6. ACS Module

Spacecraft configurations numbers 1 and 4 are undesirable for the star trackers since they would suffer severe sun interference*. Configuration number 3 is thermally undesirable since the power module has full frontal sun illumination for half an orbit with the worst condition arising at sunrise/sunset at the solstices when the sun incidence angle reaches 83.5 degrees. The pictorial sketch of StormSat in Figure 1-2 showed the MMS in this configuration.

The idea behind configuration number 2 is to assign the anti-earth side of the spacecraft to the ACS module and to mount the power module on the shady side of the orbit. The worst thermal condition for the power module will occur at equinox when the sun incidence angle for the front panel of the module reaches 60 degrees at orbit midnight. This is eclipse season and in one way it mitigates the situation, while on the other hand the increased battery charging activity after the spacecraft emerges from eclipse, makes the thermal problems more severe. Otherwise the power module receives only edge illumination so that from thermal considerations, configuration number 2 appears to be an acceptable spacecraft configuration. Figure 2-7 provides further detail of the configuration showing that a very good star tracker orientation results.

Depending on how the tracker slant angle ϕ_s is selected, the lines of sight of both trackers can easily be inclined 45 degrees to the orbit plane (toward the shaded side) with one tracker looking forward and one tracker looking aft. Here, $\phi_s = 35.3$ degrees has been selected and the total separation angle between the two tracker lines of sight is 60 degrees. Figure 2-8 shows other possible options by plotting the angle between the tracker LOS and the orbit plane versus the tracker slant angle ϕ_s . In general, a $\phi_s = 0$ is not desired because StormSat is to use the standard ACS module of the MMS. For missions other than StormSat the MMS may be flown in other orientations for which a slant angle $\phi_s = 0$ may be an unacceptable tracker orientation. A $\phi_s = 45$ degrees as indicated

*Unless the ACS module can be rotated 90 degrees about its own axis, in which case one tracker would come within about 36.5 degrees of the earth limb; this appears acceptable. See Reference 2 for further details.

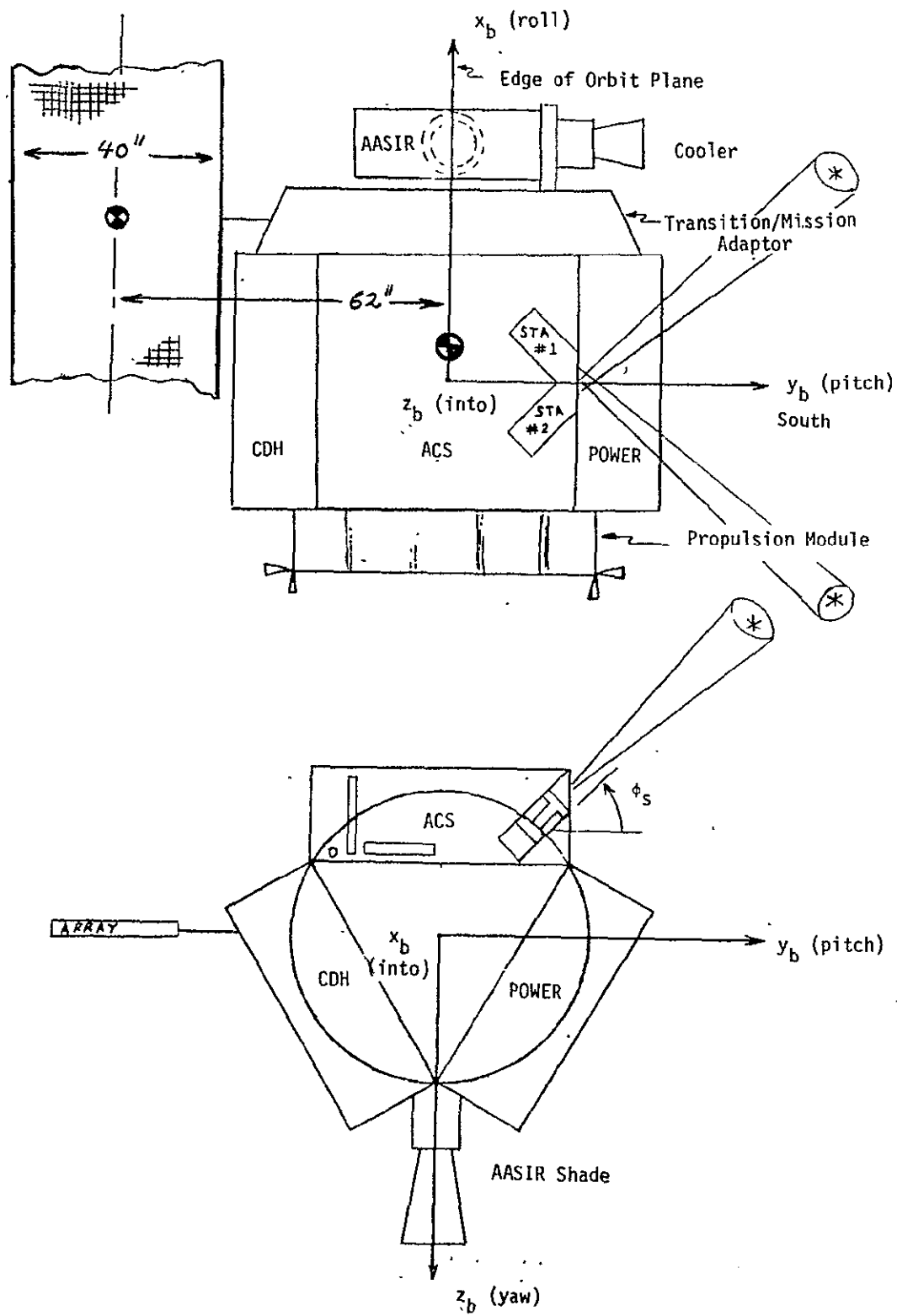


Figure 2-7. Configuration Number 2

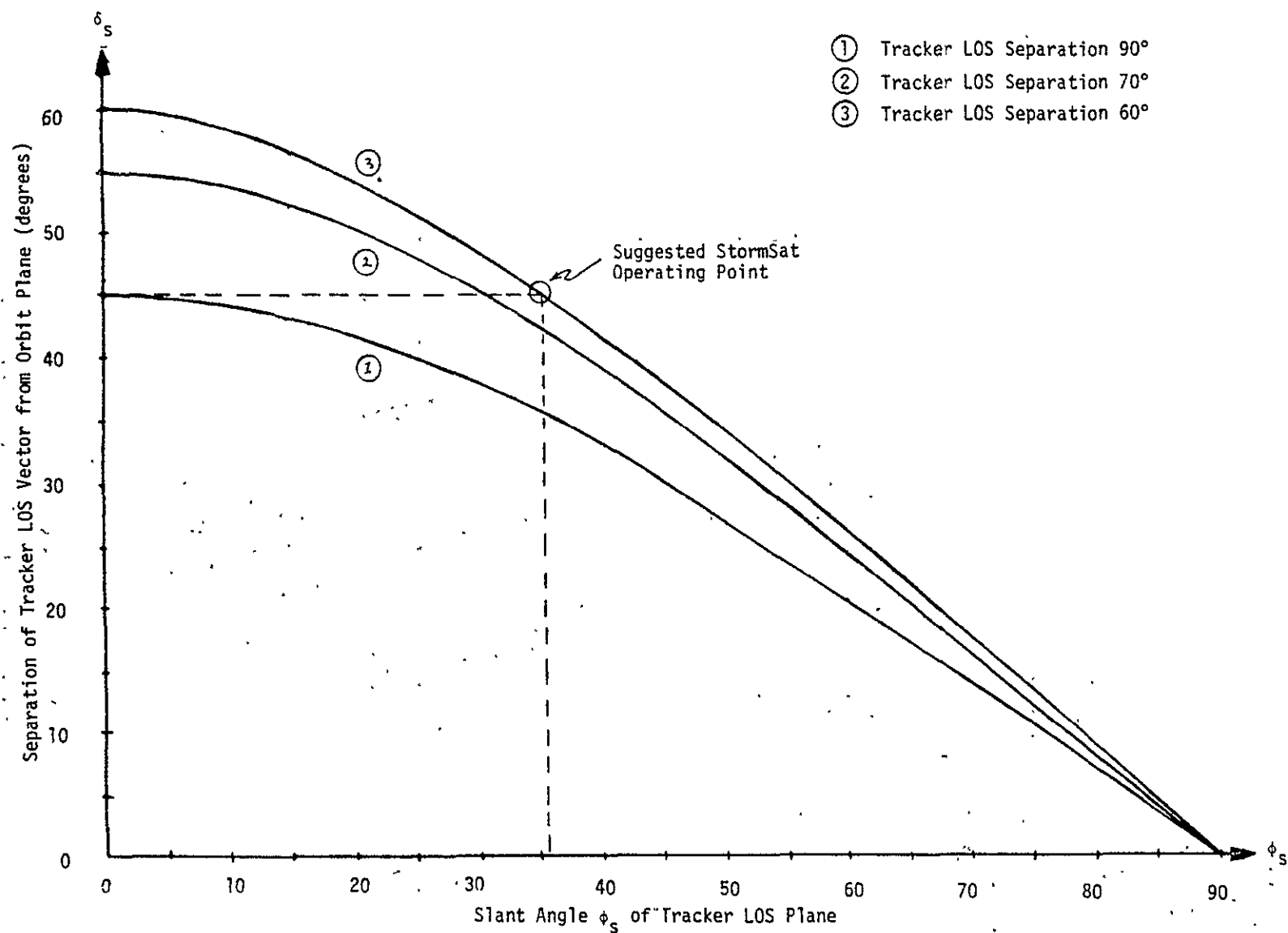


Figure 2-8. Star Tracker Orientations for StormSat/MMS Configuration Number 2

in Figure 2-6 appears most versatile with respect to different MMS orientations. However, tracker mounting constraints become severe with this slant angle because of insufficient space within the ACS module to accommodate the trackers plus their shades. A shallower slant angle of $\phi_s = 30-35$ degrees is, therefore, preferred together with a smaller tracker separation angle, and the suggested tracker orientation for StormSat appears to be the right compromise between versatility and existing mounting constraints. Should tracker mounting constraints actually force a slant angle less than 30 degrees, then this would have no impact on the StormSat mission if the MMS is flown in the orientation of configuration number 2.

More detailed configuration tradeoff considerations are documented in Reference 2 where MMS configuration number 2 was selected as the baseline spacecraft configuration for StormSat. Preliminary mass properties of the configuration are given in Table 2-1. The mass and the moments of inertia represent minimum expected values*. They include the AASIR payload with locked instrument gimbal. The self inertial of the AASIR about its gimballed (longitudinal) axis has been estimated at 5-8 slug-foot² (6.8-10.8 kg-m²). A preliminary power budget is given in Table 2-2 for the baseline Stormsat system when flying the AASIR as the only payload. Power consumptions of the subsystems listed are based on reasonable estimates obtained by increasing the budgets that were previously determined for a mission optimized spacecraft. The budgets were increased to allow for MMS standardization. But some subsystem power budgets still come out lower than the maximum permissible limits indicated in the MMS specification. Based on this power budget a single 400 watt array has been assumed for StormSat. StormSat flies with a one-sided array, because the AASIR cooler which protrudes from the spacecraft on the side opposite to the array, must have an unobstructed field of view of deep space, free from sun interference or reflection from a solar array. In sizing the array the use of light weight violet solar cells has been assumed providing

*Because the dynamic interaction between the gimballed AASIR and the spacecraft is more severe for small spacecraft inertias.

Table 2-1. StormSat Mass Properties (Preliminary)

Item	Mass (lbs)
CDH Module (minimum redundant)	101
ACS Module (four wheels)	284
Power Module (minimum redundant)	266
Propulsion Module	120
Structure	403
Thermal Control	62
Electrical Integration	73
Solar Array and Drive	125
Mission Adapter and AASIR Gimbal	200
AASIR	200
Total (Minimum Expected)	1834 (832 kg)
Principal Moments of Inertia of Spacecraft (minimum)	
Roll, I_x	240 slug-ft ² (325 kg m ²)
Pitch, I_y	270 slug-ft ² (366 kg m ²)
Yaw, I_z	300 slug-ft ² (407 kg m ²)

Table 2-2. Preliminary StormSat Power Budget (Minimum)

Item	Power (watts)
Attitude Control	130
Communications and Data Handling	100
Power Subsystem	50
Propulsion Subsystem	10
AASIR	65
Battery Charge and Contingency Margin	45
Total	400

7.53 watts/square foot of array after three years on-orbit. This yields the solar array dimensions of 40" x 192" consisting of three 40" x 64" panels. If a light weight substrate is used for these cells, the solar array weight factor is 0.51 pound/square-foot of array; if a standard substrate is used, the weight factor is 0.85 pound/square-foot of array.

2.2 Payload Description

Under the current baseline configuration the Stormsat mission will fly only one payload, the Advanced Atmospheric Sounder and Imaging Radiometer (AASIR). There is a possibility of two additional instruments; (1) a visible spectrum instrument, VSI, which at the moment is only a concept that would alleviate some AASIR operational constraints, and (2) the Microwave Atmospheric Sounding Radiometer (MASR) [5], an instrument in the planning stages. The feasibility of flying the MASR on Stormsat is addressed in more detail in Section 9. All three instruments are briefly discussed in this subsection.

2.2.1 AASIR Instrument

The purpose of the AASIR is to provide improved imaging (visible and IR) and atmospheric sounding data from geosynchronous orbit. The current configuration consists of a single axis scan system utilizing a flex pivot suspended beryllium scan mirror, a 16 inch telescope and a radiation cooler. A basic outline sketch for the AASIR is shown in Figure 2-8 [6]. The scan mirror provides line scan in the north-south direction. The orthogonal axis of scan, called the east-west frame step scan, is implemented by gimbaling the entire instrument about an axis parallel to the vehicle pitch axis and stepping it relative to the spacecraft. The gimbal consists essentially of a bearing about the 18 inch diameter section of the sensor and a linkage and direct-driven ball-screw type actuator mechanism provides the angular motion. The AASIR gimbaling concept is described in more detail in Section 3.0 of this report.

The flex pivots support the mirror at its edges and allow it to oscillate at a natural resonant frequency which allows a 20° x 20° frame to be scanned in slightly more than 20 minutes. A bi-directional scan is used. The amplitude of the scan can be controlled to provide any

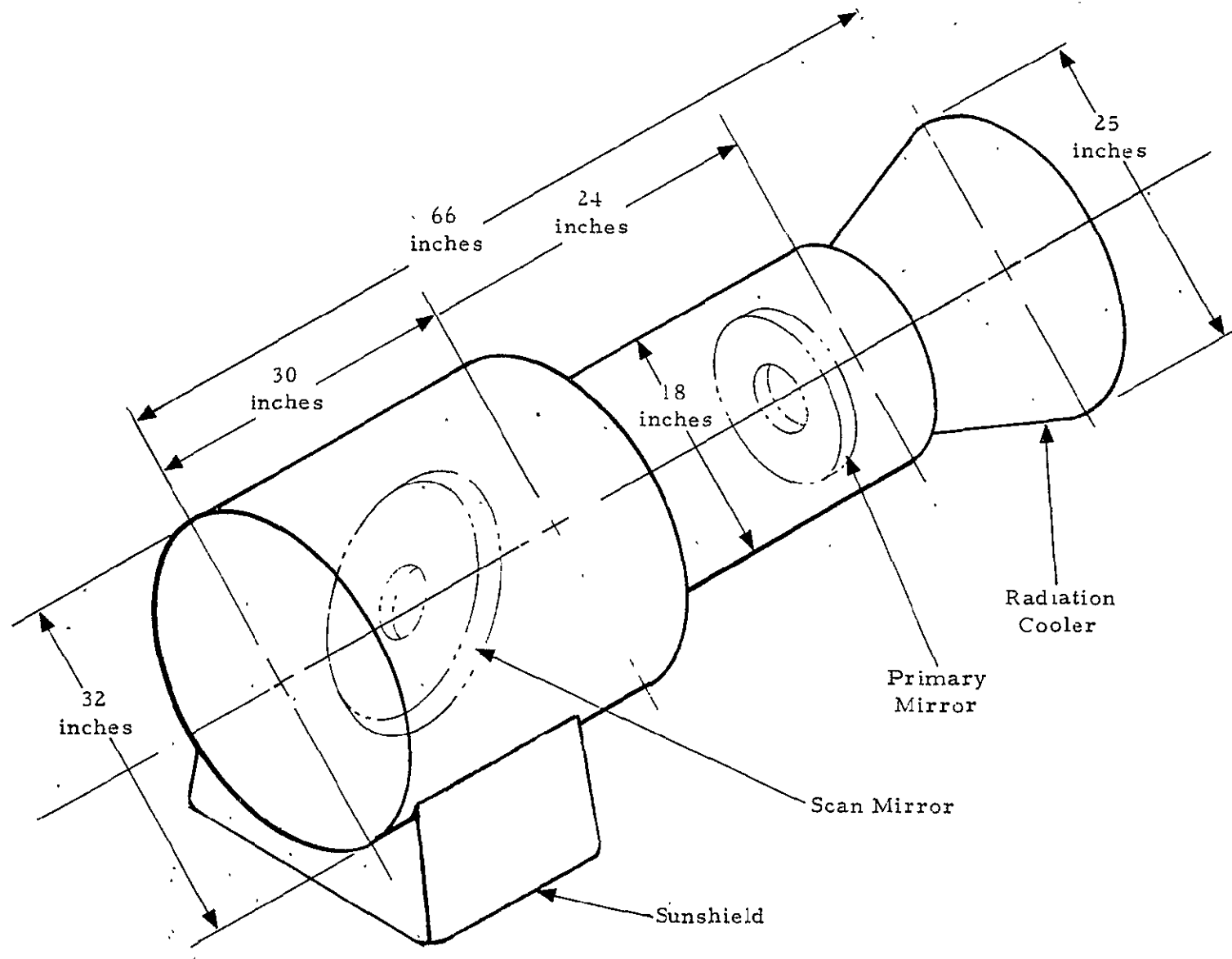


Figure 2-8. AASIR Outline Sketch

frame size up to $20^\circ \times 20^\circ$. Smaller frame sizes can be pointed to any location within the $20^\circ \times 20^\circ$ frame. The frame sizes are $20^\circ \times 20^\circ$, $4^\circ \times 4^\circ$, and $1.2^\circ \times 1.2^\circ$. Scan efficiency has been set at 60 percent; 30 percent in each direction and a turn-around time of 20 percent at each end.

Baseline Scan Pattern Used in ACS Studies

Due to the volatile nature of the AASIR design, no definite baseline scan pattern of the instrument exists at this time (April 1976). During Phase II and much of Phase III of this study, when almost all of the ACS associated investigations were conducted, the resonant line scan frequency was 0.3876 Hz. The focal plane layout of the various channels was at that time as shown in Figure 2-9. Notice that the focal plane layout also defines the projection of the detectors on the earth, and thus the detector size is also the instantaneous field of view (IFOV).

A filter wheel containing three annular bands is used in conjunction with the sounding channels. This filter wheel contains six band-pass filters in each of the three annular bands and is positioned such that the outer annulus covers the top row of HgCdTe detectors, the second annulus the middle row, and the inner annulus the bottom row of InSb detectors.

Scanning is done in the following way. Six 1 directional scans are made over the same north-south line, stepping the filter wheel at each turn-around. During the turn-around following the sixth scan the AASIR is stepped one sounding IFOV ($375 \mu\text{rad}$) in an easterly or westerly direction and the six scan sequence is repeated. Thus, after 12 half-scan periods 12 contiguous lines of data will have been scanned and each line will include all spectral channels. Following this the spacecraft steps the AASIR 11 lines ($375 \mu\text{rad}/\text{line}$) and the process is repeated. Time to accomplish a single line step equals the scan turn-around time of 0.516 second. To step 11 lines the time of an extra scan plus turn-around is added yielding 1.806 second. This scan pattern is illustrated in Figure 2-10. It is the baseline scan pattern that has been used in the ACS studies.

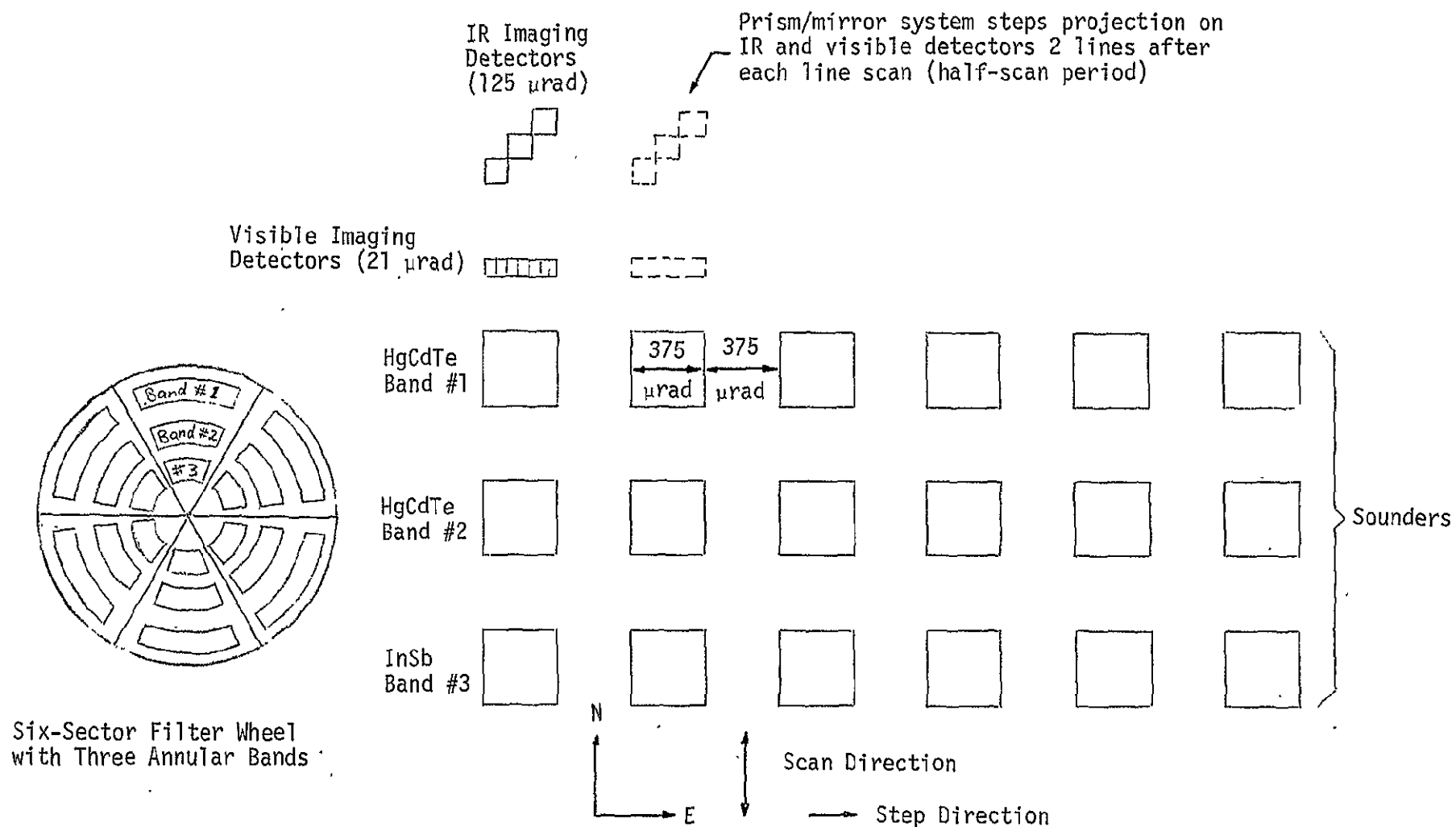
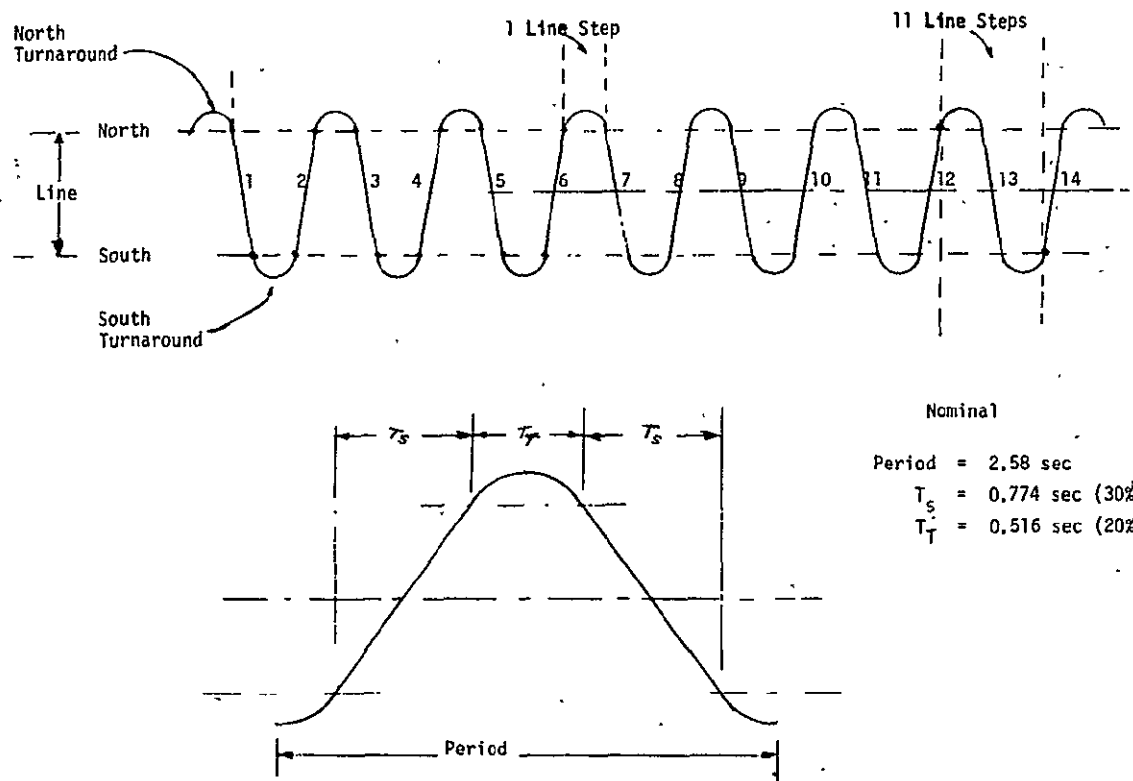
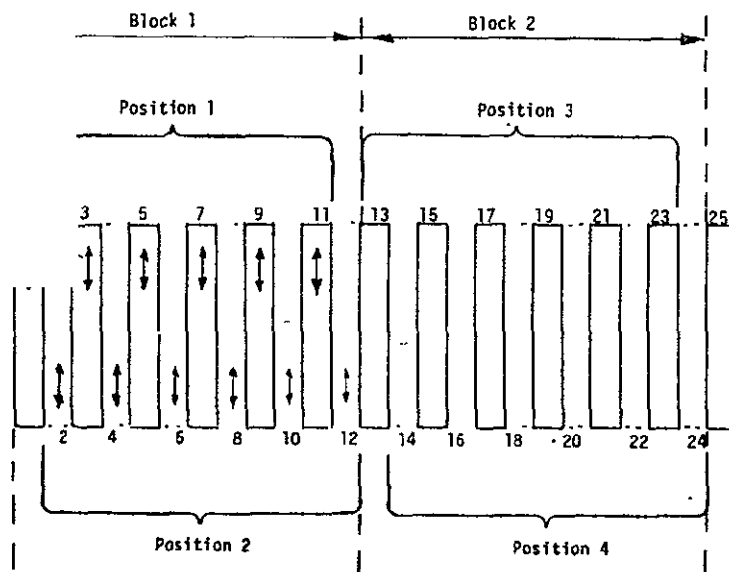


Figure 2-9. AASIR Focal Plane Layout
(Baseline for ACS Studies)



(a) AASIR Scan Timing



(b) AASIR Scan Method

Figure 2-10. AASIR Scan Pattern Used in ACS Studies

Baseline Scan Pattern Used in CDH Studies

During the middle part of Phase III of the StormSat system study the AASIR focal plane layout underwent a change which also forced a change in the scan pattern, essentially increasing the resonant line scan frequency by a factor of 1.5 yielding 0.5814 Hz. The new focal plane layout is shown in Figure 2-11. The scan pattern is essentially the same as before only that after 12 half scan periods the AASIR is stepped only seven lines instead of 11 since now only four lines are scanned simultaneously: six half scans--step 1, six half scans--step 7, six half scans--step 1, etc. Time to accomplish a single line step equals the scan turn-around time of 0.344 second. To step 7 lines the time of an extra line scan plus turn-around is added yielding 1.204 second. This is the baseline scan pattern used in the CDH studies. Tables 2-3 and 2-4 provide a summary of the line scan data and the scan frame times for both scan methods assumed in this study. Note that total frame times remain invariant. More detailed information on the AASIR can be found in Reference 6.

2.2.2 Visible Spectrum Instrument (VSI)

It is not clear if the VSI will actually become a part of the Stormsat payload. Flying of a separate VSI would overcome the following problem. When the AASIR is imaging $20^\circ \times 20^\circ$ frames full disc visible images are received. However, when the AASIR is providing higher speed smaller frames (e.g., $1.2^\circ \times 1.2^\circ$ at approximately 1.5 minute intervals) the full disc visible coverage is lost. Including a separate VSI eliminates this constraint.

The VSI has the following functional characteristics. It provides a full disc image (approximately $20^\circ \times 20^\circ$) every 30 minutes. The detectors subtend 25 μ rad which corresponds to about 0.5 miles on the surface of the earth. Therefore, there would be approximately 1.95×10^8 IFOV's in an image. Sampling each IFOV once with 8 bits gives 1.56×10^9 bits per image. Allowing 30 minutes for transmission gives an average data rate of 0.866 Mbps. Realizing that total smoothing may require an unreasonable buffer, the VSI data rate is sized at 1 Mbps. Part of the com-

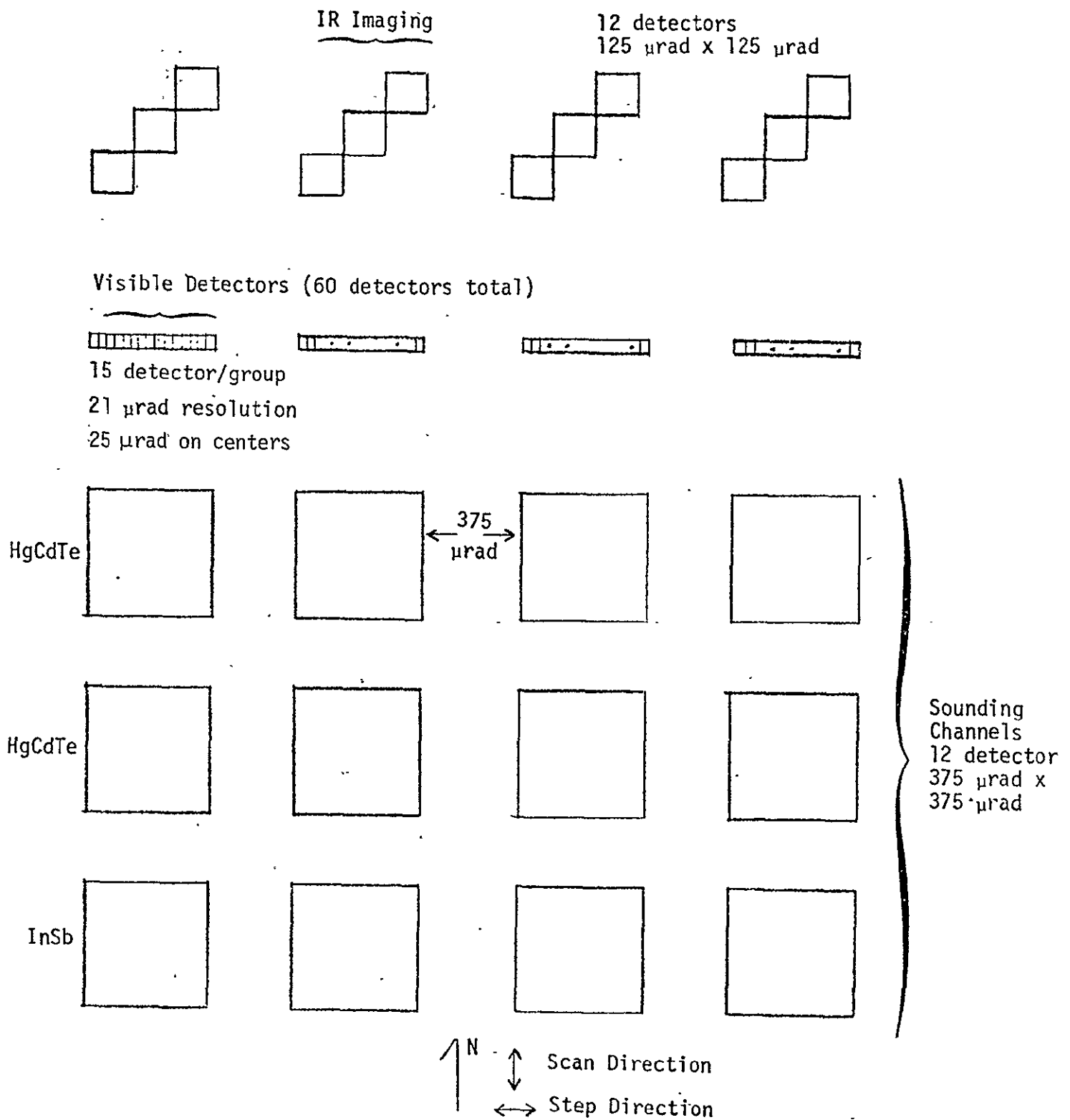


Figure 2-11. AASIR Focal Plane Layout (Baseline for CDH Studies)

Table 2-3. AASIR Scan Data

	ACS Study Baseline	CDH Study Baseline
Moment of Inertia of Scan Mirror About Line-Scan Pivot	0.43 slug-ft ²	0.43 slug-ft ²
Scan Mirror Momentum Compensation	None	None
Sinusoidal Line (Resonant) Scan Frequency (Constant for all Frames)	0.3876 Hz	0.5814 Hz
Scan Period = 1/0.3876 or 1/0.5814	2.58 sec	1.72 sec
Active Scan Time = 60% of Scan Period	1.548 sec	1.032 sec
Scan Turn Around = 20% of Scan Period	0.516 sec	0.344 sec
Maximum Mirror Amplitude for Line (Resonant) Scan	6.18 deg	6.18 deg
Frame-Scan Raster Step (1 Line = Sounder IFOV)	375 μ rad	375 μ rad
Frame-Scan Step-Time (1 Line)	0.516 sec/step	0.344 sec/step
Frame-Scan Step-Time (11/7 Lines)	1.806 sec/ 11 Lines	1.204 sec/ 7 Lines

Table 2-4. Frame Times for the AASIR

Frame Size	Number of Lines/Frame	Frame Time (sec)	Retrace Time (sec)
20° x 20°	930	1300	240
4° x 4°	186	260	48
1.2° x 1.2°	56	78	14.4

munications subsystem tasks will be to trade the use of a separate link versus unbalanced QPSK versus a multiplexed single channel for this data. Included in this trade is the realization that the VSI operates only in the daytime.

2.2.3 MASR Instrument

A spaceborne, earth viewing microwave radiometer directly measures the thermal radiation intensity (or brightness temperature) from the atmosphere and earth surface in selected spectral bands (channels). If brightness temperatures from a sufficient number of properly chosen channels are accurately measured, then one can infer from the data atmospheric temperature, water vapor, and liquid water profiles. For temperature soundings, usually several (3 to 8) channels are needed either in the oxygen complex near 60 GHz, or near a single oxygen line at 118 GHz. For water vapor, both 22 GHz and 183 GHz lines can be used.

The MASR considered here has eight channels in the 118 GHz region and eight channels in the 183 GHz region. A critical element of the MASR is a scanning reflector type antenna with an aperture diameter of 2.5 meters. At nadir, a 2.5 meter antenna will provide a half-power beamwidth of 1.3 milli-rad at 118 GHz and will project an IFOV of 47 km on the earth. At 183 GHz, the beamwidth is 0.8 milli-rad corresponding to an IFOV of 30 km. The double gimballed scanning reflector antenna mechanically provides the north-south line scan and the east-west frame step scan to image a 1500 km x 1500 km frame on the earth within 30 minutes. Both the 118 GHz and 183 GHz channels would be used with this frame. Scan efficiency is to be 80%, allowing 20% of the total frame time to be used for line turn-around and line stepping; retrace time is not included in the 30 minute frame time. In addition to the nominal 1500 km frame there exists an optional full earth coverage frame of at least $17^\circ \times 17^\circ$. Only the 118 GHz channels with beamwidth of 1.3 mrad would be used with this scan and a full earth coverage scan is to be completed within 6 hours.

The most critical component of the MASR is the double gimballed scanning reflector antenna and it will require the main effort in the development of the MASR. The double gimballed reflector antenna is also

the most critical component from a spacecraft control viewpoint. Dynamic interaction between a large scanning reflector antenna and the spacecraft may negate the pointing stability required by the AASIR. This problem is investigated in Section 9.0. Currently there exist two potential candidates for the scanning reflector antenna and the dynamic effects of both have been addressed in Section 9.0. The two candidates are: (1) the offset parabolic scanning reflector antenna and (2) the symmetrical paraboloid with a scanning mirror. Schematics of both configurations are shown in Figures 2-12 and 2-13, respectively. They are taken from Reference 5 which provides a more detailed description of the MASR.

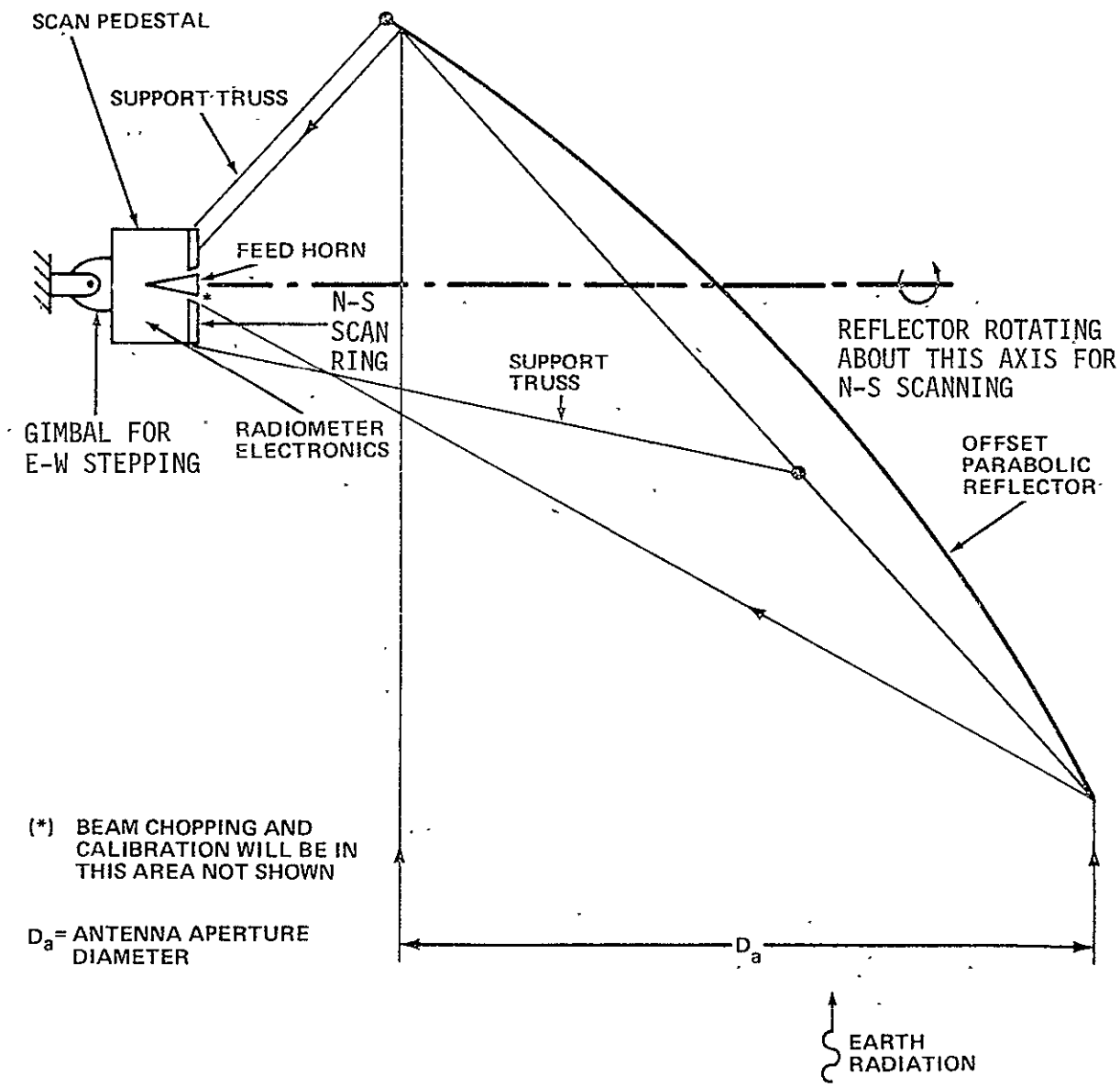


Figure 2-12. Offset Parabolic Scanning Reflector Antenna

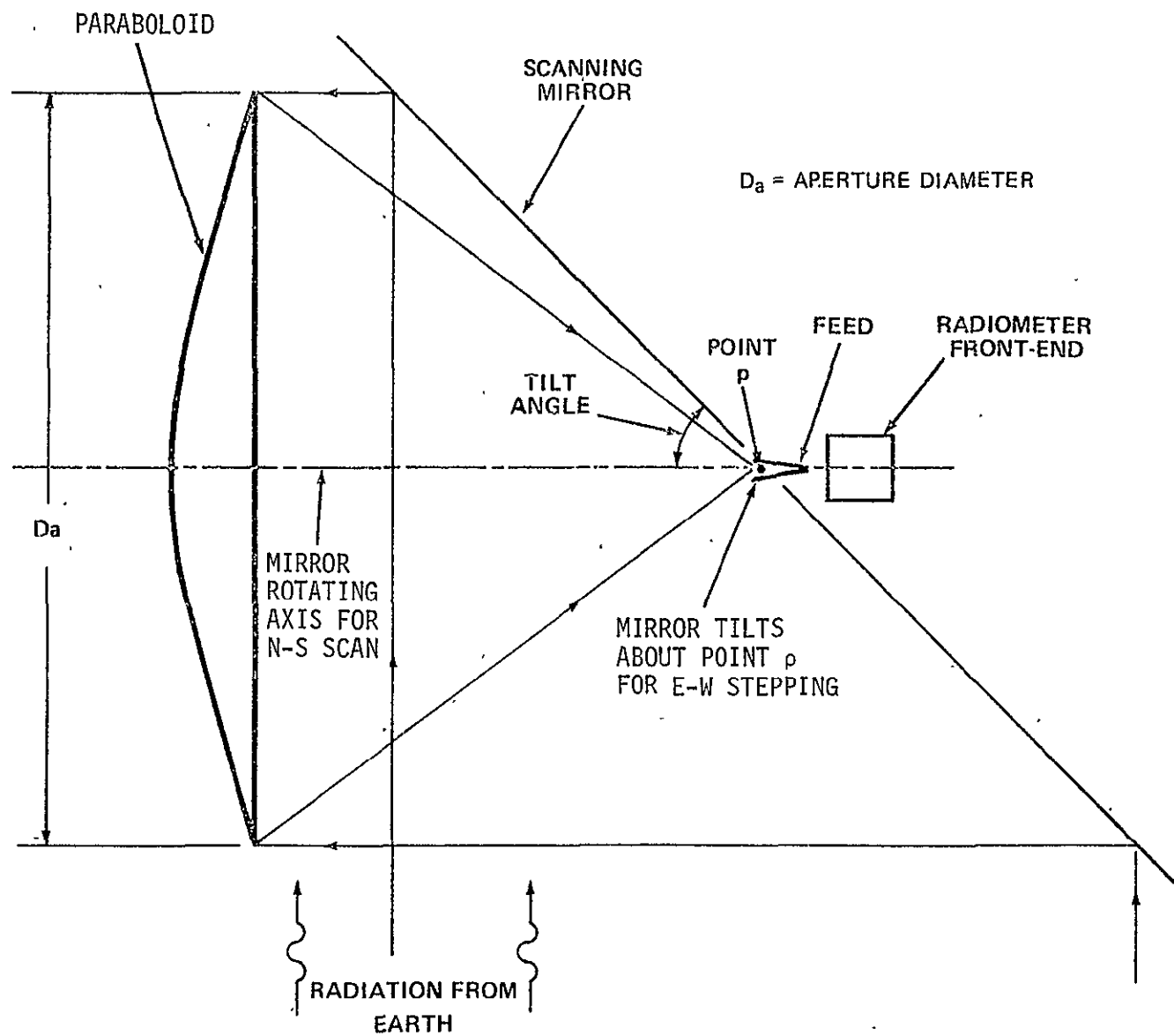


Figure 2-13. Symmetrical Paraboloid With a Scanning Mirror

2.3 StormSat Pointing Performance Requirements

The spacecraft pointing requirements are specified as follows:

- Absolute Pointing Accuracy

Roll and Pitch: 0.1 deg (1σ)

Yaw: 0.5 deg (1σ)

- Short-Term Pointing Stability Over 64 Seconds

Roll and Pitch: 4.2 μ rad (1σ) (1/5 visible channel IFOV)

Yaw: 25 μ rad (1σ)

- Long-Term Pointing Stability Over 20 Minutes

Roll and Pitch: 11 μ rad (1σ) (1/2 visible channel IFOV)

Yaw: 87 μ rad (1σ)

The short-term stability period of 64 seconds is associated with the 4.2 μ m spectral channels of the Advanced Atmospheric Sounder and Imaging Radiometer (AASIR). The baseline AASIR scan normally acquires one block of data corresponding to one scan line (one complete rotation of the filter wheel) in about 8 seconds. The 4.2 μ m channels will require 8 successive passes over the same line in order to collect sufficient radiation energy in this band. Thus, the short-term pointing stability interval which normally applies to only one block of data corresponding to the scan line, is increased eightfold, i.e., from 8 to 64 seconds. The long-term pointing stability interval of 20 minutes corresponds to the largest AASIR scan frame of 20 x 20 degrees which takes 20 minutes to complete.

Another requirement for StormSat is that spacecraft attitude data be available on the ground in real time with the following accuracy:

- Real Time Attitude Determination Accuracy

Roll and Pitch: 0.03 deg (1σ)

Yaw: 0.18 deg (1σ)

For the purposes of this study these specifications should not be interpreted as "hard" requirements, but rather as very desirable performance goals. A system that comes close to meeting these specifications could, therefore, be considered in the study, provided it had some compensating attractive feature, such as lower cost, lower weight and power, or simplicity.

The absolute pointing accuracy and the real time attitude determination specifications are not severe requirements and a spacecraft such as the MMS having a stellar-inertial attitude reference system and a reaction wheel attitude control system will have no problems meeting them. Of key concern are the pointing stability requirements which are quite severe. Since in its normal mode of operation a reaction wheel ACS can virtually stabilize the spacecraft up to the accuracy of its attitude reference, almost the entire long term pointing stability error budget can be assigned to the attitude reference system (ARS). The short term (64 seconds) pointing stability error budget will include spacecraft jitter and other disturbances acting on the payload, and the error budget must be more carefully allocated among the different subsystems. This is shown in Table 2-5.

Table 2-5. Short Term Pointing Stability Error Budget Allocation

Subsystem	1 σ Error Budget (μ rad)
Attitude Reference	2.0
Attitude Control	2.6
AASIR Gimbal Drive	2.6
Total (RSS)	4.2

2.4 On-Board Attitude Reference System

The baseline on-board attitude reference system (ARS) for StormSat uses a three-axis strapdown gyro package and two 8 x 8 degree strapdown star trackers with sensitivity $M_v = 6$. The sensor information is processed by the on-board digital computer which integrates the gyro rates to provide attitude and establishes optimal attitude and gyro rate bias updates using an extended Kalman filtering algorithm. A Kalman filtering algorithm has been chosen vis à vis a pseudo-inverse algorithm or other suboptimal techniques, because StormSat attitude reference stability requirements are very stringent. The full Kalman filter with covariance matrix propagation provides needed filter memory to smooth the star tracker random errors and also allows good on-line gyro bias calibration needed to achieve the long term pointing stability requirements of 11 μ rad over 20 minutes. Suboptimal, memoryless update algorithms, such as the pseudo-inverse, generally cannot be used to calibrate gyro biases on-board the spacecraft to the needed accuracy of 0.0015 degree/hour.

The system described above inherently provides an inertial attitude reference, and ephemeris data is, therefore, needed to obtain the spacecraft attitude relative to an earth pointing orbital reference frame as required by StormSat. Figure 2-14 shows a functional block diagram of the system. Quaternions, \bar{q} , relative to an earth centered inertial (ECI) reference frame are used as attitude variables. The time T_u between star updates depends on the mode of operation selected for the system and this will be discussed further in the sequel.

The two star trackers are oriented to prevent sun interference as discussed earlier in Section 2.1 and as shown in Figure 2-15. Using the Yale star catalog, star availability studies were conducted and it was determined that with two strapdown trackers with 8 x 8 degree FOV and sensitivity $M_v = 6$, at least one of the trackers will have a usable star in its FOV at all times. Even a single tracker will have a usable star in its FOV at all times except for one 14 minute period per orbit during the summer months (southern hemisphere swath), and two 8 minute periods

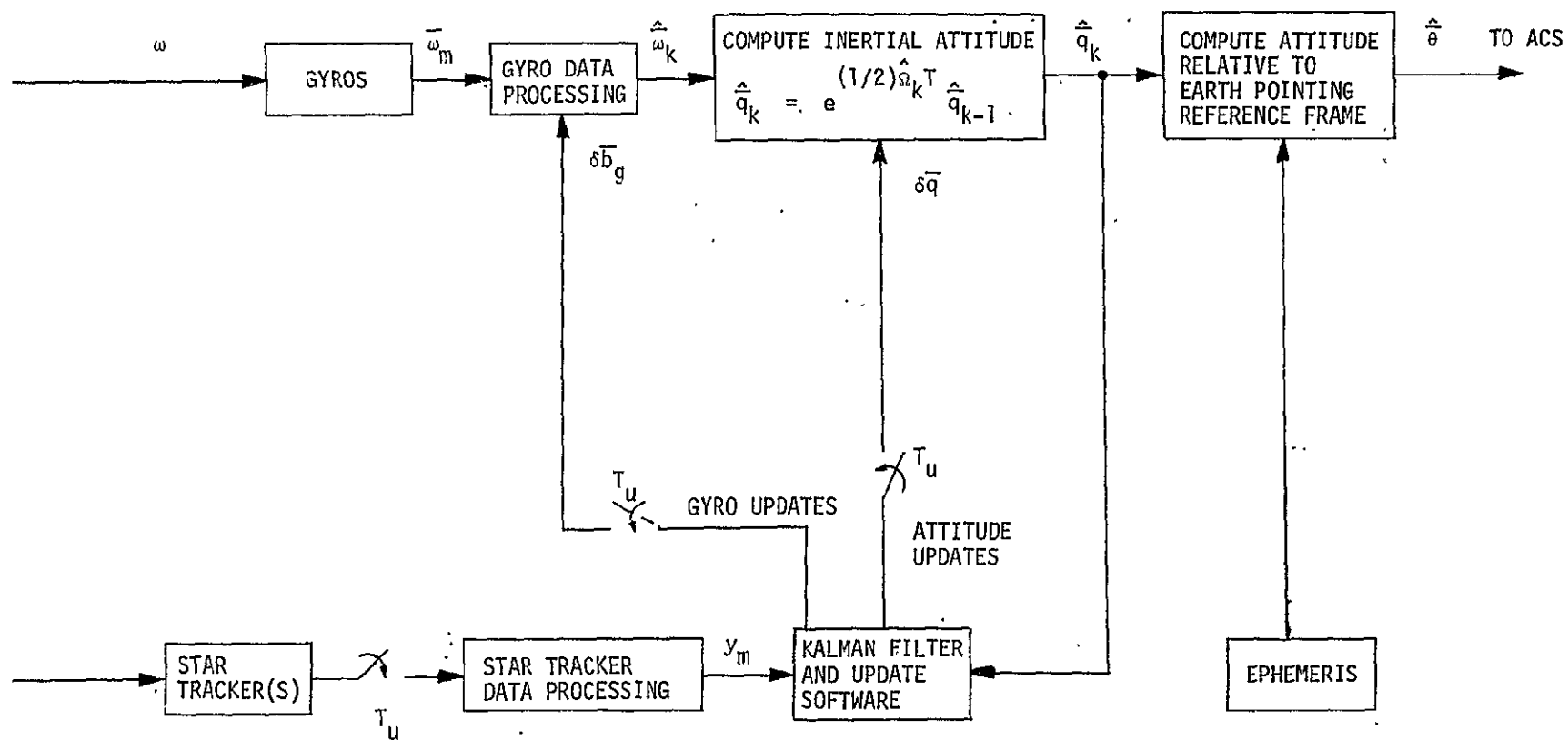
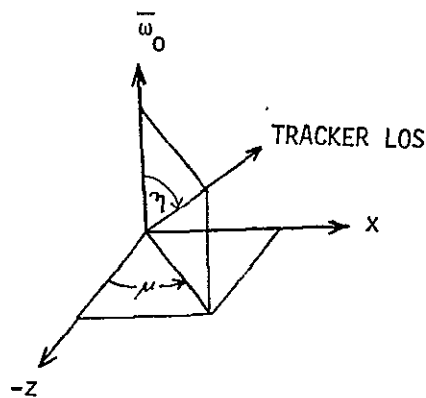
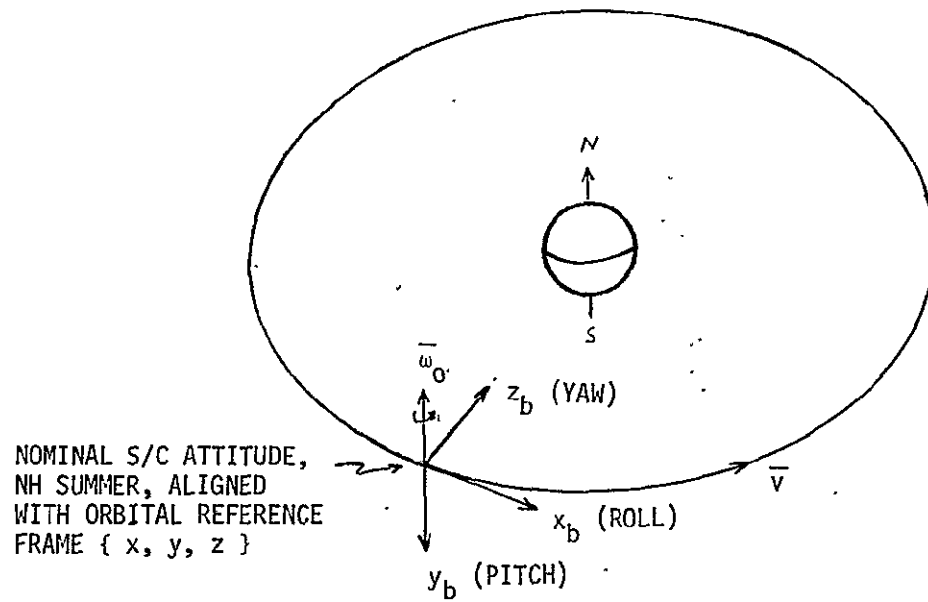


Figure 2-14. Functional Block Diagram Stellar-Inertial ARS



TRACKER NUMBER 1: $\mu_1 = +45^\circ$; $\eta_1 = 135^\circ$ (NH SUMMER) ; $\eta_1 = 45^\circ$ (NH WINTER)
 TRACKER NUMBER 2: $\mu_2 = -45^\circ$; $\eta_2 = 135^\circ$ (NH SUMMER) ; $\eta_2 = 45^\circ$ (NH WINTER)
 (NH = Northern Hemisphere)

Figure 2-15. Strapdown Tracker Orientation

per orbit during the winter months (northern hemisphere swath; the spacecraft makes a 180 degree yaw turn at the equinoxes). Thus, attitude updates could be obtained, for example, quasi-continuously, every 64 seconds (which is the short-term pointing stability period), or at the end of an AASIR imaging frame which may last anywhere from about 1 to 20 minutes. Currently available high quality gyros, such as the Bendix 64-PM-RIG, for example, can provide a one-sigma attitude stability over 20 minutes of about 1.9 arc-second and thus meet the long-term attitude stability requirements for StormSat. It, therefore, appears suitable to obtain updates whenever one large or several small AASIR imaging frames have been completed. This reduces the frequency of the update computations. For the larger frames approaching the maximum duration of 20 minutes, attitude update jumps of about 4-5 arc-seconds can be expected at the end of the frames.

These attitude update jumps at the end of the larger imaging frames appear permissible, especially since the updates are deterministic, i.e., the flight computer knows, how large an update it has computed. Attitude stability obtained in this manner may be termed "epoch time stability," or "discrete block stability." That is, the stability requirements are met for a discrete time block of no longer than 20 minutes, referenced to the initial time of the block, the so called epoch time. For StormSat, epoch times would always coincide with the beginning of AASIR imaging frames. This mode of operation of the ARS appears to be a viable choice for StormSat.

If the 4-5 arc-second attitude update jumps at the end of the longer lasting frames are not allowed, the attitude and gyro bias updates should be processed every 64 seconds in synchronism with the short-term pointing stability period. This significantly reduces the attitude update jumps, and based on three-axis covariance analyses results using the real star-field, an attitude reference stability of about 1.7 arc-second (1σ), (8.25 μ rad) relative to the mean attitude error can be maintained for all time. This easily meets the long-term stability requirements. Furthermore, it has been shown that the attitude provided by the integrated gyro rates between the 64 second updates is sufficiently smooth to assure that the short-term stability error budget of 2 μ rad allotted to the ARS, can be met.

There is no need to decide at this point which update mode should be used since it merely involves the choice of nominal update time intervals and this could actually be varied by ground command once the spacecraft was on-orbit. Tables 2-6 and 2-7 provide error analyses for the gyro induced errors over the short-term and long-term attitude stability intervals, respectively. Table 2-8 presents an error analysis for the BBRC CT-401, $8^\circ \times 8^\circ$ FOV strapdown tracker. Tracker FOV calibration by two third order polynomials (one per axis) as proposed by the MIT Center of Space Research [4] has been assumed. A performance summary of the attitude reference system when processing star measurements for attitude and gyro bias updates every 20 minutes, is provided in Table 2-9. As can be seen, all ARS accuracy and stability requirements are met and exceeded. More detailed documentation of the ARS design and analysis is contained in Section 3.0 of Reference 2.

Even though potentially better performance could be achieved with double gimballed star trackers, strapdown star trackers have been recommended for the StormSat baseline attitude reference system for the following reasons:

- (1) Star availability is no problem for the strapdown trackers available on the MMS ACS module detecting stars to sixth magnitude.
- (2) A system using strapdown trackers can meet the StormSat attitude reference stability and accuracy requirements.
- (3) The strapdown trackers are available anyway in the MMS ACS module while the gimballed trackers would be additional, mission peculiar equipment.
- (4) Even though gimballed star trackers are generally more accurate than large FOV strapdown trackers, their electro-mechanical tracking and gimbal angle encoding systems present a potential source of error with attendant accuracy degradation.

Table 2-6. Short-Term Attitude Stability: Gyro Induced Attitude Reference Errors Accumulated over 64 Seconds when Updates are Computed Every 20 Minutes

Error Source (1 σ)	1 σ Contribution per Axis (arc-sec)
Gyro Bias Uncertainty, $\delta b_g = 0.0013$ deg/hr*	0.083
Gyro White Torque Noise, $\sigma_v = 0.0156$ arc-sec/ $\sqrt{\text{sec}}$	0.125
Gyro Random Bias Drift, $\sigma_u = 2 \cdot 10^{-5}$ arc-sec/sec ^{3/2}	0.006
Gyro Scale Factor Uncertainty, $\delta k = 50$ ppm**	-----
Gyro Input Axis Alignment Uncertainty, $\delta \gamma = 3-5$ arc-sec**	-----
Signal Generator Noise, Commutation Error and Quantization ***	0.1
Computer Roundoff Error**	0.07
Total RSS (arc-sec)	0.2
	0.97 μrad

*Residual Error in Kalman Filter Estimate

**For a non-slewing spacecraft with nominally zero body rates these error sources have a negligible effect on attitude estimation. Attitude errors due to misaligned roll/yaw gyros and the orbit rate, are estimated as a part of the gyro biases.

***Gyro Sampling Period $T = 200-400$ ms

Gyro Scale Factor $k = 0.01$ arc-sec/pulse

Assuming a 24 bit Wordlength used in Calculations

Table 2-7. Long-Term Attitude Stability: Gyro Induced Attitude Reference Errors Accumulated Over 20 Minutes

Error Source (1σ)	1σ Contribution per Axis (arc-sec)
Gyro Bias Uncertainty, $\delta b_g = 0.0013$ deg/hr*	1.56
Gyro White Torque Noise, $\sigma_v = 0.0156$ arc-sec/ $\sqrt{\text{sec}}$	0.54
Gyro Random Bias Drift, $\sigma_u = 2 \cdot 10^{-5}$ arc-sec/sec ^{3/2}	0.48
Gyro Scale Factor Uncertainty, $\delta k = 50$ ppm**	----
Gyro Input Axis Alignment Uncertainty, $\delta \gamma = 3-5$ arc-sec**	----
Signal Generator Noise, Commutation Error and Quantization***	0.7
Computer Roundoff Error***	0.1
Total RSS (arc-sec)	1.86
	9 μrad

*Residual Error in Kalman Filter Estimate

**For a non-slewing spacecraft with nominally zero body rates these error sources have a negligible effect on attitude estimation. Attitude errors due to misaligned roll/yaw gyros and the orbit rate, are estimated as a part of the gyro biases.

***Gyro Sampling Time Period $T = 200-400$ ms.
Gyro Scale Factor $k = 0.01$ arc-sec/pulse
Assuming a 24 bit Wordlength used in Calculations

Table 2-8. BBRC CT-401, 8° x 8° FOV Star Tracker Characteristics

Error Source	Error Without Compensation	1 σ Error With External Compensation (arc-sec)	Comments
<u>Slowly Varying Biases</u>			
Null Offset & Nominal Dynamic Lag	18 arc-sec (1 σ)	---	Calibrated out by bench test No further compensation
Aging (Nullshifts, Dynamic Lag Shifts, etc.)	4 arc-sec (1 σ)	4.0	
Total Biases (RSS)	18.4	4.0	
<u>Errors Appearing Random for Discrete Star Observ.</u>			
Nonlinearity & Nonorthogonality	10 arc-min (peak)	3.0	} Bench calibration by polynomial fit: 60 coeffi.
Temperature & Power Sensitivity ($\pm 30^{\circ}\text{C}$)	2 arc-sec/ $^{\circ}\text{C}$		
External Magnetic Field (0.4 gauss)	10 arc-sec (peak)	2.5	} Correction factors/terms obtained from bench test
Star Intensity ($\Delta M_V = 3$)	30 arc-sec (1 σ)	2.5	
Scale Factor Changes (Aging)	10 arc-sec (1 σ)	1.5	Occasional updates from ground-based Kalman filter
Subtotal (RSS)	203.5	4.9	
<u>Noise</u>			
NEA (Noise Equivalent Angle)	5 arc-sec (1 σ) ($\tau = 0.5$ sec, $M_V = 6$)	5.0	No compensation
Total Random Errors for Discrete Star Observ. (RSS)	203.6	7.0	
Total 1 σ Accuracy (Σ Random + Bias)	222 arc-sec	11 arc-sec	

Table 2-9. Performance Summary of ARS Using Fixed Head Trackers
and Star Updates Every 20 Minutes

Error Sources	Short-Term (64 seconds) Attitude Stability per Axis (1σ) (arc-sec)	Long-Term (20 minutes) Attitude Stability per Axis (1σ) (arc-sec)	Absolute Attitude Deter- mination Accuracy per Axis (1σ), at Tracker (arc-sec)	
			Randomly Varying	Slowly Varying Biases
Gyros (see Tables 2-6 & 2-7)	0.2	1.86	1.86	
Fixed Head Star Tracker:				
Noise (7 arc-sec)	---	---	4.37*	
Fixed Residual Bias (4 arc-sec)	---	---		4.0
Spacecraft Ephemeris Position Within 1 km (3σ)	---	---		1.9
Total RSS (1σ)	0.2 arc-sec	1.86 arc-sec	4.75	4.48
			9.18 arc-sec	
	0.97 μ rad	9.0 μ rad	44.5 μ rad	

*Contribution after Kalman filtering

2.5 Attitude Control System

This subsection provides a summary of the attitude control system addressing mainly the normal on-orbit control mode. Details of the design, analysis and performance evaluation of the ACS were documented in Sections 4.0 and 5.0 of Reference 2.

2.5.1 ACS Functional Operating Modes

StormSat is a shuttle launched spacecraft and will be injected into synchronous orbit by the IUS. During injection the IUS provides its own stabilization system and the spacecraft tip-off rates after separation from the IUS are small (less than 0.3 degree/second). The ACS provides all functions associated with controlling spacecraft attitude from IUS separation to end of life. Control of the solar array is considered an ACS function.

In particular, the ACS provides the following functions.

- Earth Acquisition - After separation from the IUS the solar array is deployed and the spacecraft acquires the sun with the negative yaw axis using the reaction wheels for control and the RCS for momentum removal as required. The array-located coarse sun sensors and the precision digital sun sensor located in the ACS module serve as attitude reference. A roll about the sun line (spacecraft yaw axis) is initiated and the brightest star encountered by the trackers is identified by correlation with the on-board star catalog. The attitude described by the sun line and the brightest star vector serves to initialize the on-board stellar-inertial attitude reference system. In conjunction with ephemeris data the attitude of the spacecraft relative to the earth can be determined and a maneuver is initiated to point the spacecraft yaw axis ($+z_b$) to the center of the earth. The spacecraft pitch axis ($+y_b$) is pointed normal to the orbit plane; the positive pitch axis points south between

21 March and 21 September, and north during the remaining part of the year.

- Normal On-Orbit Attitude Control - Normal on-orbit attitude control is accomplished by four reaction wheels. The ACS is to maintain spacecraft attitude such that the body fixed reference frame $\{x_b, y_b, z_b\}$ is aligned with the orbital reference frame $\{x_r, y_r, z_r\}$ within the previously given attitude accuracy and pointing stability specifications. The z_r axis of the orbital reference frame points to the center of the earth, y_r is normal to the orbit plane pointing south between 21 March and 21 September and north during the remaining part of the year.
- Momentum Unloading - In the baseline StormSat ACS, angular momentum is removed using the RCS. The thruster pulses are preemphasis compensated by introducing precomputed wheel speed change commands at the appropriate times. The specified pointing accuracy can be maintained, but the very stringent pointing stability requirements cannot. Momentum unloading is performed between imaging frames and due to the large wheel capacity (20 Nms = 15 foot-pound-second/wheel) it could be performed as infrequently as once every 4-5 orbits. It is desirable to perform unloading once per orbit to minimize precession disturbance torques due to the interaction of the momentum stored in the system and the orbit rate. An alternate momentum unloading scheme utilizes magnetic torquing in conjunction with a large air core coil mounted on the solar array (the earth field at synchronous altitude is too weak for the standard 100,000 pole-cm ACS torquer bars to do the job alone). This scheme is analyzed in detail in Section 7.0 of this report and appears feasible. Momentum unloading would occur quasi-continuously and would not affect the normal on-orbit attitude accuracy and pointing stability.

- Solar Array Control - The solar array drive must be locked during imaging. Analysis has shown that with conventional solar array stepper drives the spacecraft pointing stability requirements cannot be met during array stepping. The solar array is, therefore, step-slewed through angles of up to 5 degrees between imaging; that is, during frame retrace times. Asynchronous stepping of the array is employed to minimize excitation of array structural bending modes. Frame retrace times are long enough to permit this mode of operation, see Table 2-4.

- E-W Stationkeeping and Repositioning - E-W stationkeeping will permit spacecraft drift up to ± 0.5 degree. Assuming a satellite station at a geographic longitude of 95 degrees West of Greenwich, stationkeeping would have to be performed about once every 90 days. The orbit adjust thrusters are used to provide the necessary E-W ΔV of about 0.5 foot/second per stationkeeping maneuver. It would take about 3 minutes to complete a stationkeeping maneuver using 10 pounds of thrust. During ΔV thrusting the spacecraft is in an all-thruster attitude control mode and the normal on-orbit spacecraft pointing accuracy and stability requirements cannot be met. AASIR imaging must, therefore, be suspended during this period.

- N-S Stationkeeping - N-S stationkeeping will probably also be required for StormSat since even for small orbit plane inclination errors the nadir point drift rate at the orbit nodes exceeds allowable limits to permit subsequent overlays of imaging frames. Section 8.0 establishes two possible N-S stationkeeping policies. One would perform N-S stationkeeping twice per day at the nodal crossings. The spacecraft attitude could be maintained by the reaction wheels but pointing stability could still not be satisfied and imaging has to be

suspended. Orbit plane inclination would be maintained within $\Delta i = 0.0013$ degree. The other scheme would perform N-S stationkeeping every 39 days maintaining $\Delta i \leq 0.1$ degree. All-thruster attitude control would be required and imaging must be suspended. The fuel consumption is 49.6 pounds per year. The N-S stationkeeping maneuver is complicated by the fact that the spacecraft needs to be reoriented for it. For more details on N-S ΔV , thruster firing times, etc., see Section 8.0.

- 180 Degree Yaw Turn - Twice per year at the equinoxes the ACS will initiate a 180 degree yaw turn of the spacecraft to keep the sun away from the AASIR cooler. This maneuver can be performed with the reaction wheels.

2.5.2 Normal On-Orbit Attitude Control

The MMS standard ACS module will provide four reaction wheels for normal on-orbit control. Each reaction wheel has a momentum capacity of 20 Nms (15 foot-pound-second) and a nominal torque capability of 0.15 Nm (21 ounce-inches). Three of the wheels are arranged orthogonally along the vehicle roll, pitch and yaw axes, respectively, and the fourth wheel is skewed at the same angle with respect to all three so that its momentum can equally contribute to any spacecraft control axis. The wheel locations in the ACS module were shown in Figure 2-6 in Section 2.1.

The solar disturbance torque due to the solar pressure unbalanced spacecraft configuration (single solar array) is the only significant external disturbance torque for StormSat, and the secular component acting in the orbit plane is given by

$$T_s = 4.4 \times 10^{-5} \text{ Nm } (3.25 \times 10^{-5} \text{ ft-lb})$$

which integrates to an angular momentum of

$$H_{ORB} = 3.8 \text{ Nms } (2.8 \text{ ft-lb-sec})$$

per orbit. The momentum capacity of 20 Nms per reaction wheel is, therefore, more than sufficient in the application of the MMS to the StormSat mission.

Figure 2-16 shows a functional block diagram of the attitude control system. Spacecraft attitude and rate data is provided by the attitude reference system as was discussed in Section 2.4. The attitude reference algorithm, the vehicle control laws, the transformation from body to wheel coordinates, momentum unloading logic, and preemphasis compensation, are all implemented in the digital flight computer which resides in the Communications and Data Handling Module. The software requirements to perform these tasks are sized in Section 2.6.

The preemphasis compensation indicated in Figure 2-16 introduces torque commands directly to the reaction wheels. It is basically an anticipatory compensation that tells the system of certain disturbances which are about to occur, thereby enhancing the response capability of the ACS without increasing the bandwidth. Preemphasis compensation is used before and during RCS thruster firings for momentum removal, and whenever the gimbaled AASIR or the GSMR reflector antenna (the latter if present) are being stepped. This will be more fully explained in a later section.

In the design and analysis of the normal on-orbit attitude control system three control approaches for using reaction wheels were pursued: torque control, momentum control, and speed-biased control. Of main concern were spacecraft jitter (pointing stability) during normal on-orbit operation and the attitude transient created by speed reversal of the roll/yaw reaction wheels occurring four times per orbit (except for the speed-biased mode of operation). For the torque and momentum control mode the three orthogonal wheels are assumed to be active with the fourth skewed wheel being standby redundant. In the speed-biased mode of operation all four wheels must be active in order to maintain a nominally zero momentum bias system.

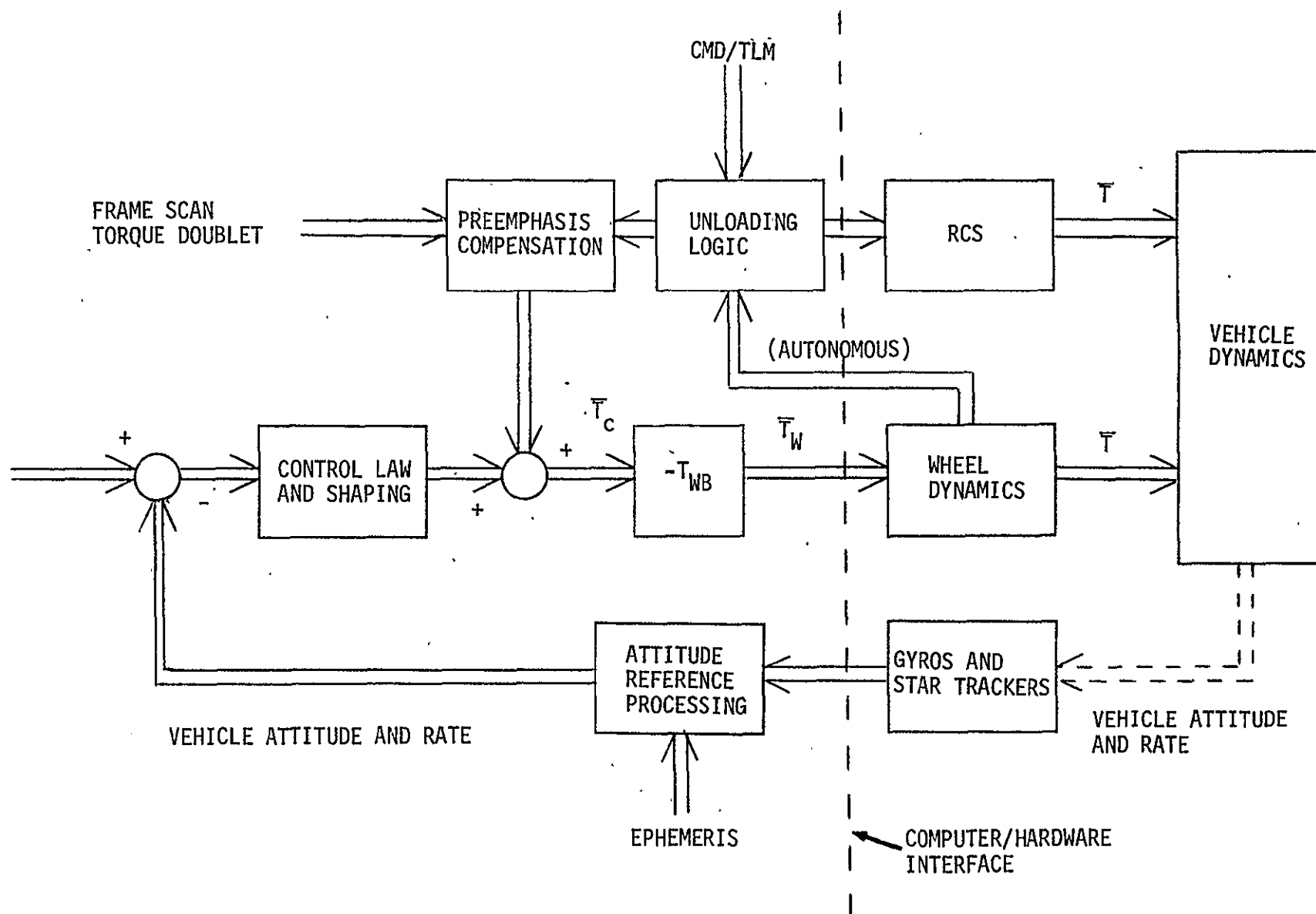


Figure 2-16. Attitude Control System Functional Block Diagram

In the torque control mode vehicle attitude errors are adjusted by torque commands to the reaction wheels, and in the momentum control mode the system error signals command wheel momentum. The main features of the two modes of control are shown by means of block diagrams in Figures 2-17 and 2-18 and a brief description of each is given here along with some of the major tradeoffs that were considered.

As shown in Figure 2-17, the torque mode requires an attitude rate feedback signal which requires the use of rate gyros and consideration of the effects of gyro signal quantization and gyro noise. When multiplied by the rate gain, the rate signals provide the vehicle damping, and thus the gyro noise effects may provide an upper limit for rate gain values. The momentum mode, Figure 2-18, avoids the requirement for gyros to determine vehicle rates, but requires a tachometer on each wheel to provide wheel speed used to form the wheel momentum error signal. Physical considerations limit the number of tachometer pulses per wheel revolution and this quantization effect produces tachometer ripple which affects overall pointing stability. In particular, the response of the tachometer loop is governed by the speed servo gain and it is desirable to have this gain high. This is equivalent to having a high servo loop bandwidth or a speed servo that responds exactly to commands. The reason for this is that lowering the bandwidth effectively reduces the equivalent "rate" damping of the momentum mode. However, because the quantization and delay involved in the tachometer loop imply that it is a sampled-data system, stability requirements place an upper limit on the loop gain even though it is basically only a first order loop.

In the speed-biased mode of operation of the wheel system, the fourth wheel is run at a fixed bias speed so that wheel speed reversal does not occur for the three main control axis wheels. If the wheel system is not operated in this way, both the momentum and torque modes must face the problem of wheel speed reversal at certain points in the orbit. At speed reversal, the wheel friction causes a transient response of magnitude and duration that must be considered in view of the stringent pointing stability requirements. The momentum mode philosophy is that the

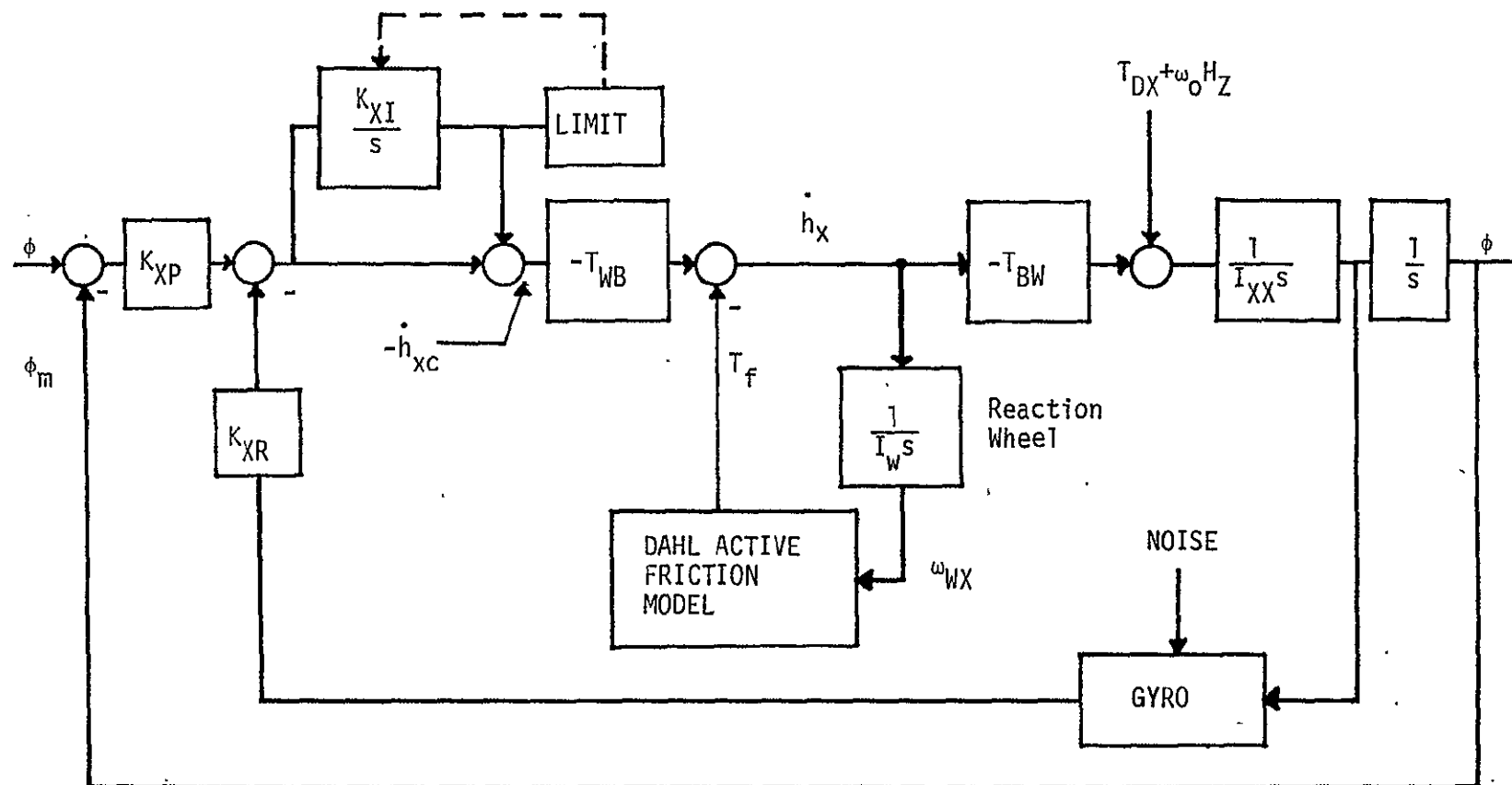


Figure 2-17. Single Axis Model of Torque Control Mode. (Transformations T_{WB} , T_{BW} are unity for single-axis analysis and for the case of three orthogonal wheels)

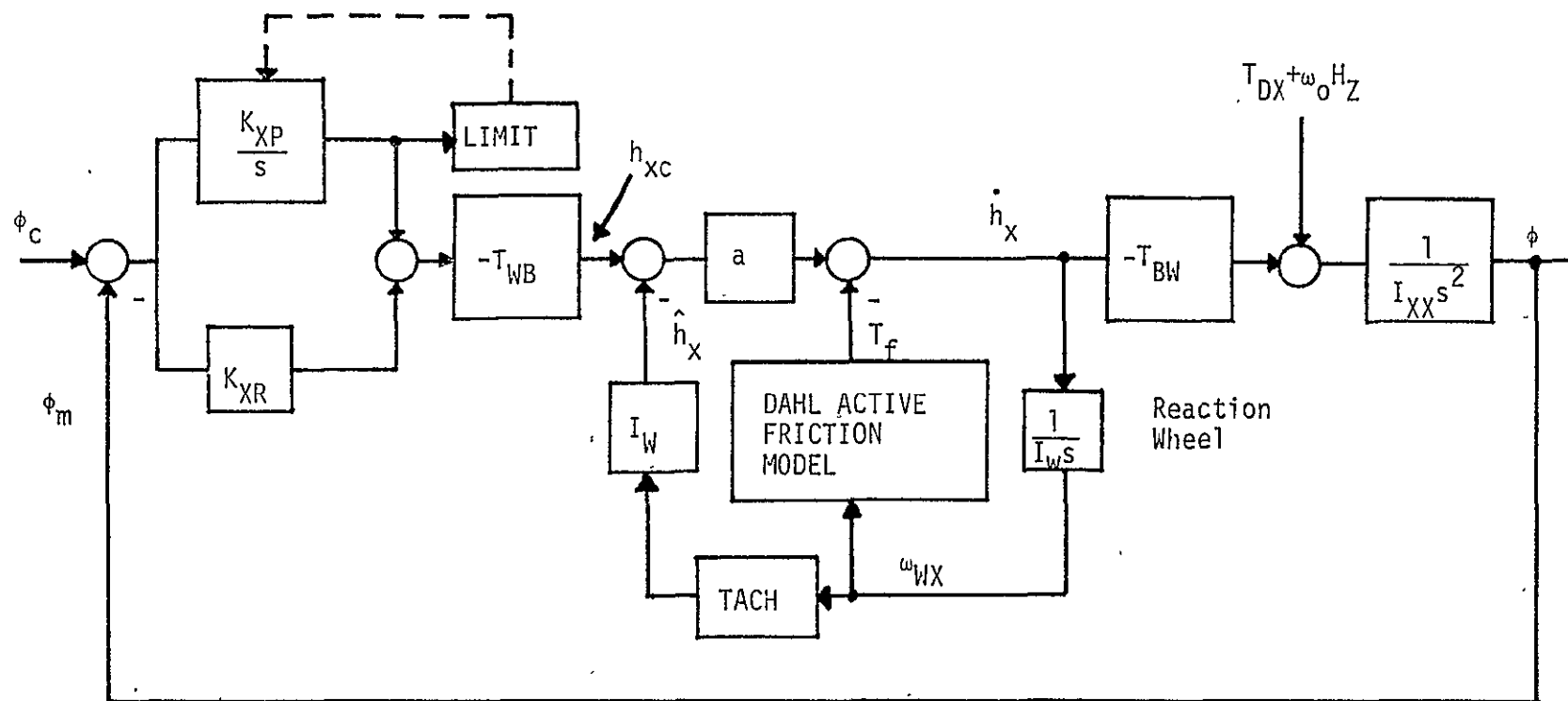


Figure 2-18. Single Axis Model of Momentum Control Mode. (Transformations T_{WB} , T_{BW} are unity for single-axis analysis and for the case of three orthogonal wheels)

nonlinearities associated with the wheel and tachometer are contained in a tightly controlled high bandwidth inner loop which minimizes their effects on the outer rate and position loops. The problem here is that the tachometer servo loop is not perfect, and, because of tachometer quantization, speed information is lost at the very low speeds preceding reversal of the wheel. The result is that the wheel is not driven smoothly through reversal and a transient does occur. In the torque mode, an integrator in the forward loop as shown in Figure 2-17, acts to reduce the magnitude of the speed reversal transient. When reversal occurs, friction torque reverses causing an attitude error buildup, and at a rate determined by the integrator gain, the integrator produces a torque command output to oppose the friction torque and thus reduce the transient response. However, the gain on the integrator is related to other system gains and to the effect of gyro noise on attitude stability (jitter), and thus a tradeoff must be considered.

Since both modes of control involve saturation limits as well as the same wheel model containing nonlinear friction modelled by Dahl's model, the systems are highly nonlinear and, therefore, not easily amenable to analytic study. Although many of the system gain values can be set by using simple linear models, the detailed response of the system needed for deciding on one mode over the other is not obtainable in this way. Thus a three-degree-of-freedom orbital simulation was developed which models both modes of control. It includes the effects of nonlinear friction, contains refinements and options to model tachometer deadzone, quantization and delay, as well as gyro quantization, noise, and sampling effects.

The simulation results obtained, showed that neither torque control nor momentum control could maintain attitude accuracy/stability within the required $11 \mu\text{rad}$ during wheel speed reversal if a reasonably low system bandwidth was to be maintained. The speed crossover error is deterministic, causing a peak attitude disturbance of about $50 \mu\text{rad}$ in the momentum control mode; and $90 \mu\text{rad}$ in the torque control mode (the latter with appropriate integral compensation). The entire crossover disturbance

lasts 1-2 minutes depending on the total momentum stored in roll/yaw at the time, and the friction characteristics of the reaction wheel. System bandwidth was kept in the 0.2-0.5 rad/second range.

In the momentum control mode a 100 pulse-per-revolution tachometer was assumed, while the attitude rate feedback required in the torque control mode was obtained from a rate gyro with appropriately modelled quantization and noise ($\sigma_{\Delta\theta} = 0.04$ arc-second, $k_g = 0.01$ arc-second/pulse). The attitude jitter/instability induced by the blipper tachometer was significantly larger than the jitter induced by the gyro noise, and the momentum control mode could hardly meet the short-term stability requirement of $4.2 \mu\text{rad}$ (1σ), while the torque control mode had no problems in this respect. Considering also that the torque control mode is simpler in its implementation, since it eliminates the design and construction of an inner servo loop, it was selected as the baseline control approach for StormSat.* For this baseline control approach, gyro noise, gyro scale factor quantization effect, and gyro sampling interval were found to have critical impact on attitude jitter. Figure 2-19 summarizes some of the simulation results obtained and it is apparent that the choice of gyro scale factor has the most significant impact on jitter. A gyro scale factor of $K_g = 0.01$ arc-second/pulse with a 400 ms sampling interval is recommended for the baseline system. Preliminary baseline control parameters are given in Table 2-10. Note that the damping of 0.25 applies only to small signals when the integrator is not saturated. The lower damping is the price one must pay for a large integral gain to help overcome wheel friction at speed reversal. For larger signals the integrator is saturated and the system has a damping of about 0.7.

*The 100-pulses-per-revolution tachometer was assumed to be a proximity device in conjunction with a notched perimeter, .8 inch diameter wheel. One hundred teeth results in a reasonable value for tooth spacing. After the completion of this study, the MMS Standard Reaction Wheel was specified to have a 240-pulses-per-revolution, optically encoded tachometer. This would change the results above somewhat but the overall conclusions reached are still believed to be valid.

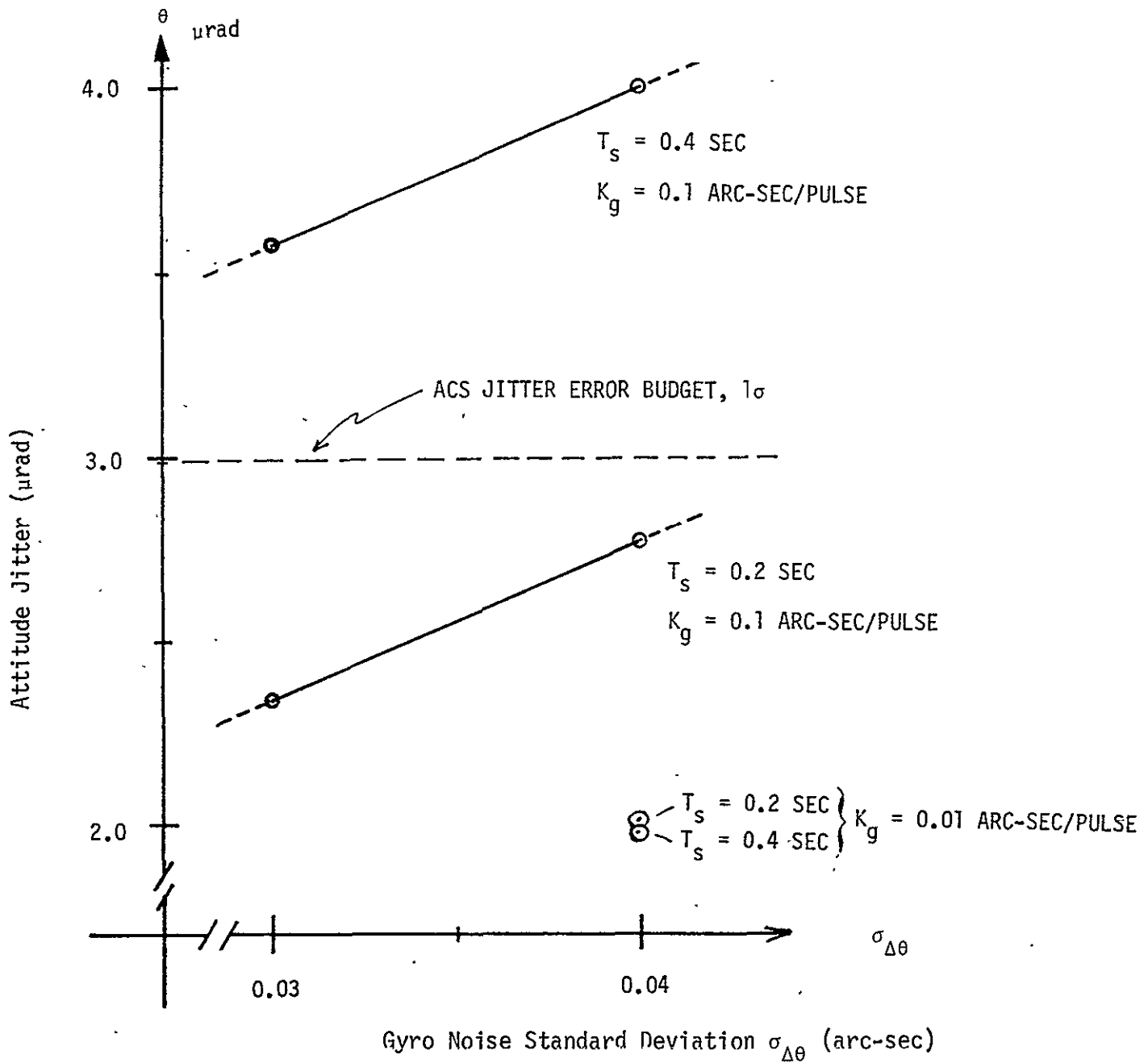


Figure 2-19. Variation of 1σ Jitter Value with Noise Standard Deviation $\sigma_{\Delta\theta}$ (Average of Roll and Pitch Simulation Values)

Table 2-10. Nominal Control Parameters

			For Small Signals Only				
Gyro Rate Feedback	Axis	Moment of Inertia I_{ij} (slug-ft ²)	Nat. Freq. ω_n (rad/sec)	Damping Ratio ζ	Position Gain K_p ft-lb/rad	Rate Gain K_R ft-lb-sec/rad	Integral Gain K_I ft-lb/rad-sec
Scale Factor: $K_g = 0.01 \frac{\text{sec}}{\text{pulse}}$ Sampling Time: $T_s = 400 \text{ ms}$	Roll (x_b)	240	0.5	0.25	9.6	67.8	0.83
	Pitch (y_b)	270	0.5	0.25	10.8	76.4	0.92
	Yaw (z_b)	300	0.5	0.25	12.0	84.9	1.0

The previous paragraph summarized the recommended on-orbit control system when only three reaction wheels are available for control. When all four wheels are available the best performance can be obtained by speed biasing the wheels such that speed reversal does not occur, while at the same time maintaining a nominally zero momentum bias system. This is accomplished by speed biasing the skewed wheel to -1250 RPM and each of the remaining three orthogonal wheels to $1250/\sqrt{3}$ RPM. The wheels are operated in the torque control mode, and the performance is the same as described earlier, only the speed reversal transient occurring twice per orbit in roll and twice per orbit in yaw (but yaw is not critical) has been completely eliminated. It is, therefore, recommended that the StormSat baseline on-orbit attitude control system use all four wheels in the speed biased mode of operation with three wheels under active torque mode control and one wheel (nominally the skewed wheel) commanded to a fixed bias speed. If any one wheel fails, the system will fall back to the normal torque control mode using the three remaining reaction wheels without a speed bias.

2.5.3 Dynamic Interaction with Stepping Payloads

After AASIR gimbaling feasibility had been studied from a mechanical design viewpoint and a preliminary design had been arrived at, the dynamic effects of a stepping gimbaled AASIR on pointing stability of the spacecraft were also examined. First it was decided that a suitable operating mode would be to keep the AASIR locked to the vehicle during imaging, either by a stepper drive or a tight continuous servo. Frame scan would be accomplished by repositioning the gimbaled AASIR relative to the vehicle. It was found that attitude disturbances of the main body could be minimized to less than 1 μ rad by preemphasizing the spacecraft ACS with a torque doublet of 0.5 second duration (for a single line step) applied directly to the pitch reaction wheel whenever the AASIR frame scan was advanced. The required torque amplitude is less than 10 ounce-inches and can easily be supplied by the reaction wheels whose maximum torque capability is at least 20 ounce-inches. The time constant of the reaction wheel motor is compatible with the duration of the torque doublet;

but if this were not the case, signal shaping could be used to enhance the response. More details of this investigation can be found in Section 5.0 of Reference 2.

A similar approach has to be taken for the MASR, should it be added as a second payload on StormSat. However, it was found to be very difficult to match the preemphasis torque so closely to the actual MASR acceleration torque (the friction torque is irrelevant) so that the vehicle is not perturbed more than the allocated 2 μ rad. This problem did not occur when the AASIR was the only payload, since the disturbances due to some torque mismatches during line stepping were of no concern. With two instruments this is not the case and small mismatches, as they inevitably must exist in any preemphasis compensation scheme, will disturb both instruments, since they do not, and cannot step in synchronism. The investigations on the MASR are treated in considerable detail in Section 9.0 of this report. The main conclusion is that flying a MASR as an additional payload on StormSat poses a number of significant operational problems. The case is not hopeless, however, if one is willing to accept a much more sophisticated attitude control system with tunable preemphasis compensation and is also willing to sacrifice some performance with regard to pointing stability and MASR scan efficiency (more time for stepping and turn-around).

2.5.4 Estimated Performance Summary

Total estimated performance for StormSat can now be assessed by combining the various error sources from the attitude reference system, the attitude control system, the AASIR gimbal drive and structural errors. This has been done in Table 2-11. A supporting error analysis for the AASIR gimbal drive mechanism is contained in Section 3.2. The given structural errors represent what are considered reasonable estimates at this time. As can be seen all the performance requirements for StormSat are met. As anticipated from the start, the 4.2 μ rad short-term pointing stability requirement over 64 seconds proved to be most difficult to achieve. The error analysis of Table 2-11 is only valid

Table 2-11. Estimated Performance Summary

ERROR SOURCE	SHORT-TERM (64 SECONDS) ATTITUDE STABILITY (1σ) μrad	LONG-TERM (20 MINUTES) ATTITUDE STABILITY (1σ) μrad	ATTITUDE DETERMINATION ACCURACY (1σ) μrad	ABSOLUTE POINTING ACCURACY (1σ) μrad
ATTITUDE REFERENCE SYSTEM			RANDOM VARYING BIASES	
• GYROS	1.0	9.0	9.0	
• STAR TRACKER (FILTERED)	---	---	21.2	19.4
• EPHEMERIS (1 KM, 3σ)	---	---		9.2
			$\Sigma(\text{RSS})$ 44.5	44.5
ATTITUDE CONTROL SYSTEM				
• GYRO NOISE & QUANTIZ.	2.0	2.0	---	2.0
• AASIR STEPPING DISTURBANCE	1.0	1.0	---	1.0
AASIR GIMBAL DRIVE				
• NON-PREDICTABLE ERRORS	2.0	2.0	2.0	2.0
• PREDICTABLE ERRORS	---	---	---	15.0
• GIMBAL SERVO HANGOFF DUE TO STICTION	1.0	1.0	1.0	1.0
STRUCTURE				
• MISALIGNMENTS	---	---	---	150.0
• THERMAL	1.0	1.0	1.0	1.0
TOTAL (RSS)	3.5	9.6	44.6	157.2 (0.009°)

*Misalignments calibrated by known landmark observations

for four wheel, speed-biased operation of the ACS. With only three wheels operating, the long-term attitude stability requirement is violated twice per day (per orbit) for about 60 seconds when the roll wheel reverses direction. Thus, with one wheel failed, the attendant performance degradation is for all practical purposes entirely negligible.

2.6 ACS and ARS Software Requirements

The on-board software capability required to perform the attitude reference algorithm and implement the attitude control laws is provided by the NASA Standard Space Computer, NSSC-1, which is located in the communications and data handling (CDH) module. This subsection will present preliminary estimates of memory and computation time requirements to perform these functions for StormSat.

2.6.1 NASA Standard Space Computer (NSSC-1) Characteristics

The central computer to be used on MMS was designed as a low cost, high speed digital computer and is an outgrowth of the On-Board Processor now flying on OAO-3. This computer, originally known as AOP, has been adopted as the NASA Standard Space Computer, NSSC-1. The computer's design possesses features that readily allow time-shared operation with sufficient inherent reliability to be trusted with mission critical functions. The computer has a modular architecture with dual interconnecting buses between memory and processor modules to avoid the possibility of a catastrophic single point failure. General characteristics of the computer are summarized in Tables 2-12 and 2-13 (Reference 3, Section 5.0).

2.6.2 ARS Algorithm Software Requirements

A summary description of the attitude reference system (ARS) has been provided in subsection 2.4. Details of the StormSat ARS design and analysis are documented in Reference 2. The ARS software is used to process gyro data, to derive rate and attitude, and to process strapdown star tracker measurements in a six-state Kalman filter to develop periodic estimates for updating attitude and gyro drift. Quaternions are used as the kinematic variables to describe spacecraft attitude.

The ARS software is organized in terms of individual software modules defined to handle specific functional requirements. The actual linking of these functions is under control of the Executive software. Functional flow of the software execution is shown in Figure 2-20, and the computer software requirements are summarized in Table 2-14. Single precision

Table 2-12. General Characteristics of NSSC-1

Word Length	18 Bits, 5 Bits Instruction ID, 1 Bit Index, 12 Bits Operand Fetch
Execution Speed	2 μ sec Cycle Time, 4 μ sec Add, 32 μ sec Multiply, and 60 μ sec Divide
Memory Capacity	Four 8192 Word Modules for Total of 32,768 Words. (Expandable to 64 K in 8 K Segments.)
Registers	One Double Length Accumulator (36 Bits), Two Registers, One Index Register
Processor Interrupts	16 Levels of Priority Interrupt
Direct Memory Access	16 Cycle Steal Channels
Memory Write Protection	Allowable Storage Areas are Assigned in Segments of 128 Words
Input/Output	I/O is Achieved through Time Multiplexing of Existing Telemetry and Command Hardware
Program Load and Dump	Any 4 K Memory Bank can be Loaded and Dumped via Command and Telemetry without Software Bootstrap

Table 2-13. Physical Characteristics of NSSC-1

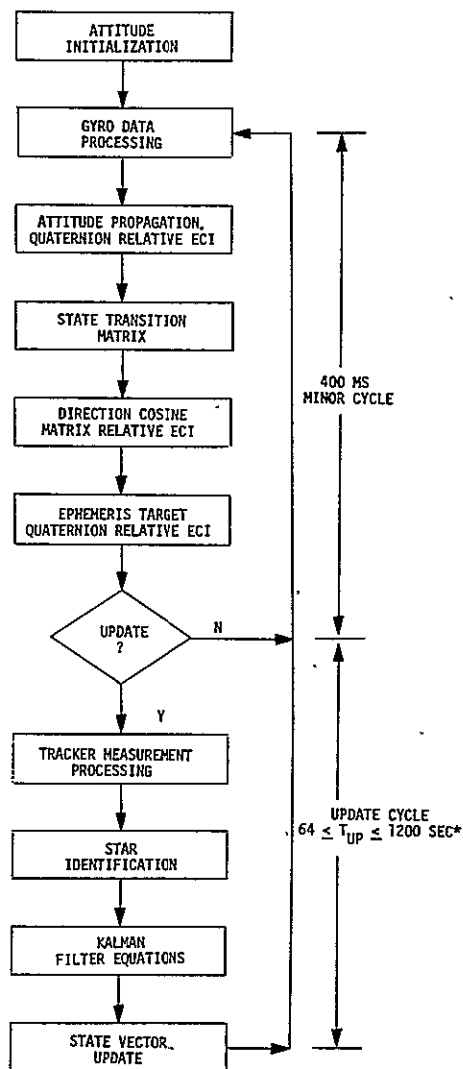
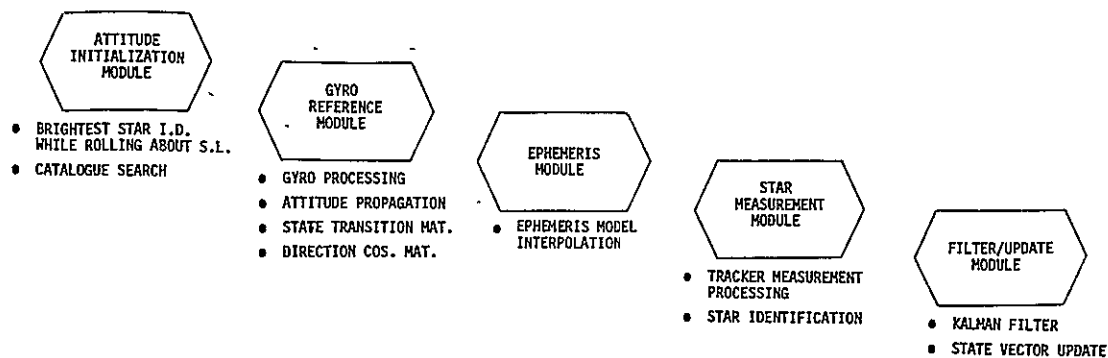
	Size (in ³)	Weight (lbs)	Power (Standby) (watts)	Power (Full Operation) (watts)	Technology
Processor	75	4	6	6	TTL-LSI
Memory 8K x 18 Bits	100	5	0.07	24	Core
Power Converter	100	5	3	8	Discrete
Total (32K) System	275	14	9	38	

Table 2-14. ARS Software Requirements Summary

Functions	Memory (18 bit words)		Computation Time/Cycle (ms)
	Program	Read/Write (Data Base)	
<u>Math Pack</u>	500	50	--
<u>Attitude Initialization Module</u>			
Roll about Sun Line: Brightest Star I.D.	150	35	5.0
Catalogue Search	175	55	122.0
<u>Gyro Reference Module</u>			
Gyro Data Processing	140	20	18.0
Attitude Propagation Algorithm	160	20	12.2
State Transition Matrix	35	10	1.8
Direction Cosine Matrix	95	20	9.7
<u>Ephemeris Module</u>			
Third Order Hermite Polyn. fit to Target Quaternion (3 samples, 16 samples/orbit)	175	410*	6.3
<u>Star Measurement Module (2 Trackers)</u>			
Star Identification	185	253**	25.6
Star Tracker Data Processing	300	50	20.3
<u>Filter/Update Module (1 Star)</u>			
Covariance Propagation	275	42	41.3
Measurement Matrix	240	40	33.0
Kalman Gain Matrix	100	20	27.0
Covariance Matrix Update	60	10	39.0
State Vector Update	95	5	5.3
Total Memory	2685	1040	

*Includes data table of (3 orbits) x (16 samples/orbit) x (8 elements) = 384 entries

**Includes star catalogue of 75 stars = 225 words (aberration corrected right ascension, declination, and brightness)



*FOR DISCUSSION SEE SECTION 2.4 AND REFERENCE 2, SECTION 3.5

Figure 2-20. ARS Software Functional Flow

arithmetic is used throughout, with double precision accumulation of dot products, utilizing the double length 36 bit accumulator of the NSSC-1. The minor cycle time for the ACS/ARS software is 400 ms. A general purpose math pack of utility subroutines is assumed available. A math pack containing matrix algebra routines (except inverse), sine, cosine, tangent, arc-sine, arctangent, and square root routines would require about 500 words of program storage and 50 words of scratch pad memory. The succeeding paragraphs provide a functional description of the modules and define underlying assumptions.

Attitude Initialization Module

To initialize attitude for synchronous orbit missions (where the magnetometer earth field measurements cannot be used) the spacecraft first acquires the sun with its negative yaw (-z) axis using the array located coarse sun sensor and the precision digital sun sensor in conjunction with the RCS and reaction wheel attitude control systems. Then a roll maneuver is initiated about the sun line and a search is made for the brightest star in the swath traced out by the star trackers. This star is then matched to the brightest star in the reduced catalogue to define the initial on-board attitude estimate. This is done by using the sun and star vectors to first approximate the attitude and then performing a regular update using the sun and star measurement residuals with the Kalman filtering algorithm (the regular update software is not contained in the initialization module).

Gyro Reference Module

This software module provides the functions associated with maintaining an inertial attitude reference in conjunction with a configuration of strapdown rate integrating gyros. The gyro outputs are processed to compensate for known misalignments, scale factor errors and biases. Rate and attitude of a known reference frame, nominally fixed with respect to the gyro configuration, is derived with respect to a known inertial reference frame, e.g., Earth-Centered-Inertial (ECI). The attitude is described by quaternions and the attitude propagation algorithm uses the closed form solution of the quaternion equations, i.e., $q_k = e^{(1/2)\hat{\Omega}_k^T} q_{k-1}$.

Ephemeris Module

The ephemeris is assumed to be provided by target quaternions expressed relative to ECI. The target quaternions uniquely define the local vertical reference frame for the spacecraft with \bar{z}_r pointing to nadir and \bar{x}_r in the direction of the orbital velocity vector. The spacecraft attitude error is defined to be zero when the body fixed reference axes $\{\bar{x}_b, \bar{y}_b, \bar{z}_b\}$ are completely aligned with the local vertical reference frame. The NASA tracking network, TDRS (Telecommunication Data Relay Satellite), or NAVSTAR/GPS (Global Positioning System) will provide ephemeris benchmarks. Using optimal estimation techniques, a ground-based processor fits the spacecraft orbital trajectory through these benchmarks, and by extrapolation predicts the spacecraft ephemeris ahead for up to 72 hours. Assuming that 16 samples per orbit of the predicted target quaternion are available to the spacecraft processor (this should be plenty for a circular synchronous orbit), a third order Hermite polynomial is used for interpolating for the local arc of the target quaternion using three samples from the data table. Since 72 hours correspond to three orbits, the data table contains 48 samples at eight elements per sample; eight elements are needed per sample since a Hermite polynomial curve fit requires also the first derivative of the function at the samples. The on-board software must provide the data table (384 entries) and the program to perform the third order Hermite polynomial interpolation. The computational requirements are very modest (6.3 ms) and could actually be performed every minor cycle. However, this is not necessary, and linear ephemeris extrapolation could be used for up to several minutes with totally negligible errors, thereby further reducing average minor cycle computational requirements. With the target quaternion and the spacecraft inertial attitude quaternion available, quaternion algebra is used to compute the small angle attitude error relative to the local vertical reference frame. This is done in the Attitude Error Module, described later with the attitude control system software.

Star Measurement Module

This software module provides the functions associated with star measurement data processing of two strapdown star trackers, assuming one

star in each tracker. The software processes and applies corrections to star tracker data based on stored correction factors generated during an in-orbit star tracker calibration. The software is based on a third order polynomial correction of the type proposed by MIT for the BBRC CT-401 tracker, Reference 4. The measurement software also provides star identification utilizing attitude information and the aberration corrected star catalogue stored in memory.

Filter/Update Module

This software incorporates the Kalman filter associated with providing an optimal estimate of the attitude determination state vector. The Kalman filter has a six-element state vector consisting of three attitude variables and three gyro bias variables. In using quaternions to represent attitude, it is noted that one of the parameters is redundant, i.e., constrained by a simple algebraic relation. This makes it possible to unambiguously represent variations in the fourth parameter in terms of variations in the first three. It follows that the Kalman filter need estimate only the three variables, and thus its state vector contains only three attitude terms. The linearization of the equations as required by the filter formulations are taken about the past filter estimate.

The equations for the extended Kalman filter are well known.

$$P = \Phi P \Phi^T + Q$$

$$K = PH^T [HPH^T + R]^{-1}$$

$$P = [I - KH] P$$

$$\hat{\delta x} = K \delta y$$

The state error covariance matrix, P , is propagated using the state transition matrix, Φ , and the state noise covariance matrix, Q . The state transition matrix is initialized at the time of each update and computed (in the Gyro Reference Module) between updates at each integration step using the gyro derived attitude. The optimal gain matrix, K ,

is computed from the measurement matrix, H , and the measurement noise covariance matrix, R . The measurement matrix relates variations in the measurement vector to variations in the state vector. The measurement noise covariance matrix, R , is 2×2 and the elements are constants whose value is selected based upon the expected (or measured) noise in the star measurement. The gain matrix, K , is used to establish a state correction $\delta \hat{x}$, to the state vector using the measurement residual, $\delta \hat{y}$. The state error covariance matrix is also updated using the gain matrix and measurement matrix, and constrained to remain positive definite.

2.6.3 Attitude Control Software Requirements

A summary description of the attitude control system has been provided in subsection 2.5. Details of the design and analysis of the normal on-orbit attitude control system are documented in Reference 2. The ACS software processes estimated attitude, gyro data and sun sensor data to provide control signals to the reaction wheel drives and/or the RCS valve drivers. It is recommended that the AASIR gimbal servo not be controlled by the flight computer since the servo will have a bandwidth of about 20 rad/second requiring a sampling interval of less than 20 msec-ond. Furthermore, precise timing signals for AASIR stepping and associated ACS preemphasis compensation are required which cannot be tied to a flight computer minor cycle of any reasonable duration. It is, therefore, recommended that the AASIR servo be controlled by a dedicated microprocessor (or special purpose analog and digital electronics) mounted in close proximity to the AASIR gimbal drive. AASIR stepping signals and ACS preemphasis compensation signals are provided by the microprocessor by counting down clock pulses and issuing the necessary commands when the appropriate registers contain zero, and then resetting the registers. The ACS preemphasis commands to decouple AASIR stepping dynamics are directly routed from the microprocessor and summed into the reaction wheel command registers. The spacecraft flight computer will only provide the necessary command interface with the microprocessor, i.e., provide necessary signals and constants that determine AASIR operation, such as frame size, frame retrace commands, and magnitude of the torque doublet, ACS preemphasis signal.

The ACS software is organized in modules defined to handle specific functional requirements. The linking of these functions is under control of the executive software. Functional flow of the software execution is shown in Figure 2-21, and the computer requirements are summarized in Table 2-15. Single precision arithmetic with double accumulation of dot products is assumed throughout. The computation cycle is 400 ms, synchronized with the ARS minor cycle. The following paragraphs provide a brief functional description of the software modules.

Sun Sensor Module

This module processes the output signals of the coarse sun sensor located on the solar array (4π steradian coverage), and the fine digital sun sensor located in the ACS module. The processing consists mainly of bias and ADC offset removal, and scale factor corrections. The processed output for each sensor consists of two quantities which define the sun vector in sensor coordinates, yielding essentially x and y errors normal to the sunline which is nominally along the sensor z-axis. For large sun angles, the bilevel signals and sun presence signals must be used.

Attitude Error Module

The spacecraft attitude errors are computed for the different modes of operation. Mode end checks are also included; for instance, when to switch from the coarse to the fine sun acquisition mode. For normal on-orbit operation the small angle attitude errors relative to the local vertical frame are computed from the spacecraft inertial attitude quaternion (obtained from the ARS) and the ephemeris target quaternion, using quaternion algebra.

RCS Control Module

This module contains the software to compute thruster actuation signals from the spacecraft attitude errors and gyro sensed rates. Mode dependent options, control law shaping filters (if required), limiters, and thruster deadzones are programmed in this module. Pulsewidth modulated thruster control is assumed. The outputs of the module are thruster

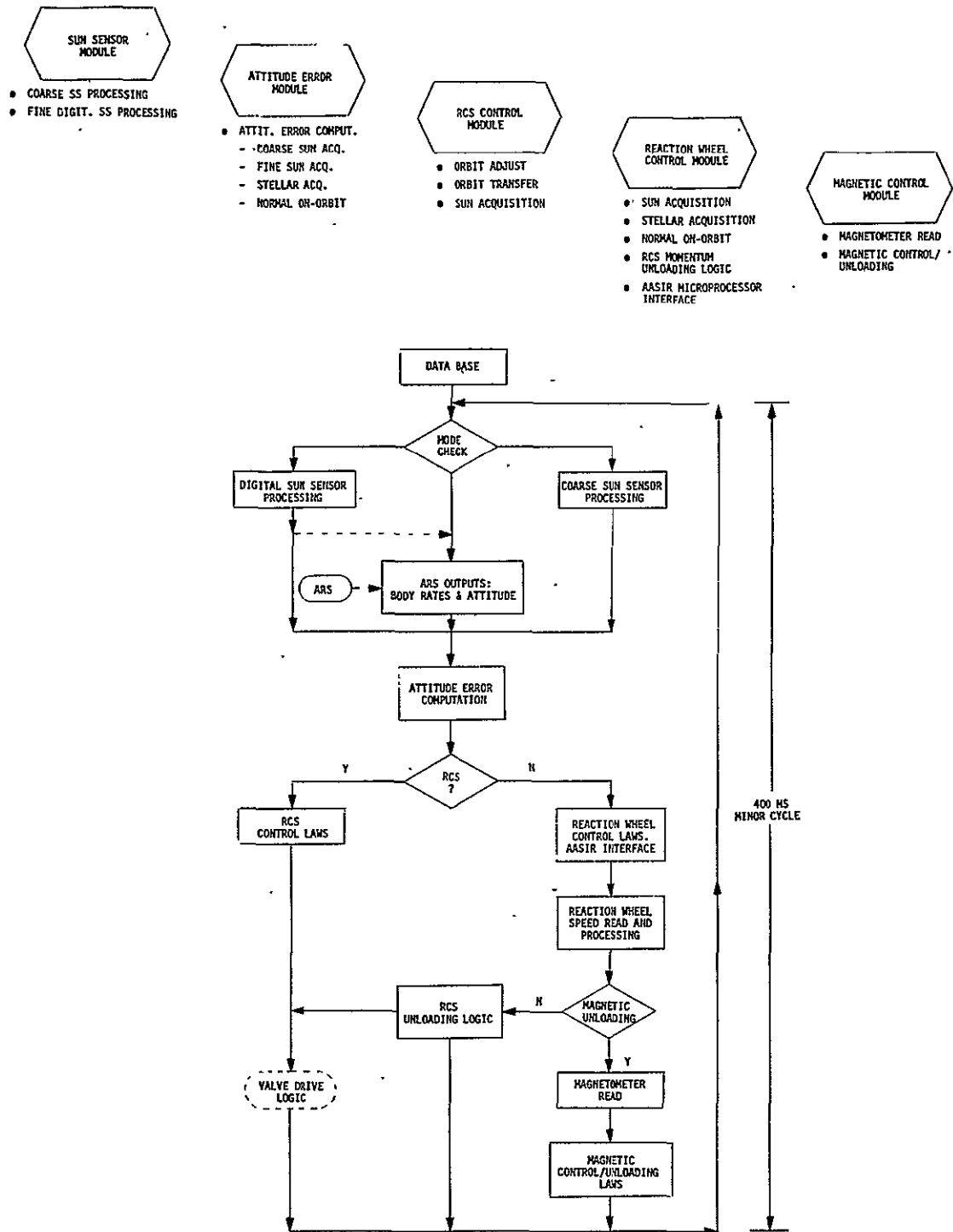


Figure 2-21. ACS Software Functional Flow

Table 2-15. Attitude Control Software Requirements Summary

Functions	Memory (18 bit words)		Computation Time/Cycle (ms)
	Program	Read/Write (Data Base)	
<u>Sensor Module</u>			
Coarse Sun Sensor Processing	60	7	3.6
Digital Sun Sensor Processing	50	7	0.6
<u>Attitude Error Computation Module</u>			
Coarse Sun Acquisition	70	17	0.7
Fine Sun Acquisition/Stellar Acquisition	60	15	0.9
Normal On-Orbit Attitude Error	60	36	3.0
<u>RCS Control Module</u>			
RCS Control Laws (Valve drive logic hard-wired, external)	310	50	5.4
<u>Reaction Wheel Control Module</u>			
Reaction Wheel Control Laws	125	36	2.9
AASIR Command Generation/ Microprocessor Interface	40	20	0.3*
Reaction Wheel Speed Read and Processing	70	10	1.5
Momentum Check/Unloading Logic Using RCS	70	23	0.6
<u>Magnetic Control Module</u>			
Magnetometer Read	70	10	1.5
Magnetic Control Laws	135	40	3.0
Total Memory	1120	271	

*Operations not synchronized with 400 ms minor cycle. Computer supplies clock pulses; constants, and command signals; computations are usually performed between AASIR frames.

on-time count-down signals in body coordinates. The thruster select logic is assumed to be hardwired, external to the processor.

Reaction Wheel Control Module

This module computes RW torque commands for the various modes of operation of the spacecraft from the attitude errors and the spacecraft rates. Integral compensation, limiters, shaping networks, transformations from body to wheel coordinates, constant speed commands, speed read and momentum computations, etc., are included. The module also contains the momentum unloading logic when using the RCS for unloading.

Magnetic Control Module (Not Baseline for StormSat)

This software processes the magnetometer signals and implements the magnetic control laws for continuously unloading the wheels, interrupted by shutdown signals (all torquer bars off) during star tracker read. The magnetic control law used is

$$\bar{M} = - \frac{K}{B^2} (\bar{B} \times \bar{H}_e)$$

where

\bar{M} = desired magnetic moment of torquer bars

\bar{B} = earth magnetic field

\bar{H}_e = spacecraft momentum error

K = a gain constant

2.6.4 Typical Normal On-Orbit Requirements

Tables 2-14 and 2-15 listed ARS and ACS software requirements for various operational modes and conditions of StormSat. Total memory requirements, are

3805 words of program memory

and

1311 words of read/write memory

Typical software requirements during normal on-orbit operations are summarized in Table 2-16. The top half assumes no attitude update and arrives at a total execution time of 46.3 ms per 400 ms minor cycle, which is very reasonable. The bottom half of the table adds to this the software requirements for an attitude update, processing both trackers, but computing update from only one star. If a second star is present, it is used for updating the state vector in the next minor cycle. Both star trackers are processed at once since it is computationally efficient and it leaves the option open to process the two star measurements simultaneously should this be required at some time. The required computation time with update of 247.5 ms still fits nicely into the StormSat 400 ms minor cycle. This is not essential, since the attitude update increment could be computed over several minor cycles and the state transition matrix could be used to finally perform the state update several minor cycles after the star measurements were made.

The results above indicate that the software requirement for the ACS/ARS fits nicely into the NSC-1 computer, leaving ample memory and computation time for the software requirements of the other subsystems.

Table 2-16. Normal On-Orbit ARS/ACS Software Requirements

Functions	Memory (18 bit words)		Computation Time/Cycle (ms)
	Program	Read/Write (Data Base)	
Math Pack	500	50	--
Gyro Data Processing	140	20	18.0
Attitude Propagation Algorithm	160	20	12.2
State Transition Matrix	35	10	1.8
Ephemeris Target Quaternion	175	410	6.3
Normal On-Orbit Attitude Error	60	36	3.0
Reaction Wheel Control Laws	125	36	2.9
Reaction Wheel Speed Read and Processing	70	10	1.5
Momentum Check/Unloading Logic Using RCS	70	23	0.6
Subtotals (no update)	1335	615	46.3
Direction Cosine Matrix	95	20	9.7
Star Measurement Module (2 Trackers)	485	303*	45.9
Filter/Update Module (1 Star)	770	117	145.6
Total (with update)	2685	1055	247.5

*Contains 225 words of star catalogue

2.7 On-Board Data Handling, Communications, and Ground Data Processing

2.7.1 On-Board Data Handling

The on-board data handling system was configured to provide the functions required for manipulating the AASIR data so that it could be accepted by the communications subsystem. The basic characteristics of the AASIR output are a sinusoidally varying data rate with a 60% duty cycle. Therefore, the data handling system is required to smooth the data to a constant rate. In performing this function it was found advantageous to also average over the 60% duty cycle thereby achieving a 40% reduction in required transmission rate. The equipment chosen, and described in Chapter 4, is straightforward. It consists of analog multiplexers, an analog to digital converter (ADC) with associated sample and hold, a buffer memory, timing logic, and a micro-controller. Figure 4-4 illustrates the conceptual configuration. Using 1980 technology CCD buffer memory and CMOS logic the weight and power of the on-board data handling equipment is estimated at approximately 5 lbs. and 15 watts. The equipment provides for one sample per Instantaneous Field of View (IFOV) per detector. The details of the timing and focal plane layout to minimize skew problems are given in Chapter 4.

Various alternates to the baseline Stormsat system were considered. There alternatives and their impact to the on-board data handling baseline are described below.

The addition of a Microwave Atmospheric and Sounding Radiometer (MASR) to the Stormsat payload is being considered. Since the data rate from such an instrument is very low (hundreds of bits per second) no impact to the on-board data handling subsystem is envisioned. This point is reinforced by the ability of the MMS C&DH module to accommodate the MASR data.

A scan mirror period of 1.5 times the strawman period is being considered for the AASIR. The result is a mirror resonant frequency of 0.386 Hz. Along with this change the focal plane is expanded (to 18 sounding channels) so that the frame time is maintained. A scan mirror period of 2.58 seconds would impact the buffer memory sizing since a longer time of active data collection would result. If the buffer memory were realized in CCD technology this would be a minimal perturbation.

The last modification to the baseline consists of the addition of a set of detectors at 3.7 μ meters. This set of detectors has not been well defined but a few preliminary characteristics are hypothesized. There would be 9 detectors in a group each being approximately 40 μ rad x 40 μ rad. The resulting data would impact the present on-board data handling system design. (The 3.7 μ meter detectors would produce ~0.5 Mbps if averaged over the 1.29 sec scan.) Therefore, changes in timing, number of multiplexers, ADC capability, and buffer memory would be required.

2.7.2 Communications

The telecommunication subsystem for STORMSAT was designed to provide all mission data communications with the following requirements:

- Geosynchronous orbit,
- S-band operation,
- STDN compatible,
- AASIR data rate of 1.6 Mbps,
- VI data rate of 1.0 Mbps, and
- Maximum use of the MMS

The baseline system consists of: a quadriphase modulator, S-band frequency source, S-band power amplifier and power converter, and an S-band earth coverage dish. The two sensor data streams are considered independent (asynchronous) and the power in the I and Q channels of the QPSK system is therefore adjusted to optimize transmission in each of the channels. The 20 inch S-band MMS antenna was chosen as baseline and allows a fixed mounting to the spacecraft.

The baseline hardware utilizes a 10 watt transmitter and the 30 ft. STDN antenna along with the already mentioned 20 inch earth coverage spacecraft dish. Assuming edge of earth spacecraft dish gain and a 10^{-6} BER a 3.9 dB margin over adverse tolerances results. This analysis assumes the power in the I and Q channels has been adjusted in proportion to their data rates for optimal transmission.

The design consists entirely of equipment that is, or will be, qualified prior to this application. Estimates for the telecommunication subsystem are 7 lbs, (excluding the dish) and 50 watts.

Several alternatives, and their impact to the communications subsystem were considered. The addition of a Microwave Atmospheric Sounding Radiometer (MASR) does not have a significant impact on the communications equipment because the MASR data rate is hundreds of bits per second. A change to the mirror scan period, 1.5 times as long, is also being considered. The resulting change to the downlink rate is a second order effect, and no communications system problems result with the change to a 2.58 sec mirror period. Finally, the addition of a group of detectors of 3.7μ meters was considered. This would impact the system since it would increase the basic system data rate by about 30 percent. The increased data rate would require a proportionately increased power (from 10 Watts to ~13 Watts) to maintain the same performance margins, etc.

2.7.3 Ground Data Processing

The data received by the Stormsat ground station requires man-machine interactive manipulation in order to extract the maximum amount of information from the data. The ground processing system which was configured to allow this manipulation is described below.

A list of desirable system features was collected (see sec. 6.3) and utilized as a baseline in order to configure the ground processing equipment. The desirable characteristics with major impact on the design are: 1) near real time capability, 2) major use of image displays, 3) storage for multiple images, and 4) maximum flexibility in the hardware and operating system to allow for simple user oriented software packages to perform a wide variety of research and operational tasks.

Translating these desirable features to hardware resulted in the selection of: 1) a flexible high speed computer capable of supporting near real time operation on a continuous basis, 2) dual, tricolor image displays with 1024×1024 pixel capability, 3) a video disc, large (300 MB) capacity digital disc and optional 10^{12} bit memory systems, and 4) an architecture which, with peripherals (eg. Hazeltine operator console), will allow great flexibility in later system development, growth and use.

The STORMSAT ground station consists of equipment performing three functions: data capture, data preparation, and information extraction. The Severe Storm Research Processor (SSRP) performs both data preparation

and information extraction functions and is of major interest in this conceptual design. The SSRP first performs the reformatting and registration processing that is required. The registration computation required ranges from virtually no processing to the use of an Algorithm Processing System (APS) to perform resampling, perhaps utilizing the cubic convolution method developed at TRW. The SSRP then supports the display of called images and sequences of images as well as performing calculations in an interactive mode.

The major hardware components selected as representative consist of two SEL 32/55 computers, multiple disc and tape (CCT and HDT) drives, peripheral controllers, two Comtal 8000 series image displays, a Hazeltine operator console, video disc, APS hardware, and an optional Terabit memory. The architecture is illustrated in Figure 6-4.

The impact to the ground processing system of various alternatives to the STORMSAT baseline system were also considered. The addition of a Microwave Atmospheric Sounding Radiometer (MASR) would not have an impact on the recommended hardware because of the low data rates involved. Of course software modules appropriate to MASR data processing would need to be developed. The modification of scan mirror period to 2.58 seconds would not affect the ground station since the data rate and information content would remain unchanged. Lastly the addition of a 2.7 μ meter band would impact the system in 2 ways. First the system throughput would be increased by roughly 30% to account for processing the additional data and second the storage requirements would increase consistent with the desire to access 3.7 μ meter data in a time frame comparable to present visible storage desires.

3. AASIR GIMBAL DRIVE

3.1 AASIR Gimbaling Concepts

3.1.1 Background and Basic Functional Requirements

The preliminary AASIR gimbaling hardware implementation study described in the Phase II report was extended to considerations of gimbaling systems categorized in terms of the basic prime movers as the direct motor, the three point suspension traction drive, and the linear actuation drive.

The principal functional requirement for each of these gimbaling concepts was to produce a frame scan of 375×10^{-6} radians within 0.20 sec*, every 7.74 sec period of time. Further requirements and constraints are identified in Table 3-1.

TABLE 3-1. Performance Requirements and Design Constraints

Requirements

- Rotation of AASIR ± 0.174 rad
- Rotational accuracy 75×10^{-6} to 150×10^{-6} rad
- Repeatability 3×10^{-6} rad
- Operation in one "g" environment — Any orientation

Constraints

- AASIR weight 200-300 lbs
- AASIR moment of inertia $< 8 \text{ ft-lb sec}^2$

3.1.2 Direct Drive Gimbal

The conceptual design of the gimbal is shown in Figure 3-1. It consists of an aluminum shaft and housing, a direct drive torquer and a cable wrap up system. The shaft interfaces directly with the AASIR instrument and the housing is supported by the gimbal structure (356 al. casting). Two angular contact bearings in a BTB configuration with a flexural preload mechanism comprise the gimbal suspension system.

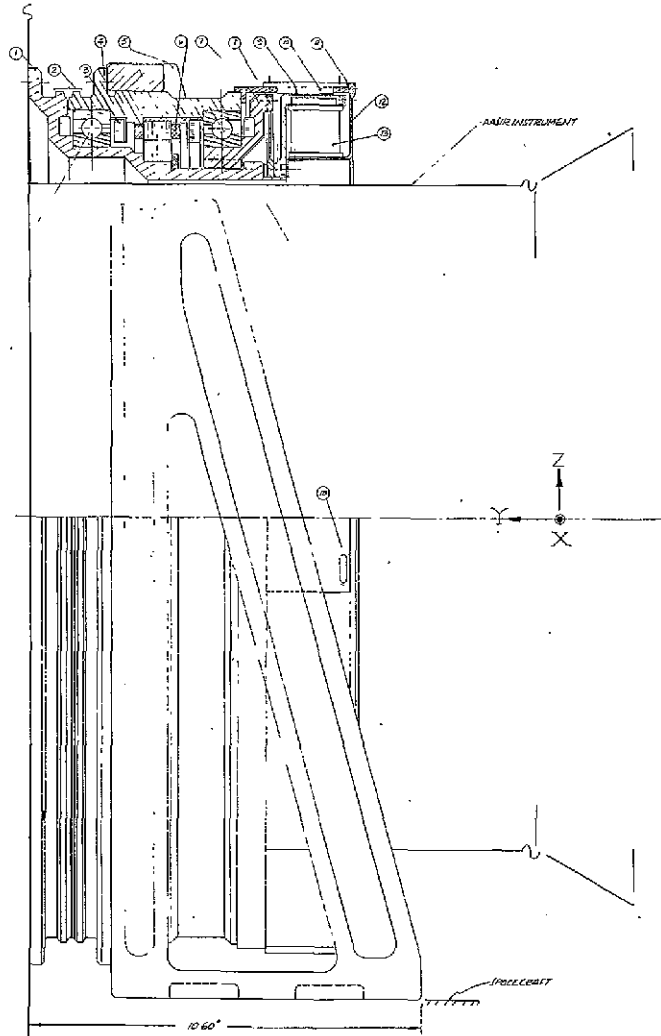
*Current requirements are either 0.516 or 0.344 second

The selection of the bearings was dictated by the diameter of the payload and the availability of their cross sections. (Cross sections smaller than the indicated choice can be procured on special orders with the delivery uncertainty longer than 10 months.) The selected bearings are 1x1x20 inch inside diameter elements manufactured by Keene Corporation. Their internal diametral clearance will produce a nominal contact angle of 30 deg of arc. A particular disadvantage of such large diameter bearings is the associated friction torque. The latter is a direct function of the coefficient of friction, the bearing geometry, dominately the pitch radius, the magnitude of external loads, the cotangent of the contact angle, the elastic hysteresis in rolling, sliding due to deformation of contacting elements and sliding between the ball retainer pockets and the rolling elements. The elastic hysteresis and the deformation effects are minimized by selecting a high capacity bearing. Hence, the larger the cross section of a bearing, lower friction and stiction values can be expected for a given bearing diameter. Exemplifying the effects of bearing capacity is the data in Table 3-2 derived for a 20 inch inside diameter bearing subjected to a 170 lbs axial preload.

TABLE 3-2: Effect of Bearing Capacity on the
Magnitude of Stiction

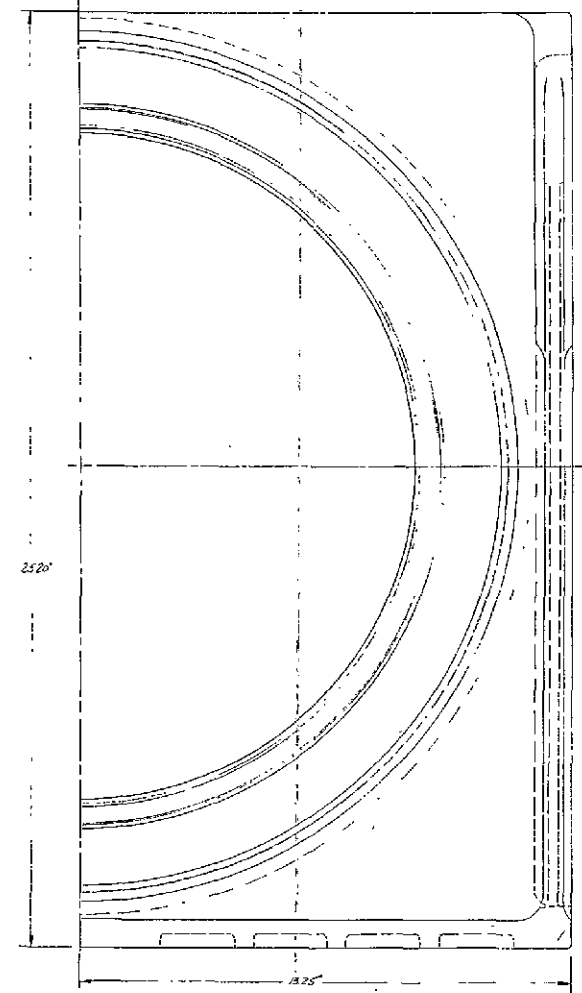
Bearing Cross Section	No. of Balls	Ball Diameter	Bearing Capacity	Bearing Pitch Diameter	Stiction Torque
<u>inch</u>		<u>inch</u>	<u>lbs</u>	<u>inch</u>	<u>inch-oz</u>
1x1	84	.0.5	37,000	21.00	385
3/4x3/4	115	0.375	28,500	20.00	415
1/2x1/2	164	0.250	18,000	20.50	480
3/8x3/8	231	0.187	14,300	20.37	510
5/16x5/16	273	0.156	11,700	18.31	590

Note: The stiction torque is defined as twice the value of running friction at low velocities



AASIR GIMBAL-DIRECT DRIVE SYSTEM 2981 MARCH 1, 1976

- 1. BASE
- 2. DRIVE CLAMP TUBES
- 3. BEARING ASSEMBLY
- 4. HOUSING 10 DEGREE
- 5. GIMBAL MOUNT STRUCTURE
- 6. LENS WITH VIEW FINDER
- 7. FILLING MOUNT STRUCTURE
- 8. FILLING FLUID
- 9. IMAGINATION OF GIMBAL 80 DEGREE
- 10. IMAGINATION OF GIMBAL 10 DEGREE
- 11. IMAGINATION OF GIMBAL 10 DEGREE
- 12. IMAGINATION OF GIMBAL 10 DEGREE
- 13. IMAGINATION OF GIMBAL 10 DEGREE
- 14. IMAGINATION OF GIMBAL 10 DEGREE
- 15. IMAGINATION OF GIMBAL 10 DEGREE
- 16. IMAGINATION OF GIMBAL 10 DEGREE
- 17. IMAGINATION OF GIMBAL 10 DEGREE
- 18. IMAGINATION OF GIMBAL 10 DEGREE
- 19. IMAGINATION OF GIMBAL 10 DEGREE
- 20. IMAGINATION OF GIMBAL 10 DEGREE
- 21. IMAGINATION OF GIMBAL 10 DEGREE
- 22. IMAGINATION OF GIMBAL 10 DEGREE
- 23. IMAGINATION OF GIMBAL 10 DEGREE
- 24. IMAGINATION OF GIMBAL 10 DEGREE
- 25. IMAGINATION OF GIMBAL 10 DEGREE
- 26. IMAGINATION OF GIMBAL 10 DEGREE
- 27. IMAGINATION OF GIMBAL 10 DEGREE
- 28. IMAGINATION OF GIMBAL 10 DEGREE
- 29. IMAGINATION OF GIMBAL 10 DEGREE
- 30. IMAGINATION OF GIMBAL 10 DEGREE
- 31. IMAGINATION OF GIMBAL 10 DEGREE
- 32. IMAGINATION OF GIMBAL 10 DEGREE
- 33. IMAGINATION OF GIMBAL 10 DEGREE
- 34. IMAGINATION OF GIMBAL 10 DEGREE
- 35. IMAGINATION OF GIMBAL 10 DEGREE
- 36. IMAGINATION OF GIMBAL 10 DEGREE
- 37. IMAGINATION OF GIMBAL 10 DEGREE
- 38. IMAGINATION OF GIMBAL 10 DEGREE
- 39. IMAGINATION OF GIMBAL 10 DEGREE
- 40. IMAGINATION OF GIMBAL 10 DEGREE
- 41. IMAGINATION OF GIMBAL 10 DEGREE
- 42. IMAGINATION OF GIMBAL 10 DEGREE
- 43. IMAGINATION OF GIMBAL 10 DEGREE
- 44. IMAGINATION OF GIMBAL 10 DEGREE
- 45. IMAGINATION OF GIMBAL 10 DEGREE
- 46. IMAGINATION OF GIMBAL 10 DEGREE
- 47. IMAGINATION OF GIMBAL 10 DEGREE
- 48. IMAGINATION OF GIMBAL 10 DEGREE
- 49. IMAGINATION OF GIMBAL 10 DEGREE
- 50. IMAGINATION OF GIMBAL 10 DEGREE
- 51. IMAGINATION OF GIMBAL 10 DEGREE
- 52. IMAGINATION OF GIMBAL 10 DEGREE
- 53. IMAGINATION OF GIMBAL 10 DEGREE
- 54. IMAGINATION OF GIMBAL 10 DEGREE
- 55. IMAGINATION OF GIMBAL 10 DEGREE
- 56. IMAGINATION OF GIMBAL 10 DEGREE
- 57. IMAGINATION OF GIMBAL 10 DEGREE
- 58. IMAGINATION OF GIMBAL 10 DEGREE
- 59. IMAGINATION OF GIMBAL 10 DEGREE
- 60. IMAGINATION OF GIMBAL 10 DEGREE
- 61. IMAGINATION OF GIMBAL 10 DEGREE
- 62. IMAGINATION OF GIMBAL 10 DEGREE
- 63. IMAGINATION OF GIMBAL 10 DEGREE
- 64. IMAGINATION OF GIMBAL 10 DEGREE
- 65. IMAGINATION OF GIMBAL 10 DEGREE
- 66. IMAGINATION OF GIMBAL 10 DEGREE
- 67. IMAGINATION OF GIMBAL 10 DEGREE
- 68. IMAGINATION OF GIMBAL 10 DEGREE
- 69. IMAGINATION OF GIMBAL 10 DEGREE
- 70. IMAGINATION OF GIMBAL 10 DEGREE
- 71. IMAGINATION OF GIMBAL 10 DEGREE
- 72. IMAGINATION OF GIMBAL 10 DEGREE
- 73. IMAGINATION OF GIMBAL 10 DEGREE
- 74. IMAGINATION OF GIMBAL 10 DEGREE
- 75. IMAGINATION OF GIMBAL 10 DEGREE
- 76. IMAGINATION OF GIMBAL 10 DEGREE
- 77. IMAGINATION OF GIMBAL 10 DEGREE
- 78. IMAGINATION OF GIMBAL 10 DEGREE
- 79. IMAGINATION OF GIMBAL 10 DEGREE
- 80. IMAGINATION OF GIMBAL 10 DEGREE
- 81. IMAGINATION OF GIMBAL 10 DEGREE
- 82. IMAGINATION OF GIMBAL 10 DEGREE
- 83. IMAGINATION OF GIMBAL 10 DEGREE
- 84. IMAGINATION OF GIMBAL 10 DEGREE
- 85. IMAGINATION OF GIMBAL 10 DEGREE
- 86. IMAGINATION OF GIMBAL 10 DEGREE
- 87. IMAGINATION OF GIMBAL 10 DEGREE
- 88. IMAGINATION OF GIMBAL 10 DEGREE
- 89. IMAGINATION OF GIMBAL 10 DEGREE
- 90. IMAGINATION OF GIMBAL 10 DEGREE
- 91. IMAGINATION OF GIMBAL 10 DEGREE
- 92. IMAGINATION OF GIMBAL 10 DEGREE
- 93. IMAGINATION OF GIMBAL 10 DEGREE
- 94. IMAGINATION OF GIMBAL 10 DEGREE
- 95. IMAGINATION OF GIMBAL 10 DEGREE
- 96. IMAGINATION OF GIMBAL 10 DEGREE
- 97. IMAGINATION OF GIMBAL 10 DEGREE
- 98. IMAGINATION OF GIMBAL 10 DEGREE
- 99. IMAGINATION OF GIMBAL 10 DEGREE
- 100. IMAGINATION OF GIMBAL 10 DEGREE



FOLDOUT FRAME

FOLDOUT FRAME 2

Figure 3-1. AASIR Gimbal - Direct Drive System 3-3

The desire to demonstrate AASIR performance in one "g" field in any orientation sets the magnitude of the axial preload required to sustain the 300 lb AASIR weight. For the suspension system discussed, the minimum preload approaches 130 lbs and a superimposed margin of 1.3 increases its value to 170 lbs. The system stiction estimate for the noted loads is given in Table 3-3.

TABLE 3-3. Gimbal Stiction Estimates for One and Zero "g" Operation

<u>System Orientation</u>	<u>Stiction Torque</u>
<u>One "g" Operation</u>	(inch-oz)
With (-) Z axis along "g" vector	750
With (+) Z axis along "g" vector	750
With (+) Y axis along "g" vector	960
<u>Zero "g" Operation</u>	
Any orientation	380

Concluding the subject of stiction, it is well to note that for the bearing preload values just sufficient to ascertain the condition of ball rolling, at least, 80 inch-oz stiction, due to ball retainers alone, can be expected for this bearing system.

The required preload is achieved by the flexural element indicated in Fig. 3-2. Utilization of this type of flexure has the advantage of eliminating the need for bearing clearance between inner race and the shaft or the outer race and the housing. The latter normally allows axial sliding. The axial motion of one of the bearings of any suspension system is necessary to avoid excessive bearing loading due to thermal expansion of the shaft with respect to the reference structure. The side effects of the diametral bearing clearance are the relative rotation of the bearing races with respect to either the shaft or the housing, the discontinuities of the sliding motion due to stiction and the attendant transverse rotation of the bearing. All these aspects are instrumental in causing random

pointing errors which can be avoided by utilization of the flexural preload mechanism. Notice from Figure 3-2 that the bearing associated with the flexure is structurally housed and retained in position by light press fits as well as the flexural preload. The flexural bearing housing itself is snubbed to allow sustainment of launch loads. The snubber's diametral and axial gaps are typically 0.001 inch and 0.004 inch, respectively.

Existence of the relatively high starting torques (stiction) implies that for a reasonably tight servo loop, the gimbal motor should be characterized by a relatively high stall torque capability. Based on the expected bearing stiction for zero "g" operation (Table 3-3), a 20 ft-lb motor was chosen. The selected torquer is tentatively a limited rotation (± 20 deg) machine. Further characterization of the motor performance is given in Table 3-4.

TABLE 3-4. Direct Drive Motor Characteristics

Torque constant	1.67 ft-lb/amp
Resistance of each winding	2.1 ohms
Power	
• To overcome stiction in 0 "g" field . .	3.00 watts
• To overcome stiction in 1 "g" field . .	18.75 watts
• To develop maximum torque	300.00 watts
Weight	≈ 20 lbs

The displacement feedback device is an "Inductosyn"-type multispeed resolver. It consists of a tape-type rotor mounted on the rotating element of the gimbal. The pitch of the tape (1 sinusoidal cycle) is 0.1 inch. To eliminate once per revolution errors, four stator heads are symmetrically located along the periphery of the stationary elements of the gimbal on a diameter that results in a resolver equivalency of 720 speeds. The conservative estimate of accuracy not including the gimbal suspension error

is estimated at 2 arc sec of arc and the repeatability is .2 arc sec. A gimbal configuration utilizing "Inductosyn" plates instead of a tape is shown in Figure 3-2. This configuration's main advantage is the slightly lesser weight and more convenient assembly. However, the "Inductosyn" plates of the required size are not available and constitute a new development.

Notice (Fig. 3-1 and Fig. 3-2) that the bearing's lubrication is being replenished by Nylasint lubrication reservoirs and that the electrical power and signal wire wrap-up is included as a subassembly of the suspension system. The wire wrap-up will provide 180, 0.3 amp each elastic link fashioned for rolamite-type angular displacements.

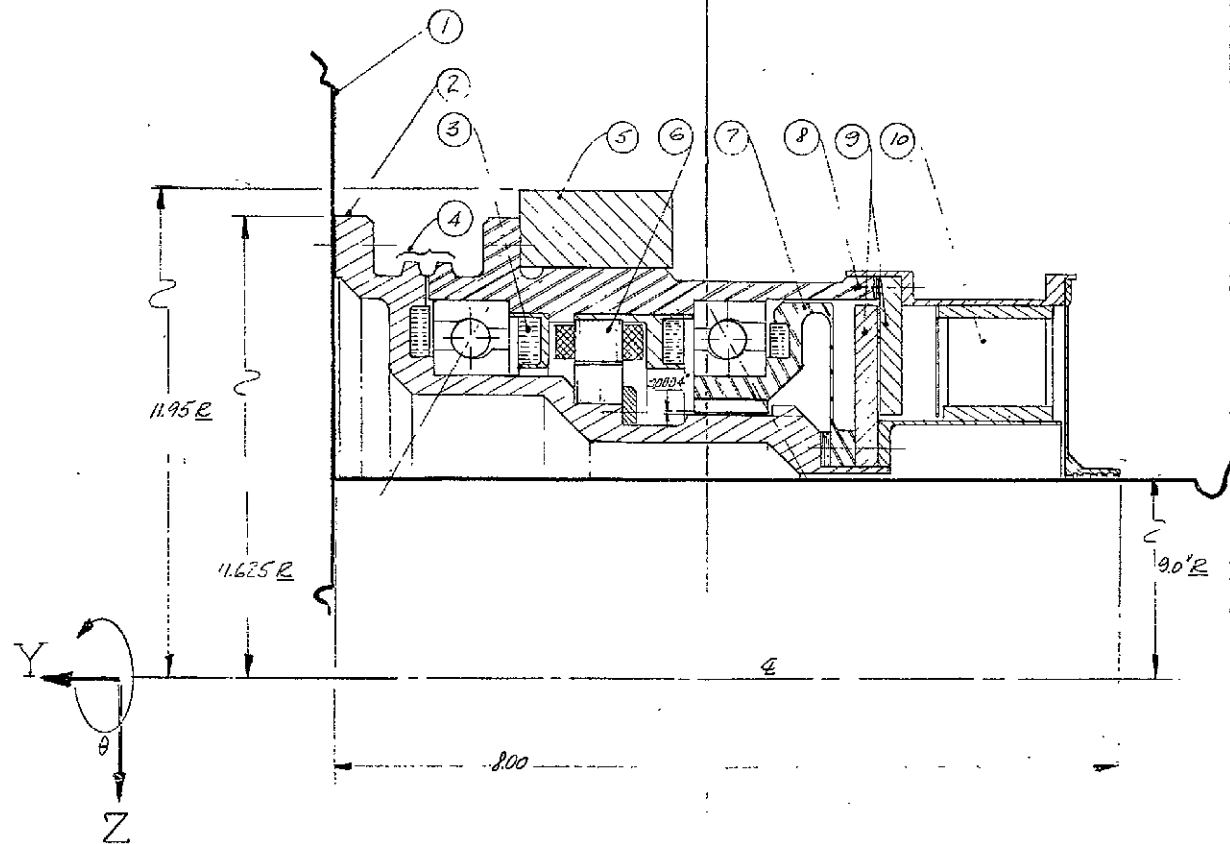
An estimate of the gimbal weights as a function of various structural materials is given in Table 3-5.

TABLE 3-5. Best Estimate of Gimbal Weight

	Weight (lbs)		
	Aluminum	Titanium	Steel
Direct Drive (Figure 3-1)	143	168	225
Direct Drive (Figure 3-2)	120	140	180

3.1.3 Three Point Suspension Gimbal

To utilize the inherent bearing friction torque due to large diameters of the payload, a tri-element gimbal suspension using traction drives was conceived. The suspension (Fig. 3-3) is comprised of three drive subassemblies symmetrically located along the periphery of the gimbal shaft. Each subassembly consists of a 140 in-lb brushless torquer motor which can be commutated via a Hall Effect Sensor or a simple optical encoder. In the case of this design, an eight-speed resolver is being used. The motor-driven shaft is terminated in two conic section cups (20 degree included angle) which retain two 0.875 inch diameter bearing balls. The balls are retained in position by a preloaded (180 lbs/drive) set of spherical curvature inner races. The inner race contact angle is nominally 30 deg of arc. Since the friction at the line contact plane



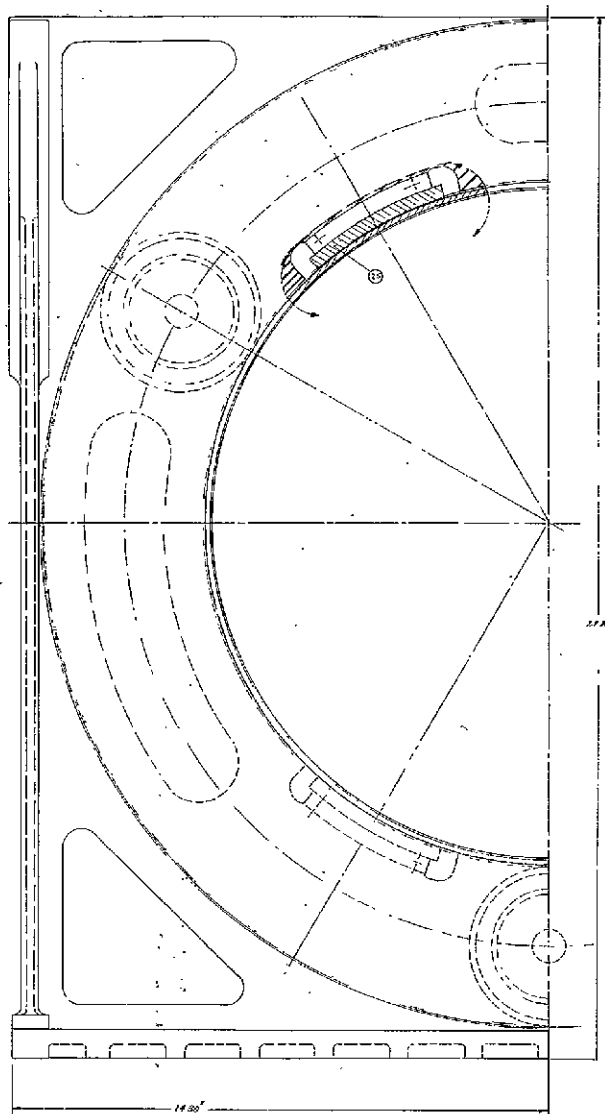
LEGEND

- ① AASIR INSTRUMENT
- ② GIMBAL SHAFT
- ③ NYLASINT RESERVOIR
- ④ MARMON CLAMP INTERFACE
- ⑤ SUPPORT STRUCTURE
- ⑥ LIMITED ROTATION MOTOR
- ⑦ PRELOAD FLEXURE
- ⑧ DRIVE HOUSING
- ⑨ INDUCTOSYN
- ⑩ WIRE WRAP

Figure 3-2. AASIR -
Direct Drive Gimbal

FOLDOUT FRAME

FOLDOUT FRAME 2



AASIR, TRI-ELEMENTS TRACTION DRIVE - GUNBALL
(DRIVE ELEMENTS ELONGATED AND 20° FROM
TRAC POSITION)

- LEGEND
- ① DRIVE SHAFT
 - ② WIRE WIND
 - ③ ROLL BEARING BEARING CAP, TRACTION ONLY
 - ④ BEARING BEARING
 - ⑤ BEARING BEARING BEARING
 - ⑥ BEARING BEARING BEARING
 - ⑦ BEARING BEARING BEARING
 - ⑧ BEARING BEARING BEARING
 - ⑨ BEARING BEARING BEARING
 - ⑩ BEARING BEARING BEARING
 - ⑪ BEARING BEARING BEARING
 - ⑫ BEARING BEARING BEARING
 - ⑬ BEARING BEARING BEARING
 - ⑭ BEARING BEARING BEARING
 - ⑮ BEARING BEARING BEARING
 - ⑯ BEARING BEARING BEARING
 - ⑰ BEARING BEARING BEARING
 - ⑱ BEARING BEARING BEARING
 - ⑲ BEARING BEARING BEARING
 - ⑳ BEARING BEARING BEARING
 - ㉑ BEARING BEARING BEARING
 - ㉒ BEARING BEARING BEARING

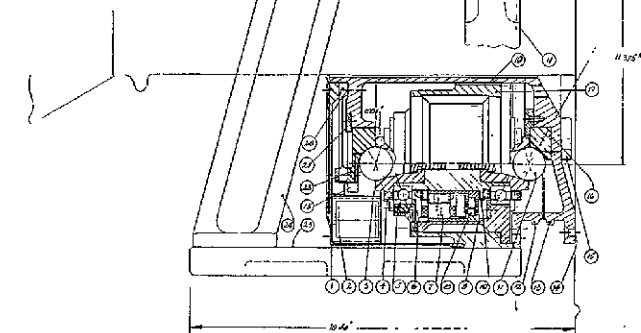


Figure 3-3. AASIR, Tri-Elements Traction Drive

FOLDOUT FRAME

FOLDOUT FRAME

of the retainer cups and the balls (by virtue of the conic section's choice of angle and the sliding coefficient of friction) is always greater than the friction at the point contacts established by the balls and the inner race curvatures, the balls will roll along the races when driven by the motor. To ascertain parallelism of the rotational axes of the drives with respect to each other, the conic retainers are purposely eccentric to afford the desired alignment. The wear of the gimbal suspension balls and races is mitigated by a special traction lubricant "Sontotrac" supplied by the Monsanto Industrial Chemical Company of St. Louis, Missouri. The "Sontotrac" lubricant exhibits rolling contact grip phenomenon, heat and oxidation stability, and mechanical durability of synthetic hydrocarbon lubricant in air and in vacuum environments. The estimated torque transfer capability of the traction system is estimated to be 2 ft-lbs. In addition to the utilization of the inherent friction, the traction drive exhibits a 25:1 motion reduction.

Other components of the gimbal system, i.e., the feedback displacement transducing system and the wire wrap for the electrical power and signal transmissions, are very similar to those described in paragraph 3.1.2 in concepts and functionalities.

The summary of the tri-suspension gimbal performance is given in Table 3-6. Notice that each suspension assembly is capable of driving the gimbal. It is intended that two motors will be energized simultaneously in the electrically parallel configuration; the third motor acts as a redundant unit.

TABLE 3-6. Tri-Suspension Gimbal Performance

Summary

• Total Stiction Torque at Shaft of Each Active Motor

One "g" Performance

(-)Z axis aligned with gravity	23 in-oz
(+)Z axis aligned with gravity	31 in-oz
(+)Y axis aligned with gravity	44 in-oz

Note: For coordinates definition, refer to figure 3-3.

Zero "g" Performance

Any orientation	~10 in-oz
---------------------------	-----------

• Motor Characteristics

Motor constant	0.32 ft-lb/amp
Winding resistance	11.1 ohms
Power required to overcome maximum stiction in one "g" field (2 motors)	11.4 watts
Power required to overcome maximum stiction in zero "g" field (2 motors)	0.6 watts
Power required to develop maximum torque	59.2 watts

• System Weight

For aluminum structure	135 lbs
For titanium structure	155 lbs
For steel structure	200 lbs

• Feedback Device

Accuracy (full revolution)	2 sec of arc
Repeatability2 sec of arc
Resolver equivalency	734 speeds
Tape Pitch (1 sinusoidal cycle)	2 mm
Number of stator heads	3

TABLE 3-6. Tri-Suspension Gimbal Performance, Continued

• Miscellaneous Characteristics

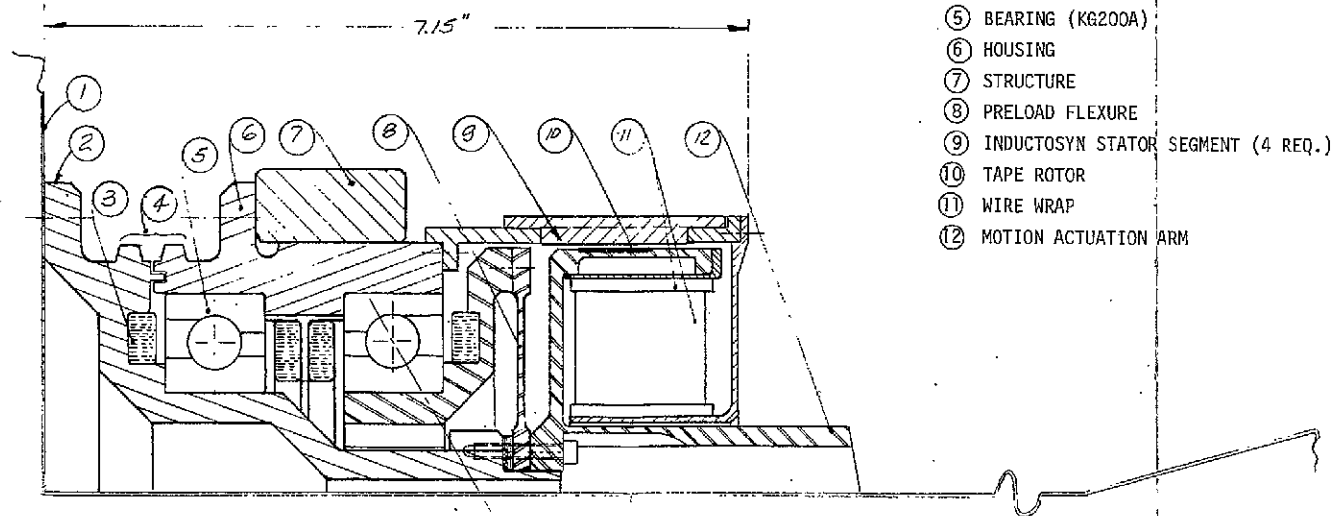
Traction torque transfer capability	2 ft-lb
Output to input torque ratio	25:1

3.1.4 Linear Ball Screw Actuator Driven Gimbal

The proposed gimbaling concept is shown on Figure 3-4. It consists of a gimbal, a support structure, and a precision bearing ball screw actuator.

The gimbal suspension system (Figure 3-5) consists of two angular contact bearings in a BTB configuration preloaded by a flexural preload mechanism. Nylasint reservoirs replenish the bearings' lubricant. Electrical power and signal wire wrap-up subassembly via its flexible flat multiwire tapes provides 180 circuits, each capable of 0.3 ampere current transfer. A 12 inch moment arm structure converts the linear actuator motion to the desired payload rotations. An "Inductosyn" multi-speed resolver is used as a displacement feedback element. It has a tape-type rotor attached to a rotating element of the gimbal and four stator heads symmetrically located along the periphery of the rotor. The suspension system is supported by a sturdy 356-aluminum casting. The gimbal has provision for Marmon clamping for the launch phase.

The linear actuator design is similar to that proposed in Phase II report [2]. The conceptual differences lie in the actuator's pivoting scheme, elimination of the harmonic gear train and the linear feedback device, and a larger motor size. The actuator (Figure 3-4) is supported by the gusset element of the aluminum casting and pivots on radially preloaded spherical bearing trunnions. It (Figure 3-6) consists of: a DC brushless torque commutated by Hall Effect devices; a precision, ball-type preloaded screw assembly; back-to-back angular contact bearing set; a flexible bellow which retains the bearing lubricant and provides torsional restraint for the screw. The actuator, including the



LEGEND

- ① AASIR INSTRUMENT
- ② GIMBAL SHAFT
- ③ NYLASINT RESERVIOR
- ④ MARMON CLAMP INTERFACE
- ⑤ BEARING (KG200A)
- ⑥ HOUSING
- ⑦ STRUCTURE
- ⑧ PRELOAD FLEXURE
- ⑨ INDUCTOSYN STATOR SEGMENT (4 REQ.)
- ⑩ TAPE ROTOR
- ⑪ WIRE WRAP
- ⑫ MOTION ACTUATION ARM

Figure 3-5. Bearing Suspension System
(For Baseline AASIR
Gimballing Concept)

FOLDOUT FRAME 1

FOLDOUT FRAME 2

TABLE 3-7. Linear Actuator-Driven Gimbal, Performance Summary, Continued

● <u>Others</u>	
Gear ratio	377:1
Axial stiffness of bellows	6.0 lb/ft
Axial stiffness of actuator	10.0 lb/ft
● <u>Predictable Errors</u>	
Coning of Gimbal (bearing effects)	9.6×10^{-6} rad
Indexing error (erroneous signal indication by the displacement feedback	9.7×10^{-6} rad
● <u>Non-Predictable Errors</u>	
Thermo effect due to uniform shaft expansion for temperature $\Delta=100^\circ\text{F}$	0.4×10^{-6} rad
Non-repeatable inductosyn errors	0.97×10^{-6} rad
Bearing noise	2.0×10^{-6} rad

3.2 Conceptual Design Ranking

The concept oriented hardware study was terminated with an attempt of the designs' ranking and the recommendation of a particular configuration. The ranking was based on the principal concerns evolved with any electro-mechanical designs and, that is, to select a concept which emits greatest promise of fulfillment of the desired functionality. Since in-depth error analyses were not conducted, the ranking was necessarily limited to such quantities as

- (a) Simplicity
- (b) Pedigree status of the major function implementing components
- (c) Adaptive flexibilities where performance can be altered by substitutions of components without major changes of the entire design
- (d) Power consumption and weight.

- Simplicity - Encompasses the relative ease of fabrication of assembly and in-process tests. From review of the pertinent configurations, Figures 3-1, 3-3, 3-4, 3-5, and 3-6, it is clear that from the parts count and the parts' relative simplicity, the direct drive is probably more facilitating than the other configurations; the three-point suspension is not simple because its parts count is high and it takes a reasonable effort and ingenuity to align the three drive assemblies with respect to each other. The linear actuator gimbal, however, is most convenient in the phases of assembly and test, mainly because of the inherent separation of the gimbal suspension from the drive system.
- Pedigree Status - The linearly articulated gimbal is perhaps the most responsive to this status. Its prime mover is a modified #100265 motor manufactured by Schaeffer Magnetics. This type of motor was successfully used in conjunction with gimballed star tracker programs (PAC, SLANT and PADS). Of interest is to note that the laboratory demonstrated "PADS" pointing performance, including the system electronics, and the laboratory instrumentation errors were within 3.8 arc sec, 1σ . This type of motor has also successfully survived environmental qualification tests in conjunction with the ComSat Solar Array Drive program. Furthermore, the linear actuator articulation concept itself is being used at TRW for laser optical train alignments. On the other hand, the direct drive gimbal requires a new development of a large diameter, thin section prime-mover of which the performance, the manufacturing, and the assembly problems, at best, are speculative.

The three point suspension concept, although pedigree components (by similarity) are used, is an entirely new gimbaling concept in the respect of the bearing suspension, lubrication, and the drive principal.

- Flexibilities - Superiority of adaptive flexibilities again belong to the linear actuation gimbal drive, simply because substitution or addition of components to achieve the desired performance

during phases of the gimbal development can be made with relative ease. Of particular concern is the system's repeatability performance of 3×10^{-6} radians in view of the motor nonlinearities in the neighborhood of small rotor displacements. One source of this nonlinear performance is the combination of the non-uniformity of the magnetic flux distribution between the pole pieces of the permanent magnet motor and the stator slots reluctance variations. The specific concern is that in the 3×10^{-6} radians region, the servo loop limit cycle may occur. Should such be substantiated by an in-depth analyses or tests, several design corrections are available. These are:

- (1) Introduction of additional gear reduction by either an additional gear stage or a decrease of the screw pitch
- (2) Introduction of velocity servo loop
- (3) Reasonable tightening of the motor performance specification.

• Power Consumption and Weight

TABLE 3-8. Power and Weight Summary

Gimbal Type	Maximum Power (Watts) (Motor Only)	Weight (lbs) (Aluminum Structure)
Direct Drive	300	143
Tri-suspension	60	135
Articulated by Actuator	20	140

Since the weights of the gimbals are essentially the same (Table 3-8) and the power consumption is smallest for the linear actuator driven gimbal, the latter is the obvious choice of this particular tradeoff.

Concluding the various tradeoffs, the linear actuator gimbal concept was chosen as the baseline concept.

3.3 Preliminary Gimbal Servo Design

In the second Interim Technical Report, Reference 2, a gimbal servo design was presented using a stepper motor. The purpose of this section is to present a preliminary design of a continuous servo for stepping the AASIR. It is assumed that the direct driven baseline gimbal configuration identified in the previous section is used.

3.3.1 Gimbal Drive Model

A mechanical model of the actuator and load is derived from Figure 3-6 and shown in Figure 3-7. The rotation of a two-phase brushless DC motor is converted to linear motion by a ball-screw assembly, and the linear motion of the lead screw causes rotation of the payload. The variables T_{f1} and T_{f2} represent stiction/coulomb friction, where the coulomb friction levels are each one-half of the associated stiction levels. The coefficients K_1 and K_L represent rotational stiffness (primarily due to shaft compliances) and K_2 represents a linear spring effect which is primarily the axial bearing stiffness within the ball-screw assembly.

This model can be put into a different form as shown in Figure 3-8 by using electrical analogs of the mechanical elements. This electrical analog is established by choosing force or torque to be analogous to current, and rate (rotation or translation) to be analogous to voltage. Then, because they satisfy the same differential equation, compliance $1/K$ is analogous to an inductance, viscous friction B to a conductance, and mass or moment of inertia to a capacitance. Note that coulomb friction torques become current sources. The parameter values associated with these two figures are given in Table 3-9. Note that the total reflected stiction associated with the ball-screw assembly, T_{ST} , is a function of the forces acting on the assembly.

If each of the compliances is considered alone, it can be shown that the three natural frequencies are:

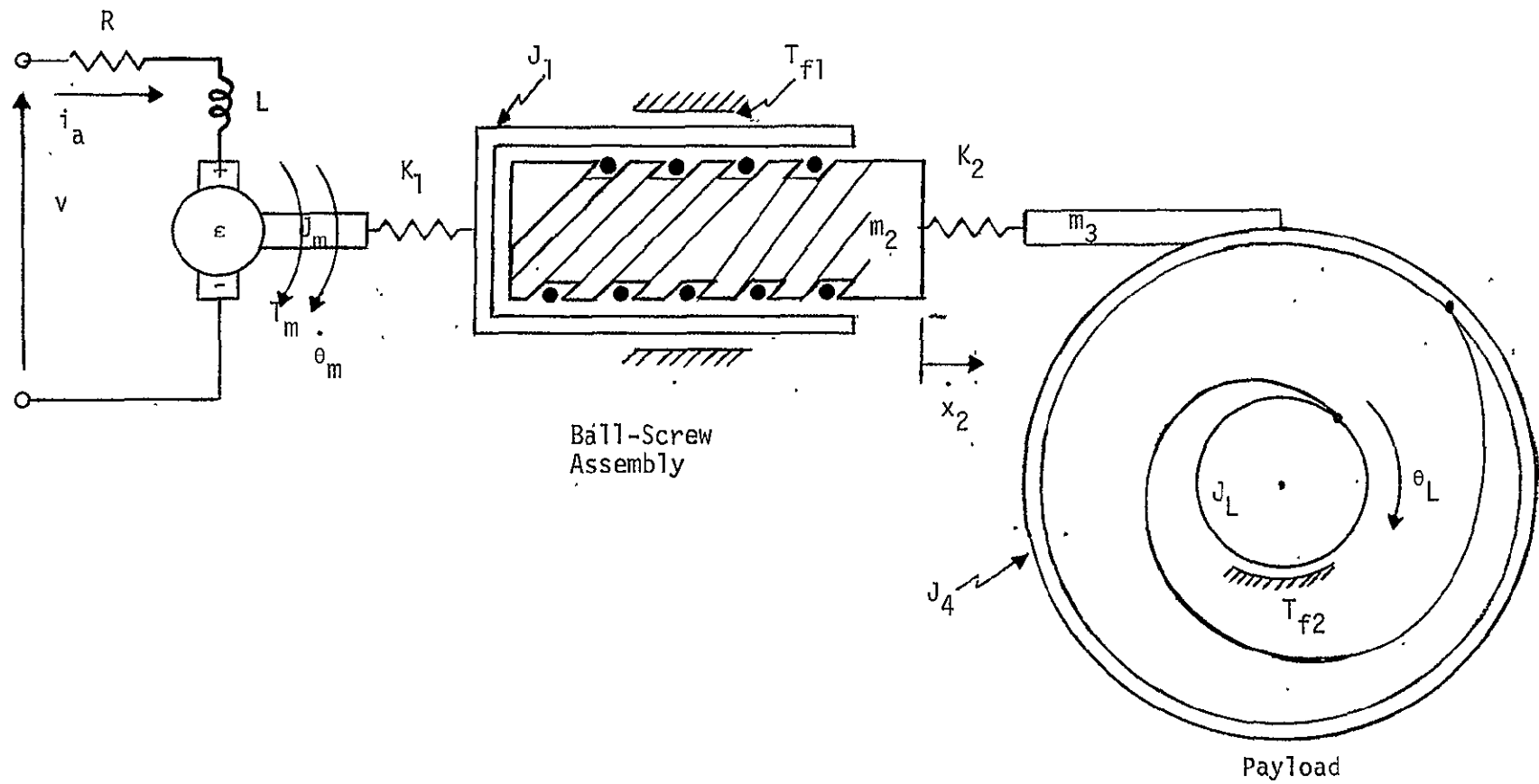


Figure 3-7. Mechanical Model of Actuator and Load

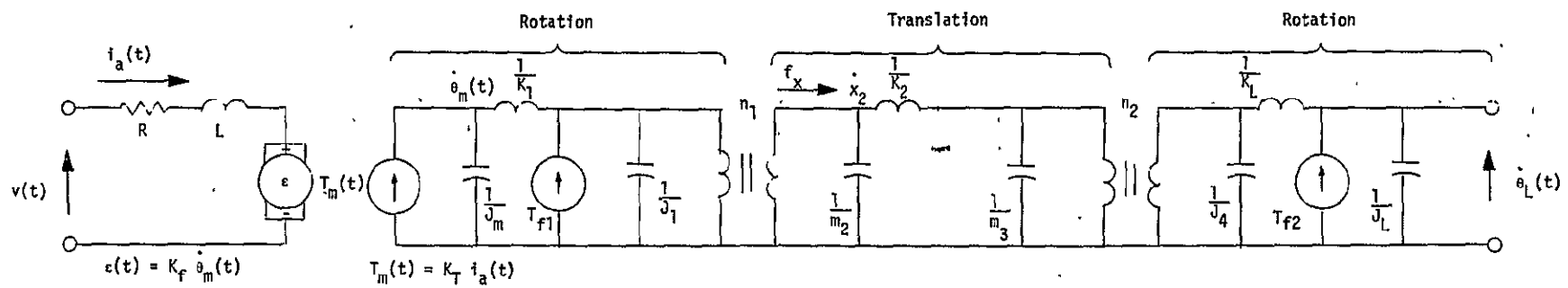


Figure 3-8. Equivalent Model of Actuator and Load

Table 3-9. System Parameters

Parameter	Symbol	Value
Motor Armature Resistance	R	28 Ω
Motor Armature Inductance	L	35 mh
Motor Back-EMF Constant	K_f	1.32 v sec
Motor Torque Constant	K_T	186 $\frac{\text{in oz}}{\text{amp}}$
Rotor and Shaft Moment of Inertia	J_m	0.115 in oz sec ²
Ball-Nut Moment of Inertia	J_1	1.421 in oz sec ²
Lead Screw Mass	m_2	0.127 oz sec ² /in
Lead Screw Mass	m_3	0.127 oz sec ² /in
Gimbal Moment of Inertia	J_4	96.15 in oz sec ²
Payload Moment of Inertia	J_L	1450 in oz sec ²
Motor Shaft Torsional Spring Constant	K_1	5.38×10^7 in oz/rad
Actuator Axial Stiffness	K_2	1.33×10^7 oz/in
Gimbal Stiffness	K_L	3.46×10^{10} in oz/rad
Lead Screw Ratio	n_1	(1/10 π) in/rad
Payload Torque Arm Ratio	n_2	(1/12) rad/in
Ball-Screw Stiction (Nut)	T_{f1}	21.12 in oz
Gimbal Bearing Stiction	T_{f2}	960 in oz (1 g) 384 in oz (0 g)
Total Reflected Stiction at Motor	T_{ST}	23.57 in oz*

$$*T_{ST} = [21.12 + 0.1 |T_m| + 1.045 \times 10^{-3} (|f_x|)^{1.3}] \text{ in oz, } f_x = \text{actuator force}$$

$$\omega_1 = 6128 \text{ rad/sec for } K_1$$

$$\omega_2 = 1108 \text{ rad/sec for } K_2$$

$$\omega_L = 4889 \text{ rad/sec for } K_L$$

Because ω_2 is much lower than ω_1 or ω_L , it was assumed for the controller design that K_2 is dominant. Thus K_1 and K_L are ignored and when the model elements in Figure 3-8 are all reflected to the motor side of the power train, the simplified model shown in Figure 3-9 results. There should be a damping term associated with each of the K's (shaft internal damping, etc.) but these terms were left out of the model because they could not be estimated accurately enough. This means that the model is conservative in this respect, and any compliance response would be damped more than the model indicates.

For the purposes of this design, the plant is defined to include the motor, the power transfer train and the load. It is assumed that the inductosyn (which senses the payload rotational position) can be modelled as a simple linear gain, K_I volts/rad. There should be no problem in designing the inductosyn readout circuitry to place K_I in the range of 10^3 or 10^4 , but a gain on the order of 10^6 could result in a high noise level. The effects of noise were not investigated in this study.

3.3.2 Performance Requirements

In order to perform its frame scanning operation, the AASIR must scan back-and-forth three times, then step one line (where 1 line = 375 μ rad) and scan back-and-forth three more times, and then step 11 lines and start the cycle over again. The timing of this cycle is shown in Figure 3-10, where the total period of the cycle is 16.76 seconds and 77.5 cycles are required to scan a $20^\circ \times 20^\circ$ frame. The AASIR inertial orientation is required to be stable within 4.2 μ rad during scan. The error budget for the gimbal servo is 2 μ rad so that the controller must be designed to maintain the gimbal angle within 2 μ rad except during the turn around periods.

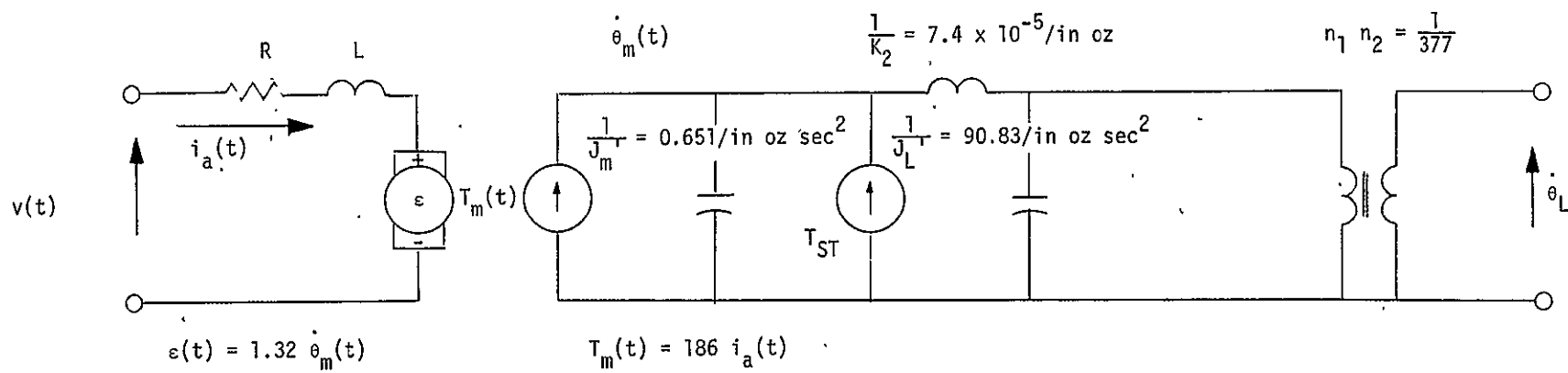


Figure 3-9. Model Used in Controller Design

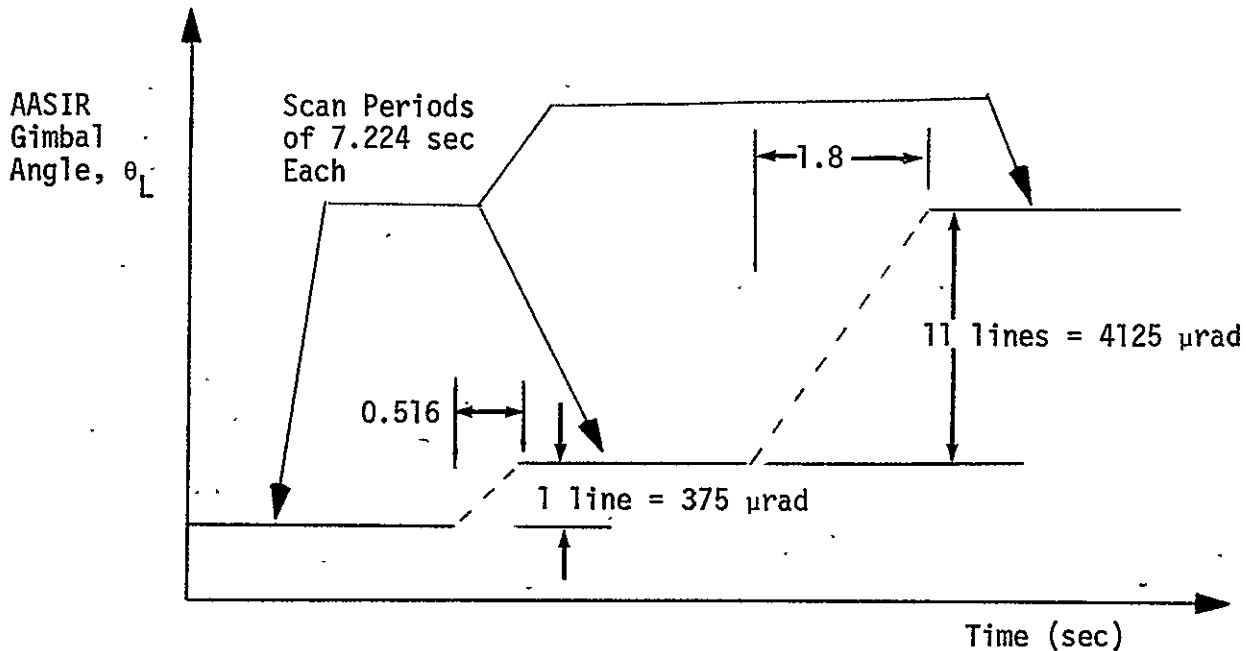


Figure 3-10. Time History of AASIR Gimbal Angle

3.3.3 Controller Design

The motor which was specified for the controller has the parameters listed in Table 3-9 and a stall torque of 160 inch-ounces. That the stall torque is more than sufficient can be shown by assuming the single-line step is accomplished using a torque doublet. The torque level required to provide the necessary acceleration is given by the equation

$$T = \frac{2 \left(\frac{\theta}{2} \right) J}{\left(\frac{t}{2} \right)^2} \quad (3-1)$$

where θ is the step size ($375 \mu\text{rad}$), t is the time to complete the step (0.516 second), and J is the inertia (the total motor inertia in Figure 3-9 is $1.547 \text{ inch ounce second}^2$). With these values, $T = 8.72 \times 10^{-3} \text{ inch-ounce}$ is the torque required of the motor in addition to the stiction/coulomb friction torque. The stiction torque at the motor shaft is less than 25 inch ounces, so the motor stall torque exceeds it by a factor of six.

It was initially assumed that the controlled system dominant roots would be underdamped with $\xi = 0.7$, so the required natural frequency (approximately the bandwidth) can be found from

$$\omega_n \geq \frac{4}{\xi T_s} \quad (3-2)$$

where $\xi = 0.7$ is the damping ratio and T_s is the two percent settling time. Using $T_s = 0.516$ second for the single-line step yields the requirement $\omega_n \geq 11.07$ rad/second, and using $T_s = 1.8$ seconds for the 11-line step yields $\omega_n \geq 3.17$ rad/second. Because of potential AASIR design changes, the time T_s to complete a step may be reduced by one-third to 0.344 second. This results in the requirement $\omega_n \geq 16.61$ rad/second and it was decided to design the controller for a closed loop natural frequency of $\omega_n = 20$ rad/second. Note that if the step is accomplished primarily by using a torque doublet introduced directly at the motor with the linear controller only removing residual errors, then the controller bandwidth could be much lower than that chosen above.

The 2 μ rad accuracy criterion requires that an error of less than 2 μ rad must be sufficient to overcome the stiction torque. In the start-up state, the stiction torque can be found by letting $f_x = 2$ foot-pounds and $T_m = T_{ST}$. Then from the equation for T_{ST} in Table 3-9, the stiction torque at the motor is found to be $T_{ST} = 23.6$ inch ounces. Overcoming this torque level requires a motor input voltage of $v(t) = (R/K_T) T_{ST} = 3.54$ volts. This in turn requires that the DC gain from the gimbal angle θ_L to the motor input $v(t)$ must be at least

$$K_{DC} \geq \frac{3.54 \text{ volts}}{2 \mu\text{rad}} = 1.77 \times 10^6 \text{ volts/rad} \quad (3-3)$$

This requirement can be met by using an integrator in the forward path, but then the time necessary for a 2 μ rad error to be integrated to the 3.54 volt level must be kept small. Two designs will be developed below: one with and one without an integrator.

In order to linearize the system, the coulomb friction was replaced with an equivalent viscous friction, B. The value of B was found from

$$B = \frac{T_f}{(\dot{\theta}_m)_{avg}} \quad (3-4)$$

where T_f is the coulomb friction torque obtained by combining all sources (20 inch ounces was used). The average motor shaft speed was estimated from the performance requirements: a 375 μ rad step in 0.516 second results in an average speed at the motor shaft of 0.27 rad/second and a 4125 μ rad step in 1.8 seconds results in a 0.86 rad/second average speed. Using the median of these two average rates, 0.57 rad/second, $B = 35.34$ inch ounce second is calculated as the equivalent viscous friction coefficient. The system resulting from this substitution is linear and its electrical analogue model is shown in Figure 3-11. Figure 3-12 shows the proposed block diagram of the controller. In that block diagram, the plant configuration is developed in a straightforward manner from Figure 3-11. By inspection $Z_m(s)$ (which is the s-domain representation of the motor load) is

$$\begin{aligned} Z_m(s) &= \frac{\dot{\theta}_m}{T_m}(s) = \frac{1}{J_m s + B + \frac{1}{\frac{s}{K_2} + \frac{1}{J_L s}}} \\ &= \frac{1}{J_m} \frac{\left(s^2 + \frac{K_2}{J_L}\right)}{\left[s^3 + \frac{B}{J_m} s^2 + \left(\frac{K_2}{J_m} + \frac{K_2}{J_L}\right) s + \frac{K_2 B}{J_m J_L}\right]} \end{aligned} \quad (3-5)$$

The other parameters shown in the block diagram are K_I to represent the inductosyn, the amplifier gain K_a , and a compensator because it is not likely that the system will perform as required without some compensation. Substituting the parameter values given in Table 3-9 into the plant model allows it to be simplified as shown in the block diagram in Figure 3-13.

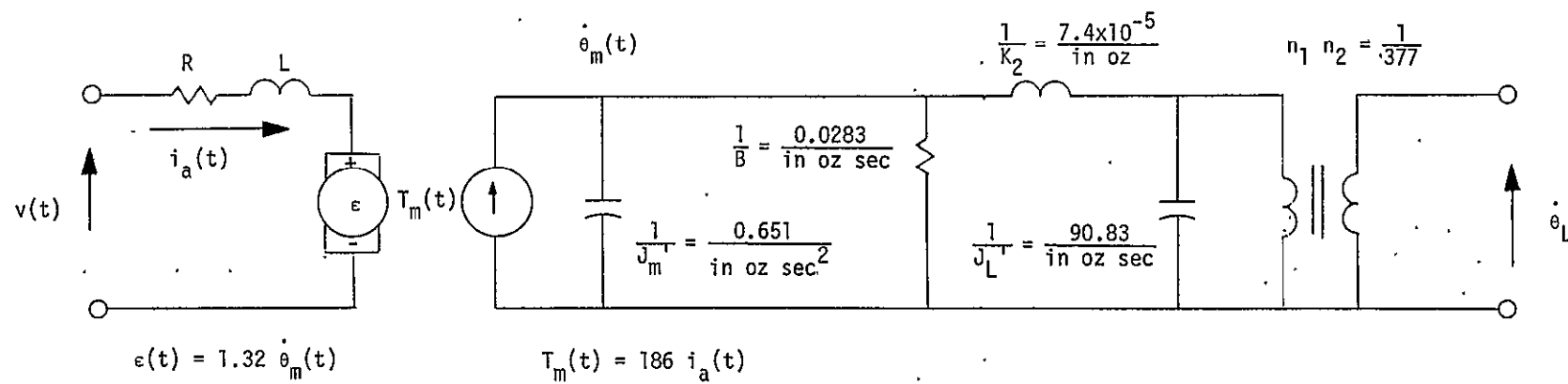
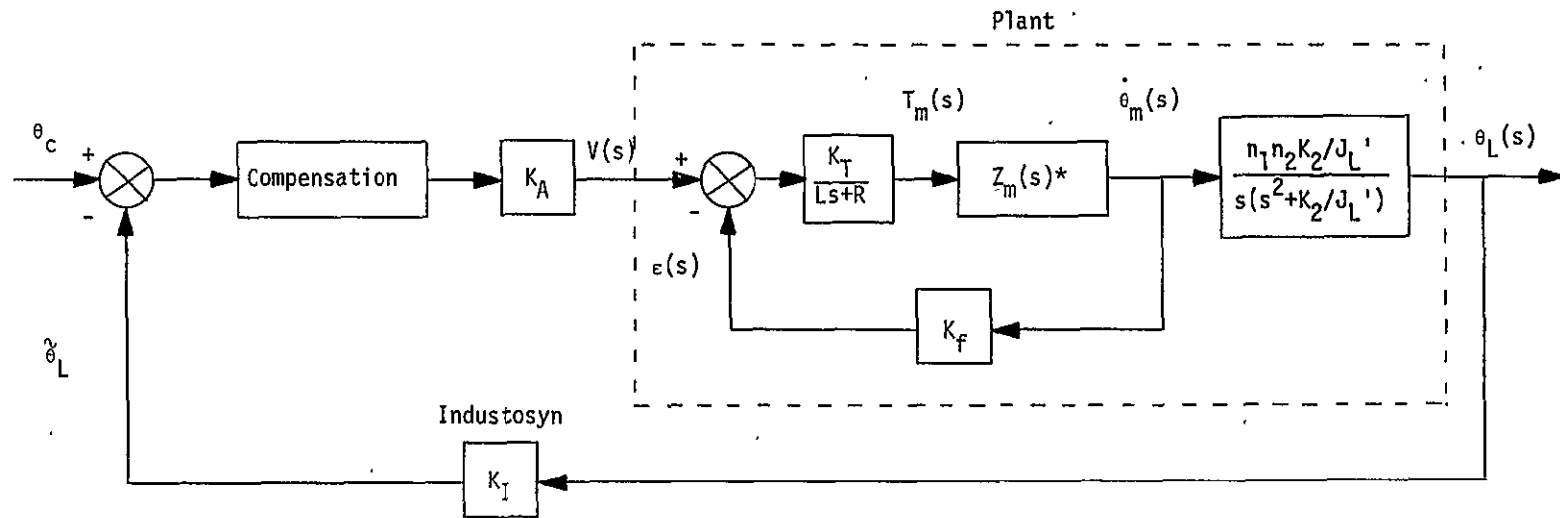
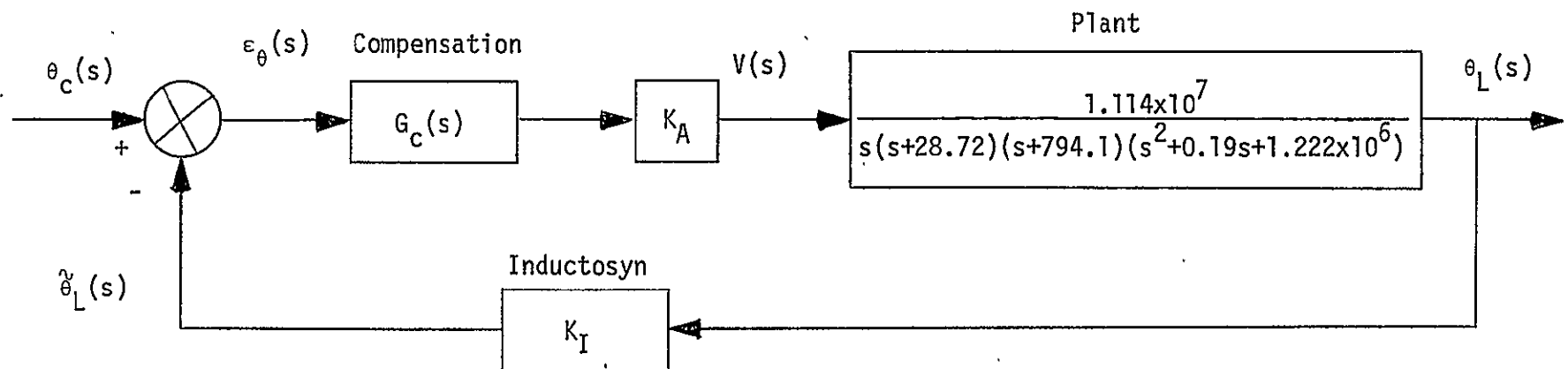


Figure 3-11. Model of Linearized System



$$* Z_m(s) = \frac{1}{J_m} \frac{\left(s^2 + \frac{K_2}{J_L}\right)}{\left[s^2 + \frac{B}{J_m} s^2 + \left(\frac{K_2}{J_m} + \frac{K_2}{J_L}\right) s + \frac{K_2 B}{J_m J_L}\right]} = \frac{1}{J_m} \frac{(s^2 + 1.213 \times 10^6)}{(s + 22.84)(s^2 + 0.16s + 1.222 \times 10^6)}$$

Figure 3-12 Linearized System Block Diagram



$$G_c(s) = \frac{1.48(s+40)}{(s+59)} \times \frac{0.01(s+1.0)}{(s+0.01)} \times \frac{100}{(s+100)}$$

Figure 3-13. Simplified System Block Diagram

The system design goals can be met by supplying a three-part compensation $G_c(s) = G_1 G_2 G_3(s)$ where

$$G_1(s) = \frac{1.48(s+40)}{(s+59)} \quad (3-6)$$

is a lead filter to place the root locus on the selected dominant roots ($s = -14 \pm j 14$). The second part is

$$G_2(s) = \frac{0.01(s+1.0)}{(s+0.01)} \quad (3-7)$$

which is a lag filter to raise the steady-state gain, K_{DC} , and keep the steady-state error small. Finally,

$$G_3(s) = \frac{100}{s+100} \quad (3-8)$$

is a simple lag filter that helps to control the compliance terms both by reducing the gain at high frequencies and by directing the loci into the left half-plane. With this pole added, the compliance poles can be neglected because they will not affect the (low frequency) response. In order to place the dominant roots, the gain is chosen so that

$$K_I K_A = 3.35 \times 10^6 \text{ volts/rad}$$

Because $V(s)/\theta_L(s)$ has the steady-state value $K_I K_A$, the error necessary to overcome stiction is $1.06 \mu\text{rad}$. The root locus plot for this system is shown in Figure 3-14 and the gain-phase plot is shown in Figure 3-15.

A similar system was designed with the dominant roots at $s = -20 \pm j 20$ which corresponds to a bandwidth of 28 rad/second. In this system the compliance peak was higher (-6.95 DB) but the steady-state error necessary to overcome stiction was only $0.72 \mu\text{rad}$. This example demonstrates the fact that a higher bandwidth will help to overcome the effects of stiction. The 20 rad/second bandwidth of the system above is used because it is adequate to meet the requirements. The

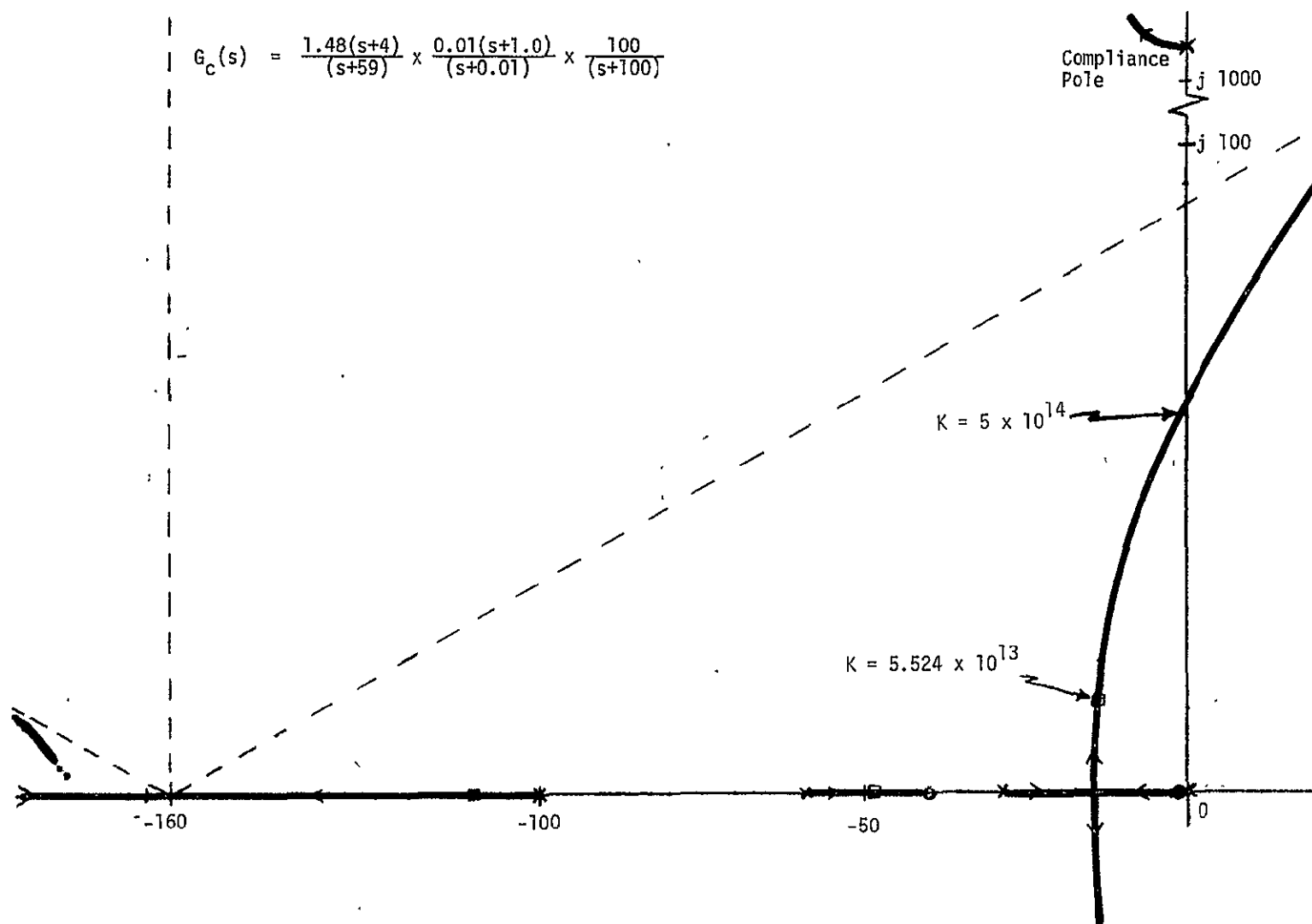


Figure 3-14. System Root Locus Plot

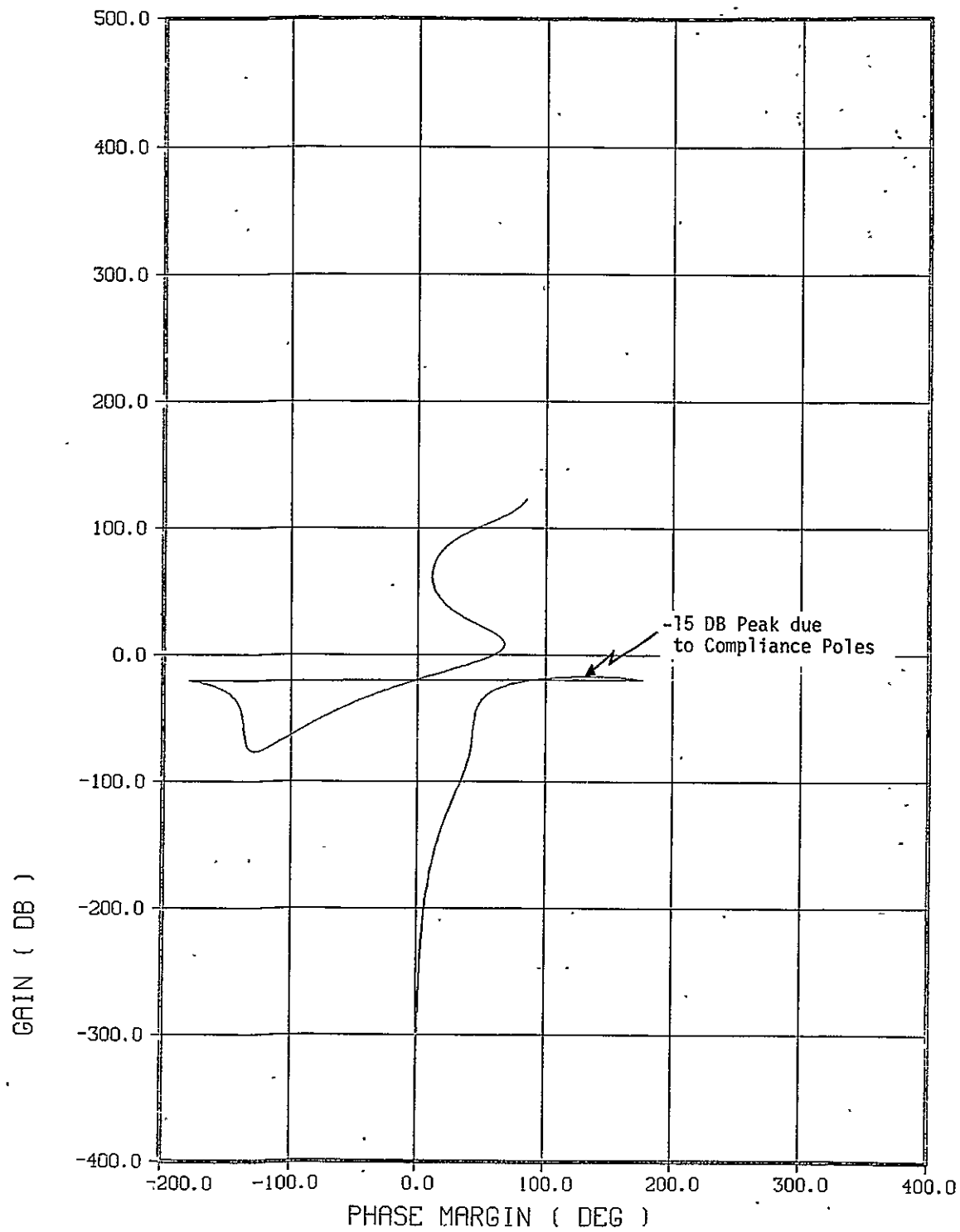


Figure 3-15. System Gain-Phase Plot

design is summarized in Table 3-10. The damping effect of the viscous friction B was found to be negligible in this system, so the real system (with coulomb friction) should behave in much the same manner. This should be investigated with a simulation.

An alternate design was attempted using an integrator in the forward loop to make the gain $K_{DC} \rightarrow \infty$. This was done by making $G_C(s) = G_1 G_2(s)$ where

$$G_1(s) = \frac{s+20}{s} \quad (3-9)$$

represents the integral control and

$$G_2(s) = \frac{3.45(s+20)}{(s+69)} \quad (3-10)$$

a lead filter to place the root locus at the dominant root locations (here chosen to be $s = -20 \pm j 20$). With $K_I K_A = 5.68 \times 10^4$ the "dominant" roots are correctly placed, but there is an extra pair of roots at, or near, $s = -20 \pm j 20$. Further,

$$\frac{\dot{v}(s)}{\theta_L(s)} = \frac{3.45 K_I K_A (s+20)^2}{(s+69)} \quad (3-11)$$

which has a steady-state gain of 1.14×10^6 volts/rad second. This means that a borderline error of $\theta_L = 2 \mu\text{rad}$ would change $v(t)$ at the rate of 2.27 volts/second, and the 3.54 volt stiction level would be reached after 1.56 seconds which is too slow. This design can be improved by increasing the integrator gain at the expense of reduced system damping. This often leads to viable designs if the integrator is also sharply limited and in effect turned off for larger signals, restoring the damping. Additionally, logic may be provided to "dump" the integrator at torque reversal, usually sensed by motor current reversal. Because of the increased complexity of this design and its nonlinear nature it has

Table 3-10. Summary of Linear Controller

Design Parameter	Value
Damping Ratio of Dominant Roots	0.7
Natural Frequency of Dominant Roots	20 rad/sec
Combined Gain of Inductosyn and Forward Loop Amplifier, $K_I K_a$	3.35×10^6 volts/rad
Steady-State Error Required to Overcome Stiction	1.06 μ rad
Forward Loop Compensation	$\frac{1.48(s+40)}{(s+59)} \times \frac{0.01(s+1)}{(s+0.01)} \times \frac{100}{(s+100)}$

not been further evaluated here and it is not recommended at this time. Hardware tests on the friction and stiction actually present in the gimbal drive are needed before the magnitude of the friction problem can be assessed and the need for more complex designs becomes acute.

3.3.4 Recommendations for Further Study

The design presented in this section is a preliminary design for controlling a linearized system; there are several areas in which further study is desirable. The greatest area of concern is the relatively high level of stiction and coulomb friction. To achieve steady-state accuracy, either a lag filter or an integrator (or both) must be used, but both of these elements respond relatively slowly, so the system may take a long time to settle to its final value. The effect of the coulomb

friction on the system dynamic response should also be studied. It is recommended that a detailed dynamic simulation be constructed and used to study these (and any other) nonlinear effects and system performance as well. Such a detailed simulation was beyond the scope of the present investigation.

Other matters that were not included in the scope of this investigation but which should be looked at are:

- (a) The effect of noise (primarily from the inductosyn with its high gain) and the ability to reduce it.
- (b) The integral control concept, especially with regard to switching it, limiting its output, and discharging it.
- (c) Similarly to (b), the slow settling effect of the lag compensation used to increase the DC gain.
- (d) Other methods of overcoming stiction (e.g., a larger motor or, properly constructed, a higher level of gear reduction): both of these could alleviate the need for high inductosyn gains and/or a lag filter.
- (e) Effects of a structurally flexible solar array on AASIR and spacecraft motion.

4. ON-BOARD DATA HANDLING

4.1 INTRODUCTION

On-board data handling for Stormsat includes those functions nominally required for monitoring, controlling and commanding the spacecraft, plus any special functions needed to prepare sensor data for transmission. Since it is intended that Stormsat use the MMS and the MMS has reasonably well defined capabilities and procedures for accomplishing normal telemetry processing, on-board computation and command decoding and distribution, no significant challenge exists in these areas. Instrument data rates, on the other hand, involve requirements which must be dealt with outside the MMS concept and it is these "mission peculiar" data handling tasks which are covered in the following paragraphs.

4.2 AASIR DATA HANDLING REQUIREMENTS

The AASIR configuration is still evolving and various combinations of focal plane geometry and scanning patterns have been considered baseline at various times. The data handling system discussed here is premised on a sensor which makes sinusoidal scans at a rate of 0.5814 scans per second. During each scan data are collected during 60 percent of the scan in each direction. The focal plane arrangement of detectors and the line stepping sequence have been discussed in Section 2.2.1.

The nature of the AASIR design is such that data samples must be taken from each of the sensors at several different rates, with two different accuracies (8 bit and 10 bit) and, to preserve registration and minimize skew, in definite phase relationships to each other despite the six mirror passes. Combined with these are the facts that the mirror moves sinusoidally, yielding a variable sampling rate and that dead spaces occur during mirror turn around and after every 12 active mirror scans during which time data collection is suspended while the AASIR steps seven lines in its gimbal.

4.3 DESIGN CONSIDERATIONS

The design which has been selected to manage the sensor data provides for analog multiplexing the various inputs in a way that yields a minor frame containing all data collected during 375 microradians of field-of-view scan. These minor frames are repeated throughout each pass of the mirror. During

successive mirror passes, new minor frames will be employed until six lines have been completed and the AASIR is ready to step. This interval of six scans corresponds to a major data frame.

Registration of samples collected during successive mirror scans and freedom from skew among the four lines collected simultaneously are assured by: (a) proper layout of the focal plane, (b) precisely periodic sampling of super commutated sensors within each minor frame, (c) adjustments in the order of sampling depending on the direction of mirror travel, and (d) accurately slaving all timing to signals generated directly from the mirror position. A micro-programmer driven by the mirror position data is used to control all input formatting.

The formatted data stream which arises as the various samples are collected will still have gaps for mirror turn around and a sinusoidal pulse rate modulation during active scan. A buffer is used to smooth this incoming data stream to yield a continuous and constant-rate data stream (over six mirror scans) for transmission to earth. Because a large increase in buffer size would be required to eliminate the data gap every 14 scans these have not been removed; instead idling data are inserted.

Key issues in the design of the on-board data handling system are: layout of a minor frame which satisfies all the necessary requirements; sizing and designing the smoothing buffer; achieving a consistent data stream despite the bi-directional scan of the mirror; providing interpolated sampling pulses between the sinusoidally varying mirror position data. These are covered in the following paragraphs.

4.4 MINOR FRAME DESIGN

Referring to Figure 2-11 it can be summarized that during the time the field of view scans out 375 microradian, 12 sounder detectors must be sampled, one sixth of the 12 IR detectors must each be sampled three times (the other sixths are obtained on successive mirror scans), and one sixth of the sixty visible detectors must each be sampled 15 times. To permit the periodic sampling of the visible and IR detectors, the minor frame size must be a multiple of 15. The lowest multiple of 15 which accommodates all the data is 12. With careful layout of the minor frame, 12 is also sufficient to include a minor frame sync symbol and a word identifying the mirror position at the start of the frame. Figure 4-1 illustrates the format

SYNC	S1A	$V_1 + 10k$	$V_2 + 10k$	$V_3 + 10k$	$V_4 + 10k$	$V_5 + 10k$	$V_6 + 10k$	$V_7 + 10k$	$V_8 + 10k$	$V_9 + 10k$	$V_{10} + 10k$
SYNC	S2A										
SYNC	S3A										
SYNC	S4A										
$IR_1 + 2k$	$IR_2 + 2k$										
SYNC	S1B										
SYNC	S2B										
SYNC	S3B										
SYNC	S4B										
$IR_1 + 2k$	$IR_2 + 2k$										
MIRROR ANGLE	S1C										
MIRROR ANGLE	S2C										
MIRROR ANGLE	S3C										
MIRROR ANGLE	S4C										
$IR_1 + 2k$	$IR_2 + 2k$	$V_1 + 10k$	$V_2 + 10k$	$V_3 + 10k$	$V_4 + 10k$	$V_5 + 10k$	$V_6 + 10k$	$V_7 + 10k$	$V_8 + 10k$	$V_9 + 10k$	$V_{10} + 10k$

Figure 4-1. Minor Frame Format

of a possible minor frame. Subscript numbers refer to the position of the detector from the left hand edge in the focal plane. Subscript letters in the sounding channels refer to the three spectral bands. The letter, k , identifies which of the six scans is being considered ($0 \leq k \leq 5$).

Because the visible detectors are integrally assembled on chips in a straight line and yet must be sampled sequentially (if only one analog to digital, A/D converter is used) an inherent skew in the data will occur. This skew can be minimized at a small price in accuracy by accelerating the A/D process. Actually, since high accuracy and registration are not requirements for visible data the skew can probably be ignored or removed on the ground, if desired.

Skew in the IR and sounder channels can easily be eliminated by a slight alteration in the focal plane layout. Figure 4-2 illustrates a new layout which would correspond to the minor frame sequence shown in Figure 4-1. It appears that skewing the physical location of the detectors would cause problems on reverse scans. Such is not true, however, if the minor frame is sampled in reverse order. It should be noted that in addition to moving certain detectors, the arrangement of the IR detectors has been altered so that the pair of samples in successive mirror scans always bear the same relation to each other.

A slight complication arises when it is noted that only 8 bit accuracy is required for visible and IR words while 10 bit accuracy is required for the sounder channels. To accomplish commonality of analog and A/D circuits, 10 bit conversion accuracy is provided for. During transmission, however, this would create a 20 percent increase in data rate. Our suggestion to minimize the transmitted rate is to reduce all words to 8 bits except the sounder channels and let the extra two bits carry over into the sync and mirror position words in the minor frame. Thus, in computing data rates we consider each of the 180 words in a minor frame as having 8 bits for a total of 1440 bits per minor frame.

4.5 DATA RATES AND BUFFER SIZING

Data exiting from the analog-to-digital converter (in the 20 degree scan mode) have a rate which varies sinusoidally according to the formula

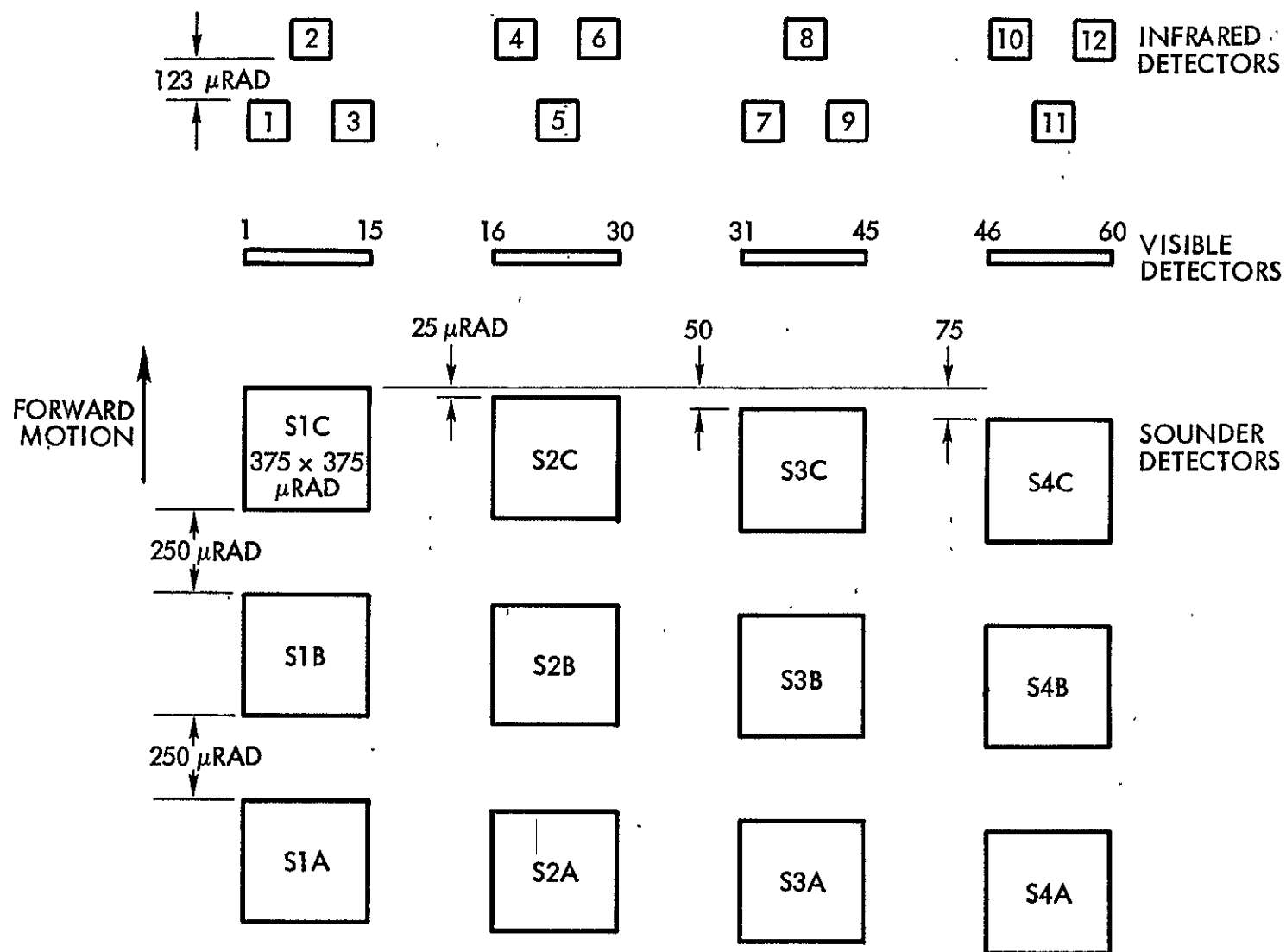


Figure 4-2. Revised Focal Plane Layout

$$R = \frac{3615}{T} B \cos 2\pi \frac{t}{T} \quad (-0.15T \leq t \leq 0.15T)$$

where

R represents the data rate in bits/sec,

B represents the number of bits per minor frame,

t is the time from the mirror's center position, and

T represents the period of a complete mirror cycle.

From this we see that at the center of scan the data rate is highest and for a period, T, of 1.72 seconds equals 3.0265 megabits/second. Similarly, at the edge of the active scan the rate is 1.78 megabits/second. The total number of minor frames collected over the 20 degree scan interval is 931, the data rate to be transmitted is $\frac{931 \times 1440}{0.86} = 1.559$ megabits/second. It should be noted that this is lower than the rate data generated during any part of the entire scan interval; an important consideration in the buffer design.

Figure 4-3 illustrates the data delivered from the sensor and the data transmitted to the ground as a function of time over one scan of the mirror. At the start of active scan it is assumed that no data reside in the buffer. At the end of the active scan the buffer contains 372 minor frames or 536 Kbits. In actuality the buffer would be organized into smaller segments and one additional segment would be required to ensure that reading and writing are never required at the same time in any one segment.

4.6 TIMING DERIVATION

While the output transmission rate is controlled by a master clock, data from the AASIR are generated at a rate controlled by the mirror motion. Mirror synchronization signals are generated each 375 microradian of motion. The time interval between these pulses varies due to the sinusoidal scan. Furthermore, this varying interval must be divided by 720 equally spaced clock pulses which are used to accomplish the sampling and the analog-to-digital conversion of each word in the minor frame. This is accomplished with a voltage controlled oscillator whose nominal 1.3 MHz output is divided by 720 to give pulses which should be coincident with the occurrence of the mirror pulses. When an error is detected the input to the VCO is incremented or decremented by an amount proportional to the error. Thus, between

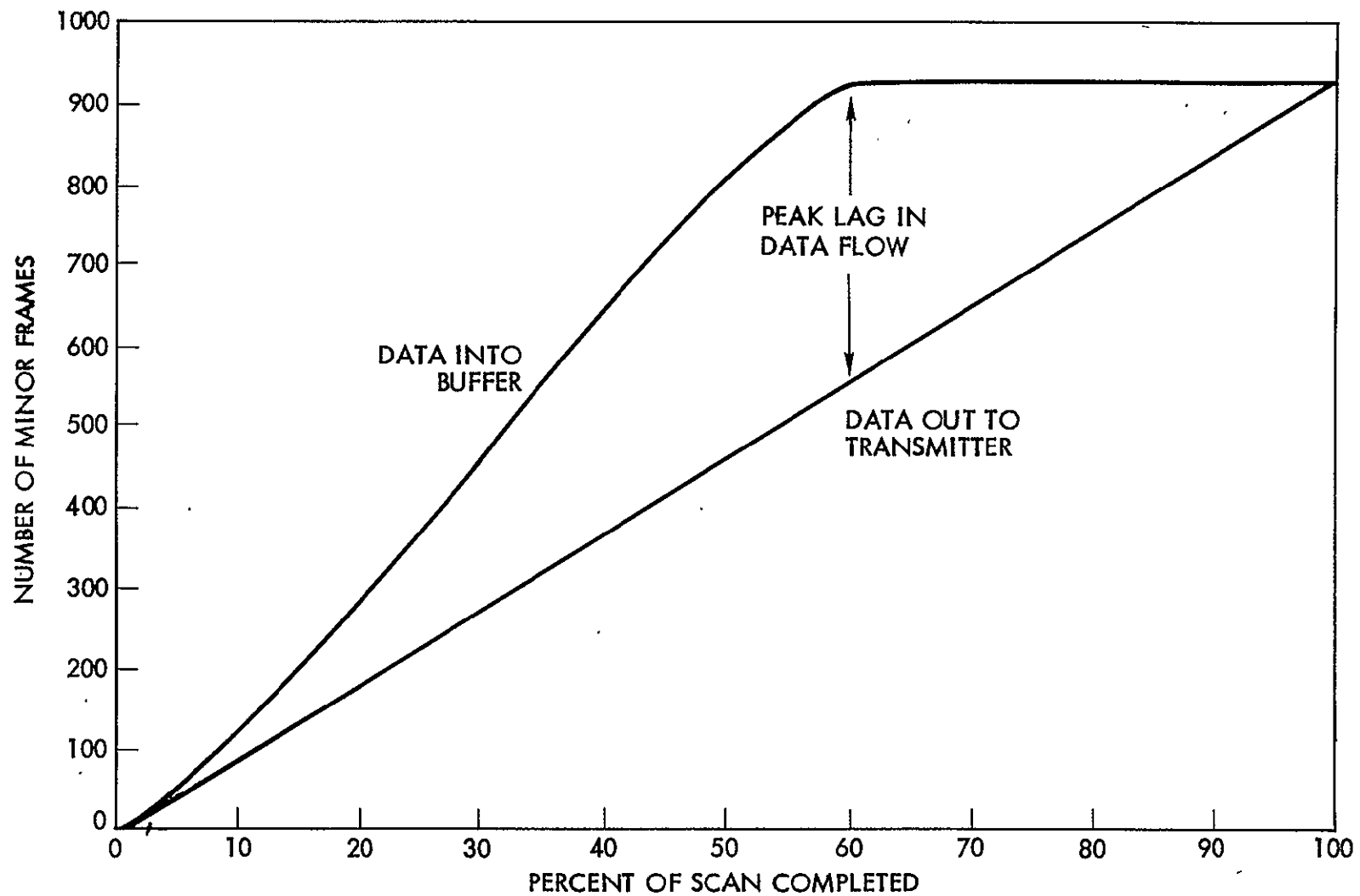


Figure 4-3. Buffer Data Flow Characteristics

the each successive pairs of mirror pulses the rate is the same as for the previous pair plus a change sufficient to reduce the previous error to zero provided the mirror rate has not changed. Since the mirror rate is continually changing a small error will generally exist. Determination of the worst magnitude of this error yields one part in 493 which is adequate to achieve the desired 1 percent registration.

4.7 HARDWARE IMPLEMENTATION

4.7.1 Analog Circuits

Multiplexing the outputs of the various detectors is accomplished in two levels of analog gates. The first level gate is used to select inputs within a minor frame for all major frames. The second level gates select which group of sensors is to be sampled in accord with the particular mirror sweep within the major frame. See Figure 4-4. Near the trailing edge of each multiplex interval the analog value is fixed in a sample-and-hold circuit. This value is then converted to a digital word in the A/D converter. The A/D converter operates on an input voltage range of 0 to 10 volts and delivers a 10 bit output.

4.7.2 Digital Formatter and Buffer Memory

Only the most significant 8 bits of each converted word (except the sounder channels) are stored in the buffer memory. The digital formatter rounds off the extra bits on those words requiring it and carries the least significant 2 bits over to the next word for the sounder channels. It also inserts the frame sync symbols and the mirror position data. Therefore, the data stream which enters the buffer is already for transmission without further manipulation. In Section 4.5 it was shown that the buffer memory had to be at least 536K bits. Using 4K chips the memory requires approximately 135 chips. These can be packaged 15 to a bank, thus, requiring 9 banks. An average power dissipation for MOS 4K chips is 648 mW, so this size memory would require 87.5 Watts. To reduce power consumption CMOS could be used but the largest memory slice presently available is 1K (1024 x 1). This would require 36 banks of 1K x 15 for a total of 540 chips. With 16 mW (@5 volts and 2 MHz) per chip the power dissipation would be 8.65 Watts. But using the 1K slices would require more off-chip address decoding which would not add too much to power but would add to parts counts. Other possibilities are CCD memories which are becoming available

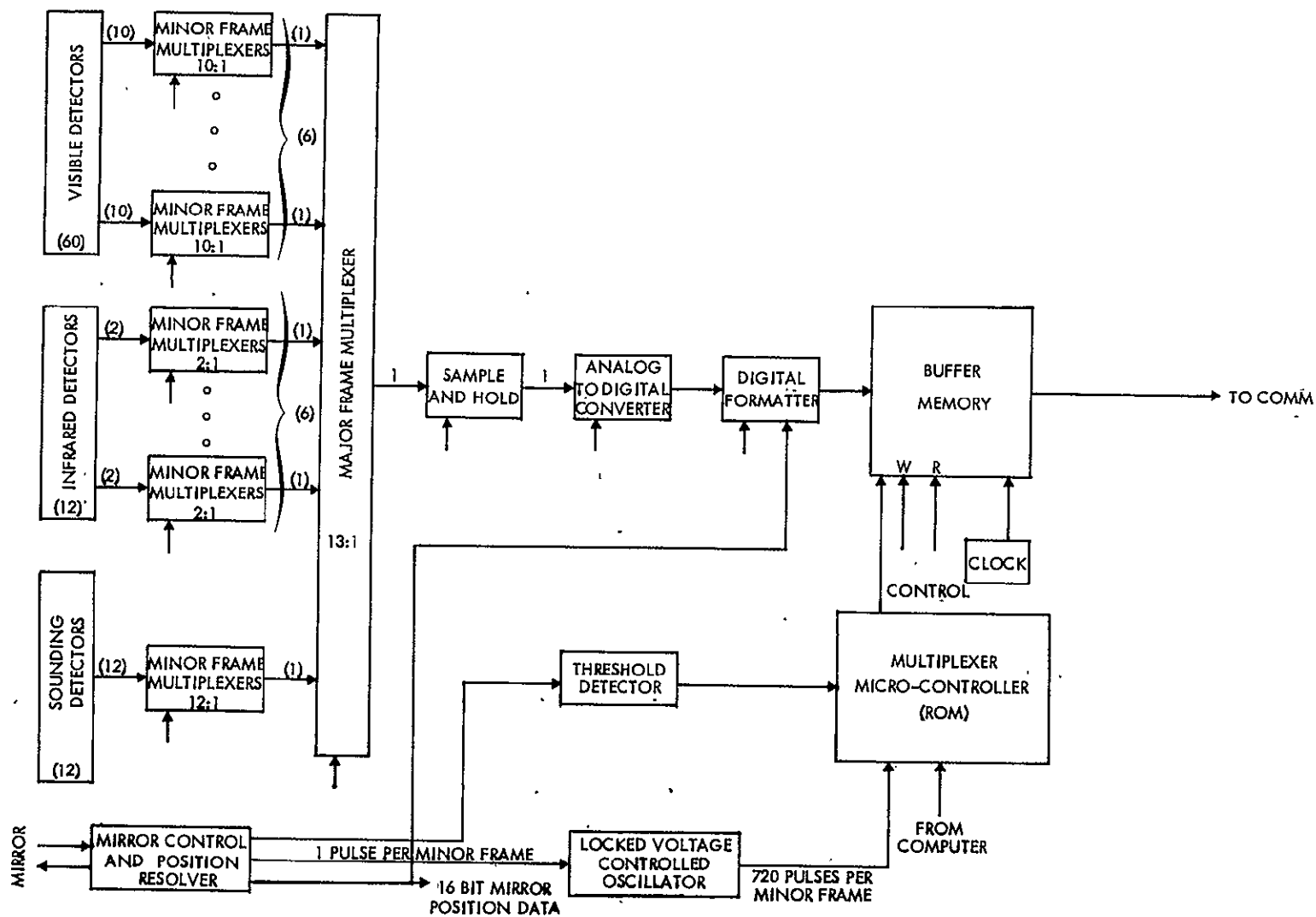


Figure 4-4. Block Diagram AASIR On-Board Data Handling

and which have much higher densities per chip. Estimates for the 1980 time frame would give 4 Watts, 1 pound and only a few cubic inches for a 1 Mbit CCD memory.

4.7.3 Micro-Controller

The micro-controller's program which is stored in ROM provides the control for the data handling system. Using a clock provided by the mirror position resolver and passed through a phase locked frequency multiplier to provide the proper instruction timing for sampling. The micro-controller generates instructions which select the correct multiplexer for each sample, and clock operation of the sample and hold, the analog to digital converter, the digital formatter and data input to the buffer.

4.7.4 Technology

Standard CMOS chips are available for the micro programmer, analog to digital converter, all digital registers and multiplexers, analog multiplexers and the phase locked loop which meet the requirements of speed and voltage and provide very low power consumption. The sample and hold circuit can also be produced by standard IC's and components. Only the buffer memory requires special consideration as already stated.

An estimate for the non-memory part of the data handling system described is one 10" x 13" printed circuit board weighing 3 pounds and consuming 10 watts. This assumes CMOS, Silicon on Sapphire technology.

5. TELECOMMUNICATION

5.1 INTRODUCTION

The telecommunication subsystem conveys all Stormsat mission data (AASIR and VSI) to the ground during orbit operations. The subsystem interfaces with the STDN ground stations, the on-board mission data handling subsystem, and the multimission spacecraft command and data handling (C&DH) subsystem and power subsystem.

The telecommunication subsystem has been designed to provide conservative performance margins for the mission data links, flexibility in data transmission, i.e., AASIR and VSI simultaneously, AASIR only, or VSI only, and employs NASA standard equipment and flight-proven hardware designs from other space programs.

A detailed description of the recommended baseline subsystem is provided in the next subsection and includes the configuration, operation, and interfaces. The subsections following contain the link performance analysis and hardware component characteristics and description.

The final subsection contains the various trade studies and the rationale used in selecting the baseline subsystem.

5.2 DESCRIPTION

Two independent data streams are generated by the on-board sensors. The AASIR data consist of a PCM NRZ encoded digital data stream sequenced at approximately 1.6 MBPS and the VSI data consist of a PCM NRZ encoded digital data stream sequenced at 1 MBPS. This dual-channel communication may be performed using standard techniques of frequency or time division multiplexing. An alternative is to transmit the two data channels on orthogonal carriers such as quadriphase.

The quadriphase modulated signal (QPSK) is formed by summing two independent bi-phase data channels in quadrature with one another (see Figure 5-1). The channels are designated the inphase (I) channel and the quadrature (Q) channel which corresponds to the inphase and quadrature S-band carrier components of the quadriphase signal. The I and Q data inputs to the quadriphase modulator may be independent and asynchronous,

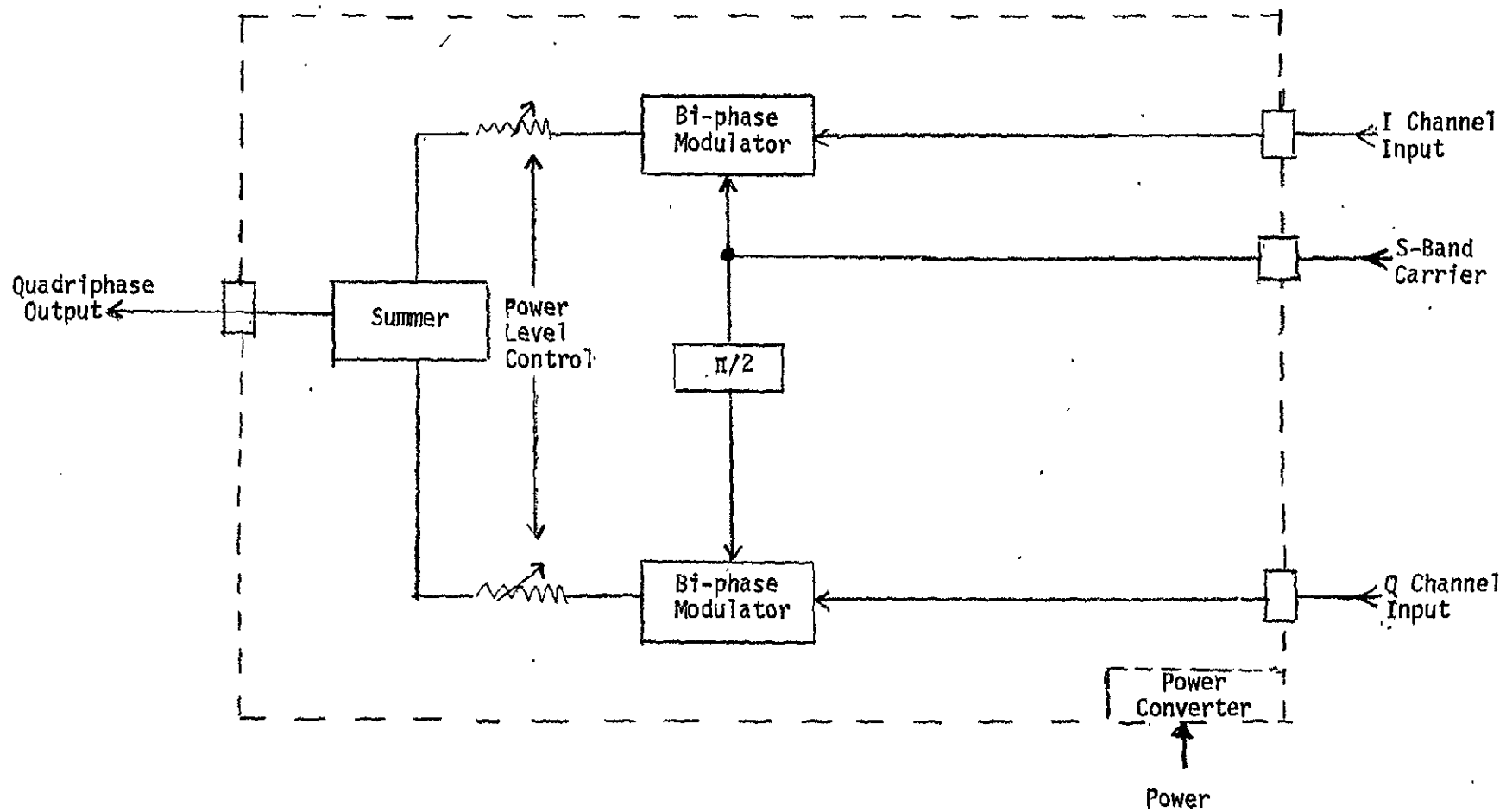


Figure 5-1. S-Band Quadriphase Modulator

independent and synchronous, or identical data streams. Furthermore, the data rates may be equal or unequal. If the data to the I and Q channels are independent and are of unequal rates, then the error probabilities for the two channels will be different. In order to balance performance, the powers in the channel should be selected to equalize the error rates. This leads to the generation of the unbalanced quadriphase signal (UQPSK). The UQPSK signal can be generated by adding two quadrature PSK signals with the rates and powers adjusted appropriately. This sum is still a constant envelope signal and can be communicated on systems using present hardware technology. While the equalization of error rates on a narrow bandwidth unbalanced QPSK signal set is an advantage, the nature of the signal leads to problems in the recovery of the carrier phase. Specifically, the ground station should provide a fourth order carrier tracking loop to recover the received carrier.

The recommended baseline configuration for the telecommunication subsystem is shown in Figure 5-2. The non-redundant subsystem consists of a quadriphase modulator, S-band frequency source, S-band power amplifier and power converter, and a S-band high gain parabolic antenna. Should redundancy be required, the dash lines in Figure 5-2 show the additional equipment and connections.

The subsystem is configured to transmit two independent data streams or a single data stream. The transmission flexibility is achieved with quadriphase modulation. The input to the quadriphase modulator I and Q channels are selected in the mission data handling subsystem. When simultaneous transmission of AASIR and VSI data are desired, AASIR data are fed to the I channel and VSI data are fed to the Q channel. Since the AASIR and VSI data rates are not the same, the I and Q channel powers are adjusted to optimize the AASIR and VSI link performances. When AASIR or VSI data only transmission is desired, identical data are fed to the I and Q channels and the I and Q powers are equalized by command or automatically adjusted if desired.

The output of S-band quadriphase modulator is fed to a S-band power amplifier and then transmitted to the STDN ground station via the earth coverage parabolic S-band high gain antenna.

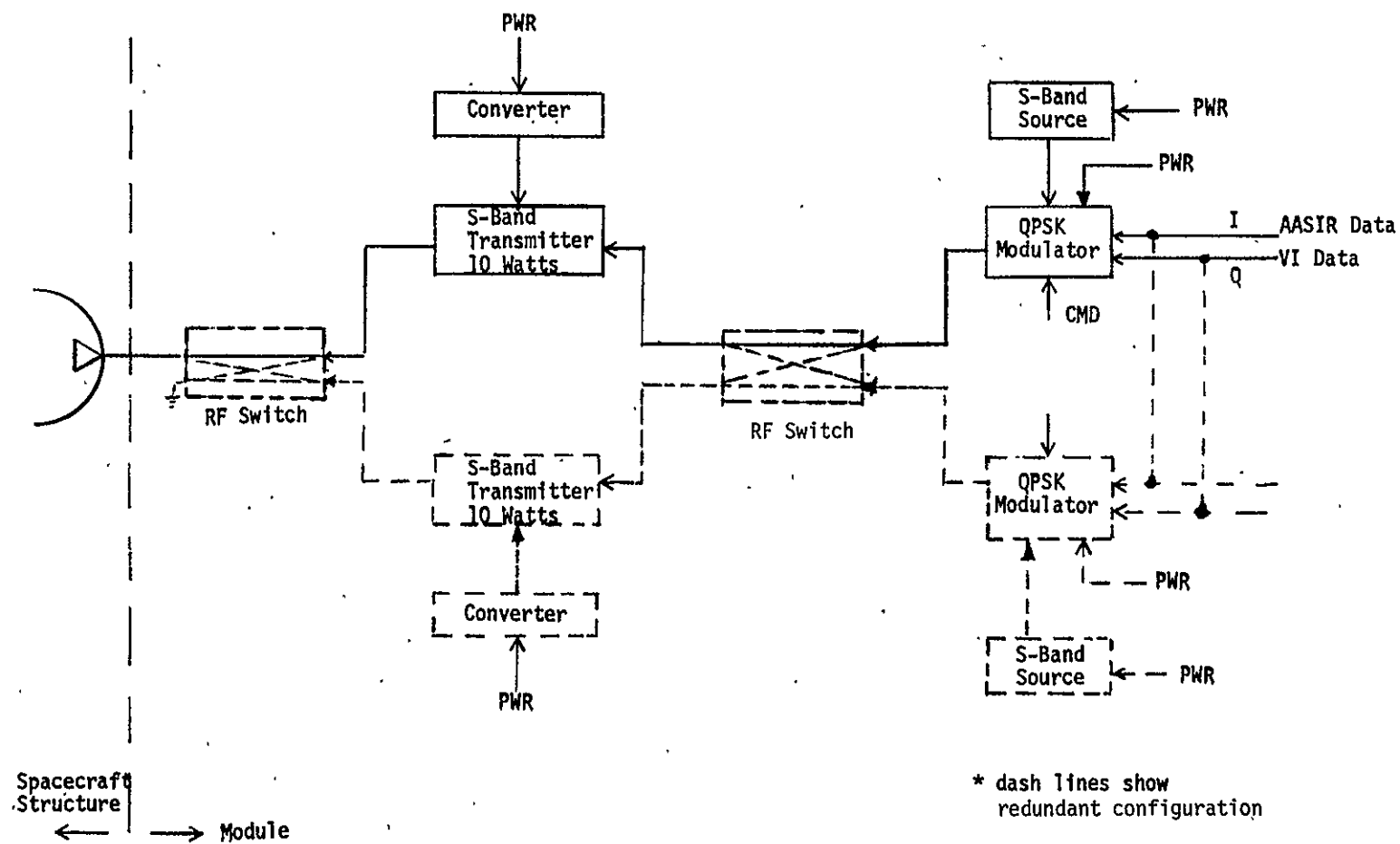


Figure 5-2. Telecommunication Subsystem Configuration

The multi-mission spacecraft 20-inch parabolic S-band high gain antenna is adequate for the antenna coverage requirements at geostationary attitude, i.e., providing earth coverage. The antenna is fix mounted on the multi-mission spacecraft structure such that it maintains an earth center equatorial line-of-sight for either winter or summer spacecraft configuration. Edge of earth antenna coverage gain is used in the link performance analysis.

In the redundant configuration, RF transfer switches are employed to provide cross-strapping for the QPSK modulators and S-band amplifiers.

The electrical interfaces for the telecommunication subsystem are shown in Figure 5-3 and they include the STDN ground station, mission data handling subsystem, multimission spacecraft C&DH subsystem, and the multimission spacecraft power subsystem.

The STDN ground station interface is the electromagnetic S-band signal from STORMSAT. The STDN ground station interface parameters are given in the link performance analysis subsection.

The mission data handling subsystem is the source of the mission data which is to be quadriphase modulated. The T^2L levels of the digital signals are transformed to ECL (Emitter Control Logic) 0, -0.5 voltage levels in the mission data handling subsystem before they are fed to the quadriphase modulator.

The modulator I and Q power adjustments are controlled via commands from the spacecraft C&DH subsystem as are the on/off control of the telecommunication equipment. Telemetry data providing status of the telecommunication subsystem are routed to the spacecraft C&DH subsystem.

The multimission spacecraft power subsystem supplies the prime power to the telecommunication equipment, i.e., the S-band power amplifier converters, the S-band frequency source, and the QPSK modulator.

5.3 LINK PERFORMANCE ANALYSIS

Conservative performance margins are achieved for the AASIR and VSI data links with a 10 watt transmitter, 20 inch S-band parabolic high gain antenna and STDN 30 ft ground station antenna and cooled paramplifier.

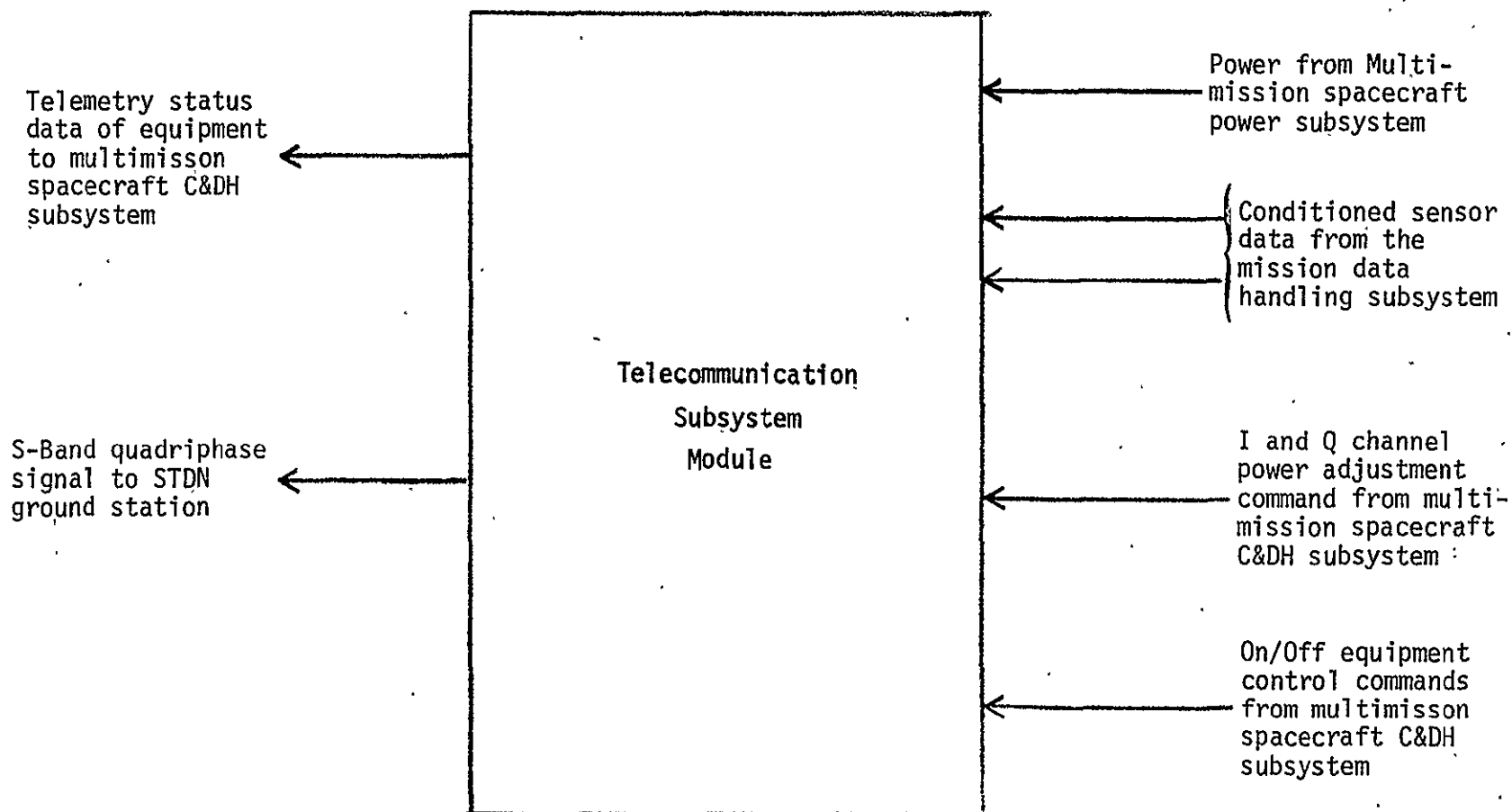


Figure 5-3. Telecommunication Subsystem Module Electrical Interfaces

The links are optimized for any transmission combination. When AASIR and VSI data are transmitted simultaneously, their respective I and Q channel powers are adjusted in proportion to the ratio of their data rates. When only AASIR or only VSI is transmitted, the I and Q channel power are equalized.

Table 5-1 contains a detail link performance analysis. Adverse tolerances are summed and comments are added to clarify or substantiate the entries to the link calculations.

The results show that 3.9 dB margin over summed tolerances is achieved with flight proven hardware.

5.4 HARDWARE CHARACTERISTICS

The hardware components of the telecommunication subsystem consists of an S-band quadriphase modulator, S-band frequency source, S-band 10 watt transmitter, S-band 20 inch parabolic high gain antenna, and cables and connectors. All components are flight proven equipment (Table 5-2):

S-Band Quadriphase Modulator

The quadriphase modulator is a TRW space qualified unit designed for balanced QPSK. A minor modification is necessary for generating unbalanced QPSK. Such a modification is shown in Figure 5-4 along with key features and measured data for the unit. The modulator will operate from the multimission spacecraft power bus since it contains its own power converter and it has an S-band driver amplifier to provide sufficient drive power for the S-band transmitter.

The modulator accepts the I and Q channel mission data and bi-phase modulates the S-band carrier with them. A single RF carrier provided by the S-band frequency source is used to generate the I and Q carrier components.

S-Band Frequency Source

The frequency source is a companion to the quadriphase modulator and it is also a TRW space qualified unit. The source offers excellent frequency stability and low phase noise. Figure 5-5 contains a summary of the key features and measured data for the unit.

Table 5-1. Mission Data Communication Performance

	Nominal Value	Adverse Tolerance	Notes
1) Modulation	QPSK	-	-
2) Frequency (MHz)	2250	-	2200 to 2300 MHz
3) S/C Transmit Power (dBm)	40.0	1.0	10 watts
4) S/C Transmit Losses (dB)	1.5	0.5	Estimated
5) S/C Transmit Antenna Gain (dB)	15.5	0.0	MMS 20 inch parabolic antenna Earth Coverage gain (3 dB bandwidth = 19°)
6) S/C EIRP (dBm)	54.0	1.5	Tolerances summed
7) Space Loss at 5° Elevation angle (dB)	-191.8	0.0	Geosynchronous
8) Atmospheric Attenuation (dB)	0.4	0.0	Hogg & Mumford, "The Effective Noise Temperature of the Sky", Microwave Journal, March 1960
9) Polarization Loss (dB)	0.5	0.0	-
10) STDN Ground Station Antenna Gain (dBi)	43.0	0.0	STDN User's Guide 101.1, Rev. 2, May 1974; 1 dB less than stated for modification of 30 ft antenna for Ku-Band reception
11) Total Received Signal Power (dBm)	-95.7	1.5	Tolerances summed
12) STDN System Noise Temperature Referred to Antenna Output Port (°K)	121.8	0.0	Cooled paramp temperature at 95°K + 26.8° increase in sky tempera- ture at 5° elevation

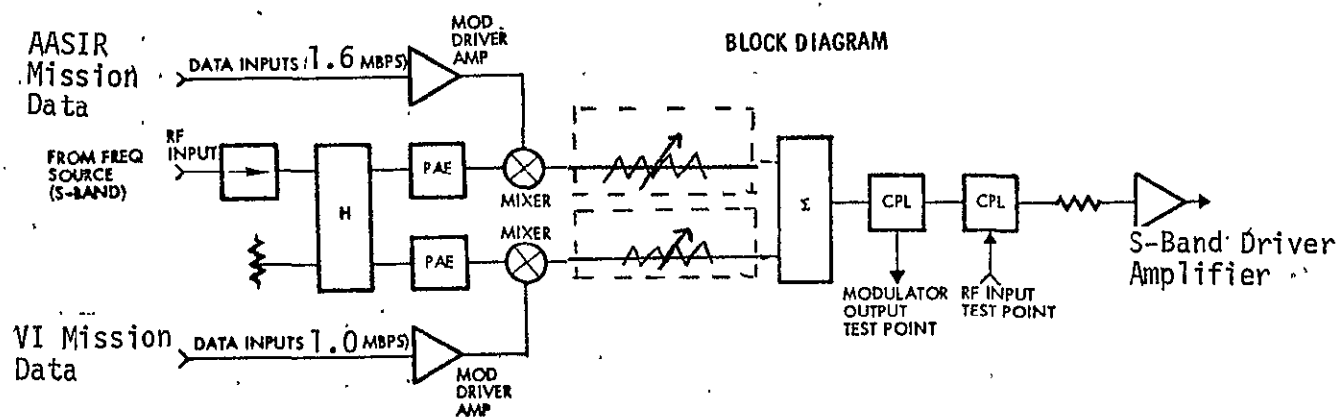
Table 5-1. Mission Data Communication Performance (Con't)

	Nominal Value	Adverse Tolerance	Notes
13) STDN System Noise Spectral Density (dBm/Hz)	-177.7	-	-
14) Received Signal-to-Noise Spectral Density Ratio (dB·Hz)	82.0	1.5	Tolerances summed
15) Data Rate (dB)	64.1	0.0	Total Data Rate 2.6 MBPS (1.6 MBPS for AASIR and 1 MBPS for VI)
16) Received Energy to Noise Spectral Density Ratio for 10^{-6} BER	17.9	1.5	Tolerances summed
17) Required Energy to Noise Spectral Density Ratio for 10^{-6} BER	10.5	0.0	Optimum detection of coherent PSK
18) Degradation due to Non-Optimal Detection (dB)	2.0	0.0	Assumption
19) Data Performance Margin (dB)	5.4	1.5	Tolerances summed
21) Data Performance Margin Less Adverse Tolerance (dB)	3.9		

Table 5-2. Telecommunication Subsystem Hardware Characteristics

Components	Quantity	Weight (lbs)	Per Unit Size (inxinin)	Power (watts)	Source
S-Band Quadriphase	1	2.4	1.6x6.0x10.5	3.1	TRW: includes power converter
S-Band Frequency Source	1	0.8	13.5x6.0x2.0	4.5	TRW: includes oven controlled crystal oscillator
S-Band 10 Watt Power Amplifier	1	1.2	3.5x7x1	33.3	Shuttle Program
DC-DC Power Converter	1	1.8	5.3x6.2x2.2	6.8	Shuttle Program
Cable Set	1	1.0	-	-	TRW

QPSK MODULATOR



[- -] Modification to existing unit

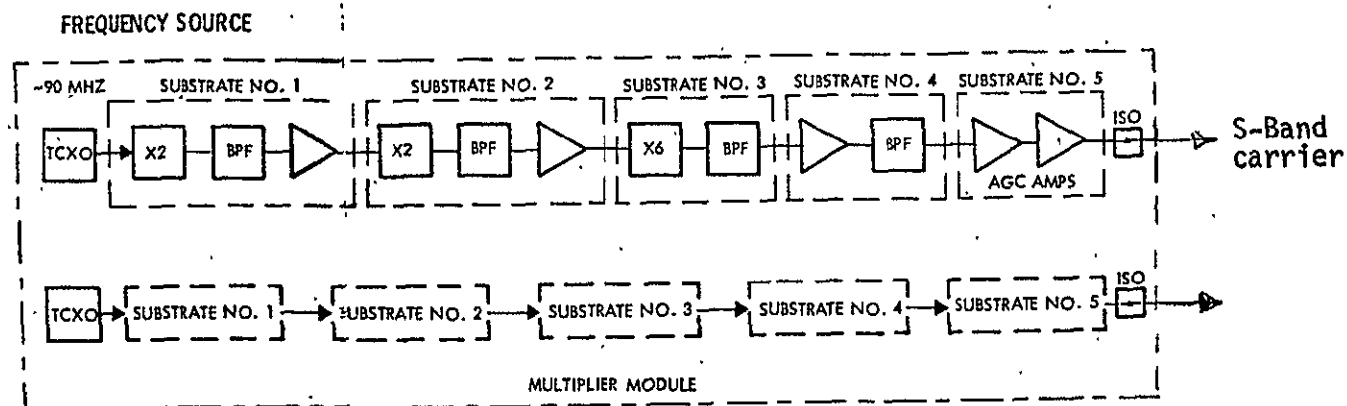
KEY FEATURES

- SPACE-QUALIFIED DESIGN
- HIGH DATA RATE CAPABILITY - QUALIFIED AT 300 MBPS AND VERIFIED UP TO 800 MBPS
- "MODULATOR OUTPUT" AND "RF INPUT" TEST POINTS ARE PROVIDED - ENABLES MODULATOR AND POST-MODULATOR EVALUATION DURING SECTION LEVEL TESTS
- QPSK MODULATOR INCORPORATES A TEMPERATURE INSENSITIVE BALANCE MIXER MODULATION TECHNIQUE

MEASURED DATA (MEASURED OVER 0 TO 100°F)

- | | |
|-------------------------|----------------|
| • DATA RATE | 300 MBPS |
| • DATA TRANSITION TIME | ≤ 0.5 NSEC. |
| • PHASE ORTHOGONALITY | < ±1.0 DEGREES |
| • AMPLITUDE IMBALANCE | < ±0.15 DB |
| • DATA ASYMMETRY | < 1.0 PERCENT |
| • OUTPUT RF POWER LEVEL | +14 DBM |
| • DC POWER | 3.05 WATTS |
| • WEIGHT | 2.4 LBS |

Figure 5-4. S-Band Quadriphase Modulator



KEY FEATURES	
• SPACE-QUALIFIED UNIT	
• DESIGN - INTERNALLY REDUNDANT AND CROSS-STRAPPED WITH QUAD HYBRID	
• CRYSTAL-CONTROL FREQUENCY STABILITY PERCENT ± 0.0004 TEMPERATURE AND AGING	
• LOW LEVEL SPURIOUS OUTPUTS VIA OPTIMIZED FREQUENCY MULTIPLICATION SEQUENCE AND FILTERING	
• LOW PHASE NOISE - 0.05 DEG/RMS VIA OPTIMIZED CRYSTAL DESIGN	
• HIGH MANUFACTURABILITY - USE OF MICROWAVE INTEGRATED CIRCUIT (MIC) SIMPLIFIES FABRICATION AND CLOSELY CONTROLS CIRCUIT PARAMETERS	

MEASURED DATA	
• OUTPUT POWER	
• MEDIUM LEVEL	TO 10 DBM
• HIGH LEVEL	TO 27 DBM
• OUTPUT POWER VARIATION VS TEMPERATURE (0 TO 140°F)	
• MEDIUM LEVEL	0.4 DB
• HIGH LEVEL	0.3 DB
• OUTPUT FREQUENCY	2200-2300 MHz (CRYSTAL-CONTROLLED)
• OUTPUT FREQUENCY VARIATION VS TEMPERATURE (0 TO 140°F)	0.0004 PERCENT
• SPURIOUS ($F_0 \pm 1$ GHz) VERSUS TEMPERATURE (0 TO 140°F)	-85 DBC

Figure 5-5. S-Band Frequency Source

S-Band Transmitter

A ten watt S-band transmitter has been sized for the STORMSAT telecommunication link. TRW proposes the use of a solid state power amplifier developed for the Shuttle program. The unit is scheduled to be flight qualified by mid 1977. Figure 5-6 contains the power amplifier block diagram and associated data.

S-Band Antenna

The S-band antenna is assumed to be furnished by the multimission spacecraft. The unit is a 20 inch RHCP parabolic antenna. The antenna parameters used in the link analysis are nominal and can be achieved by a simple design. An alternate choice is the space qualified 24 inch DSP parabolic antenna which has nearly the same performance at earth coverage.

Cable Set

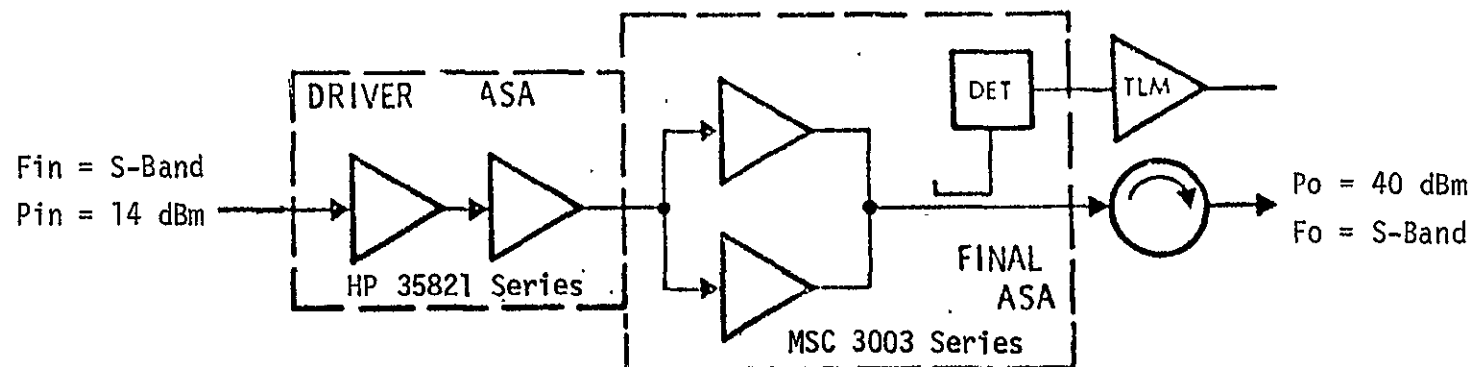
The cable set consists of a combination of space qualified semi-rigid and flexible coaxial cables and associated connectors.

5.5 TRADES

Several trade studies were initiated to arrive at the recommended baseline. They include configuration, antenna versus transmitter power, and RF modulation.

5.5.1 Configuration

An alternative configuration for Stormsat is shown in Figure 5-7. This configuration makes use of the multimission spacecraft C&DH module for transmitting the AASIR data. The data are phase modulated directly on the C&DH S-band downlink carrier. Link performance analysis shows that a five watt transmitter and the 20 inch parabolic antenna will support the AASIR data transmission. Multimission spacecraft interface data indicate that a five watt power amplifier and the 20 inch parabolic are optional for the C&DH module.



DATA

- Frequency Range: 2.2 to 2.3 GHz
- DC/RF Efficiency: 30%
- Power Output: 40 dBm
(10 watts)
- Input Power: 14 dBm
- Supply Voltage: +24 VDC, -14 VDC
- Operating Temp: 0 to 50°C
- Weight: 1.2 lbs
- Size: 3.5" x 7" x 1"

Figure 5-6. S-Band Power Amplifier

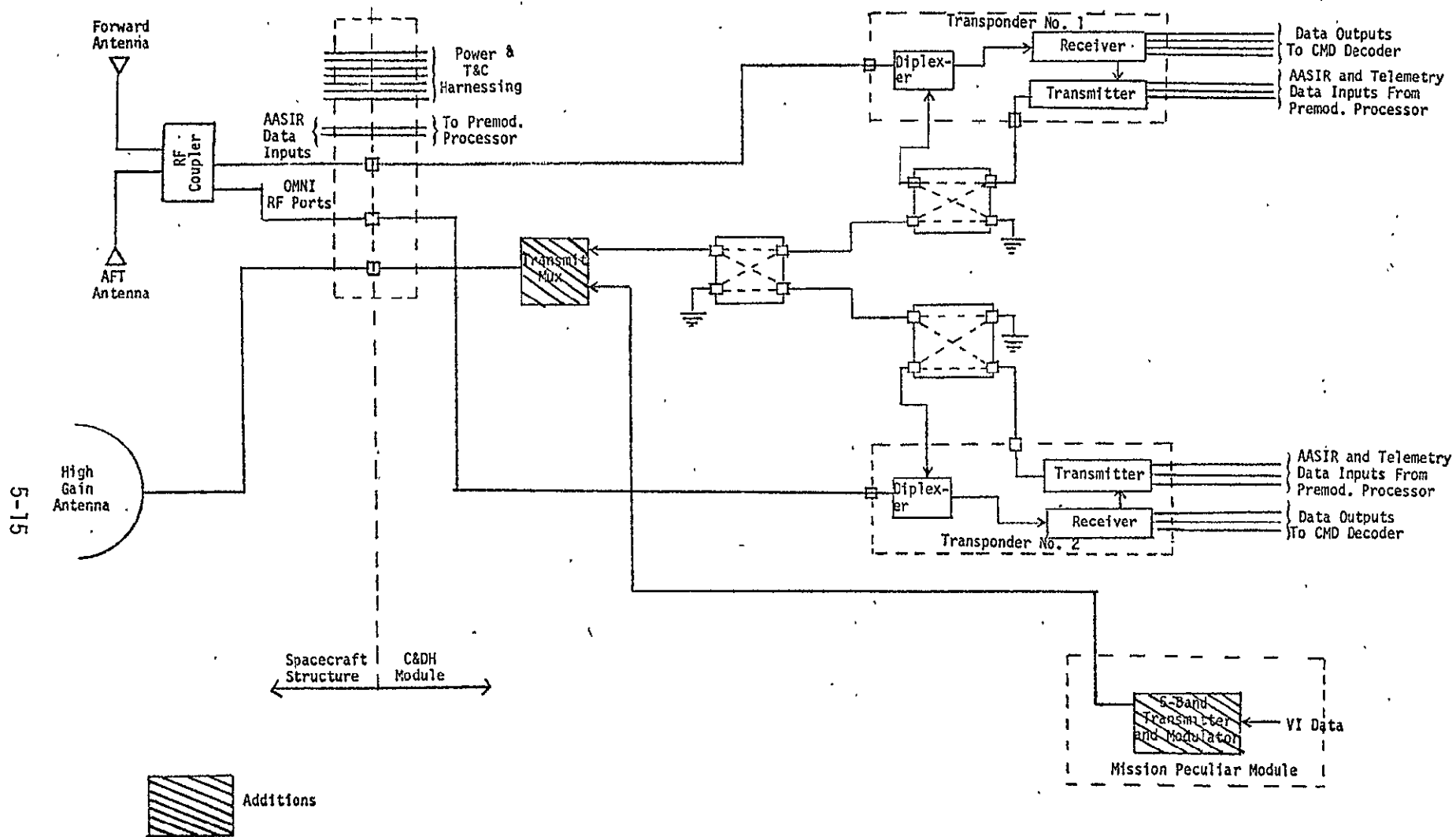


Figure 5-7. Alternate Configuration 1

The advantage of this approach is that no new RF hardware is required for the transmission of AASIR data. The disadvantage is that the AASIR data signal spectrum and the telemetry data signal spectrum will interfere with one another when they are transmitted simultaneously.

In order to transmit the VSI sensor data simultaneously with AASIR data, a separate and independent transmitter is employed as shown in Figure 5-7, and the VSI signal is frequency multiplexed with the AASIR data signal.

The reason this approach was considered is that if the VSI sensor was not flown or if simultaneous transmission of AASIR or VSI data was not desired, then a separate communication subsystem would not be needed. AASIR or VSI data would be time shared with telemetry on the downlink C&DH S-band carrier.

Should the time sharing of telemetry and sensor data be unacceptable because of degraded performance caused by the spectral interference of the telemetry and the AASIR sensor data signals, a separate communication subsystem must be flown. It should be noted that negligible degradation due to spectral interference is anticipated if VSI sensor data and telemetry data signals are transmitted simultaneously. The reason for the negligible degradation is that the spectral nulls $(\sin x/x)^2$ of the VSI data signal lie near the telemetry 1.024 MHz subcarrier frequency.

Since there will be a reasonable requirement to transmit simultaneously two sensor data signals, the baseline approach offers the most attractive configuration for the STORMSAT mission. Furthermore, the C&DH S-band link should not be used to transmit the sensor data unless the sensor data rates are approximately 1 MBPS and only one sensor data stream is transmitted at a time.

5.5.2 Antenna Versus Transmitter Power

An effective isotropic radiated power (EIRP) of 54.0 dBm for the STORMSAT communication link was computed in Table 5-1, thus, required antenna gain and transmitter power product in decibels is 55.5 dBm. The antenna gain versus transmitter power trade shown in Figure 5-8 assumes antenna pointing.

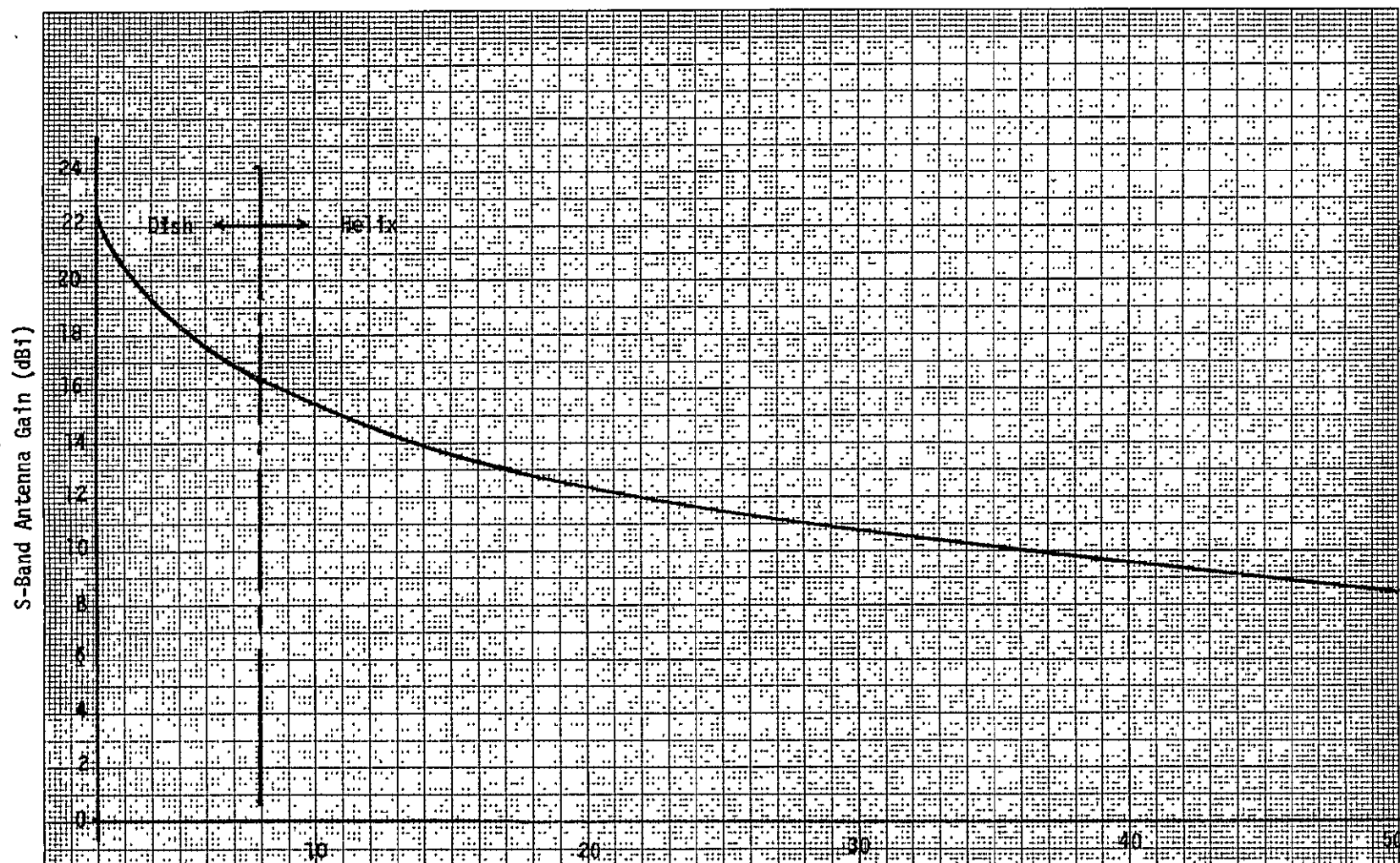


Figure 5-8. Antenna Gain Versus Transmitter Power

Figure 5-8 also shows the type of antenna suitable for the communication subsystem for various antenna gains. The antenna choice boundary is by no means a firm boundary but chosen to illustrate a rough cutoff between the choice of parabolic antennas and helix antennas.

Since antenna pointing requires added complexity of antenna gimbaling and on-board software for program pointing the antenna, a fixed earth coverage antenna configuration was chosen. The recommended choice was reinforced in light of an optional earth coverage 20 inch parabolic antenna provided by the multimission spacecraft and the low risk in securing a 10 watt transmitter.

5.5.3 RF Modulation

Several modulation techniques were studied. They include direct phase-shift-key (PSK), quadriphase (QPSK) and, frequency shift-key (FSK).

A major consideration in choosing the type of modulation technique is the transmission requirement. For example, if it is desired to transmit one sensor data stream at a time, the PSK technique is more attractive than the FSK technique because it requires less EIRP (3.7 dB) than the FSK technique. However, both these techniques are attractive in terms of the hardware availability. The FSK hardware is flown on the ERTS Satellites and the PSK hardware is flown on a large number of Satellite programs as part of S-band transponders and as separate units on TRW built DSP satellites. Another option for transmitting one sensor data stream at a time is the use of the multimission C&DH link as described earlier.

The quadriphase technique was chosen because of its flexibility in transmitting simultaneously two independent sensor data streams or only one data stream at a time. Furthermore, the quadriphase hardware is space qualified and offers the same performance as PSK.

6. GROUND DATA PROCESSING

6.1 INTRODUCTION

Data collected by the AASIR and communicated to the ground requires interactive manipulation before its full value can be extracted. This section describes the requirements for ground data processing and presents a system which can accomplish the task.

To establish processing requirements, discussions were arranged with various experts. These included:

Dr. T. Fujita, University of Chicago
Mr. V. Oliver, NOAA/NESS
Dr. D. Miller, NOAA/NESS
Mr. W. Shenk, NASA/GSFC
Ms. B. Walton, NASA/GSFC

In addition to these personal discussions, a limited amount of research on this subject was conducted by members of the study team; results of this research have been incorporated into the baseline compilation of requirements listed in Section 6.3.

The results of this analysis are considered suitable for use in designing a conceptual Stormsat data-processing system. However, it should be noted that all our contacts stressed the importance of flexibility in the data-processing system to permit modification of techniques and procedures during the early period of Stormsat operations. Accordingly, it is strongly recommended that provisions be made for modification, expansion and refinement of both hardware and software in the Stormsat data-processing system.

6.2 BACKGROUND

The pertinent features of Stormsat/AASIR that impact data-processing requirements include the following:

- a) Selectable scan areas
 - full-disc images every 30 minutes
 - $4^{\circ} \times 4^{\circ}$ images every 5 minutes
 - $1.2^{\circ} \times 1.2^{\circ}$ images every 1.5 minutes.

- b) simultaneous visible and IR images of clouds and/or earth's surface.
- c) Simultaneous observations of atmospheric brightness values (CO₂ band) for determination of temperature profiles.

It is also assumed that Stormsat data will be part of a typical data set for a functional meteorological facility. Such a facility will have routine access to weather maps (analyses) and prognostic charts, surface observations, radiosonde data, pilot weather reports, SMS/GOES data, and ITOS data.

The complete data-set will be used to monitor and predict the development of weather systems. On a near-real-time (NRT) basis, demonstration forecasts of weather-system development will be prepared. In addition, the data-set will be used for research aimed at a better understanding of storm dynamics. Accordingly, the data-processing requirements must consider both NRT and off-line processing.

The baseline requirements listed in Section 6.3 have been developed in consideration of these factors and on the experience of both operational and research meteorologists.

6.3 DISCUSSION

The individual data-processing requirements include the ideas and recommendations presented to the study team during the discussions listed in the introduction. The rationale for these recommendations follows each requirement.

Item A

Design for a continuous duty cycle, i.e., for continuous observations by the AASIR in its most demanding mode.

Experience has shown that meteorological data systems are always used to their maximum capacity. For Stormsat/AASIR, there will be such a wide community of users that it would be unwise to design any down-town into the data-processing system. For example, full-disc observations will be wanted by synoptic forecasters, for support to international commitments, by climatologists, by aviation (transoceanic) forecasters and by researchers; a minimum of three sequential frames every three hours would be needed,

based on the need to derive winds from cloud movements frame-to-frame. The $4^0 \times 4^0$ frames can be an essential tool for both research and operational forecasters, who would like a time history of weather-system development over an area of this size. The $1.2^0 \times 1.2^0$ scans are essential for severe-storm monitoring, prediction and research; for this purpose, continuous frames will be desired throughout the life cycle of severe-storm systems. As for the soundings, they may well become as useful as the visible and IR images, and their concurrence with image data will dictate simultaneous observations at all frame sizes.

Item B

Design for overlaying IR, visible and/or sounding (radiometric⁶) data. Color coding may be desirable for emphasizing the various sets of data.

To understand the meteorological situation, it is necessary to compare all the available atmospheric parameters. For example, the height of the cloud tops (from the IR) and the atmospheric stability (from the soundings) are used together to identify severe-storm development. The use of color coding will enhance the readability of the data.

Item C

Use display modes that enhance near-real-time (NRT) display, e.g., that avoid film processing.

Based on experience at NOAA/NESS, the use of film loops is too cumbersome for operational purposes. Not only is there a built-in time lag, but the processing is expensive in terms of equipment and manpower. Further, film is restrictive in terms of flexibility, e.g., the order in which the frames are shown cannot be easily changed.

Item D

Provide storage for up to 36 hours of full-disc data; 24 hours of $4^0 \times 4^0$ data; 16 hours of $1.2^0 \times 1.2^0$ data. If possible, design for expansion of these periods as a future option.

The number of frames to be stored is based on the life cycles of weather systems within each frame size. That is, full-disc frames show weather systems that have life cycles on the order of a week, while $1.2^0 \times 1.2^0$ frames are typified by small-scale disturbances that last only

hours. The recommended storage capacity is a compromise that appears reasonable for the conceptual data-processing system, but it should be noted that experience may dictate a need for additional storage capacity later.

Item E

Design for enhancement of selected portions of the observational spectrum, e.g., to separate the finest spectral resolutions measurable by the AASIR.

From experience with SMS/GOES and ITOS data, it has been learned that enhancement of selected spectral bands is a vital tool. This makes it possible to isolate very high clouds, cold surface temperatures, ocean currents and snow fields, for example. The meteorologist is thus able to selectively look at the features that pertain to his problem, rather than having these salient features masked within the total image or sounding.

Item F

Provide for storage of any processed (selectable) set of data for comparison with a later version of the same data set. Make this flexible enough so that the parameter, the desired processing, and the Δt for the comparisons can be selectable (by software changes).

Weather analysis has long relied on the degree and rate of changes in the atmosphere for understanding and predicting weather. A drop in mean-level temperature, for example, denotes the presence of a cold front and can lead to a prediction of precipitation. To facilitate the use of Stormsat data, for both operational and research purposes, it is important that changes in any measurable parameter be computed and displayed. The parameters to be compared and the length of time between observed values should be completely flexible.

Item G

Provide for geographic/governmental gridding for any FOV (full-disc, $4^{\circ} \times 4^{\circ}$, $1.2^{\circ} \times 1.2^{\circ}$).

Geographic/governmental grids are needed to show the rate and direction of movement, principally for images of cloud systems. They are also useful for quick understanding of where severe weather may be a factor, as in the case of warnings for disaster-warning officials. The size of the

identifiers should be legible but unobtrusive. Flexibility is needed to provide for selection of many different geographic/governmental entities. Also, the system should provide for fade-in/fade-out capability, at the discretion of individual users.

Item H

Provide for superimposing alpha-numerics on any image, e.g., textual comments for labeling the severity of any storm system, expected time of danger, direction of movement, etc.

Annotation of the data, in alpha-numeric and graphic form, will be useful for recording and distributing information. Among the information to be generated and overlaid are vectors, labels, numerical values, and limited text.

Item I

Design to permit holding a single (selectable) cloud element stationary and to display the movement of every other cloud element relative to the stationary element (for wind-shear determination).

Wind shear is a critical parameter in meteorology. NOAA has found that shear can be determined by measuring the relative movement of adjacent cloud cells, using a technique that holds one cloud stationary and computes/displays the relative movement of all other cloud cells. This capability should be integrated into the visible and IR data-processing for Stormsat/AASIR.

Item J

Provide for automatic wind determination by measuring the frame-to-frame movement of cloud fields and by picking-off individual cloud elements frame-to-frame (may require manual selection of the measurable elements). Wind data to be computed and displayed in vector form.

Geostationary satellites provide a unique capability for determining winds by measuring the frame-to-frame movement of individual cloud cells (visible or IR). Manual identification of a cloud cell at t_0 and at $t_0 + \Delta t$ is usually required for precision, but a less precise, general wind could be derived automatically by using an algorithm that selects large cloud shields that are unlikely to change from frame-to-frame; the edges of

these shields could then be used for a rough wind computation. It is more desirable that a man-machine interface be defined so that the meteorologist could pin-point the cloud cells (on both frames) and the machine could compute the winds. This operation is necessary for all three frame sizes in the IR and visible.

Item K

Provide for input of selectable IR values from which measured (observed) cloud-top extremes can be measured and displayed.

Cloud tops that pierce the tropopause, or that exceed any pre-selected altitude, are of particular interest for severe storm research. For the IR images, it is desirable that the meteorologist be able to specify the radiance level he wishes to use as a baseline, and that the processor then identify all cloud observations that exceed that value (in terms of radiances converted to altitude). This information will permit quick identification of the most-active cloud cells. By combining this with the rate-of-change requirement (Item F), it will be possible to measure the pulsations of cloud turrets, which are believed to be a precursor to tornados and thunderstorms.

Item L

For soundings, consider temporal "smoothing" to eliminate cloud effects in the FOV. A large number of observations of a selected FOV would have to be stored, called up, averaged for each spectral band in the sounding spectrum, then displayed and stored.

Clouds in the FOV of the atmospheric sounder will distort the data. By taking many sequential observations of a FOV that contains only scattered clouds, it appears likely that the effect of these clouds can be minimized. An algorithm will be needed for selecting the individual radiance measurements that indicate minimum (or no) clouds in the FOV. These selected values could then be used to represent a (semi-) cloud-free FOV, and thus a valid sounding.

Item M

For soundings, it may be desirable to automatically identify FOV's that are cloud-free. This could be done by comparing the relative brightness in corresponding FOV's in the visible and IR imager; the existence of a cloud yielding a substantially different ratio than the earth's surface.

As a sub-set of Item L, soundings could be taken for only those FOV's that are cloud-free; alternately, all the available FOV's could be observed but processing and recording could be accomplished for only those that are cloud-free. Determination of the cloud-free FOV's could be from image data (visible and IR) or from the radiance values themselves, i.e., from those soundings whose radiance values indicate a lowest-level temperature close to that of the known surface temperature.

Item N

Design for hard-copy printout of both raw and processed Stormsat/AASIR data. Printout should be selectable in graphic or tabular form and should be capable of inclusion of all data reaching the facility, or portions thereof. Selectability of mode and amount of hard-copy printout is desirable.

For both operational and research purposes, there will be a desire to use hard-copy printouts for study of the data, testing of new manipulation techniques, and for verification of data-processing algorithms. Printouts enhance the opportunity to do detailed investigations of limited data-sets, to exchange information among remotely located investigators, and for group discussions of meteorological interpretations.

Item O

Provide for an archival copy of all data received at the facility, in an unadulterated form.

All scientific data are subject to recall for use in developing and testing new techniques, for climatological records, and for administrative uses. Stormsat/AASIR data will become part of the meteorological archives, probably in an untreated condition; however, it is desirable that the degree of preprocessing and the format of the archive should approximate that of SMS/GOES data to provide for compatibility.

Item P

Provide for a capability to develop film loops of any selected set of Stormsat/AASIR data.

For such purposes as training, public relations, and public dissemination, film loops will remain a useful tool. Only non-real-time preparation is required.

6.4 TRANSLATION OF OBSERVATION REQUIREMENTS INTO FUNCTIONAL NEEDS

A study of the requirements just documented reveals that a system which incorporates certain key features including a computer system supported by some specific software routines can flexibly provide all the services desired. These features include:

- A large moderately rapid disk storage system (3 to 300 megabyte disks) for reformatting images and for holding several scenes for time lapse comparisons such as in the determination of wind velocity from cloud movements. Each disk is capable of holding one full disc AASIR image (approximately 208 mbyte) with space left for small frames (i.e., 40×40 and 1.20×1.20 images).
- A large capacity, on-line storage system for use as a reference library. Call-up time from data anywhere in the memory should be no more than 30 seconds to 1 minute.
- A digital radiometric calibration system for referencing all readings to the same datum despite drifts in detectors or other equipment.
- A digital geometric correction capability using at least cubic interpolation techniques for converting images to a common overlayable format. This capability is essential, e.g., for automatic wind determination; two images of the same terrain but taken at different time may be overlayed using temporal registration technique, thus permitting measurement of the frame-to-frame movement of cloud fields.
- A temperature inversion capability for converting sounder radiometric readings to temperature versus altitude profiles.
- A dual tricolor interactive CRT display system (e.g., COMTAL 8000 series) having automatic refresh and a 1024 bit resolution in both directions. Pixel skip techniques may be employed to display a full disc image on the CRT screen. By assigning visible image, IR image/or sounding data to different CRT image channel/or unit and gridding/annotation

to CRT graphic channel, the analyst can compare all available information by flipping from one CRT unit to another in order of a fractional second. To improve the readability of data, enhancement schemes such as pseudo color/or true color display, contract stretch, edge sharpening, etc., can be used to enhance the features that pertain to his problem. Man-machine interface is the key factor in the search for better understanding of storm dynamics. It is desirable that the meteorologist be able to monitor the changes of weather via CRT/TV equipment. Near real time processing is required to track and predict the development of the weather system. In addition, the off-line processing capability is needed for research and development purposes. Various geographic gridding systems for any selectable frame sizes must be stored on the disk. The alpha-numerics display may be initiated either through operator or program control.

- A capability to produce hard copy images in both black and white and in color; transparencies and opaques. The hard copy printout of raw and processed AASIR data can be generated using a nonchemical, dry process recording technique on dry silver paper. For browse/quick-look film generation, a micro-film camera (16 mm) may be used to take a photograph of a visual display on CRT screen.
- A medium-capacity high-speed computer system for control of the system.
- A highly supportive software operating system which facilitates insertion of new research algorithms. For example, one user wants an algorithm to perform automatic searching of cloud cells that exceed a predetermined radiance/or altitude values. This will permit quick identification of cloud tops that are particular interest for severe storm research. Another algorithm would search for cloud-free or sparsely scattered clouds areas.
- CCT and HDT tape recorders for getting data in and out of the system.

6.5 STORMSAT DATA HANDLING SYSTEM OVERVIEW

The remaining parts of this section provide a conceptual baseline design of the Stormsat Ground Data Handling System. Sufficient detail has been included to insure incorporation of all desirable data processing features/capabilities and near-real-time (NRT) data handling.

The overall structure of the Stormsat ground system is illustrated in Figure 6-1. The system consists of three major functional blocks: the data capturing function; the data preparation function; and the information

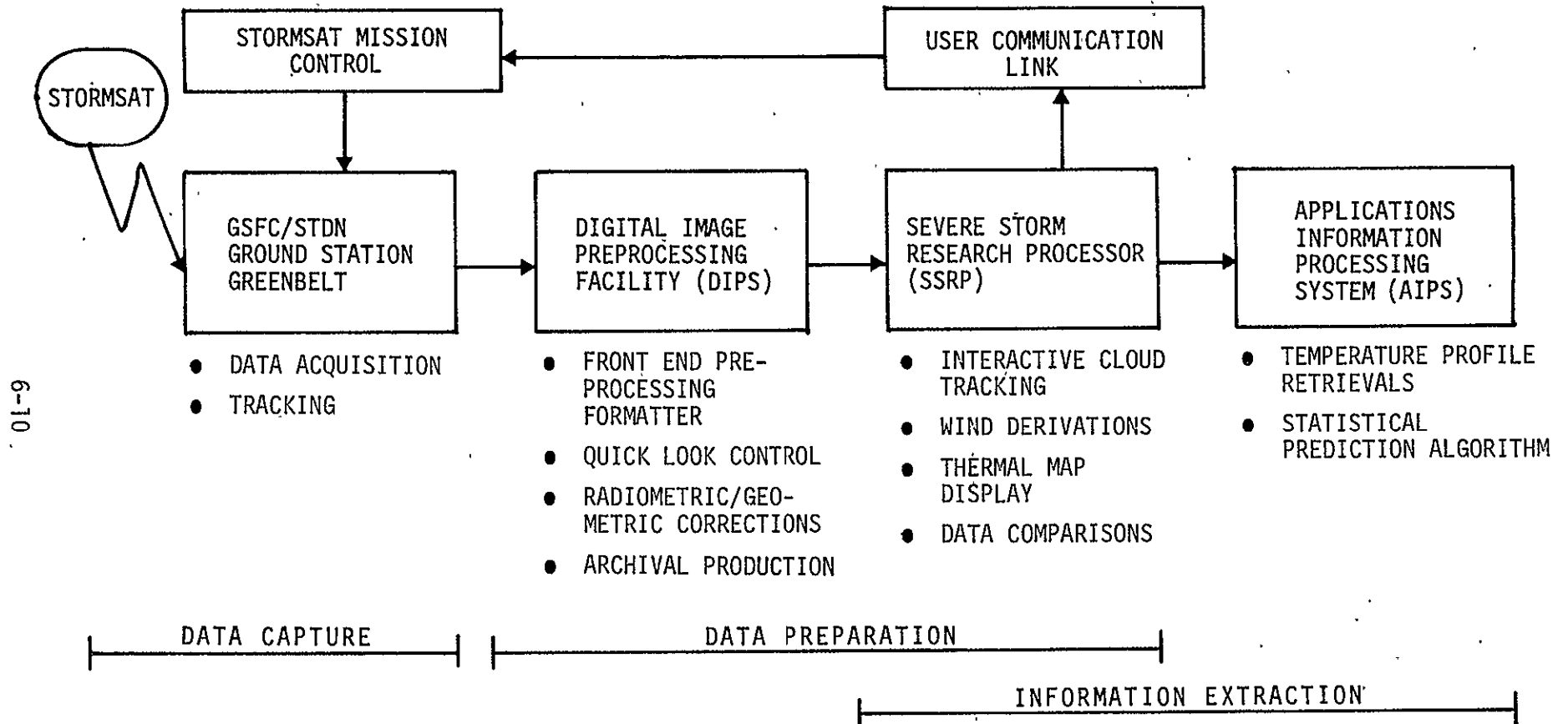


Figure 6-1. Stormsat Ground Station System Overview

extraction function. The ground track and data acquisition station is shown in Figure 6-2. In general, the acquisition equipment consists of an antenna/tracker/pedestal subsystem, preamplifier, receiver, and bit synchronizer. The tracker is designed to satisfy the pointing requirement, and the preamplifier is used to improve S/N ratio of the communication channel. The receiver is a demodulator together with the bit synchronizer to insure the best signal recovery. The frame synchronized telemetry data stream is recorded on video tapes. Provision is also made for selected subsets to pass in real time directly to the Severe Storm Research processor for display. The Digital Image Preprocessing System (DIPS) copies the video data onto High Density Digital Tape (HDT) in a compact format, screens tapes for data quality, and provides a log of data reproduced. It is also capable of performing a variety of functions selected by operator or program control. These may range from simple data reformatting to radiometric calibration and temporal registration*. Provisions is also made in DIPS to transform formatted data on HDT onto film and makes HDT or CCT copies. The functions accomplished in DIPS could easily be accomplished in the soon to be available GSFC MDP system. However, because MDP is a general purpose image processor operating 16 hours daily, it may not be suitable as the designated front end formatter and error correction processor for the SSRP/AASIR system, which requires a near-real-time data processing speed and around-the-clock operation. Therefore, we have provided for performance of all these functions in the basic Severe Storm Research Processor.

Besides processing Stormsat/AASIR data, SSRP will have routine access to other meteorological facilities such as SMS/GOES, AIPS, ITOS, etc. The complete data set, including AASIR data, will be used to monitor and predict the development of the weather system. In addition, the data-set will be used for meteorological research aimed at a better understanding of severe storm dynamics.

* Spatial registration of data collected at a different time from the same sensor so that picture elements (pixels) correspond to the same ground positions for all scenes.

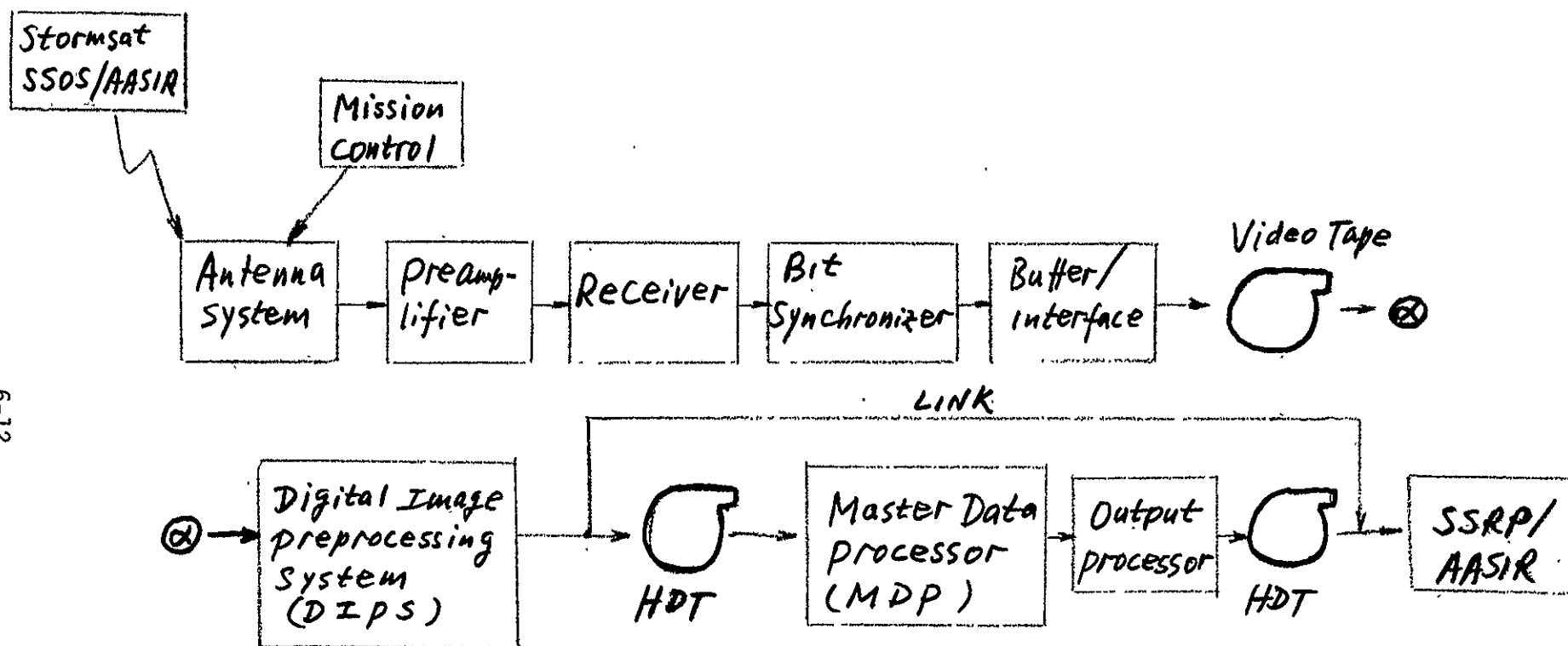


Figure 6-2. Stormsat Data Acquisition System

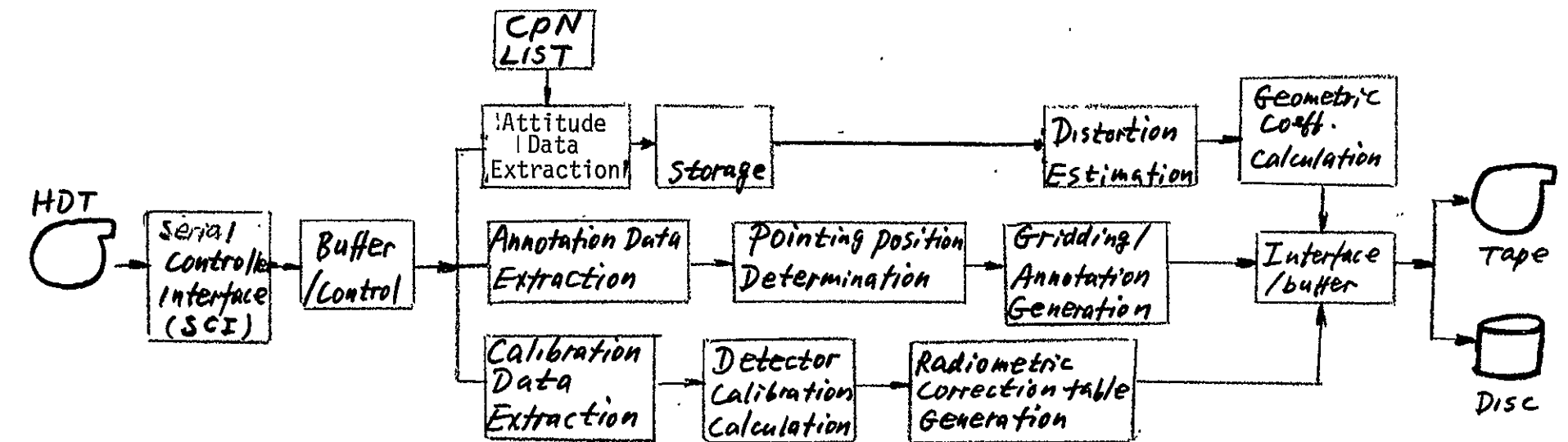
6.6 SSRP CONCEPTUAL DESIGN

The input data to the SSRP is in the format generated by the AASIR; that is, the data from several detectors in each of several spectral bands are interleaved and alternate lines are reversed in scan direction. Furthermore, calibration data are inserted periodically in the data stream. Before further processing or data display can occur a reformatting operation is necessary which yields a line or frame sequential format. This means the data stream consists of a sequence of lines or frames of data where all words in each line or frame are from the same detector and for each line in a left to right order. Thus, interleaving of spectral bands occurs on a line or frame basis rather than word by word.

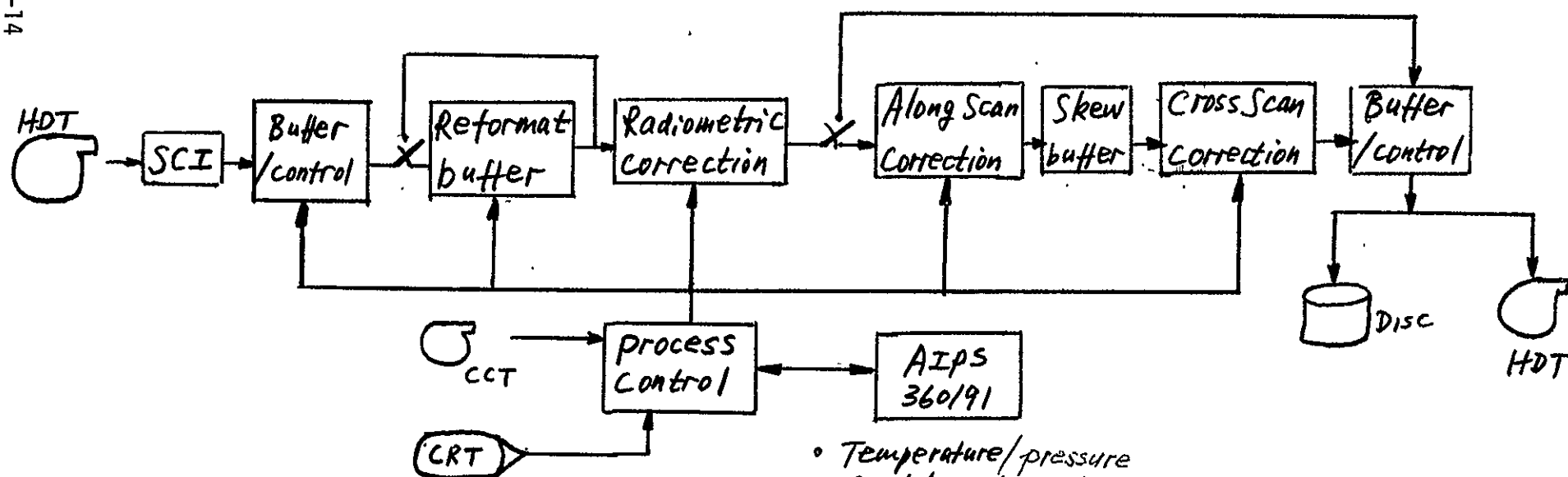
Registration of images, both spectrally as required for temperature inversion and temporally as required for cloud movement, are needed. Further, more registration between AASIR data and data from other sources (e.g., weather maps) may be necessary. Registration of spectral bands is inherent in the AASIR design. Provision must be made for geometric manipulation of images, however, for temporal registration and overlaying. Where geometric or radiometric alterations of images is desired, a two-pass data processing concept is implemented. (See Figure 6-3) PASS I, the Distortion Coefficient and Gridding Calculation Station, computes the selectable gridding features and/or radiometric, geometric correction coefficients which are subsequently used in the high throughput image correction process of PASS II, the Distortion Correction Station. The two-pass system makes possible the near-real-time data processing and off-line research capability where registration on overlays are necessary. It minimizes system failure and increases system reliability. Furthermore, the two-pass system permits future modification, expansion, and refinement of both hardware and software. The average data processing for the systems have been computed using the AASIR characteristics described in Section 2.2.1. Table 6-1 summarizes the processing rates required for near-real-time operation.

Formatting/Demultiplexing Processing

The exact input data format to the SSRP/AASIR system has not yet been determined. The SSRP, however, shall be capable of accepting input data in either band interleaved by line (BIL) format or band sequential (BSQ) format from HDT tape produced by MDP or DIPS systems.



PASS I



- Temperature/pressure profile retrievals.
- Statistical prediction algorithm

PASS II

Figure 6-3. SSRP/AASIR Data Processing System Function Flow

Table 6-1. Characteristics of AASIR Data for 20°x20° Frame

Channel	IFOV (μrad)	No. of Detectors	No. of IFOVs Per Line	Bits/Sample	No. of Lines/Frame	Total Bits/Frame	Average Data Rate Bits/Sec.	Dwell* Time/IFOV (μsec)	Samples /Sec./Detector	Maximum Data Rate Bits/Sec.
Sounding	375	12	931	10	931	2.6×10^7 (3 det/line)	1.83×10^4	695.1	1438	1.72×10^5
IR Imaging	125	12	2793	10	2793	7.8×10^7	5.5×10^4	231.7	4316	5.18×10^5
Visible	25	60	13962	8	13962	1.56×10^9	1.11×10^6	46.3	21579	1.29×10^6
TOTAL	NA	84	NA	NA	NA	1.66×10^9	1.18×10^6	NA	NA	1.98×10^6
									Maximum Instantaneous Data Rate	

* Minimum dwell time at center scan is assumed which will give maximum instantaneous data rate.

NOTE: Frame time of 23.3 minutes assumed
one sample per IFOV

The digital data are then demultiplexed yielding three data streams: sensor data, pointing/annotation measurement data, and detector calibration data. These data will be used as input to subsequent modules.

Pointing Determination and Image Gridding/Annotation Generation

One of the requirements for Stormsat is that spacecraft attitude data shall be available on the ground in real-time with the following attitude determination accuracy: 0.03 degrees (1 σ) for roll/pitch and 0.18 degree (1 σ) for yaw. The SSRP shall be capable of processing pointing data which will be used as an input parameter for image correction and gridding/annotation processor.

Geographic/governmental grids are needed to show the rate and direction of cloud movement. Gridding features such as state boundaries, cities, lakes, rivers, and latitude/longitude coordinates are useful for quick location of severe storms. Flexibility and selectivity are also required so as to provide many different geographic/governmental grids for graphic overlay, or merging with processed image data for output product generation.

Radiometric Calibration

The AASIR has 84 detectors. Measurements of detector/amplifier gain per detector at several points on the response curve are transmitted to the ground station for radiometric calibration. The most flexible method of radiometric correction is table-lookup, using the uncalibrated pixel value as the table address and the corresponding calibrated value as the table entry. The table lookup operation is implemented most conveniently in hardware during along-scan correction in pipeline format. Also, radiometric calibration can be implemented in point/slope (multiply/add) hardware during along-scan correction. The time required to calculate point/slope constants should be less than the computation of lookup tables. The tradeoff in cost is the point/slope hardware vs. lookup table memory.

Image Correction

Geometric manipulation in the Stormsat image is accomplished by calculating the exact locations for a subset of image points (sometimes called pseudo-reseau points) and applying a piecewise bilinear distortion model

to determine geometric corrections for all other points. The precise distortions on pseudo-reseau points are computed and the warp at all other locations is determined by bilinear interpolation of the surrounding pseudo-reseau points. The accuracy of the bilinear model increases as the number of pseudo-reseaux is increased; however, processing time also increases. The bilinear model can be described mathematically as follows:

$$U(x,y) = x + \delta_x(x,y)$$

$$V(x,y) = y + \delta_y(x,y)$$

where U,V are the input (distorted) image coordinates corresponding to the precision reference coordinates x,y, and δ_x , δ_y are the distortion in the x and y axes at the same location which can be modelled bilinearly as

$$\delta_x(x,y) = a_0 + a_1x + a_2y + a_3xy$$

$$\delta_y(x,y) = b_0 + b_1x + b_2y + b_3xy$$

The a_i 's and b_i 's can be computed from the distortion at the four surrounding pseudo-reseau points by solving the simultaneous equations as follows:

$$a_0 = \delta_x(0,0)$$

$$a_1 = [\delta_x(x_m,0) - a_0]/x_m$$

$$a_2 = [\delta_x(0,y_m) - a_0]/y_m$$

$$a_3 = [\delta_x(x_m,y_m) - a_0 - a_1x_m - a_2y_m]/(x_my_m)$$

where x,y position within a given block are measured with respect to the upper left corner (first pixel, first line) of the block, and x_m , y_m are the last pixel and line in the block. Similar four equations can be used to compute the b coefficients thus completing the distortion coefficients (i.e., warp function) calculation.

Given the warp function which will transform the geometry of the scene to the desired output coordinate system, the process of image resampling^{*}

* The process of image reconstruction, that is, determination of the entire image from a set of samples of the image.

or interpolation will be performed to produce image samples on the desired output coordinates.

Besides the heuristic "nearest neighbor" and "bilinear interpolation" resampling techniques, a popular approach, developed at TRW Systems and named Cubic Convolution, utilizes a four section cubic spline function as the interpolation kernel.

To speed up the distortion correction process, the along-scan direction is first corrected; this allows correction of individual sensor scan lines for scan nonlinearity and for the output coordinate system transformation. Consequently, the across-scan direction is corrected for distortion resulting in the desired output precision image.

Temporal Registration Process

SSRP/AASIR data processing system shall be capable of performing automatic wind determination by measuring the frame-to-frame movement of cloud fields. This legislates the most stringent accuracy requirement for temporal scene/scene registration.

As successive images are made over a given site, it is possible to re-correct the geometry of an image by using information gained on later images to achieve greater geodetic accuracy. But, for Stormsat application, the relative geometry between the two scenes is far more important than the absolute geodetic accuracy. For this reason, it is necessary that once the geodesy of a given scene is defined, it must remain invariant, i.e., regardless of the geodetic accuracy of a reference scene, data from successive scanning of the spacecraft must be registered to it precisely.

Desirable System Outputs

The exact nature of the output products needs to be determined. However, we may assume that for both operational and research purposes, there will be a need to transmit the processed data over a communications link to remotely located investigators for group discussions; to use hard copy printouts/films for study of the data and for quality control; to store the data on magnetic tapes as part of the meteorological archives. It is also desirable that the format of the output products should be compatible to that of SMS/GOES data.

SSRP/AASIR Data Processing Hardware Configuration

The computer hardware for SSRP/AASIR data processing systems are presented in this section. A multiple CPU computer configuration is designed to meet the processing requirements. The SEL 32/55 (Systems Engineering Laboratories) was chosen to be the basic building block for the SSRP/AASIR system. The characteristics of SEL 32/55 computer are given in Table 6-2 together with DEC 11/70 and DC 6024 medium size computers for comparison purposes. SEL 32/55 offers the computational capacity and the I/O flexibility and memory structure of a much larger system. It is also known that SEL has been used in the Severe Storm Laboratory in Washington.

System Capabilities and Options

The SSRP/AASIR data processing system hardware configuration is shown in Figure 6-4.

In PASS I station, one SEL 32/55 computer with associated 32-bit words of 600 nanoseconds (ns) core memory is configured to perform the tasks of buffer control, coefficient generation, and process control.

Inputs to the system are the HDT, CCT, and/or direct communication link to Data Acquisition Station, or DIPS. The HDT and Serial Controller Interface (SCI) are interfaced to the SEL 32 bus, which provides 26.6 million byte transport capacity with 150 nanoseconds per word transfer time, through a General Purpose I/O Module (GPIO Model 9102). GPIO is a microprocessor with up to 4K, 32-bit words of 150 ns control ROM with a nominal throughput of 1.2 million bytes per second; thus it is quite well-suited to handle the input data rate of 550K bytes of HDT. The microprocessor contains a high speed general purpose arithmetic and logic unit for operations to be performed on the input data.

The CCT magnetic tape is assumed to be 1600 bpi, 9-track in industry compatible format. The tape input is interfaced to the SEL bus via a standard magnetic tape controller and formatter to permit high-speed operation. The 80M byte CPN buffer and the 80M byte CPL data storage unit are configured to be the moving head disc type with up to 1.2M byte transfer rate. Two separate moving head disc controllers (Model 9010) allow concurrent operation at maximum speed.

Table 6-1. Characteristics of SEL 32/55

INSTRUCTION TIMES (Register to Memory)	DEC. 11/70	DC 6024	SEL 32/55
16 Bit Fx. Pt.			
Add	1.8	NA	1.2
Multiply	3.9	NA	6.0
Divide	8.3	NA (24 bits)	10.8
32 Bit Fx. Pt.			
Add	NA	1.5	1.2
Multiply	NA	6.0	6.0
Divide	NA	11.3	10.8
32 Bit Flt. Pt.			
Add	8.2	2.2	2.25
Multiply	11.2	5.2	3.90
Divide	12.2	9.2	6.75
Maximum DMA Rate	4 MB	4 MB	4.7 MB
Maximum MUX I/O Rate		NA	6 MB
Architecture Size in Bits	16	24	32
Number of General Reg.	2x8	1x6	1x8
Maximum Address Capability	64 KB	192 KB	512 KB
Maximum Memory Size	2 MB	768 KB	1 MB
Number of Instructions	100		152
Automatic Multiplexed Hardware I/O	NO	NO	YES
Estimated			
Price (64 KB CPU)	NA	51,000	31,300
Price (256 KB CPU)	68,800	81,000	69,100
Price (512 KB CPU)	101,800	164,000	119,500

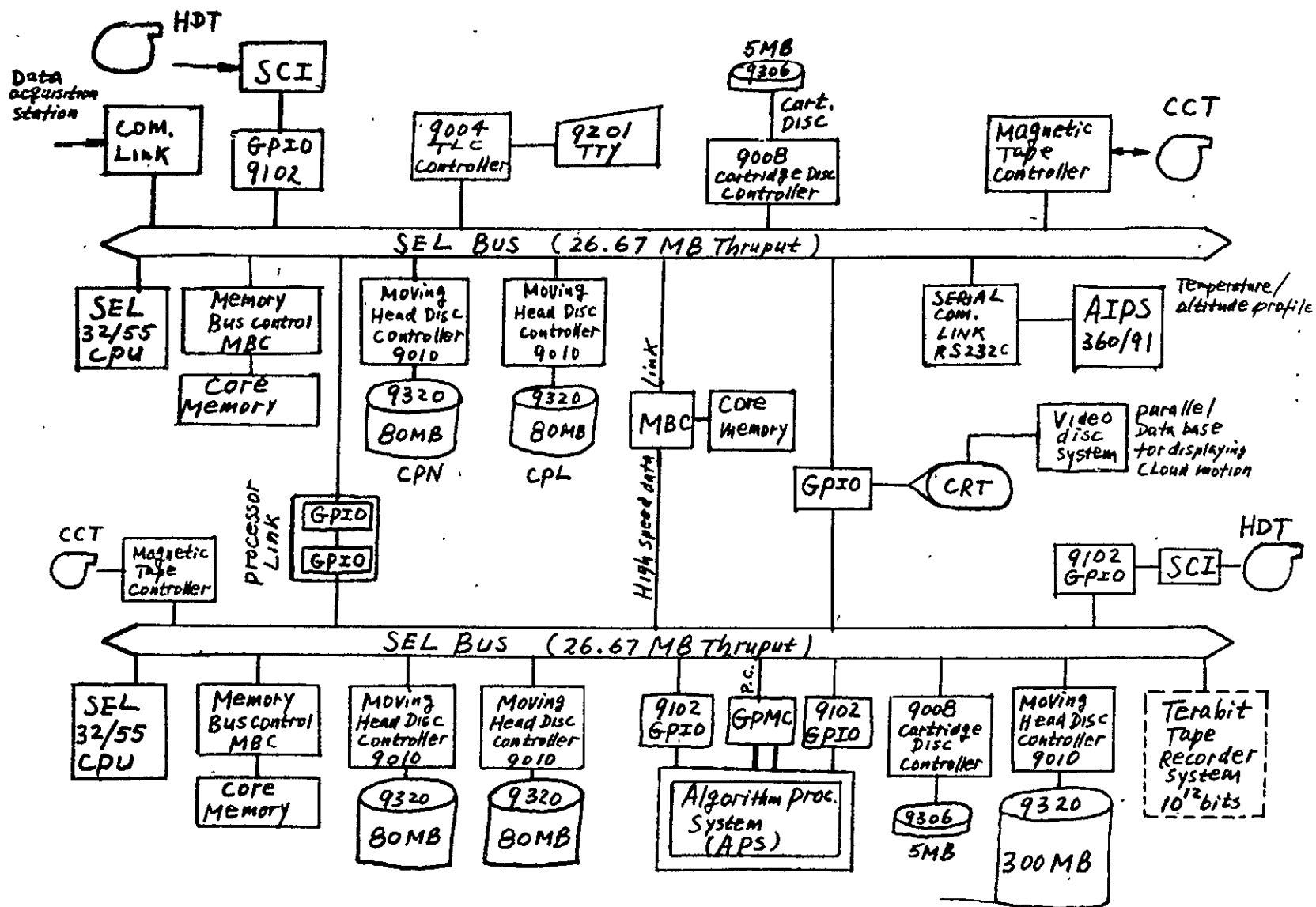


Figure 6-4. SSRP/AASIR Data Processing Hardware Configuration

PASS I station outputs are to either the CCT magnetic tapes which are compatible with the other CCT's in the system or moving head disc (i.e., 300MB disc).

Operational control of the system is accomplished via a combination of small (5MB) removable cartridge disc unit, an operator's teletype (Model KSR-33), and a high-speed images/graphics CRT unit. The CRT is also interfaced with PASS II station via a GPIO. To assist the analyst in picking the proper cloud field for study, a video disc system with fade-in and fade-out display capability is also included. The controller for the operator's teletype will also connect to and control any of SEL's standard line printers and card readers if so required.

As for the PASS I configuration, the PASS II correction station consists of one SEL 32/55 computer with associated memory, I/O microprocessors, and high-speed SEL bus. The system's operational control is accomplished via the cartridge disc and KSR-33 operator's teletype.

Inputs to the PASS II station are provided through HDT or 300MB moving head disc. During direct communication link processing mode, input sensor data is channeled through the PASS I SEL bus and high-speed data link, which is actually a core memory together with its MBC, to be stored on 300MB disk. The moving head disc is capable of holding one full disc AASIR imagery and more discs can be connected to the SEL bus via MHC (Model 9010) if so desired.

It is desirable that SSRP/AASIR system provide data storage for up to 36 hours of full-time disc images; 24 hours of $4^\circ \times 4^\circ$ images, 16 hours of $1.2^\circ \times 1.2^\circ$ images. The storage problem may be solved by using a tera-bits (10^{12} bits) mass memory system. Examples of such systems are Ampex Tera-bit Memory System and System Development Corporation Mass Storage System MMSS-1 and MMSS-2 incorporating the International Video IVC-1000 recorder.

The reformat buffer consists of two 80MB moving head disc drives, each interfaced through its own controller to the SEL bus for parallel operation at full thruput capacity.

The Algorithm Processing System (APS) is configured to the SEL bus as an available device for handling image resampling process described in 6.2.6. APS is a special purpose hardware dedicated to perform pixel interpolation

to achieve the best thruput/performance for image correction/registration processes. Control of APS is accomplished via GPIO and two channels of the General Purpose Multiplexor Controller (GPMC). The GPMC is an I/O interface for 16 DMA channels with a bandwidth of 200 half-word (16-bit) transfers/sec. It should be noted that resampling algorithms can be implemented in software; (for example, TRW Cubic Convolution software with an average processing rate of 10^{-4} sec/pixel). Figure 6-5 indicates the resampling processing rate required for the SSRP/AASIR system to achieve a real-time data processing for each of the three image frames (i.e., $20^\circ \times 20^\circ$, $4^\circ \times 4^\circ$, and $1.2^\circ \times 1.2^\circ$). The APS having an estimated average data processing rate of $1\mu\text{s/pixel}$ is well-suited for real-time correction/registration processing

Interface with MDP and AIPS

The SSRP/AASIR data processing system is designed to interface with NASA's Master Data Processor (MDP) through the HDT, or CCT (9-track, dual density 800/1600 bpi) data tapes. Therefore, the SSRP shall be capable of accepting MDP output data in accordance with its data format. Inputs from HDT will be provided in a standard telemetry format (i.e., minor/major frame) in band sequential (BSQ) structure. Image data on CCT will be formatted with interrecord and file gaps that are standard practice in computer compatible operations, or it may be formatted similarly to that on HDT. The SSRP/AASIR is configured to interface with AIPS through standard serial communication links such as RS232C, to provide a data transfer rate of 4800 bps. The AIPS is used to furnish temperature/pressure profile and/or statistical prediction algorithms.

Conclusions

A conceptual design of Stormsat ground data handling system is presented. The system may be divided into three major subsystems: Data Capture/Acquisition Station, Image Error Correction Station, and Data Information Extraction Station. The existing GSFC/STDN data capture system will be utilized as the Stormsat front end data collection station, the MDP and/or SSRP will be employed as the data reformatting and error correcting subsystem; the SSRP coupled with the AIPS will be used to extract useful information and to provide statistical prediction.

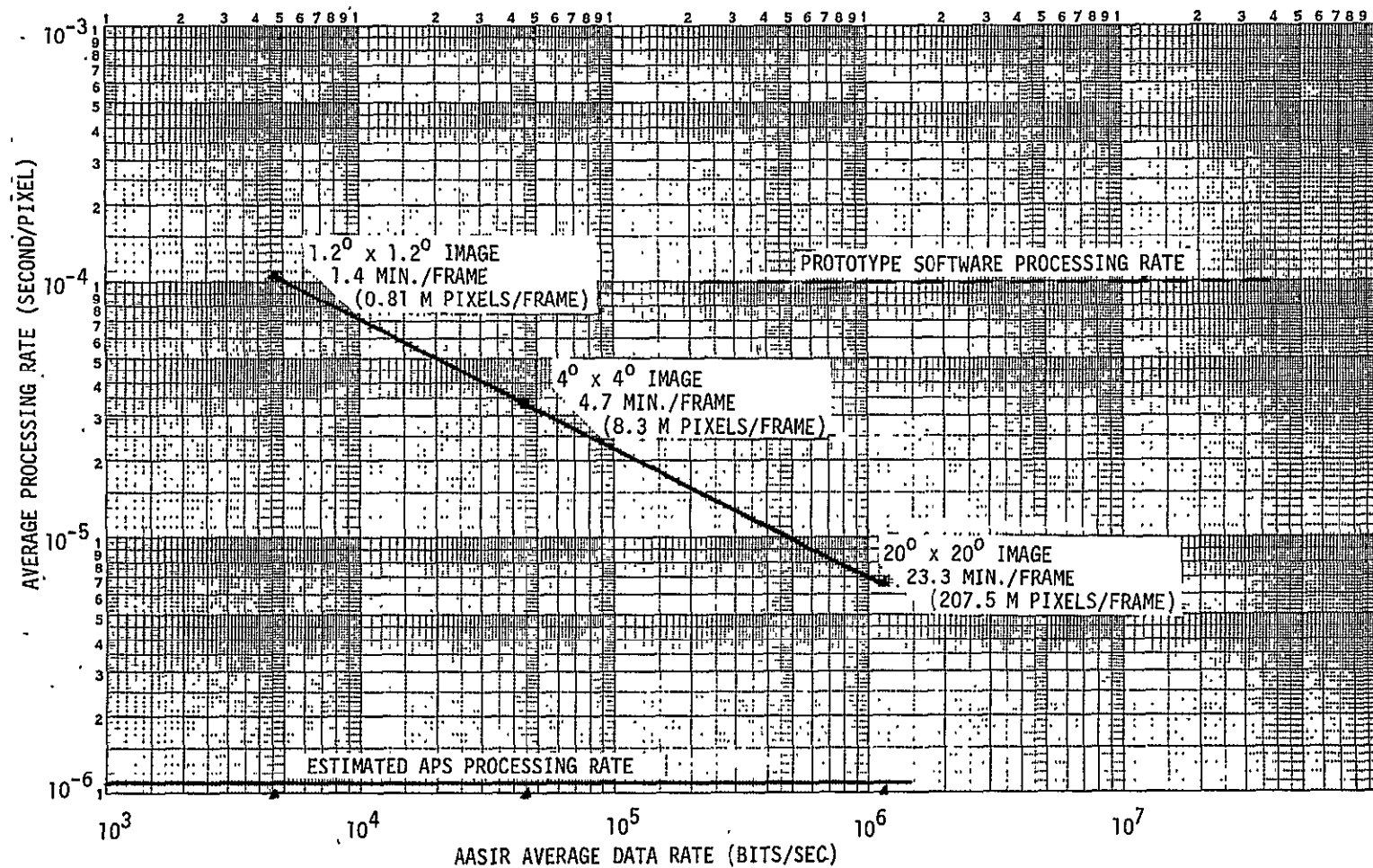


Figure 6-5. Real Time Processing Resampling Rates

The pertinent concepts of system flexibility and man-machine interface have been incorporated in the SSRP/AASIR data processing system design. Provisions have been made for future modification and expansion. The two-pass data handling approach makes possible the near-real-time data processing and off-line storm research. SEL32/55 computer was chosen to be the basic building block for the SSRP/AASIR system. SEL 32/55 offers the computational capacity, the I/O flexibility, and the memory structure of a large system. APS is configured to the hardware system to provide real-time image correction/registration for any possible size image frames. For future storage expansion, terabit (10^{12} bits) memory system may be included as a possible solution.

7. MOMENTUM UNLOADING USING MAGNETIC TORQUING

7.1 Summary and Introduction

This section addresses the feasibility of using magnetic torquing on StormSat for momentum unloading. This is the standard mode of operation for low and medium altitude MMS missions where the earth field is relatively strong and well defined by its dipole model. But it is not clear if magnetic unloading is a viable mode of operation for synchronous missions since the geomagnetic field at synchronous altitude is quite weak, about 120 gamma ($= 1.2 \times 10^{-3}$ gauss) on the average. In fact, a simple calculation reveals immediately that under these conditions the MMS standard 100,000 pole-cm torquer bars are not sufficient to cope with the secular solar disturbance torque mainly due to StormSat's single solar array (solar pressure unbalanced configuration). The investigations conducted here focus, therefore, on the concept of using an air core coil (or coils) wound near the edges of one (or all three) solar array panels to cancel the secular solar disturbance torque. The coils are excited in an open loop manner based on a priori solar torque estimates. The angular momentum due to the residual disturbance torque is then removed by closed loop operation of the torquer bars. This section is primarily concerned with sizing of the required array mounted coil(s).

It has been estimated that StormSat will require a 400 watt array, including a 20 watt allowance for the excitation of an air core magnetic coil. Based on this array size, solar disturbance torques were computed, predicting a secular torque of $T_s = 4.4 \times 10^{-5}$ Nm (3.26×10^{-5} foot-pound). It was determined that an air core coil having a magnetic moment of $M = 370 \text{ ATm}^2$ (370,000 pole-cm), wound at the edges of one of the three (assumed) 1.6×1 m panels of the solar array, would be sufficient to cancel the secular solar disturbance torque. Using aluminum, the weight-power product of this coil was found to be 110.5 watt-kg; for copper it was 221 watt-kg. Even though aluminum resulted in only one half the weight-power product, copper wire should be used since aluminum wire is too brittle to withstand the flexing of the array and reliable solder connections are also difficult to achieve. To obtain a reasonable weight,

a steady state power of 20 watts was allowed for the coil, resulting in a bare copper wire weight of 11.05 kg. Adding 1/4 mm thick mylar insulation and allowing some weight for fasteners and connectors, the total weight of the coil was determined as 14.8 kg (32.5 pounds). The coil was assumed to be excited by 28 volts dc resulting in 324 turns of a 0.968 mm diameter wire (approximately #19 wire AWG), carrying 0.741 amps.

Mounting a 14.8 kg (32.5 pounds) coil to one of the solar panels did not seem very attractive and means were sought to lighten the coil. At first three smaller coils were sized, one per panel, in order to obtain a better weight distribution across the array. The total power was kept at 20 watts resulting in a weight of 6.7 kg (14.75 pounds) per coil, which still seemed too heavy. Since the weight-power product of a coil of specified dimensions and magnetic moment is constant, lighter coils can be obtained by reducing weight at the expense of power. However, if more than 20 watts of power are required, then the solar array must be increased in size, which itself adds weight to the system and also increases the secular solar disturbance torque, which in turn requires an increased coil size. Taking all these interrelationships into account, coil weight may be reduced by increasing coil power until the sum of the coil weight and the additional weight due to the larger solar array is minimized. Such a weight optimized design yielded three coils of 3.35 kg (7.4 pounds) each, consuming a total of 63 watts (21 watts/coil), with the solar array panel size having increased from 1 x 1.6 m to 1.11 x 1.6 m per panel (3 panels = total array). This looks like a reasonable design and magnetic unloading appears feasible for StormSat. The coil sizing results are summarized in Table 7-1.

While the array mounted air core coils are operated open loop, possibly from an unregulated bus, the torquer bars are operated in a closed loop fashion and would, therefore, benefit from a magnetometer since significant changes in magnetic field strength occur at synchronous altitudes due to solar activity. As mentioned already, the nominal average magnetic field at geosynchronous altitude is about $1.2 \cdot 10^{-3}$ gauss (120 gamma). This typically is below the accuracy/bias level of magnetometers flown at

Table 7-1. Coil Sizing Summary

Assumptions

Available supply voltage: 28 V-DC (need not be regulated)

1/4 mm mylar insulation and 1.5 kg for fasteners
and connectors added to bare copper wire weight

	Characteristics per Coil			
	400 Watt Array		Weight Optimized Design: 443 Watt Array	
	System Using 1 Coil on Center Panel	System Using 3 Coils, 1 Coil per Panel	System Using 1 Coil on Center Panel	System Using 3 Coils, 1 Coil per Panel
Magnetic Moment	370 ATm ² (370,000 pole-cm)	123.3 ATm ² (123,300 pole-cm)	420 ATm ² (420,000 pole-cm)	140 ATm ² (140,000 pole-cm)
Weight	14.8 kg (32.5 lb)	6.7 kg (14.75 lb)	6.3 kg (13.9 lb)	3.35 kg (7.4 lb)
Power	20 w	6.67 w	63 w	21 w
Wire Size	0.97 mm (AWG #19)	0.56 mm (AWG #23)	1.0 mm (AWG #18)	0.58 mm (AWG #23)
Number of Turns	324	324	105	105
Length of Wire	1685 m	1685 m	569.1 m	569.1 m
Coil Current	0.714 amp	0.238 amp	2.25 amp	0.75 amp
Additional Array Weight	0	0	2.2 kg (4.85 lb)	2.2 kg (4.85 lb)

low and medium altitudes operating over the fairly standard ± 0.5 gauss range. Thus, a different magnetometer will be required at synchronous altitude and it should not be mounted within the ACS module. The residual magnetic moment of a torquer bar that was fully excited is as high as 1400 pole-cm, resulting in a magnetic field of $0.63 \cdot 10^{-3}$ gauss at the magnetometer when torquer bars and magnetometer are located at opposite corners of the ACS module. This is half the field one wants to measure and the magnetometer should, therefore, be located at a greater distance from the torquer bars. If the magnetometer is located near the AASIR cooler, which in a practical sense is as far away as one can go from the torquer bars without using extension booms, then the residual field from two bars that were previously fully excited is still approximately 0.28×10^{-3} gauss, i.e., 23% of the quantity one wishes to measure. This may, however, be acceptable since the bars are operated in a closed control loop and since there is ample wheel capacity so that the control law need not compute the commanded unloading torque that precisely.

The magnetic field due to the array mounted coil will be less than 0.49 gauss anywhere within the AASIR instrument. Only for a few points closest to the array will the field strength reach 0.49 gauss; at the center of the AASIR and near the cooler where the detectors and associated electronics are located the field will be less than 0.1 gauss. Since the AASIR will be designed (and tested) so as to operate properly in the earth ambient field of about 0.4 gauss, no payload operational problems due to the array mounted dipole are expected. The field at the magnetometer due to the array mounted coil can be calculated from the coil current and then compensated for in the measurements. The magnitude of the coil current must be made available through a current monitor.

The remainder of this section will present more details of the investigations conducted.

7.2 System Concept

The system concept is described best by Figure 7-1. A coil having a magnetic moment \vec{M} is mounted to a solar array panel such that the torque

$$\vec{T} = \vec{M} \times \vec{B} \quad (7-1)$$

due to reaction with the earth field \vec{B} will cancel the secular solar disturbance torque. Gravity gradient and aerodynamic disturbance torques are completely insignificant at synchronous altitude. The coil excitation is not under closed loop control but is based on an a priori estimate of the secular solar disturbance torque that must be cancelled. The momentum due to the residual secular disturbance torque is then removed by closed loop operation of the standard 100,000 pole-cm torquer bars located in the ACS module.

A schematic spacecraft/solar array geometry is shown in Figure 7-2. The preliminary power budget shown in Table 7-2 has been used to establish array size. The use of ultraviolet solar cells has been assumed, mounted on a standard substrate. Ultraviolet cells can actually be mounted to a light weight substrate, however, a standard substrate has been assumed here, since it must also provide support for the coil(s). Using solar array design data from the StormSat Study proposal, the violet cells yield 81.2 watts/m² (7.54 watts/foot²) of array after three years on-orbit. This yields the proposed 400 watt array size of 4.9 x 1 m (192" x 40") consisting of three panels, each having a usable coil area of about 1.6 x 1 m (64" x 40"). The weight factor for this array is 4.15 kg/m² (0.85 pound/foot²).

7.2.1 Solar Disturbance Torque

The solar disturbance torque acting on StormSat is predominantly due to the single array which causes a solar pressure unbalanced spacecraft configuration. In obtaining solar torque estimates only the array need be considered since the remainder of the spacecraft will be very nearly solar pressure balanced. From Figure 7-2 it follows then that the magnitude of the secular solar disturbance torque acting in the orbit plane

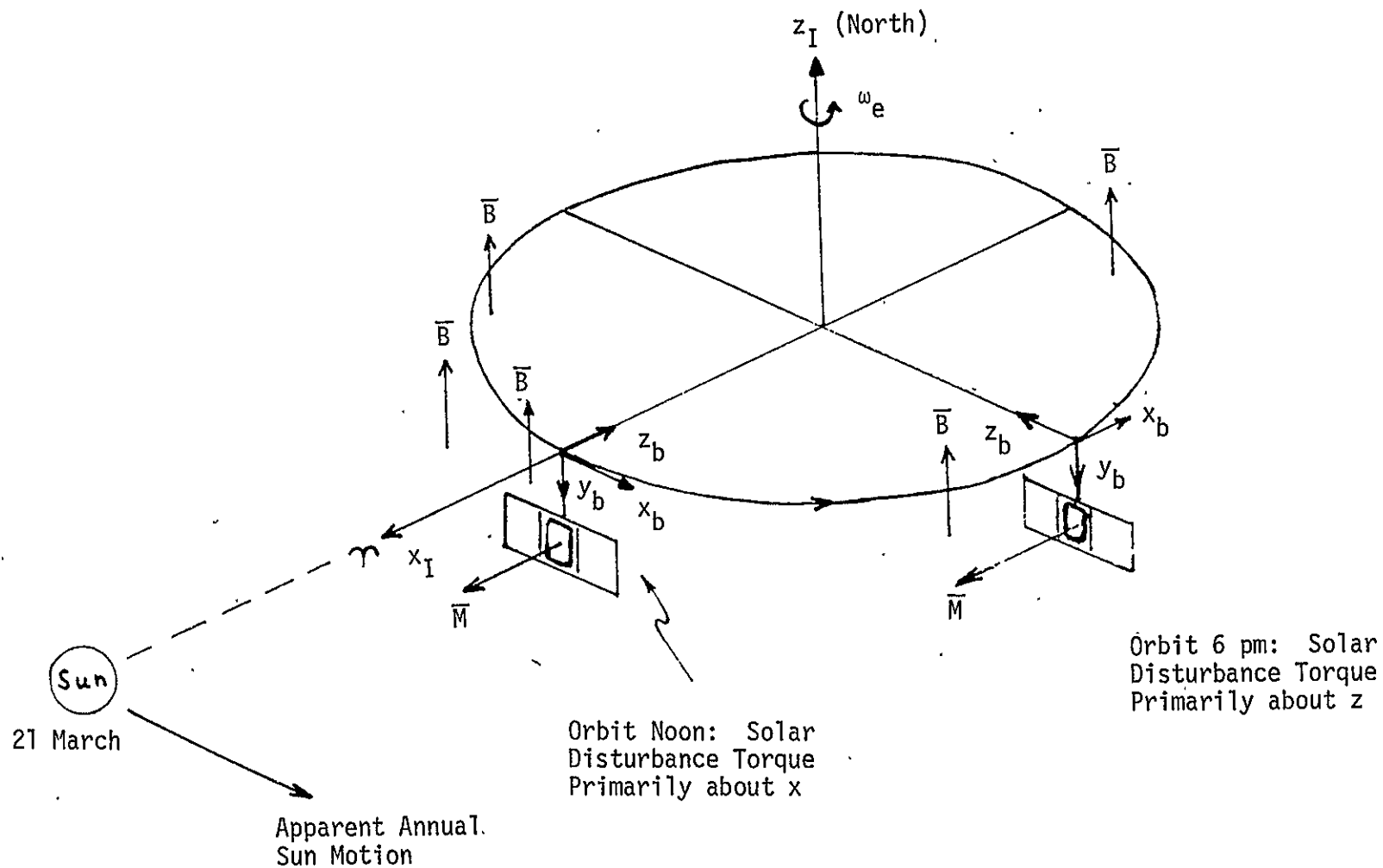


Figure 7-1. Sun - Spacecraft - Magnetic Field
Orbital Geometry

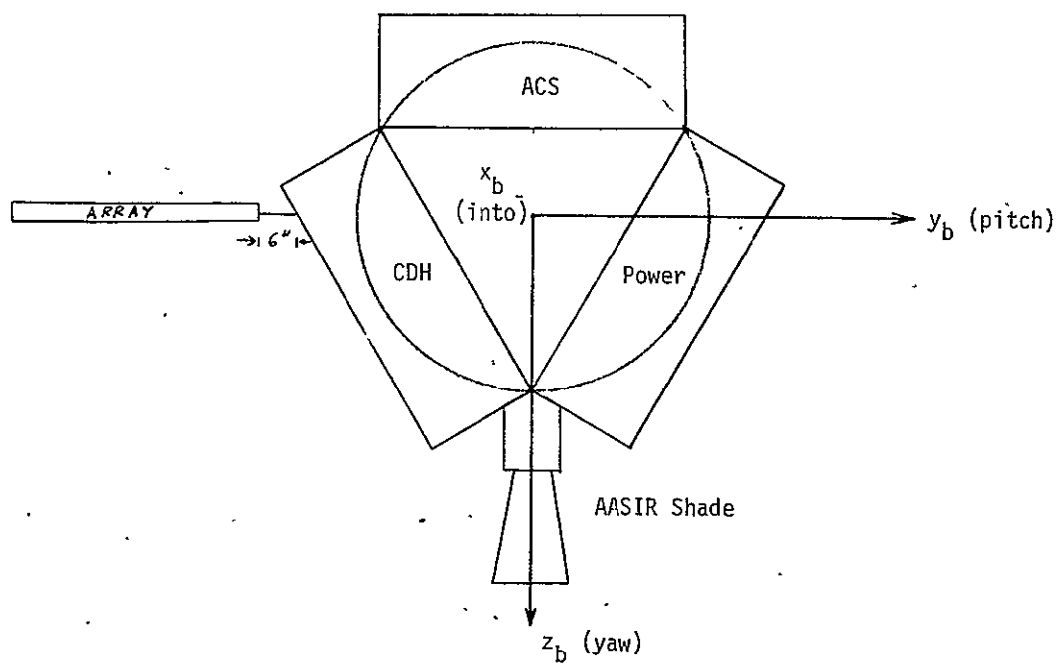
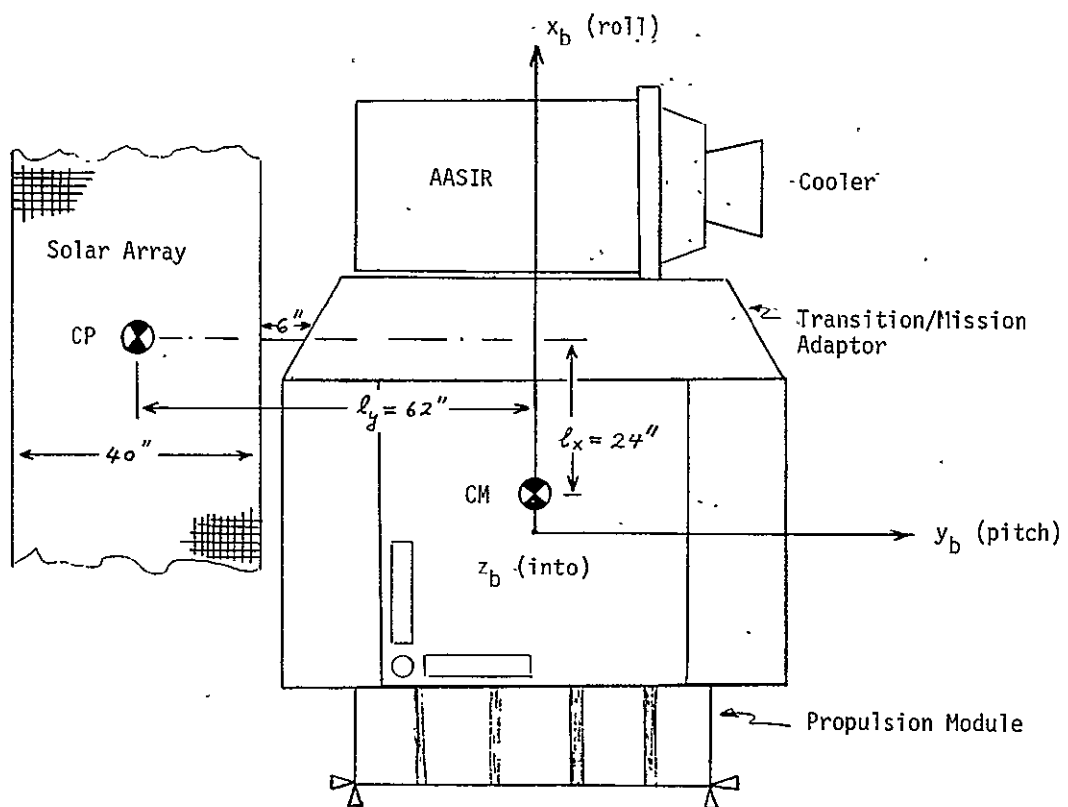


Figure 7-2. Spacecraft/Solar Array Geometry (Noon Condition)

Table 7-2. Preliminary StormSat Power Budget

Item	Power (watts)
Attitude Control	130
Communications and Data Handling	100
Power Subsystem	50
Propulsion Subsystem	10
AASIR	65
Array-Mounted Coil	20
Battery Charge	25
Total	400

(alternately about the spacecraft roll (x) and yaw (z) axes, but inertially fixed) is given by

$$T_s = v (1+v_n) A \ell_y \quad (7-2)$$

where

$$v = 4.5 \times 10^{-6} \text{ N/m}^2 \text{ (} 9.4 \times 10^{-8} \text{ lb/ft}^2 \text{)} = \text{solar pressure constant}$$

$$v_n = 0.26 = \text{normal reflectivity coefficient (EOL)}$$

$$A = 4.9 \text{ m}^2 \text{ (} 53.4 \text{ ft}^2 \text{)} = \text{array area}$$

$$\ell_y = 1.58 \text{ m (} 62 \text{") } = \text{moment arm from array CP to S/C CM}$$

After substitution of the numerical values,

$$T_s = 4.4 \times 10^{-5} \text{ Nm (} 3.25 \times 10^{-5} \text{ ft-lb)} \quad (7-3)$$

A cyclic torque at orbit rate ω_0 about the spacecraft pitch (y) axis is caused by the array axis offset ℓ_x , see Figure 7-2, with amplitude

$$\hat{T}_y = v (1+v_n) A \ell_x \quad (7-4)$$

For $\ell_x = 0.61$ m (24 inches)

$$\hat{T}_y = 1.7 \times 10^{-5} \text{ Nm } (1.26 \times 10^{-5} \text{ ft-lb}) \quad (7-5)$$

Relative to the wheel capacity of 20 Nms (15 foot-pound-second) this cyclic torque is small and can be handled entirely by cyclic operation of the pitch wheel with no momentum unloading required. The magnitude of the secular solar torque $T_s = 4.4 \times 10^{-5}$ Nm is, therefore, the sole driver in the design of the array mounted coil.

7.2.2 Geomagnetic Field at Synchronous Altitude*

The geomagnetic field is the result of complex, and as yet incompletely understood, physical processes. Probably the best available information on the geomagnetic field at synchronous altitude is based on measurements made by three-axis magnetometers on-board ATS 1 and ATS 5. Much of this data has been published in the Journal of Geophysical Research; see References 7 to 16. The model of the nominal (quiet-day) field seems to be fairly complete and accurate. The observed fields during the frequent (several per month) geomagnetic storms are usually published on a case-by-case basis because of the extreme variations between storms. There is probably insufficient data available to completely characterize the frequency and intensity of these storms.

Tilted Dipole Model

The simplest model of the quiet-day geomagnetic field with a reasonable claim to validity consists of a dipole at the center of the earth

*The material in this section was compiled earlier by V. A. Spector of the Design, Analysis and Simulation Department at TRW Systems

tilted 11.7 degrees from the spin axis. This model is illustrated in Figure 7-3.

The tilted dipole model predicts the actual geomagnetic field to within 1% at the earth's surface and at low altitude orbits. At geosynchronous altitude, the actual quiet-day field differs from the tilted dipole field by as much as 20% in magnitude and 10 degrees in direction. During geomagnetic storms, the tilted dipole model is totally incapable of predicting the actual field at geosynchronous altitude.

Actual Geomagnetic Field

The actual quiet-day geomagnetic field, as measured by numerous satellites, is illustrated in Figure 7-4. Instead of extending through all space, the field is confined to a definite region (the magnetosphere) with a discrete boundary layer (the magnetopause). Solar wind pressure compresses the field on the sunlit side of the earth, with the magnetopause nominally at $10 R_E$ (R_E = earth radii) at the noon local time meridian. On the dark side of the earth, the field extends in a tail for at least $30 R_E$ at the local midnight meridian. The longest field lines in the tail originate (and terminate) at a high latitude (critical latitude) on the day side of the earth and are bent back over the pole. In the transition region between field lines that extend into the day and night sides, near the critical latitude, the field is weak and turbulent, allowing particles (electrons and protons) to penetrate the magnetosphere at the neutral points. These particles can act as an electric current, producing a magnetic field, both before and after getting trapped in the equatorial particle belts.

At synchronous altitude ($6.6 R_E$) at least four significant sources of the observed quiet-day field can be identified

- The tilted dipole field internal to the earth, B_g
- The field from current flow in the magnetopause plasma, B_{mp}
- The field from the tail and associated current flows, B_t
- The field from the quiet-day current ring, B_r

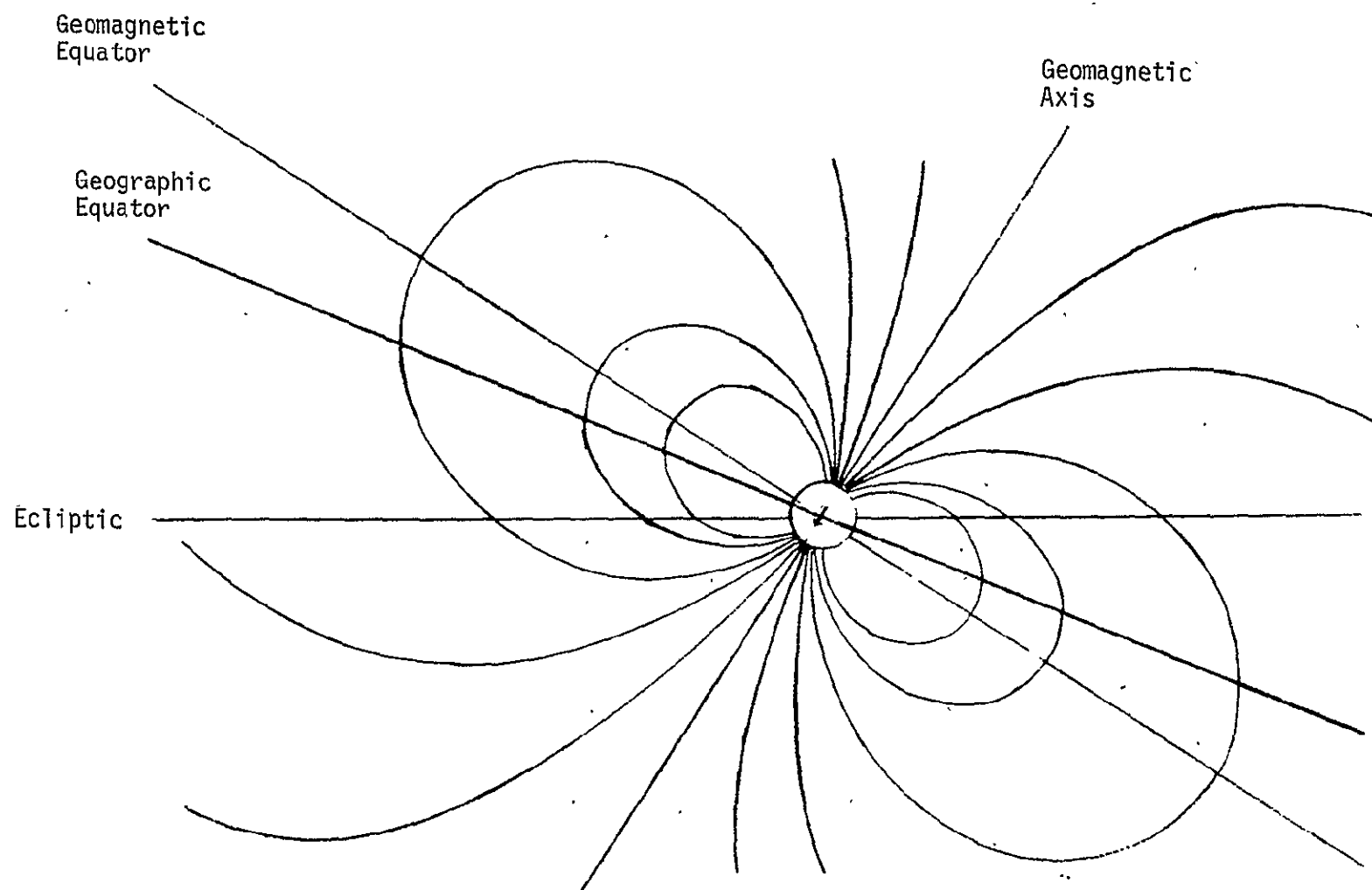


Figure 7-3. Tilted Dipole Geomagnetic Field Model (Winter Solstice)

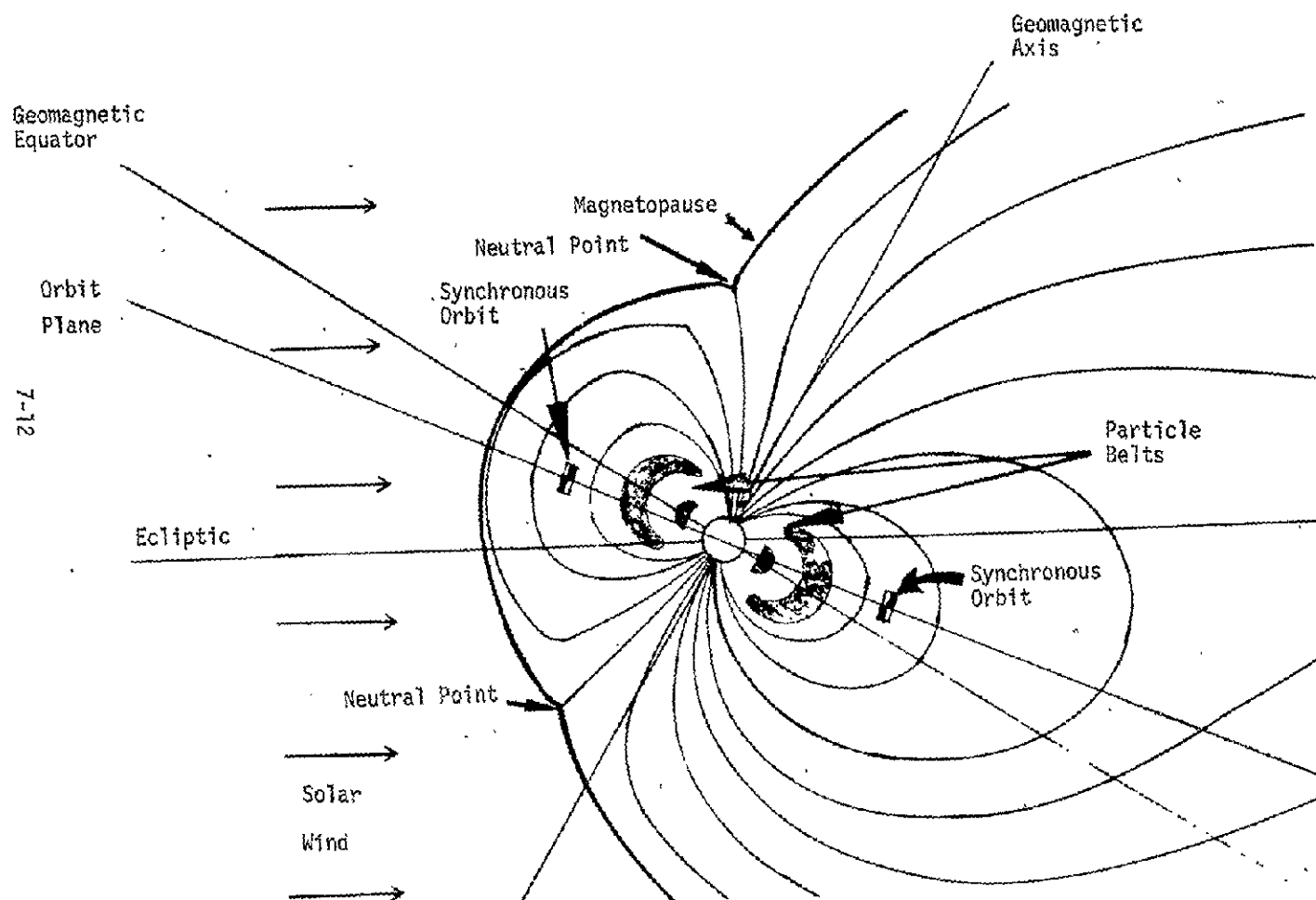


Figure 7-4. Actual Geomagnetic Field (Winter Solstice)

Typical quiet-day geomagnetic field components at synchronous altitude in spacecraft body coordinates are plotted in Figure 7-5. The field is seen to be predominately along the negative y (pitch) axis with an average value of about 120 gamma. Since a synchronous satellite corotates with the earth, the contribution from the tilted dipole field B_g is constant at a given longitude and can account for only the average field values.

All three components of the observed field exhibit daily variations, B_y having the largest. Its daily fluctuation is typically 30 to 40 gamma, with the maximum occurring near local noon and the minimum near local midnight. The variation pattern of B_y does not change appreciably with season. The x (geographic east) and z (nadir) components exhibit smaller daily fluctuations (10 to 15 gamma). The form of the B_x and B_z daily variations is strongly dependent on season and possess slight seasonal asymmetries in their daily ranges, the range in summer being larger than in winter. The daily and seasonal variations are caused by the relative motion of the satellite and the magnetopause, ring, tail and neutral-sheet current systems.

Geomagnetic Storms

The detailed physics of geomagnetic storms is beyond the scope of this report. Basically, storms are triggered by a sudden increase in solar wind pressure due to, for example, a solar flare. The increased solar wind pressure increases the compression of the geomagnetic field on the day side and pushes additional field lines into the tail on the night side. The moving magnetic field lines induce electric currents in the magnetopause and tail plasma that in turn produce magnetic fields that oppose the original field motion (i.e., Lenz's law). The situation is further complicated by Hall effect currents, partial current rings, and the trapped particle belts. Eventually, the induced currents decay and the field returns to its prestorm values. The net effect at synchronous altitude is usually a decrease in the magnitude of B_y of from 30 to 70 gamma lasting 3 to 7 hours. The changes in the x and z components vary from storm to storm over a wide range. On occasion, B_x and B_z may exceed B_y in magnitude. The field components during a typical moderate storm

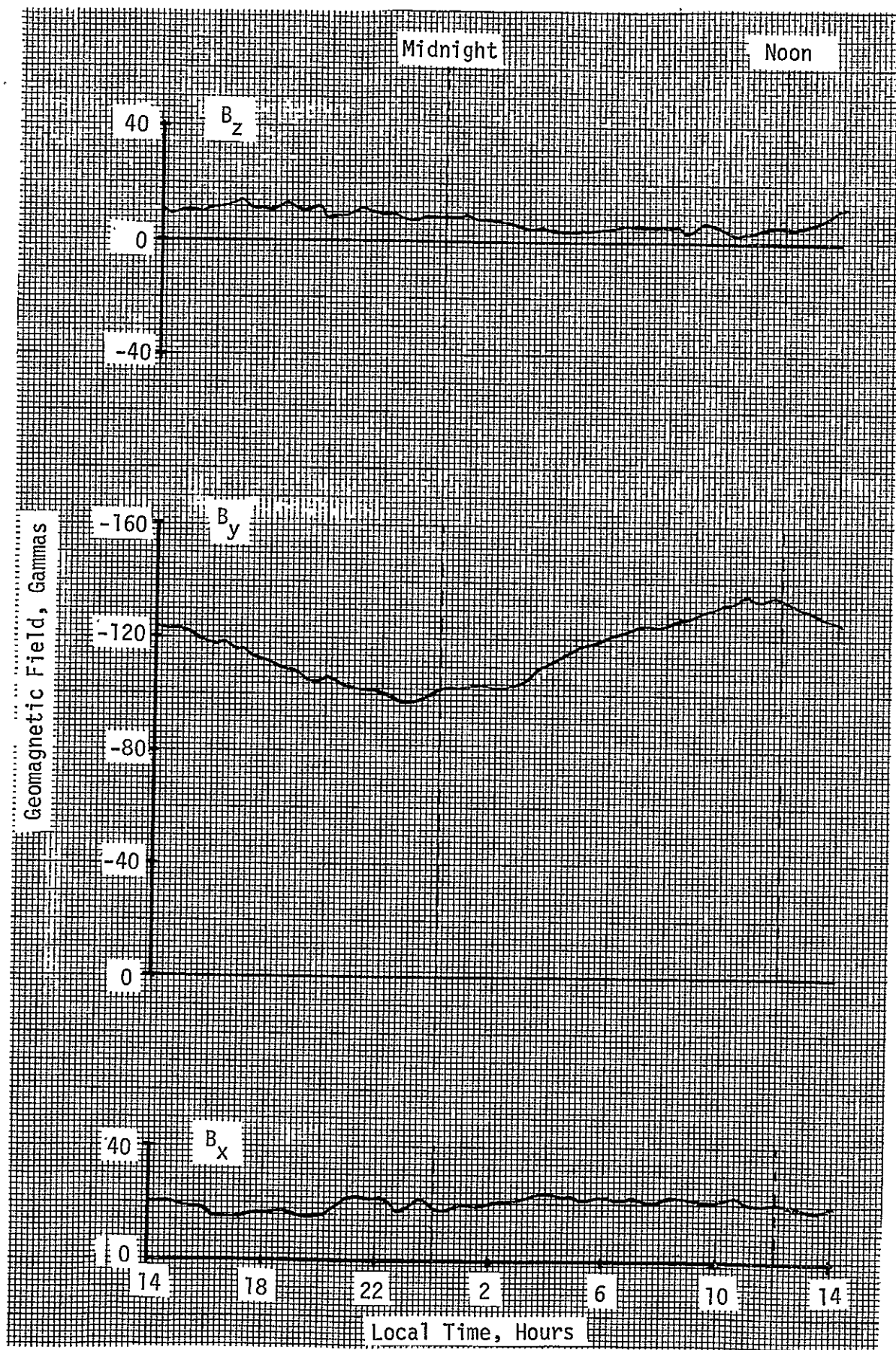


Figure 7-5. Typical Quiet-Day Geomagnetic Field at Synchronous Altitude .

(December 25, 1966) are plotted in Figure 7-6. Storms of this magnitude can be expected several times per month. Magnetograms of more severe storms can be found in Reference 15.

On at least three occasions (January 14, 1967; May 25, 1967; and September 29, 1969) extreme compression of the geomagnetic field caused the magnetopause to move in beyond synchronous altitude near the local noon meridian. Figure 7-7, derived from Reference 14, shows the y component of the field at ATS 5 on September 29, 1969. The field increased over a period of 5 hours to a peak magnitude of over 300 gamma, instantaneously jumped 410 gamma (changing direction) as the magnetopause passed by, jumped back as the magnetopause recrossed the orbit, and stayed at an unusually high level an additional 3 hours. The actual frequency of this phenomena cannot be determined from available data because of its localized (i.e., near noon local time meridian) nature and limited (i.e., two satellites) observation history.

Table 7-3 summarizes the relevant geomagnetic field data under the three conditions considered. A nominal average field strength of $B_y = -120$ gamma ($= -1.2 \times 10^{-3}$ gauss $= -1.2 \times 10^{-7}$ webers/m²) will be used for sizing the array mounted coil(s).

Control Aspects of the Synchronous Altitude Geomagnetic Field

Magnetic control torques can only be generated by reacting against the available geomagnetic field. The above discussed variations in the geomagnetic field have the effect of introducing time varying gains and inter-axis coupling into the control problem. Magnetometer field measurements on-board can reduce at least the effects of the magnitude variations. Less accurate magnetometers would be required if they were used only to indicate the existence of a magnetic storm to disable magnetic control and if required, switch to momentum unloading using thrusters. Magnetic storms at synchronous altitude are usually detectable at the earth's surface with a short time delay, although the surface field gives little indication of the actual field at the spacecraft. Ground commanded mode switching at the onset of a magnetic storm may, therefore, eliminate the requirement for an on-board magnetometer.

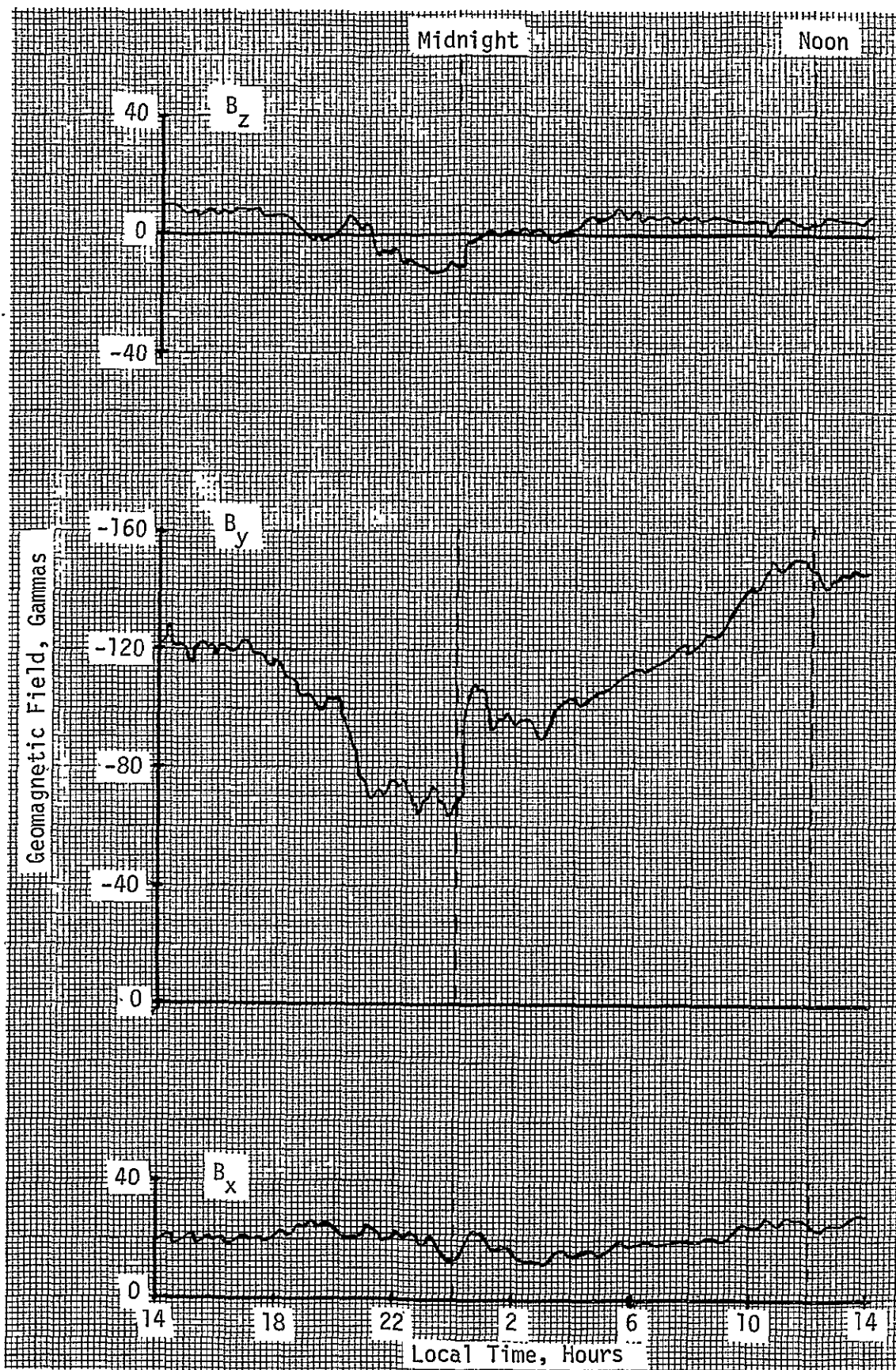


Figure 7-6. Typical Geomagnetic Field During Moderate Magnetic Storm at Synchronous Altitude

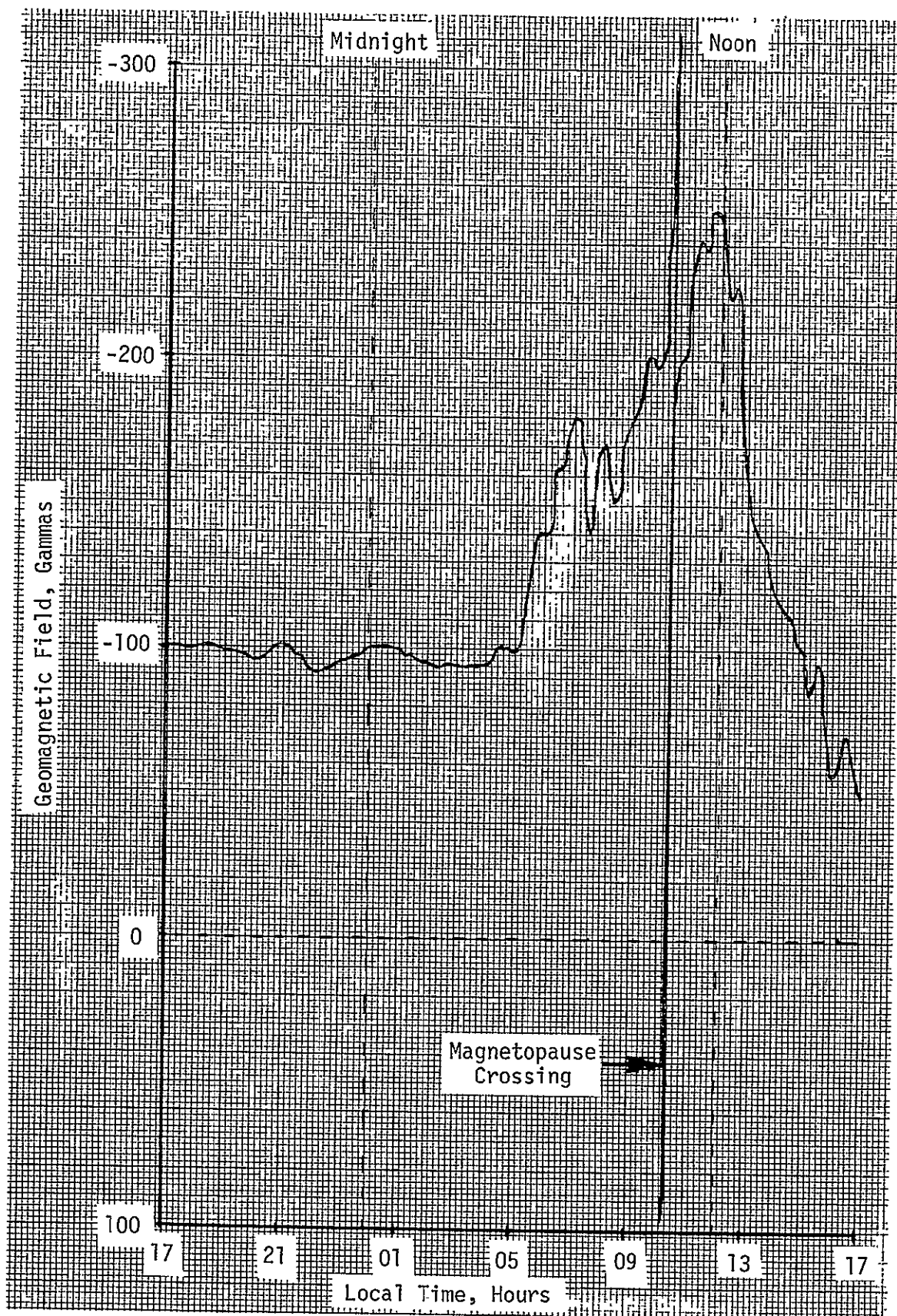


Figure 7-7. Extreme Variation of Y Component of Geomagnetic Field at Synchronous Altitude During Magnetopause Crossing

Table 7-3. Summary of Geomagnetic Field at Synchronous Altitude

Condition	Frequency of Occurrence	Duration of Disturbance	Geomagnetic Field, Gammas		
			B_x	B_y	B_z
Nominal	Approximately 98% of time	---	10 to 40	-95 to -145	-20 to +20
Moderate Storm	3 to 5 per month	1 to 7 hours	-100 to +50	-20 to -170	-40 to +120
Magnetopause Crossing	At least three reported cases	Up to 10 hours, field reversed up to 3 hours	-120 to +60	-310 to +160	-60 to +150

7.3 Array Mounted Coil Sizing

7.3.1 Coil for 400 Watt Array

For the spacecraft configuration of Figure 7-2 with a 400 watt array the secular solar disturbance torque was determined as

$$T_s = 4.4 \times 10^{-5} \text{ Nm}$$

The reaction torque \bar{T} obtained from a coil having magnetic moment \bar{M} and located in an external magnetic field \bar{B} is given by

$$\bar{T} = \bar{M} \times \bar{B} \quad (7-6)$$

Since in a synchronous equatorial orbit the geomagnetic field is nominally perpendicular to the array mounted coil mount \bar{M} , it follows that the coil must have a magnetic moment of

$$M = \frac{T_s}{B} = \frac{4.4 \times 10^{-5} \text{ Nm}}{1.2 \times 10^{-7} \text{ webers/m}^2} = 367 \approx 370 \text{ ATm}^2 \quad (7-7)$$

in order to cancel the solar torque T_s . The solar array is assumed to be composed of three panels, each having a usable area of 1.6 x 1 m (64" x 40") as illustrated in Figure 7-8. First a single coil will be sized for mounting on the center panel, such that it will circumscribe the panel area (see also Figure 7-1).

The following relationships follow directly from elementary physical laws.

$$\begin{aligned} m &= \rho \ell A_w \\ R &= \frac{\sigma \ell}{A_w} \\ P &= I^2 R \\ M &= NIA = NI(LW) \\ \ell &= 2N(L+W) \end{aligned} \quad (7-8)$$

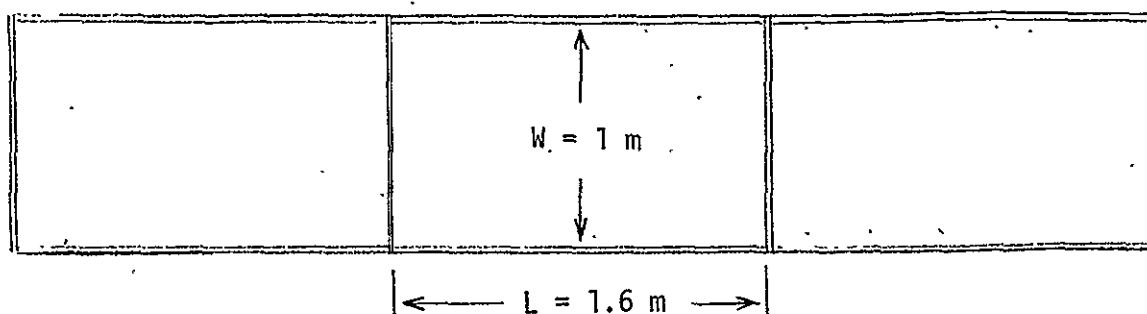


Figure 7-8. Solar Array with Three Panels

where

- m = mass of wire in coil (kg)
- A_w = cross-sectional area of wire (m^2)
- ℓ = length of wire in coil (m)
- ρ = density of wire (kg/m^3)
- σ = resistivity of wire (ohm-m)
- R = resistance of wire in coil (ohms)
- I = current (amps)
- P = power consumption of coil (watts)
- A = area enclosed by coil loop (m^2)
- L = length of panel = length of coil (m)
- W = width of panel = width of coil (m)
- N = number of turns of coil around A
- M = magnetic moment (amp-turn- m^2)

Combining the relationships in (7-8) yields the following:

$$P = \frac{2\sigma(L+W)M^2}{(LW)^2 N A_w} \quad (7-9)$$

$$m = 2\rho N (L+W) A_w \quad (7-10)$$

and

$$\delta \triangleq mP = 4\rho\sigma M^2 \frac{(L+W)^2}{(LW)^2} \quad (7-11)$$

The last expression is the bare wire mass-power product of the coil which is independent of wire size and number of turns. For a chosen wire material and fixed coil area the mass-power product of a coil having magnetic moment M is constant.

Table 7-4 lists the physical properties of three wire materials that may be used. From expression (7-11) for the mass-power product of the coil it is clear that one would like to use a material with a low $\rho\sigma$ product. Using aluminum the weight power product for the $M = 370 \text{ ATm}^2$ coil is 110.5 watt-kg; for copper it is 221 watt-kg. Even though aluminum results in only one half the weight-power product, copper wire should be used since aluminum wire is too brittle to withstand the flexing of the array and reliable solder connections are also difficult to achieve.

The resistivity of a given material decreases with temperature and it is tempting to argue that in the cold space environment a resistivity much lower than earth ambient should apply. However, the substrate on the backside of the solar array where the coil would be mounted is typically at about 90°F for a synchronous spacecraft. Using reasonable coil mounting techniques to the substrate, and also accounting for the fact that the coil must radiate its own power, a coil wire temperature of 70°F seems just about right. A detailed thermal analysis for the array mounted coil must eventually be conducted before a final design can be established. Based on the resistivity and density given in Table 7-4, the mass-power products of an aluminum and a copper coil are plotted versus the coil magnetic moment M in Figure 7-9.

Table 7-4. Physical Properties of Wire Materials

Material	Resistivity σ (70°F) ohm-m	Density ρ kg/m ³	$\sigma\rho$ kg-ohm/m ²
Aluminum	2.824×10^{-8}	2.7×10^{-3}	0.764×10^{-4}
Copper	1.724×10^{-8}	8.89×10^{-3}	1.53×10^{-4}
Silver	1.59×10^{-8}	10.5×10^{-3}	1.67×10^{-4}

To obtain a reasonable weight a steady state power of 20 watts was allowed for the coil resulting in a bare copper wire weight of 11.05 kg. Assuming a nominal coil excitation voltage of 28 volts d-c and applying the relationships of (7-8) through (7-11) allows one to specify the coil completely. Weight for insulation material and fasteners and connectors must be added to the bare wire weight. Mylar does not deteriorate in a free space environment due to particle bombardment and weight for 1/4 mm thick mylar insulation has been added. This weight can easily be calculated from

$$m_{ins} = \rho_{ins} \pi l (r_2^2 - r_1^2) = 2.25 \text{ kg} \quad (7-12)$$

where

$$\begin{aligned} r_1 &= \text{radius of bare copper wire} = 0.484 \times 10^{-3} \text{ m} \\ r_2 - r_1 &= 0.25 \times 10^{-3} \text{ m (insulation thickness)} \end{aligned}$$

and

$$\rho_{ins} = \rho_{mylar} = 1.4 \times 10^3 \text{ kg/m}^3$$

The weight for fasteners and connectors has been estimated as 1.5 kg for a single panel coil, being comprised of 20 fasteners at 70 gram each and 100 gram for connectors. The total resulting coil weight was then

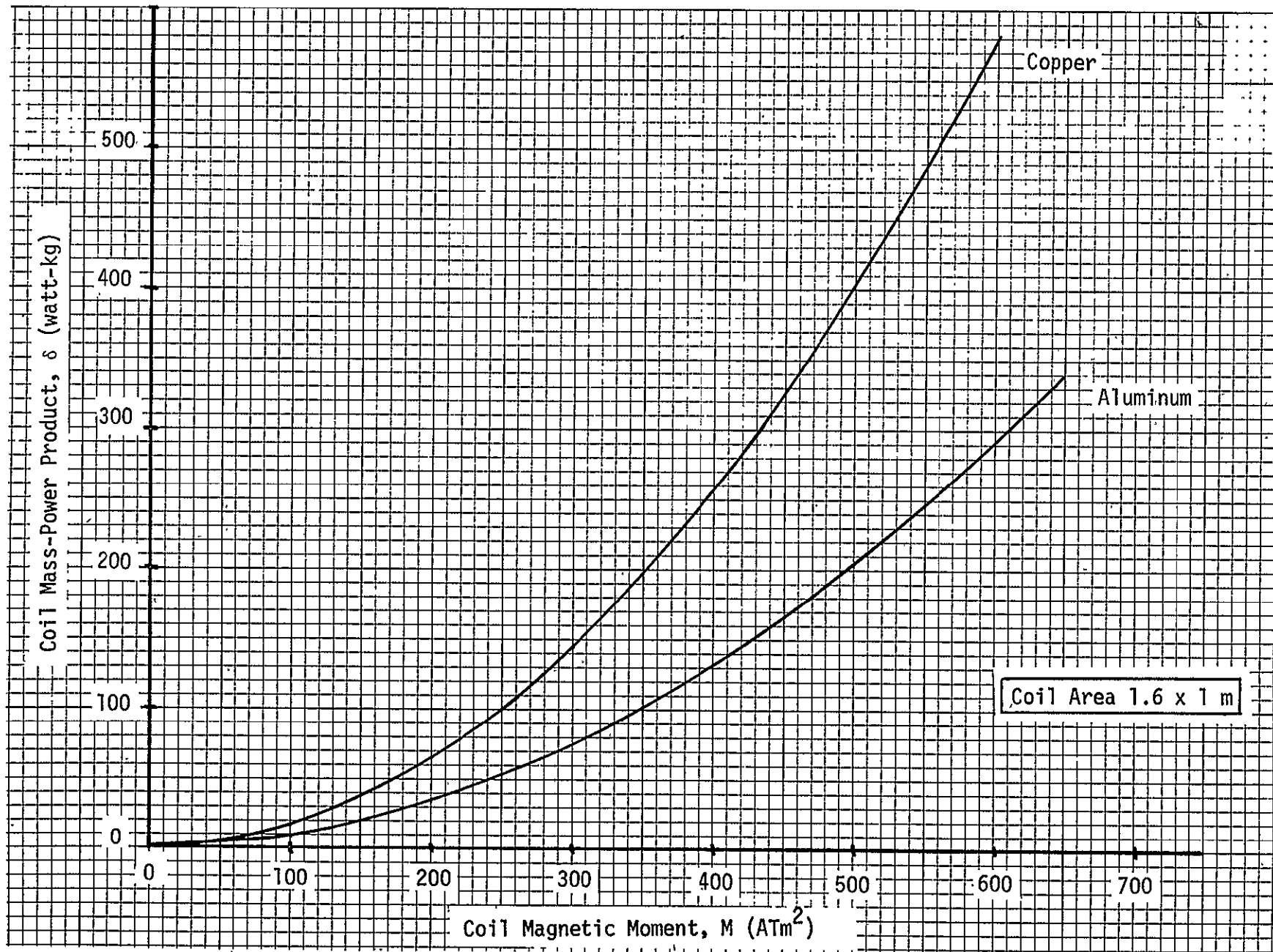


Figure 7-9. Mass Power Product Versus Coil Magnetic Moment

determined as 14.8 kg (32.5 pounds). It consists of 324 turns of a 0.968 mm diameter copper wire (approximately AWG #19) carrying 0.741 amps.

The desirability/feasibility of mounting a 32.5 pound coil to one panel of the solar array is highly questionable, however. Distributing the weight over the entire solar array by using three smaller coils of 123 ATm^2 (123,000 pole-cm) each, one per array panel, was, therefore, investigated next. The total power consumption for all three coils was to remain fixed at 20 watts. The bare wire weight of the smaller coils is only 1/3 of the wire weight of the single large coil, but by the time weight allowances for insulation and fasteners are added, the weight per coil becomes 6.7 kg (14.75 pounds). It consists of 324 turns of a 0.559 mm diameter wire (approximately AWG #23) carrying 0.238 amps. This is still rather heavy and means were sought to further reduce the weight of the coils.

7.3.2 Minimum Total Weight Design

Since the weight-power product for an air core coil of specified dimensions and magnetic moment is constant, a lighter coil may be obtained by reducing weight at the expense of power. However, if more than 20 watts of power are required then the size of the solar array must be increased which itself adds weight to the system and also increases the secular solar disturbance torque, which in turn requires a larger coil (larger magnetic moment). Taking all these interrelationships into account coil weight has been reduced by increasing coil power until the sum of coil weight and additional solar array weight was minimized. Referring to Figure 7-10 and using the previously assumed (Section 7.2) array characteristics of 81.2 watts/m^2 and 4.15 kg/m^2 , the needed mathematical relationships are as follows:

- Increased Array Weight and Array Width (P = total coil power)

$$\Delta m_a = 0.05125 (P-20) \text{ kg}$$

$$\Delta W = 2.515 \times 10^{-3} (P-20) \text{ m}$$

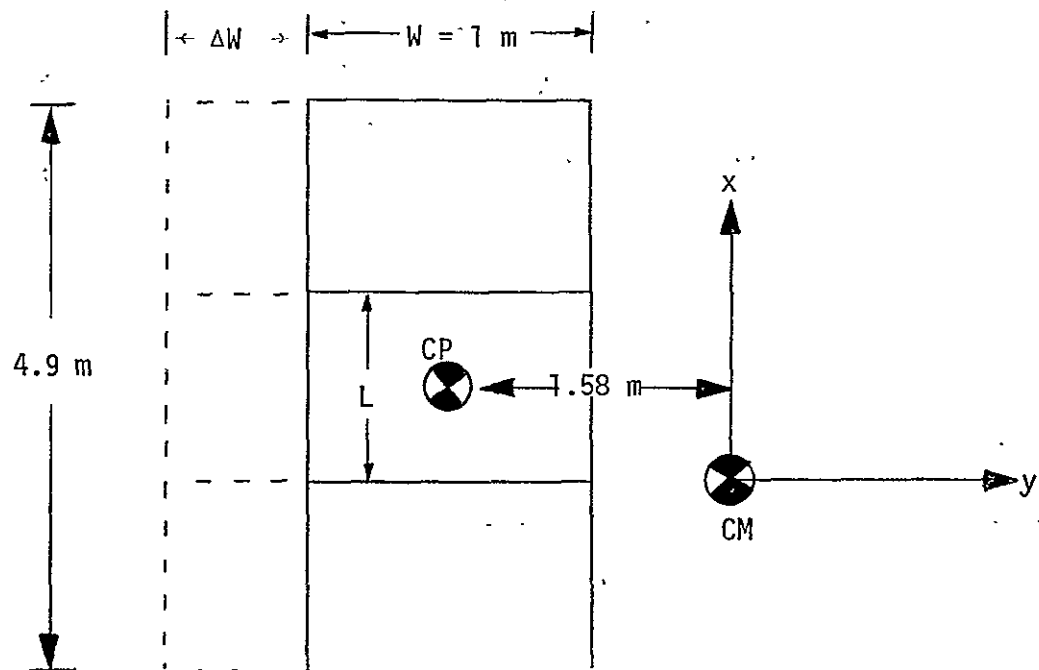


Figure 7-10. Increased Array Geometry

- Secular Solar Torque

$$T_s = (4.4 + 5.78 \Delta W + 1.39 \Delta W^2) \times 10^{-5} \text{ Nm}$$

- Magnetic Moment

$$M = \frac{T_s}{B} = \frac{T_s}{1.2 \times 10^{-7}} \text{ ATm}^2$$

- Mass-Power Product (single coil, one panel)

$$mP = 4\rho\sigma \left(\frac{L+W+\Delta W}{L(W+\Delta W)} \right)^2 \text{ M}^2 \text{ watt-kg}$$

- Total Weight to be Minimized

$$m_{\text{tot}} = m + \Delta m_a \text{ kg}$$

These equations can be programmed on a digital computer in exactly the same order as shown, and entering with coil power P as the independent parameter, the total weight m_{tot} can be plotted as a function of P . The results are shown in Figure 7-11 which shows that m_{tot} assumes a minimum of 6.2 kg at 63 watts. The corresponding weight optimized parameters are:

$$\begin{aligned}P &= 63 \text{ watts} \\ \Delta m_a &= 2.2 \text{ kg} \\ \Delta W &= 0.11 \text{ m} \\ M &= 420 \text{ ATm}^2 \text{ (420,000 pole-cm)} \\ mP &= 252 \text{ watt-kg} \\ m &= 4 \text{ kg (bare wire weight, single coil)}\end{aligned}$$

Proceeding now as before, assuming 28 volt d-c excitation, and adding weight for 1/4 mm thick mylar insulation and 1.5 kg for fasteners and connectors per panel, one arrives at the following coil designs:

- Single Coil on Center Panel:

Weight: 6.3 kg (13.9 lb)
Power: 63 watts
Wire: 105 turns of 1 mm diameter copper wire (~AWG #18)
Current: 2.25 amps

- Three Coils, One per Panel:

Weight: 3.35 kg/coil (7.4 lb)
Power: 21 watts/coil
Wire: 105 turns of 0.577 mm wire (~AWG #23)
Current: 0.75 amps

The latter design of three coils of 7.4 pounds each looks very reasonable and appears structurally feasible regarding the solar array substrate. It is recommended that this design be used for magnetic unloading for StormSat.

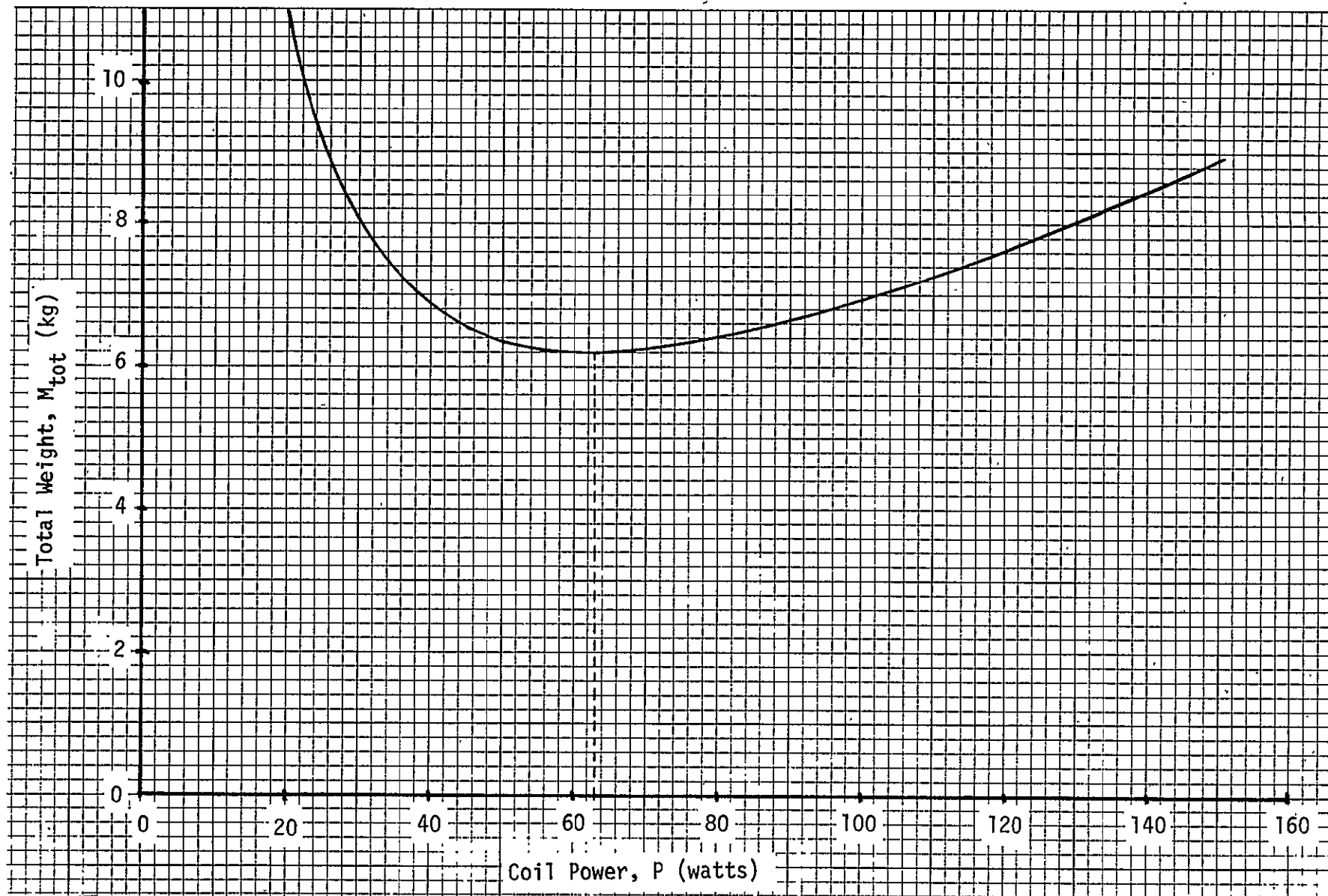


Figure 7-11. Coil Plus Incremental Array Weight Versus Coil Power

7.4 Effects of Generated Magnetic Fields

Excitation of the torquer bars and the array mounted coil will produce magnetic fields that potentially could affect the operation of the payload (AASIR), the star trackers, and the magnetometer. This section will assess these effects.

7.4.1 Magnetometer Considerations

The residual magnetism in one of the 100,000 pole-cm torquer bars after full excitation may be as large as 1400 pole-cm. The strength of the resultant magnetic field B due to this residual dipole moment M may be computed from the relationship

$$|\vec{B}| = \frac{Mr}{4\pi\left(r^2 - \frac{d^2}{4} \cos^2 \theta\right)^{3/2}} (1+3\cos^2 \theta)^{1/2} \quad (7-13)$$

where the symbols are defined in Figure 7-12 and must have the following units:

r, d = meter

M = weber-meter ($1 \text{ ATm}^2 = 4\pi \times 10^{-7}$ weber-meters)*

B = webers/m²

For the MMS torquer bars the effective $d = 0.306$ m. Locating the magnetometer in the opposite corner from the torquer bars yields a distance $r = 1.5$ m at an angle $\theta = 52.7$ degrees. The resultant field strength at the magnetometer is 0.63×10^{-3} gauss due to the residual magnetism of just one torquer bar. This is half the field strength one wishes to measure with the magnetometer. Since the total residual field due to all three torquer bars is unpredictable, because it depends on the exact behavior of the core material and the torquer excitation history before

*The MKS unit for M is the weber-meter. The magnetic torque expression $\vec{T} = \vec{M} \times \vec{B}$ is actually wrong in the MKS sense. It should be:
 $\vec{T} = \vec{M} \times \vec{H} = \vec{M} \times \vec{B}/\mu_0 = \vec{M}/\mu_0 \times \vec{B} = \vec{\bar{M}} \times \vec{B}$, where $\vec{\bar{M}}$ is in ATm^2 , M in weber-meters, and $\mu_0 = 4\pi \times 10^{-7}$.

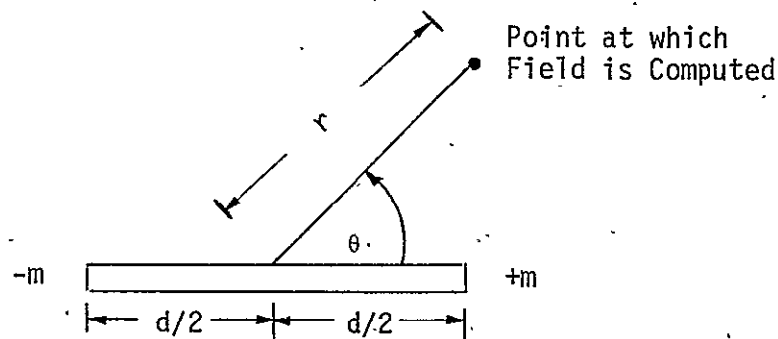


Figure 7-12. Magnetic Dipole Having Moment $M = md$

shut-off (hysteresis), it must be concluded that the magnetometer cannot be located within the ACS module for measuring the geomagnetic field at synchronous altitude. Locating the magnetometer close to the payload near the AASIR cooler is just about as far away as one can go from the torquer bars without using extension booms; the distance is approximately 2.3 m and the angle θ varies from 30 to 90 degrees depending on the torquer bar in question. The resultant field is expected to be no larger than about 0.2×10^{-3} gauss due to the residual magnetism of one bar, or a maximum from two* bars of about 0.28×10^{-3} gauss. This worst case field is still rather large relative to the 1.2×10^{-3} gauss one wishes to measure, but it may be acceptable since the bars are operated in a self-correcting closed control loop, and since there is ample wheel capacity so that the control law need not compute the commanded unloading torque that precisely.

Another consideration is that the standard MMS magnetometer of ± 0.6 gauss range cannot be directly used in synchronous altitude applications, since the geomagnetic field of 1.2×10^{-3} gauss is typically below the achievable accuracy/bias level of such an instrument. The standard

*The third bar will most likely not be used since the in-orbit-plane field is practically zero.

magnetometer must, therefore, be modified to a smaller dynamic range, say $\pm 5 \times 10^{-3}$ gauss, with attendant accuracy of 0.05×10^{-3} gauss.

The magnetometer will, of course, also be affected by the field generated by the array mounted coils. However, this field can be precisely computed from the currents flowing in the air core coils and the effect on the magnetometer can be compensated for. This will not be as straightforward as it sounds, since with the magnetometer mounted near the AASIR cooler the corresponding field strength due to the coils would be 30×10^{-3} gauss. But it was just pointed out above that for accuracy purposes the dynamic range of the magnetometer must be reduced to $\pm 5 \times 10^{-3}$ gauss. Some electronic bias compensation internal to the instrument would, therefore, be necessary. This may be further complicated if the coils operate from an unregulated bus and the coil currents undergo large variations so that this biasing scheme must be made adaptable.

In summary, measuring the geomagnetic field at synchronous altitude with a magnetometer in the presence of other strong magnetic dipoles is not a trivial task and requires considerable attention to magnetometer design and location. One should seriously consider to do away with the magnetometer all together, rely on the nominal field strength of 1.2×10^{-3} gauss along the spacecraft pitch axis, and shutdown the magnetic unloading system when a severe solar storm is observed by ground stations. The RCS system can then be used for backup momentum unloading since StormSat needs to fly with a propulsion module east-west station-keeping; north-south stationkeeping will probably also be required.

7.4.2 Payload and Star Tracker Considerations

For the array mounted coil the dipole separation distance d is very small relative to r , so that Equation (7-13) becomes

$$|\vec{B}| = \frac{M}{4\pi r^3} [1 + 3 \cos^2 \theta]^{1/2} \quad (7-14)$$

The minimum distance r from the $M = 420 \text{ ATm}^2$ ($420 \times 4\pi \times 10^{-7}$ weber-meter) dipole, located at the CP of the array, to the AASIR is about 1.04 m; the angle θ varies between $\theta = 60$ degrees and $\theta = 90$ degrees, depending on array orientation. The distance to the center of the AASIR is about 1.85 m, and to the AASIR cooler about 2.65 m. The maximum field in the AASIR due to the array mounted coil is, therefore, obtained as follows:

AASIR Points Closest to Array: 0.494 gauss

Center of AASIR: 0.088 gauss

Points Near AASIR Cooler: 0.030 gauss

Only the points closest to the array exceed the field at the earth surface of about 0.4 gauss, the conditions under which the AASIR must pass operational tests. Since the sensitive electronics, i.e., detectors, etc., are all located near the cooler end of the AASIR, no payload operational problems due to the array mounted coil should be expected.

The field at the star tracker locations due to the coil dipole will be about 0.04 gauss. Depending on precise tracker locations, the firing of one full-on torquer bar of 100,000 pole-cm would result in a field of 0.38 gauss at the trackers; for all three torquers it would be as high as 0.66 gauss. The latter are significant magnetic field strength levels for the BBRC CT-401 tracker, having significant impact on accuracy. Tracker tests at MIT [4] have shown that the uncompensated effect of an external magnetic field of 0.4 gauss can produce peak tracker errors of 10 arc-seconds. Thus, the star trackers must either be shielded (difficult, because they must look into space along their optical boresight), or the torquer bars must be turned off whenever the star trackers are being read. The latter is the recommended mode of operation. The residual field from the torquer bars would at most be 9.2×10^{-3} gauss, which combined with the array mounted dipole would create a maximum field of 0.049 gauss at the trackers. This will produce some deterioration in tracker accuracy (linear extrapolation from the MIT test data would suggest about 1 arc-second maximum), but some minimum shielding may eventually render this error insignificant.

7.5 Conclusions

The above investigations have shown that magnetic unloading for StormSat is feasible. Three array mounted coils of 7.4 pounds each, producing a total magnetic moment of 420,000 pole-cm, would be used to cancel the estimated nominal secular solar disturbance torque primarily due to the solar pressure unbalanced spacecraft configuration. The standard ACS module torquer bars, having 100,000 pole-cm capability each, would be used in a closed control loop to remove the residual secular momentum.

Use of a magnetometer for the closed loop operation of the torquer bars poses some problems because of the relatively weak field that must be measured at synchronous altitude in the presence of strong magnetic dipoles located on the spacecraft. It appears that these problems can be overcome if care is exercised in the design and location of the magnetometer. However, serious consideration should be given to deleting the magnetometer entirely, relying solely on the knowledge of the nominal field, and using the RCS for backup unloading during solar storms. The magnetic field of the array mounted coils does not seem to cause any problems for the AASIR or the star trackers.

8. NORTH-SOUTH STATIONKEEPING ANALYSIS

Satellite north-south stationkeeping is the process of periodically removing accumulated errors in the orbit inclination angle. This is done by firing thrusters normal to the orbit plane so as to cause a change in the linear momentum of the spacecraft. This is most efficiently accomplished near the orbit nodes. The purpose of this section is to propose a north-south stationkeeping policy for StormSat. First the nominal requirements are discussed and two possible methods for supplying the necessary ΔV are presented. Propellant consumption and thruster burn times are determined in Section 8.3. Disturbance torques and their effects are studied in 8.4 and the recommended stationkeeping policy is summarized in 8.5.

8.1 Nominal Requirements

The north-south requirements are found by computing the required momentum change at the orbit nodes from the momentum equation

$$\Delta M = m \Delta V = F \Delta T_B \quad (8-1)$$

where $m = 910$ kg is the spacecraft mass, ΔV is the change in velocity along the pitch axis (normal to orbit plane), F is the thrust from the stationkeeping jets and ΔT_B is the time interval over which the thrusters are fired. As shown in Figure 8-1, the change in orbit inclination is related to ΔV by

$$\Delta V = R \omega_o \Delta \theta_i \quad (8-2)$$

where $R = 4.224 \times 10^7$ m is the orbit radius and $\omega_o = 15$ degrees/hour is the orbit rate. Combining Equations (8-1) and (8-2) yields:

$$\Delta M = m R \omega_o \Delta \theta_i = F \Delta T_B \quad (8-3)$$

The orbit inclination angle changes due to natural phenomena, primarily luni-solar gravitational effects, and its rate of change reaches

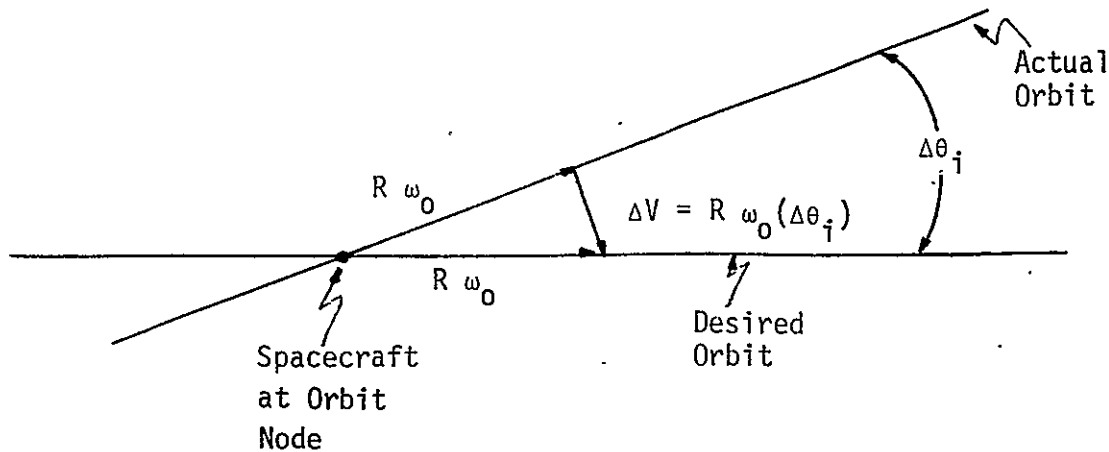


Figure 8-1. North-South Stationkeeping

a peak of $\dot{\theta}_i = 0.936$ degree/year. This peak rate will next occur in 1986, but assuming conservatively that $\dot{\theta}_i$ is constant at that maximum value, the rate at which north-south stationkeeping momentum must be supplied is

$$\frac{\Delta M}{\Delta t} = \frac{m R \omega_0 \Delta \theta_i}{\Delta t} = m R \omega_0 \dot{\theta}_i = 125. \frac{\text{N sec}}{\text{day}} \quad (8-4)$$

As an example, this could be accomplished by firing a 0.2 pound thruster for 140 seconds every day.

Another approach is to observe the error and start the stationkeeping procedure when that error reaches a preselected value, θ_{DZ} . The amount of momentum needed to remove that error is found from (8-3) to be

$$\Delta M = F \Delta T_B = m R \omega_0 \theta_{DZ} = 4.887 \times 10^4 \theta_{DZ} \text{ N sec} \quad (8-5)$$

where θ_{DZ} is measured in degrees. Thus the necessary momentum is $\Delta M/\theta_{DZ} = 4.887 \times 10^4$ N second/degree and the error builds up in a period of 390 days per degree of error.

8.2 Use of 0.2 Pound Thrusters

The available spacecraft thrusters and their locations are shown in Figure 8-2. One potential method for obtaining the required ΔV for north-south stationkeeping is to use the 0.2 pound thrusters, numbers 7, 10, 13, or 5, 2, 15, depending at which orbit node the ΔV corrections are made; this would yield 0.6 pound of thrust. The thrusters could also be fired in pairs, that is 7 and 13 or 5 and 15, yielding 0.4 pound of thrust; or individually, that is numbers 2 or 10, yielding 0.2 pound of thrust. But as can be seen from Figure 8-2, use of these thrusters for stationkeeping will also impart a significant yaw torque since the thrusters are offset from the center of mass of the spacecraft. The associated moment arm is 50.6 inches with the MASR included as part of the payload, and 45.7 inches without the MASR, based on a 1700 pound spacecraft plus 200 pounds for the AASIR and 100 pounds for the MASR.

Originally the idea was to use a low level thrust of 0.2 pound twice per day at each nodal crossing, continue to control spacecraft attitude with the reaction wheels, and absorb the resulting yaw disturbance momentum in the yaw wheel. This momentum was to be stored in the reaction wheels for 12 hours until firing at the opposite node would automatically remove it again. This would have avoided all-thruster attitude control during stationkeeping and unnecessary wheel unloadings. Stationkeeping interference with normal spacecraft operations would also have been minimized.

Unfortunately, this method of north-south stationkeeping does not work. Firstly, when firing ΔV thrust at the opposite node, opposite thrusters must also be used, i.e., at one node ΔV is directed along the positive pitch (+y) axis, at the other node it is directed along the negative pitch (-y) axis. Thus a positive yaw disturbance torque is imparted at one node and a negative yaw disturbance torque at the other. But angular momentum remains fixed in inertial space so that the disturbance momentum absorbed in positive yaw at the ascending node, turns out to be stored in negative yaw 180 degrees later at the descending node. Incurring at that time a negative yaw disturbance torque due to ΔV thrusting would, therefore, not remove the momentum but rather compound the

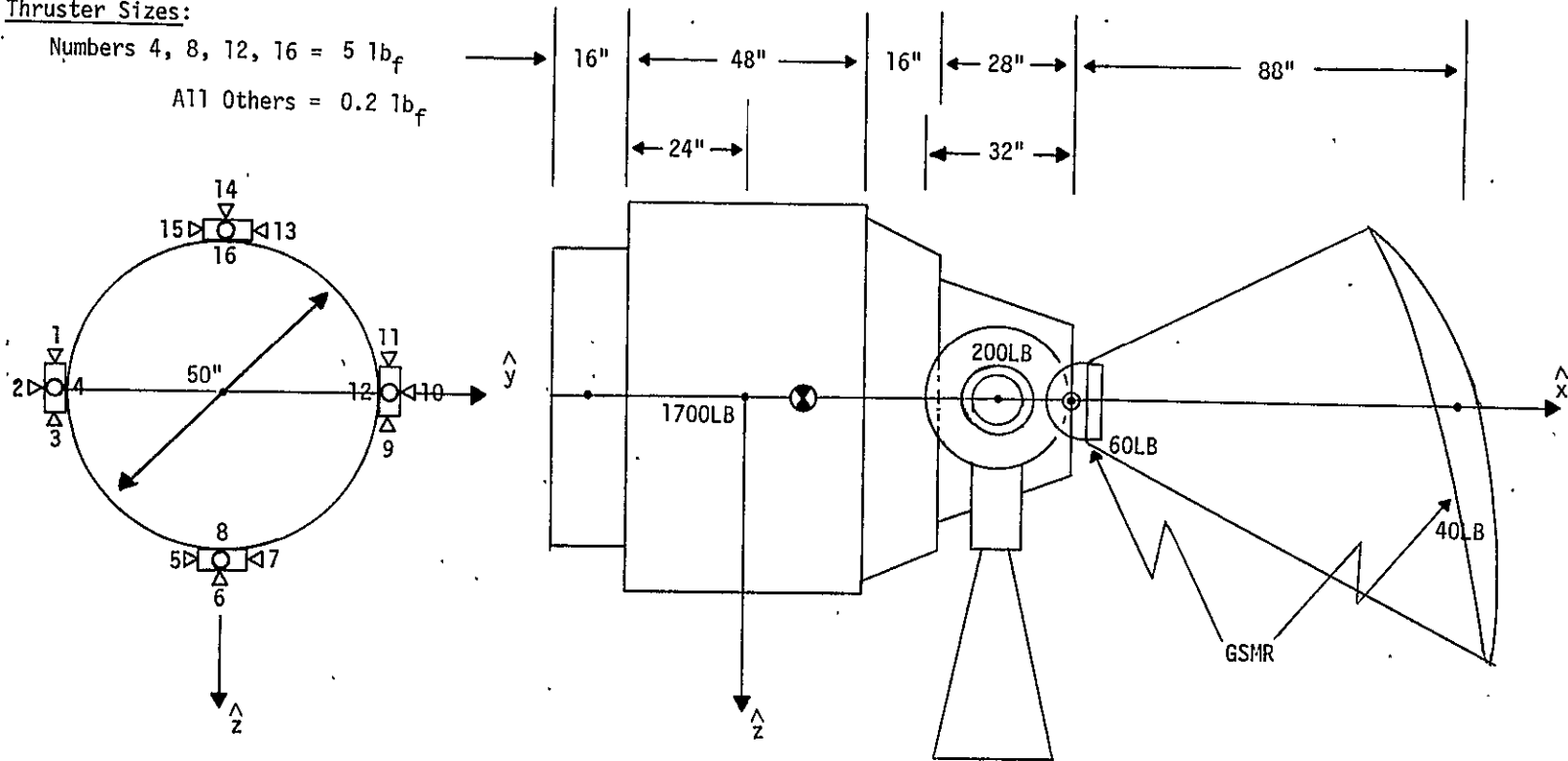
Thruster Sizes:Numbers 4, 8, 12, 16 = 5 lb_f All Others = 0.2 lb_f 

Figure 8-2. Two View of Spacecraft Showing Mass Distribution and Thruster Positioning

problem, i.e., even more momentum would have to be stored in yaw. The idea of avoiding separate yaw unloading thruster firings is, therefore, unworkable.

Secondly, even if one were willing to unload the absorbed yaw momentum, little by little over a 12 hour period without interfering with normal on-orbit spacecraft operations, the scheme of using the 0.2 pound thrusters for north-south stationkeeping still does not work since the standard MMS reaction wheels (even if the fourth skewed wheel is included) cannot store sufficient momentum. For the nominal stationkeeping requirements derived above, it follows that a 0.2 pound thruster would have to be fired for 70 seconds every 12 hours when crossing the nodes. This would impart a minimum yaw momentum (no MASR) of

$$\Delta H_z = (0.2) (45.7/12) (70) = (53.4 \text{ ft-lb-sec}) = 72.4 \text{ Nms (8-6)}$$

This is much too large a momentum in view of the capacity of 20 Nms (15 foot-pound-second) per wheel). The idea of using the 0.2 pound thrusters for north-south stationkeeping must, therefore, be abandoned.

8.3 Use of 5 Pound Thrusters

In order to use the 5 pound orbit adjust thrusters for north-south stationkeeping the spacecraft must be rotated 90 degrees about its yaw axis. Referring to Figure 8-2, there are four 5 pound orbit adjust thrusters, namely thrusters 4, 8, 12 and 16. As long as all four thrusters are fired simultaneously, or they are fired in pairs (4 and 12 or 8 and 16), a nominally balanced thrust is obtained and no large angular disturbance momentum is imparted to the spacecraft. The direction of the 90 degree reorientation about yaw depends on the orbit node at which firing will occur. The spacecraft rotation is done using the yaw reaction wheel, so the only propellant required will be for the actual orbit adjust thruster firing, and subsequent removal of attitude errors. The nominal propellant mass requirement to deliver a linear momentum M is given by

$$P = \frac{M}{g \times I_{sp}} \quad (8-7)$$

where $I_{sp} = 220$ pound_f-second/pound_m is the specific impulse associated with the thruster. At the momentum rate shown in (8-4)

$$P = \frac{(365)(125 \text{ N sec/day})}{(9.8 \text{ m/sec}^2)(220 \text{ sec})} = 21.2 \text{ kg/yr (46.6 lb}_m\text{/yr)}$$

is the nominal rate of propellant consumption for north-south station-keeping.

The necessary thruster burn times depend on the number of thrusters fired (2 or 4) and the amount of error that must be removed which is inversely proportional to the time interval between firings. Three intervals will be considered: (i) every 12 hours, (ii) whenever $\theta_{DZ} = 0.01$ degree, and (iii) whenever $\theta_{DZ} = 0.10$ degree. Depending on whether two or four thrusters are fired, the thrust is 10 pounds or 20 pounds, respectively. The burn times for the six cases are summarized in Table 8-1. The largest of the burn times $\Delta T_B = 110$ seconds corresponds to firing over an orbit angle of 0.46 degree.

To obtain the total time for a stationkeeping maneuver, the time required to rotate the spacecraft 90 degrees and then back again must be computed. If a constant wheel torque is used to accelerate the spacecraft, and an equal but opposite wheel torque is later used to stop it, the maximum rotation rate is determined either by the available wheel momentum (20 Nms) or by the torque that is applied. Assuming that the maximum available momentum is not the limiting factor, the spacecraft acceleration time interval Δt_a lasts for half the maneuver and can be computed from

$$\Delta t_a = \sqrt{\frac{I_{zz} \Delta \psi}{T_{RW}}} \quad \text{if } T_{RW} \Delta t_a < 20 \text{ Nms}$$

where $\Delta \psi = \pi/2$ is the total yaw reorientation, $I_{zz} = 407 \text{ kg-m}^2$ (300 slug-ft²) is the largest expected yaw inertia (see Reference 2), and

Table 8-1. Nominal Thruster Firing Times

Nominal Thrust Level (lb)	Nominal Burn Time, ΔT_B (sec)		
	$\theta_{DZ} = 0.00128$ deg (Every 12 hrs)	$\theta_{DZ} = 0.01$ deg (Every 3.9 days)	$\theta_{DZ} = 0.10$ deg (Every 39 days)
10	1.40	11.0	110.0
20	0.70	5.5	55.0

and $T_{RW} = 0.15$ Nm (21.2 ounces-inch) is the maximum available reaction wheel torque. It follows that a torque of 0.15 Nm applied for $\Delta t_a = 65.3$ seconds would bring the rotation angle to 45 degrees and change the wheel momentum by 9.8 Nms which is well within the wheel capacity. This torque pulse would be followed by an equal and opposite pulse to bring the spacecraft to rest with a net rotation of 90 degrees in 130.6 seconds. The minimum total time for maneuvering back and forth is thus 261.2 seconds. To obtain the total time spent on one north-south stationkeeping maneuver the time of ΔV thrusting must be added to the total spacecraft reorientation time. Table 8-2 summarizes the time spent per stationkeeping maneuver. Note that the time spent is about the same with four thrusters as with two thrusters, because the time spent rotating the spacecraft is large compared to the burn time. The time spent in stationkeeping per unit of mission time is minimized by increasing the time interval between maneuvers, i.e., allowing $\theta_{DZ} = 0.1$ degree.

If the MASR is included, I_{zz} increases and is given by

$$I_{zz} = 752 \text{ kg m}^2 \text{ (554.6 slug-ft}^2\text{)}$$

This inertia could be rotated 90 degrees using the 0.15 Nm torque from the yaw reaction wheel in 177.5 seconds. Maneuvering back and forth would then take 355 seconds, almost 6 minutes.

Table 8-2. Minimum Time Spent per Stationkeeping Maneuver

Nominal Thrust Level (lb)	Stationkeeping Time (sec)		
	$\theta_{DZ} = 0.00128$ deg (Every 12 hrs)	$\theta_{DZ} = 0.01$ deg (Every 3.9 days)	$\theta_{DZ} = 0.10$ deg (Every 39 days)
10	262.6	272.2	371.2
20	261.9	266.7	316.2

8.4 Stationkeeping Disturbance Torques

Due to uncertainties in the location of the spacecraft center of mass and in the thruster magnitude and alignment, torques are exerted on the spacecraft by the stationkeeping thrusters. These torques cause angular momentums to be added to the system and they must be removed.

The location vector of the i^{th} thruster in body coordinates is represented by \bar{x}_{Ti} . The vector \bar{x}_{cm} represents the location of the true center of mass: its elements are assumed to have 3σ variations of 0.0125 m (0.5 inch) and it is nominally 0.145 m (5.7 inches) from the origin along the \hat{x} axis, see Figure 8-2. Each thruster is nominally aligned with the \hat{x} axis with a 3σ angular misalignment of 1.75×10^{-3} rad (0.1 degree) about the \hat{y} and \hat{z} axes. The thrust uncertainty δF is assumed to be 20 percent, 3σ , and the thruster location uncertainty is assumed to be zero. These assumptions result in the following vectorial means and standard deviations:

$$\bar{\mu}_{cm} = \begin{bmatrix} 0.145 \\ 0 \\ 0 \end{bmatrix}, \quad \bar{\sigma}_{cm} = \frac{0.0125}{3} \begin{bmatrix} 1 \\ 1 \\ 1 \end{bmatrix} \quad (8-8)$$

$$\bar{\mu}_{\epsilon} = \bar{0}, \quad \bar{\sigma}_{\epsilon} = \frac{1.75 \times 10^{-3}}{3} \begin{bmatrix} 0 \\ 1 \\ 1 \end{bmatrix} \quad (8-9)$$

$$\mu_{\delta F} = 0, \quad \sigma_{\delta F} = \frac{1}{3} (0.20) \quad (8-10)$$

$$\bar{\mu}_T = \bar{l}_T, \quad \bar{\sigma}_T = \bar{0} \quad (8-11)$$

where $\bar{\mu}$ denotes the mean and $\bar{\sigma}$ denotes the standard deviation, and the subscripts cm, ϵ , δF and T refer to the center of mass, thruster alignment error, thrust magnitude and thruster location, respectively.

Assuming a pair of thrusters is used and each has nominal thrust F, it can be shown that the normalized mean of the torque vector is

$$\frac{\bar{\mu}_T}{F} = \begin{bmatrix} 0 \\ -(l_{Tz1} + l_{Tz2}) \\ (l_{Ty1} + l_{Ty2}) \end{bmatrix} = \bar{0} \quad (8-12)$$

as long as the two thrusters are nominally mirrored about the \hat{x} axis. The normalized thrust variance is given by

$$\frac{\bar{\sigma}_T^2}{F^2} = \begin{bmatrix} 2 l_{Ty}^2 \sigma_{\epsilon y}^2 + 2 l_{Tz}^2 \sigma_{\epsilon z}^2 \\ 2 (l_{Tx} - \mu_{cmx})^2 \sigma_{\epsilon y}^2 + 2 l_{Tz}^2 \sigma_{\delta F}^2 + 4 \sigma_{cmz}^2 \\ 4 \sigma_{cmy}^2 + 2 (l_{Tx} - \mu_{cmx})^2 \sigma_{\epsilon z}^2 + 2 l_{Ty}^2 \sigma_{\delta F}^2 \end{bmatrix} \quad (8-13)$$

where the square of the vector implies that each of its elements has been squared. Depending on which pair of thrusters is used, either

$$\bar{x}_T = \begin{bmatrix} -1.016 \\ 0 \\ \pm 0.635 \end{bmatrix} \text{ m}, \quad \text{or} \quad \bar{x}_T = \begin{bmatrix} -1.016 \\ \pm 0.635 \\ 0 \end{bmatrix} \text{ m}$$

Using the first of these thruster pairs (8 and 16)

$$\frac{\bar{\sigma}_T}{F} = \begin{bmatrix} 0.00058 \\ 0.06688 \\ 0.00840 \end{bmatrix} \text{ m}$$

and using the second pair of thrusters (4 and 12)

$$\frac{\bar{\sigma}_T}{F} = \begin{bmatrix} 0.00058 \\ 0.00840 \\ 0.06688 \end{bmatrix} \text{ m}$$

The major contribution to the 0.06688 m elements is thrust level uncertainty due to the 1.3 m thruster separation.

If all four of the five pound thrusters are used for stationkeeping, the disturbance torque vector can be formed by RSS'ing the normalized torque vectors given above, to get

$$\frac{\bar{\sigma}_T}{F} = \begin{bmatrix} 0.00082 \\ 0.06741 \\ 0.06741 \end{bmatrix}$$

Note that the \hat{y} and \hat{z} components are only slightly larger than the 0.06688 m elements resulting from using one pair of thrusters. The increased level of disturbance torque that must be present with the increased thrust level is manifested in two large components instead of only one. Table 8-3 lists the disturbance torques and associated disturbance momentum in spacecraft body coordinates corresponding to a nominal thrust of $F = 22.25 \text{ N}$ (5 pounds).

Table 8-3. Disturbance Torques and Momentum in Body-Fixed Coordinates due to North-South ΔV

Thrusters Fired (Numbers refer to Figure 8-2)	Nominal Thrust Obtained (N)	Body Disturbance Torques (1σ)* (Nm)	Angular Disturbance Momentum per N-S ΔV Burn (Nms)		
			$\theta_{DZ} = 0.00128$ deg (Every 12 hours)	$\theta_{DZ} = 0.01$ deg (Every 3.9 days)	$\theta_{DZ} = 0.1$ deg (Every 39 days)
4 and 12	44.5 (10 1b)	$T_x = 0.013$ $T_y = 0.187$ $T_z = 1.49$	Burn Time = 1.4 sec $H_x = 0.0182$ $H_y = 0.262$ $H_z = 2.086$	Burn Time = 11 sec $H_x = 0.143$ $H_y = 2.057$ $H_z = 16.39$	Burn Time = 110 sec $H_x = 1.43$ $H_y = 20.57$ $H_z = 163.9$
8 and 16	44.5 (10 1b)	$T_x = 0.013$ $T_y = 1.49$ $T_z = 0.187$	Burn Time = 1.4 sec $H_x = 0.0182$ $H_y = 2.086$ $H_z = 0.262$	Burn Time = 11 sec $H_x = 0.143$ $H_y = 16.39$ $H_z = 2.057$	Burn time = 110 sec $H_x = 1.43$ $H_y = 163.9$ $H_z = 20.57$
4, 8, 12, 16	89.0 (20 1b)	$T_x = 0.018$ $T_y = 1.5$ $T_z = 1.5$	Burn Time = 0.7 sec $H_x = 0.013$ $H_y = 1.05$ $H_z = 1.05$	Burn Time = 5.5 sec $H_x = 0.099$ $H_y = 8.25$ $H_z = 8.25$	Burn Time = 55 sec $H_x = 0.99$ $H_y = 82.5$ $H_z = 82.5$

*Note that the spacecraft has been reoriented such that the roll-axis (\hat{x} -axis) is normal to the orbit plane with yaw (\hat{z} -axis) still pointing at nadir

As can be seen, the dominant disturbance torque of about 1.5 Nm exceeds the nominal wheel torque of 0.15 Nm by an order of magnitude. However, if stationkeeping is performed every 12 hours, the thrusters are fired for only a very short time interval (1.4 or 0.7 second), and only about 2 Nms of momentum need be absorbed by the reaction wheels. The thruster disturbance can be preemphasized by applying 0.15 Nm of opposing wheel torque for a period of ten times the thruster firing interval; the thruster pulse is centered within this period. The vehicle disturbance can then be held to about 0.5 degree of attitude error if one pair of thrusters is used, or to 0.13 degree (in two spacecraft axes) if four thrusters are used. This is acceptable and preferred over all-thruster attitude control during stationkeeping. The fact that it violates the pointing accuracy and stability requirements for StormSat is of no concern, since during stationkeeping no payload data will be acquired.

If stationkeeping is performed every 3.9 days ($\theta_{DZ} = 0.01$ degree), then the firing times of 11 seconds or 5.5 seconds and the associated disturbance momentum are too large to be handled by the reaction wheels and all-thruster attitude control during stationkeeping is required; the 0.2 pound thruster would be used for this with one pair of thrusters being able to deliver about 2 Nm of torque. The only possibility of using the reaction wheels for attitude control during stationkeeping would be to break up the ΔV pulse into a train of shorter pulses, allowing time for attitude settling between the pulses. This would further increase the time interval required for stationkeeping (when no useful payload data can be taken), which is already long (see Table 8-2) because of the required reorientation of the spacecraft. When stationkeeping is performed every 39 days, the entries in Table 8-3 clearly indicate that all-thruster attitude control is needed.

Irrespective of how attitude control is accomplished during stationkeeping, the imparted angular momentum must eventually be unloaded. Even if magnetic unloading would be provided for StormSat, the magnetic field is too weak at synchronous altitude to be able to unload the stationkeeping momentum in addition to the momentum accumulated due to solar

disturbance torque (see Section 7.0 for details on magnetic unloading for StormSat). Thus, thrusters must be used to unload this momentum and additional propellant is required. From Table 8-3, it follows that the angular momentum that must be removed may be as large as 1550 Nms/year which corresponds to a propellant mass of

$$m_p = \frac{H/\ell}{g \times I_{sp}} = \frac{1550/1.16}{9.81 \times 220} = 0.62 \text{ kg/yr (1.4 lb}_m\text{/yr)}$$

when 100% unloading efficiency is assumed. It is a relatively insignificant amount of propellant. Assuming only 50% unloading efficiency, 1.24 kg are added to the previous propellant budget, yielding a total propellant estimate for north-south stationkeeping of

$$P_{tot} = 22.5 \text{ kg/yr}$$

8.5 Recommended Stationkeeping Policy

Based on the preceeding results, it is recommended that when the orbit inclination angle error reaches 0.1 degree, north-south stationkeeping be performed with the four 5 pound thrusters shown as (4, 8, 12, 16) in Figure 8-2. The spacecraft is rotated 90 degrees about its yaw axis (\hat{z} -axis) before firing the stationkeeping pulse, with the direction of rotation depending on the location in orbit (at which node). This can be done by applying a 0.15 Nm torque with the yaw reaction wheel for 65.3 seconds and following it immediately with an equal and opposite torque for an equal amount of time. Once the spacecraft is rotated, the four thrusters can be fired for a 55 second period centered at the orbit node. Simultaneously, the momentum resulting from any disturbance torques must be removed; this will require the use of the 0.2 pound pitch and yaw torque thrusters for attitude control and momentum unloading (the vehicle roll momentum can be stored in the reaction wheel temporarily, if necessary). With the stationkeeping firing completed, the yaw reaction wheel is used to rotate the spacecraft through 90 degrees back to its original orientation.

Should a 0.1 degree orbit inclination error be too large for StormSat, then unloading every 12 hours using all four 5 pound thrusters is recommended. Attitude control can then be maintained with the reaction wheels. The orbit inclination error would be kept below 0.0013 degree.

9. MICROWAVE ATMOSPHERIC SOUNDING RADIOMETER (MASR)

A second payload may be flown on Stormsat in addition to the AASIR, namely the Microwave Atmospheric Sounding Radiometer (MASR), formerly called Geosynchronous Sounding Microwave Radiometer [5]. The MASR field of view (FOV) corresponds to a beamwidth of either 0.8 or 1.3 mrad. Using a double gimballed microwave antenna reflector a frame can be traced out on the earth by rotating the reflector north-south for scanning out lines, and by stepping it east-west by one FOV width (beamwidth) at the end of each line. The spacecraft must act as a base or platform for both the AASIR and the MASR and scanning and stepping motions of either payload will cause a reaction by the spacecraft, which in turn causes attitude perturbations in the other payload. This section investigates the dynamic interaction between the spacecraft and the two payloads, examining primarily the dynamic effects of a scanning and stepping MASR on the pointing stability of the AASIR. Possible solutions to the dynamic interaction problem are presented, and the overall feasibility of flying the MASR on Stormsat in addition to the AASIR is assessed. Figure 9-1 shows a sketch of a Stormsat carrying both payloads. Basic geometry and mass distribution are indicated. All MASR data is based on Reference 5.

9.1 Requirements For Spacecraft Pointing and Payload Control

For the purposes of this study, the StormSat ACS is assumed to be a linear second-order control system with a damping ratio of 0.7 and a natural frequency of 0.5 rad/sec; the damping ratio may be as low as 0.3, but 0.7 is used because it yields more conservative results. The AASIR stepping compensator is assumed to be as described in Reference 2.

The normal frame size of the MASR is 1500 km x 1500 km. An alternate frame size is the full earth coverage frame of 18 degrees subtended angle which is used only with the 1.3 mrad FOV. Eighty percent of the time is used for line scanning (data acquisition) and the remaining 20 percent of the time is used for scan turn-around and line stepping. The required frame scan times are 30 minutes for the 1500 km frame and six hours for the full earth coverage frame.

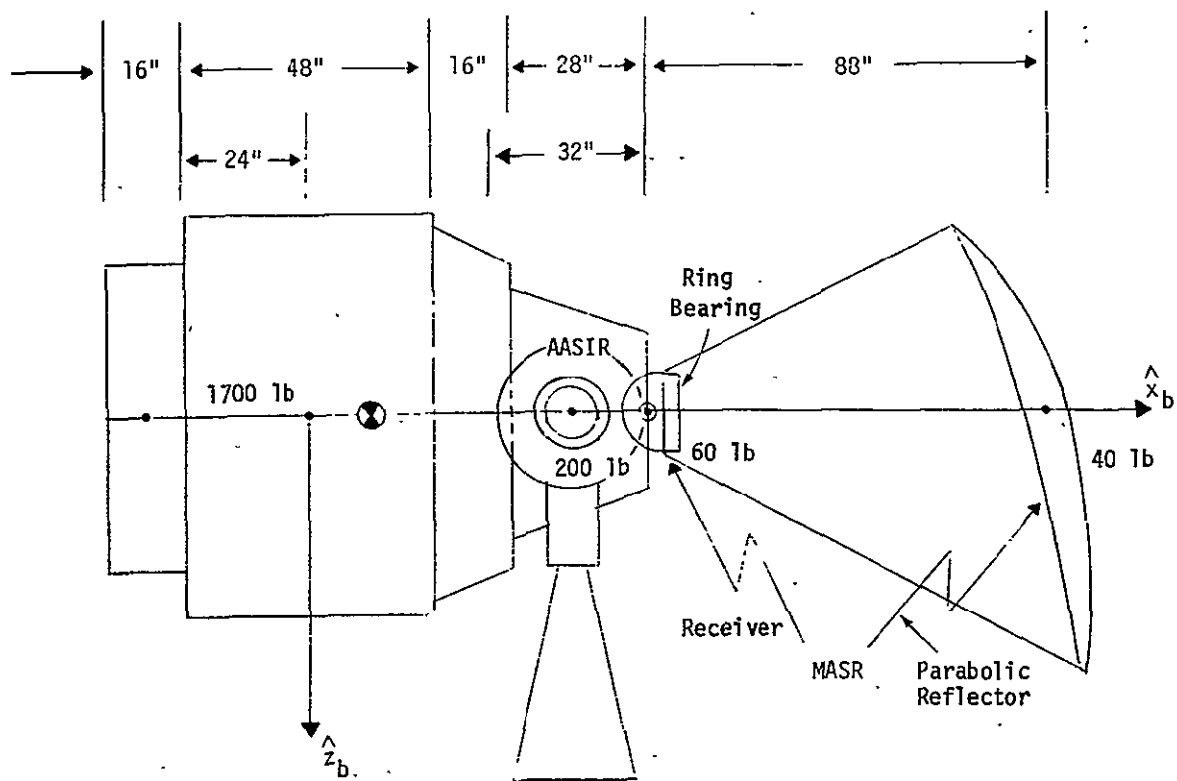


Figure 9-1. View of Spacecraft Showing MASR Location

There are two potential MASR configurations proposed in Reference 5; each has a parabolic reflector to collect the radiation and focus it on the horn. In the first configuration, the parabolic reflector is caused to scan back-and-forth and step at the end of each scan; in the second configuration, the parabolic reflector is stationary and a flat mirror is scanned and stepped so as to reflect the incident radiation onto the parabolic reflector. These two MASR configurations along with the options in beamwidth and frame size result in six different systems to investigate. In addition, there are two motions to control--line scanning and stepping--leaving 12 different control systems to include in this study. These 12 systems are shown in Figure 9-2.

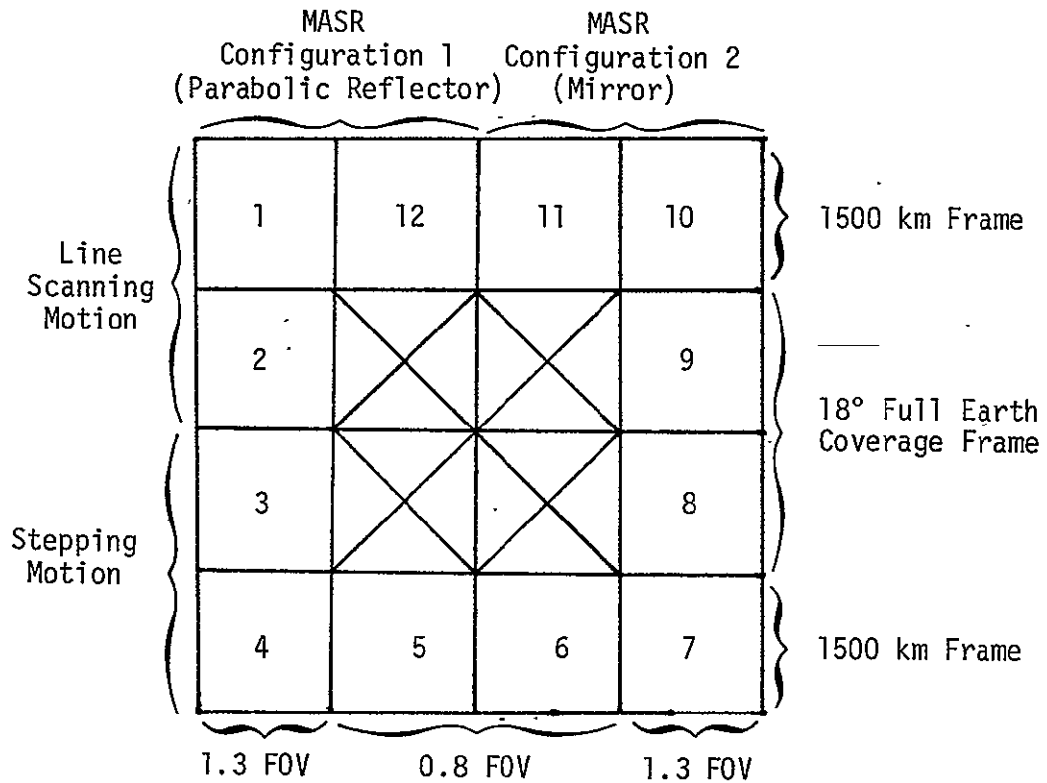


Figure 9-2. The 12 Control Systems Included in This Study

The various stepping and scanning requirements can be reduced to system response requirements by determining the scan slew rate, the turn-around time and the step size for each of the six systems. For example, in the case of the full earth scan, the 18 degree frame can be scanned by approximately 240 lines with the 1.3 mrad FOV. Since six hours are allowed for the frame scan, this leaves 90 seconds for each line; and at the rate of 18 degrees in 80% of that time, the required slew rate is 4.36 mrad/second. The turn-around time is 20% of the 90 seconds or 18 seconds, and the step size is the FOV size, 1.3 mrad. This information is summarized for the three cases in Table 9-1.

Table 9-1. System Requirements

FOV Size (mrad)	0.8	1.3	1.3
Frame Size	1500 km	1500 km	18 deg
Step Size (mrad)	0.8	1.3	1.3
Lines/Frame	50	32	240
Line Scan Time (sec)	36	56.25	90
Slew Rate (mrad/sec)	1.39	0.92	4.36
Turn-Around and Line Step Time (sec)	7.2	11.25	18.0
Scan Reversal Acceleration (mrad/sec ²)	0.386	0.164	0.485

The final requirement is pointing accuracy. The AASIR must scan while maintaining a pointing stability of 11 μ rad over 20 minutes and 4.2 μ rad over 64 seconds. It was assumed in this study that these requirements can be met if the spacecraft pointing stability is better than 2 μ rad in both roll and pitch. The MASR accuracy has not been specified, the assumed requirement in this study was taken as one-tenth of the beamwidth--i.e., ± 0.13 mrad or ± 0.08 mrad.

9.2 System Parameters

Some of the system parameters were given in References 2 and 5, but some also had to be estimated. The main item which was estimated in this study was the mass distribution of the MASR and thus the inertias. MASR configuration 1 has the moving parabolic reflector and is sketched in Figure 9-3 for scanning at nadir, where the stepping motion is a rotation about an axis parallel to the y-axis and the line scanning motion is a rotation about the x-axis. The mass of the spacecraft, excluding the MASR, is 800 kg, (1750 lb); 18 kg (40 lb) was used as the mass of the reflector, and 28 kg for the receiver electronics and horn.

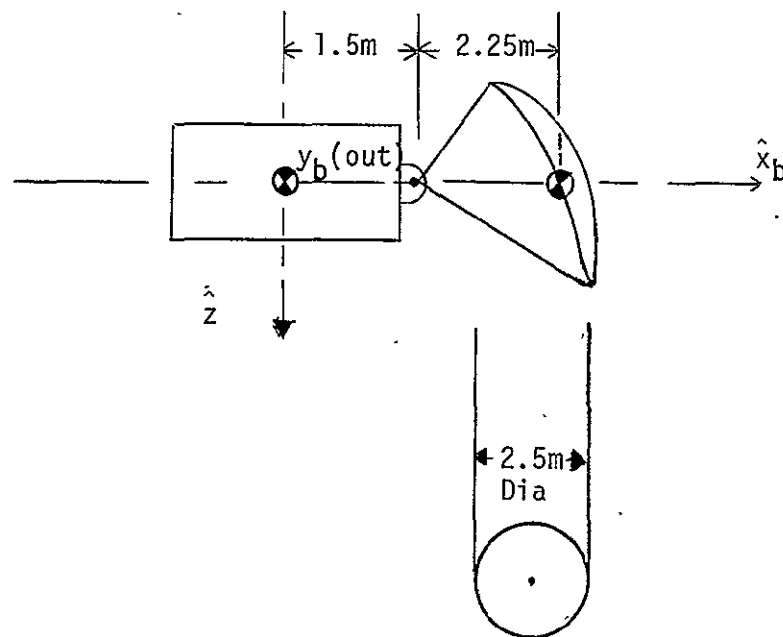


Figure 9-3. MASR Configuration 1

It was assumed that the \hat{x} , \hat{y} , and \hat{z} axes are the principal axes of the spacecraft, and that their moments of inertia I_{xx} and I_{yy} are each 325 kg m^2 (240 slug ft^2)--these are conservative numbers. In order to estimate the MASR inertias, it was assumed that the reflector is a flat elliptical plate tilted at 45 degrees to the \hat{x} - \hat{y} plane so as to provide a circular projection onto the \hat{x} - \hat{y} plane. It was also assumed that the reflector rotates about an axis through its center of mass--CM--for line scanning. Then its inertia I_{xx}^R is found by using the equation for a circular disc:

$$I_{xx}^R = \frac{1}{2} m r^2 = 14.06 \text{ kg m}^2, \quad (9.1)$$

where $m = 18 \text{ kg}$ and $r = 1.25 \text{ m}$;

the inertia used in the analysis is 15 kg m^2 . The inertia I_{yy}^R is found by using the equation for an elliptical disc:

$$I_{yy}^R = \frac{1}{4} m a^2 = 14.06 \text{ kg m}^2, \quad (9.2)$$

where $m = 18 \text{ kg}$ and $a = \frac{1.25}{\sin 45^\circ} \text{ m}$; the inertia used in the analysis is 15 kg m^2 .

Configuration 2 with a scanning mirror and fixed reflector is sketched in Figure 9-4.

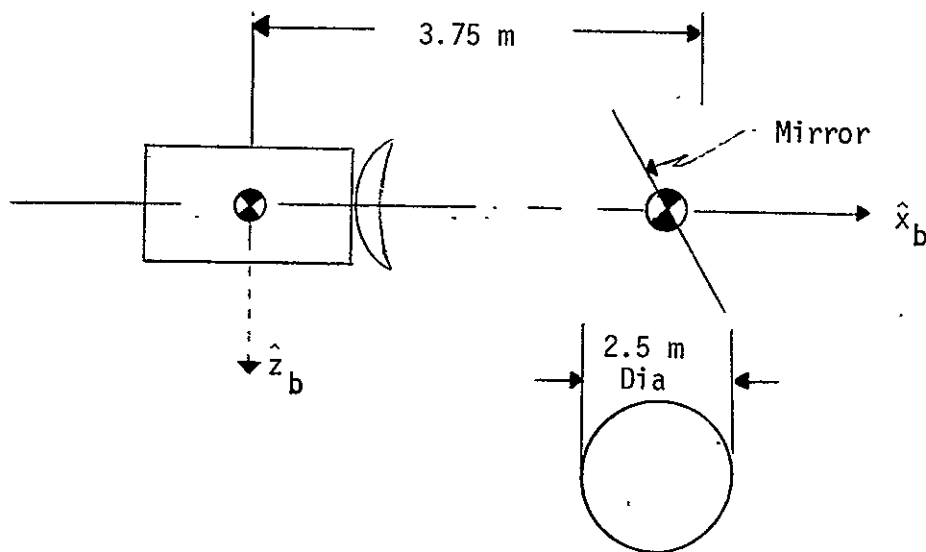


Figure 9-4. MASR Configuration 2

The spacecraft mass properties are assumed to be the same as in Configuration 1; this payload rotates about its CM in both motions and has a mirror mass of 36 kg. Thus I_{xx}^R and I_{yy}^R are double those of Configuration 1, namely 30 kg m^2 . In addition, the receiver and horn are mounted stationary at the mirror center and have a mass of 28 kg. The total payload mass used in the analysis is 64 kg. The mass properties and dimensions for the two configurations are summarized in Table 9-2. Note that in configuration 1 the receiver steps with the parabolic antenna but is rigidly attached to the spacecraft in configuration 2; this means that the receiver's self inertia is part of the payload inertia in configuration 1 only. But, assuming the receiver is a sphere with $D = 0.5 \text{ m}$ and $m = 23 \text{ kg}$, this self inertia is only 0.7 kg m^2 and is ignored in the analysis.

9.3 Dynamic Equations

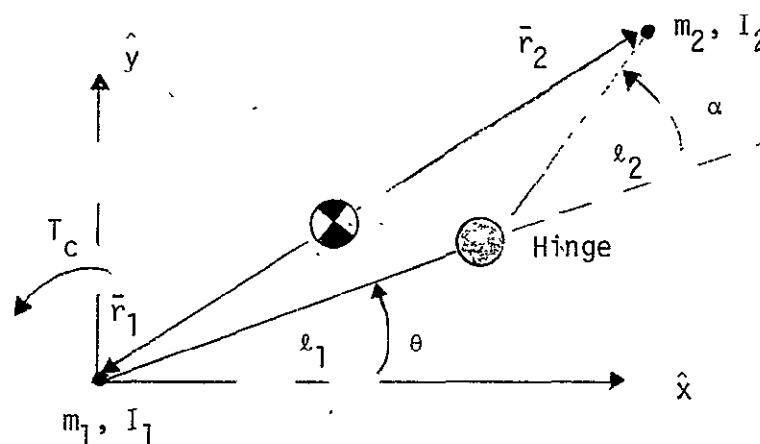


Figure 9-5. Physical Model for Analysis

Table 9-2. System Parameters Used in the Analysis

	Configuration 1 (Moving Reflector)	Configuration 2 (Moving Mirror)
Spacecraft Mass (kg)	800	800
Payload Mass (kg)	46	64
Spacecraft Inertia, I_{xx} (kg m ²)	325	325
Spacecraft Inertia, I_{yy} (kg m ²)	325	325
Payload Inertia, I_{xx} (kg m ²)	15	30
Payload Inertia, I_{yy} (kg m ²)	15*	30
Spacecraft cm From Hinge Point (m)	1.5	3.75
Payload cm From Hinge Point (m)	2.25*	0

*Reflector only

The physical model of the system shown in Figure 9-5--note that the coordinate system shown does not necessarily coincide with that shown in Figures 9-3 and 9-4 -- is valid for either configuration and for scanning or stepping. In the figure, body 1 is the spacecraft and body 2 is the MASR payload; also, T_c is the vehicle control torque and θ is the spacecraft pointing error in the plane shown.

Since translation of the bodies is not of interest in the analysis, only two equations need to be used. The first is found by setting the torque T_c equal to the derivative of the total system momentum:

$$T_c = \dot{\bar{H}}_T, \quad (9.3)$$

where:

$$\dot{\bar{H}}_T = \bar{H}_1 + \bar{H}_2 + \left[I_1 \dot{\theta} + I_2 (\dot{\theta} + \dot{\alpha}) \right] \hat{z}, \quad (9.4)$$

where \bar{H}_1 and \bar{H}_2 are the momentum components of the two bodies due to motion of the masses. These are given by:

$$\bar{H}_1 = m_1 \bar{r}_1 \times \bar{v}_1 = m_1 \bar{r}_1 \times \dot{\bar{r}}_1, \quad (9.5)$$

and

$$\bar{H}_2 = m_2 \bar{r}_2 \times \dot{\bar{r}}_2. \quad (9.6)$$

The vectors \bar{r}_1 and \bar{r}_2 can be found from:

$$\bar{r}_{12} = \bar{r}_2 - \bar{r}_1 = [\theta]_z \left\{ \ell_1 \hat{x} + \ell_2 [\alpha]_z \hat{x} \right\}, \quad (9.7)$$

where the notation $[\beta]_{\hat{z}} \hat{x}$ means the vector obtained by rotating the \hat{x} unit vector through the angle β about the \hat{z} -axis. Since the cm location is defined by the relation:

$$m_1 \bar{r}_1 + m_2 \bar{r}_2 = \bar{0}, \quad (9.8)$$

the position vectors are given by:

$$\bar{r}_1 = - \frac{m_2}{m_1 + m_2} \bar{r}_{12}, \quad (9.9)$$

and

$$\bar{r}_2 = \frac{m_1}{m_1 + m_2} \bar{r}_{12}. \quad (9.10)$$

Thus,

$$\begin{aligned} \bar{H}_1 + \bar{H}_2 &= \frac{m_1 m_2}{m_1 + m_2} \bar{r}_{12} \times \dot{\bar{r}}_{12} \\ &= \frac{m_1 m_2}{m_1 + m_2} \left[\ell_1^2 \dot{\theta} + \ell_2^2 (\dot{\theta} + \dot{\alpha}) + \ell_1 \ell_2 (2\dot{\theta} + \dot{\alpha}) \cos \alpha \right] \hat{z} \end{aligned} \quad (9.11)$$

Combining Equations (9.3) and (9.11) yields:

$$\begin{aligned} T_c &= \left[I_1 + I_2 + \frac{m_1 m_2}{m_1 + m_2} \left(\ell_1^2 + \ell_2^2 + 2\ell_1 \ell_2 \cos \alpha \right) \right] \ddot{\theta} \\ &\quad + \left[I_2 + \frac{m_1 m_2}{m_1 + m_2} \left(\ell_2^2 + \ell_1 \ell_2 \cos \alpha \right) \right] \ddot{\alpha} \\ &\quad - \frac{m_1 m_2}{m_1 + m_2} \ell_1 \ell_2 (2\dot{\theta} + \dot{\alpha}) \dot{\alpha} \sin \alpha \end{aligned} \quad (9.12)$$

The second equation is obtained from body 2 alone; the variables are shown in Figure 9-6. T_m is the torque applied to body 2 at the hinge to obtain either scanning or stepping; F_h is the force applied to body 2 at the hinge and is given by:

$$F_h = m_2 \ddot{r}_2 = \frac{m_1 m_2}{m_1 + m_2} \ddot{r}_{12}. \quad (9.13)$$

The torque equation, similar to (9-3), is:

$$\bar{T}_m + \bar{r}_h \times \bar{F}_h = \frac{d}{dt} [\bar{H} + I_2 (\dot{\theta} + \dot{\alpha})] \hat{z}. \quad (9.14)$$

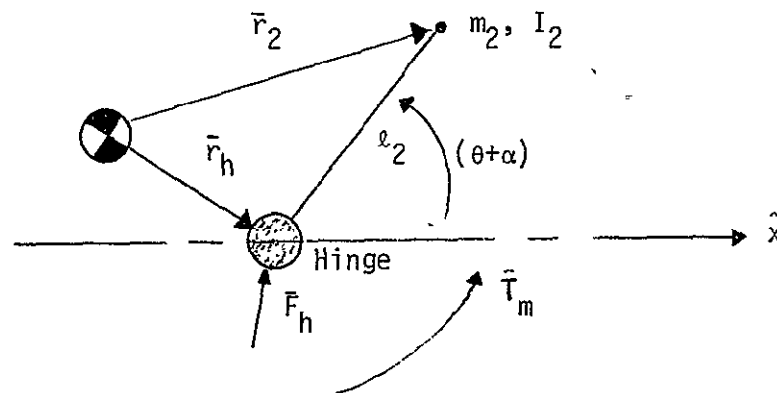


Figure 9-6. Relationships for Body 2

The vector \vec{r}_h is given by:

$$\vec{r}_h = \vec{r}_2 - \ell_2 [\theta + \alpha]_z \hat{x}. \quad (9.15)$$

By substituting for \vec{r}_h , \vec{F}_h and \vec{H}_2 , Equation (9.14) can be rearranged to yield:

$$\vec{T}_m = - [\vec{r}_2 - \ell_2 [\theta + \alpha]_z \hat{x}] \times m_2 \ddot{\vec{r}}_2 + I_2 (\ddot{\theta} + \ddot{\alpha}) \hat{z} + m_2 \frac{d}{dt} [\vec{r}_2 \times \dot{\vec{r}}_2] \quad (9.16)$$

This last equation can be simplified to:

$$\vec{T}_m = I_2 (\ddot{\theta} + \ddot{\alpha}) \hat{z} + m_2 \ell_2 \{ [\theta + \alpha]_z \hat{x} \} \times \ddot{\vec{r}}_2, \quad (9.17)$$

and substitution of (9.10) yields:

$$\begin{aligned} T_m = & \left[I_2 + \frac{m_1 m_2}{m_1 + m_2} (\ell_2^2 + \ell_1 \ell_2 \cos \alpha) \right] \ddot{\theta} \\ & + \left[I_2 + \frac{m_1 m_2}{m_1 + m_2} \ell_2^2 \right] \ddot{\alpha} + \frac{m_1 m_2}{m_1 + m_2} \ell_1 \ell_2 \sin \alpha \dot{\theta}^2 \end{aligned} \quad (9.18)$$

Equations (9.12) and (9.18) are the model of the system for any of the four cases. To study the scanning motion, the inertias are the values of I_{xx} in Table (9.2) and the moment arms, ℓ_1 and ℓ_2 , are both zero; for stepping, the inertias are given by the I_{yy} values. As an example, in the parabolic reflector case:

$$T_c = 340 \ddot{\theta} + 15 \ddot{\alpha} \quad (9.19)$$

and

$$T_m = 15 \ddot{\theta} + 15 \ddot{\alpha}, \quad (9.20)$$

9.4 MASR and Spacecraft Control

9.4.1 Spacecraft Control

Regardless of which MASR configuration is being controlled and whether scanning or stepping is being controlled, the MASR payload must be rotated relative to the spacecraft, and this will tend to make the spacecraft rotate in the opposite direction to conserve momentum. It was stated in Section 9.1 that this spacecraft rotation must be limited to 2 μ rad. As an example, consider the case of the 0.8 mrad step: this maneuver must be completed within 7.2 seconds, so the ACS with $\zeta = 0.7$ and $\omega_n = 0.5$ rad/sec corresponding to a settling time on the order of 10 seconds, cannot react fast enough to keep the spacecraft rotation within the prescribed limits, although it will prevent the major part of the potential spacecraft rotation. Thus it will be necessary to further control the spacecraft when moving the payload. Although the ACS bandwidth is assumed to be 0.5 rad/sec, it can be higher if necessary; the upper limit used in the analysis will be 1.0 rad/sec.

Neglecting the nonlinear terms by assuming α is a small angle the system equations become:

$$T_c = I_{11} \ddot{\theta} + I_{12} \ddot{\alpha} \quad (9.21)$$

$$T_m = I_{21} \ddot{\theta} + I_{22} \ddot{\alpha} \quad (9.22)$$

where the coefficients can be determined by comparison with Equations (9.12) and (9.18). The equation for spacecraft rotation obtained from these equations is:

$$\ddot{\theta} = \frac{I_{22} T_c - I_{12} T_m}{I_{11} I_{22} - I_{12} I_{21}} \quad (9.23)$$

Now it is evident that the spacecraft will not react to the hinge torques applied to the payload if the normal control torque is augmented by a torque:

$$T_c = \frac{I_{12}}{I_{22}} T_m \quad (9.24)$$

This approach will be used.

Specifically, it is assumed that the electrical signal driving the payload control motor, which is proportional to T_m , can be properly modified and added as a feed forward to the ACS input to the wheel motor. This will be done in both roll and pitch. This approach cannot be perfectly effective due to unavoidable errors such as variations in motor torque constants and friction estimates, and differences in delays in the two motor circuits (the wheel motors have effective delays of 0.025 seconds). These matters will be discussed further in Section 9.5.

As an indication of the need for spacecraft control consider the spacecraft reaction to stepping the payload with no control torque. This is done by setting $T_c = 0$ in (9.21), to obtain:

$$\ddot{\theta} = - \frac{I_{12}}{I_{11}} \ddot{\alpha} \quad (9.25)$$

This leads to the approximation:

$$|\theta| \approx \frac{I_{12}}{I_{11}} |\alpha| \quad (9.26)$$

As an example, in the case of stepping the mirror $I_{11} = 1188 \text{ kg m}^2$ and $I_{12} = 30 \text{ kg m}^2$, so for the 0.8 mrad step $\theta_{\max} = 20.2 \text{ } \mu\text{rad}$ or approximately 10 times the allowable rotation. This is the smallest reaction as indicated in Table X.3.

Table 9.3. Approximate Uncontrolled Spacecraft Rotation When Stepping the MASR

Step Size (mrad)	Spacecraft Rotation (μ rad)	
	Configuration 1 (Moving Reflector)	Configuration 2 (Moving Mirror)
0.8	222.7	20.2
1.3	361.8	32.8

9.4.2 Stepping Control of the MASR

Two approaches are considered for stepping the MASR:

- 1) design a continuous controller and let it move the MASR in response to a change in the input, or
- 2) let most of the MASR movement be accomplished by a predetermined torque profile--with zero average value--with any small residual error being removed by a continuous controller.

The latter approach can be implemented in one of two ways:

- 2a) open the payload control loop while the torque profile is moving the payload, then close the loop with the new input and let it remove any positioning error, or
- 2b) let the payload controller make continuous adjustments throughout the process, which requires changing its input in a predetermined way to correlate with the torque profile being applied.

No matter which of the above methods is used, it is necessary to have a continuous controller for the payload. A second-order controller with $\zeta = 0.7$ will be used. Since the envelope of the response to a step input is given by $e^{-\zeta\omega_n t}$, the 10 percent settling time is

$$T_s = \frac{2.3}{\zeta \omega_n} \quad (9.27)$$

Thus, for the 0.8 mrad step where $T_s \leq 7.2$ sec, $\omega_n \geq 0.46$ rad/sec; and for the 1.3 mrad step where $T_s \leq 11.25$ seconds, $\omega_n \geq 0.29$ rad/sec. So that a single controller can be used in both cases with a small safety factor, $\omega_n = 0.5$ rad/sec is chosen for the initial design. The linearized system block diagram with the controllers for stepping the MASR is shown in Figure 9.7. The predetermined torque profile, if used, is represented by T_0 . For method 2b, the controller input α_c could be developed as:

$$\alpha_c = \left(1 + \frac{K_2}{K_1} s\right) \frac{T_0}{I_{22} s^2} \quad (9.28)$$

where the factor $\left(1 + \frac{K_2}{K_1} s\right)$ is necessary to account for the rate $\dot{\alpha}(t)$.

It should be noted here that the compensation torque T_c can be developed with the spacecraft reaction wheel. Using method 2a and neglecting friction the reflector can be stepped 1.3 mrad in 11.2 seconds by applying a constant torque of 0.0043 nt m for 5.6 seconds followed by a constant torque of -0.043 nt m for another 5.6 seconds. The torques required for this and other stepping cases are summarized in Table 9-4. Since the available wheel torque is about 0.15 N m it is more than sufficient to generate T_c . The value of T_0 for the example

is computed by noting that $I_{22} = 104.12 \text{ kg m}^2$ and the payload movement is given by $\alpha = (T/2I)t^2$ where $\alpha = 0.65 \text{ mrad}$, $I = 104.12 \text{ kg m}^2$ and $t = 5.6 \text{ seconds}$.

Step Size (mrad)	Torque (Nm)	
	Reflector	Mirror
0.8	0.0064	0.0019
1.3	0.0043	0.0012

Table 9-4. Control Torque Needed to Step the MASR (No Friction)

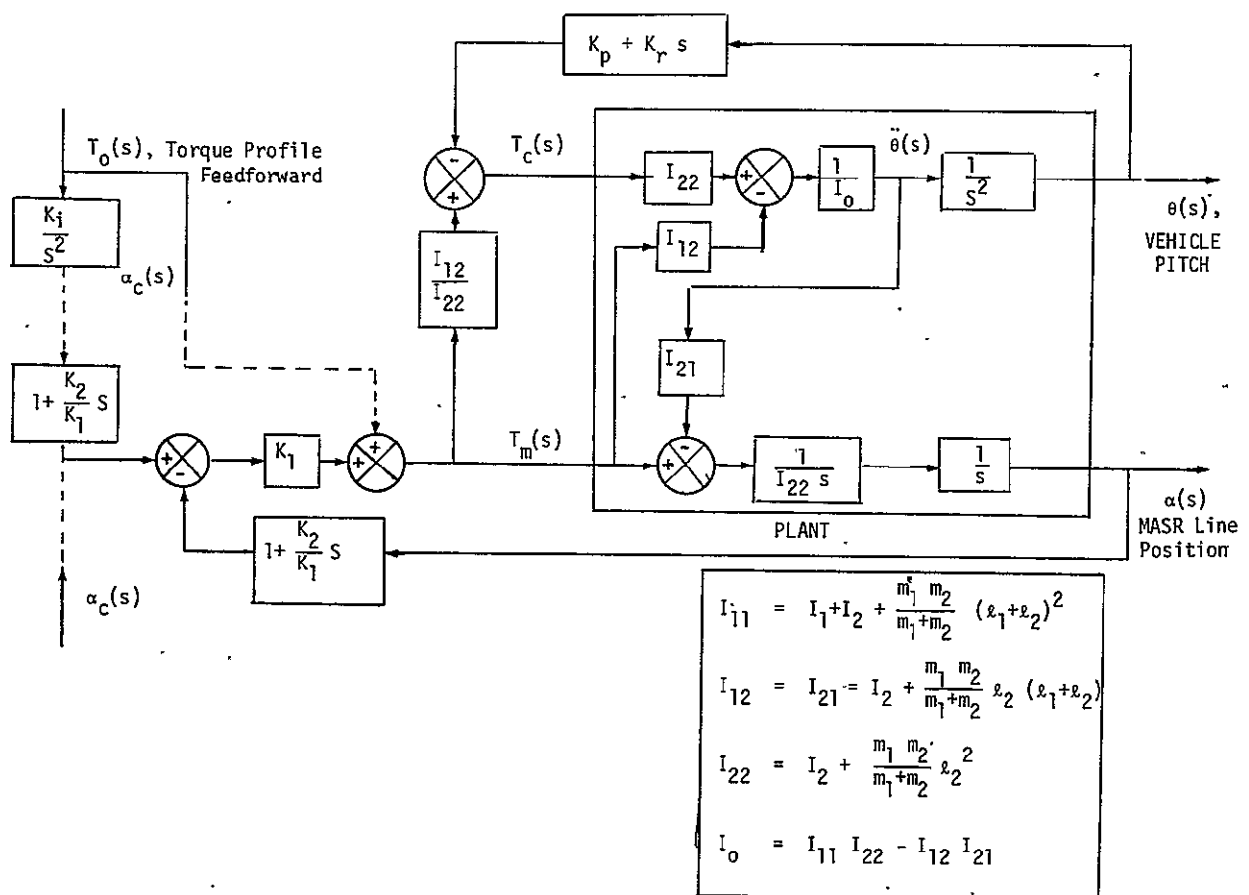


Figure 9-7. Linearized Control System for MASR Stepping

9.4.3 Line Scanning Control of the MASR

For line scanning, the moving member of the MASR (parabolic reflector or mirror) must scan the length of the line at constant slew rate then turn around in a fixed time interval to scan the next line. In order to do this, three things must be controlled simultaneously: rate, position and time. A means of doing this has not been devised, but two possible approaches are:

- 1) determine both the $\alpha(t)$ and the $\dot{\alpha}(t)$ profiles a priori and control both with an appropriate controller which may be aided by a constant torque pulse during the turn-around interval which forces the scan to keep pace with the data taking equipment,
- 2) design a controller, which may include a constant torque pulse during the turn-around interval, to control the MASR scan rate and let the data taking be started when the FOV crosses the leading edge of the scan frame in order to accommodate the resulting small variations in the turn-around time.

The problems with the first method are the determination of $\alpha(t)$ and the problem of coordination with the data taking equipment since there will be errors in the MASR control. The potential difficulty with the second method is the possibility of insufficient flexibility in the data taking process.

Since this study is concerned with the effects of the scanning operation on the spacecraft and not on the means of controlling the scanning, it is assumed that the scan reversal is achieved primarily by a constant torque pulse and secondarily with a rate controller to make minor adjustments. It is further assumed that the data taking operation has sufficient flexibility to accept the variations that do occur, and that the data taking is started and stopped by timing signals at the ends of the scan period. These timing signals can be developed from the gimbal readout.

The rate control loop is a first order system with the linear transfer function:

$$\frac{\dot{\alpha}}{\dot{\alpha}_c}(s) = \frac{a}{s + a} \quad (9.29)$$

For this system to have a settling time (10%) of 7.2 seconds, $a = 0.32$ rad/sec is needed. This relatively slow response should be good enough because the linear controller is only needed to remove the small errors left after (during) application of the torque pulse. The scan control system is shown in Figure 9-8, and the input time functions $T_o(t)$ and $\dot{\alpha}_c(t)$ are shown in Figure 9-9.

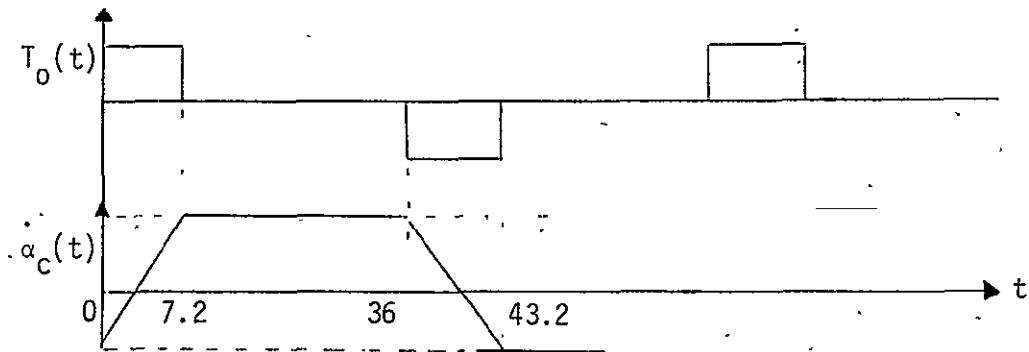


Figure 9-9. Inputs to Scanning Controller

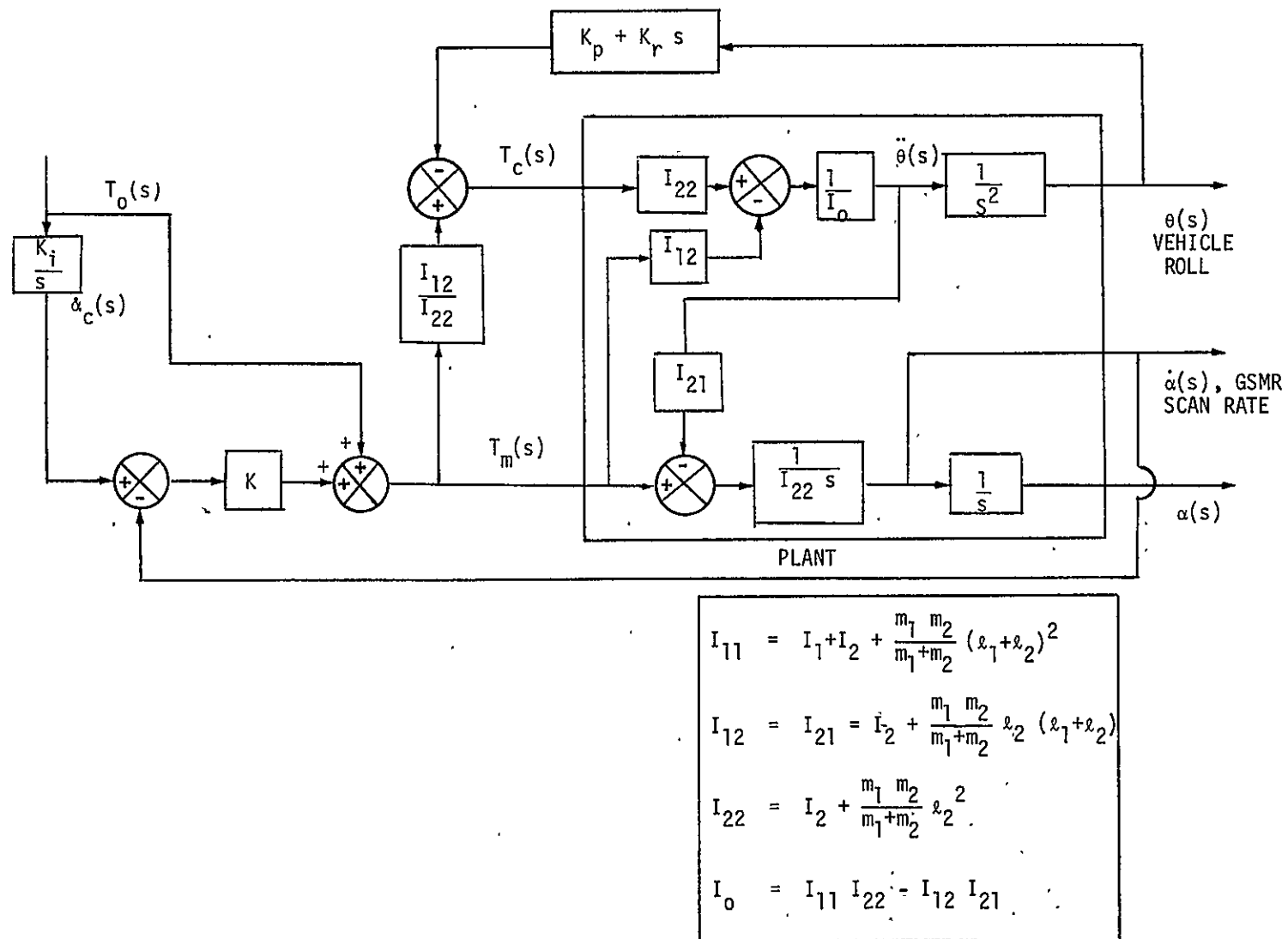


Figure 9-8. Linearized Control System for MASR Line Scanning

For the case of scan reversal $I_{22} = I_2$ so the mirror is the harder of the two payloads to remove with $I = 30 \text{ kg m}^2$. Further, from Table 9-1 the full earth scan requires the most acceleration, $\ddot{\alpha} = 0.485 \text{ mrad/sec}^2$. For this case, the required constant torque is:

$$T_0 = \ddot{\alpha} I = \left(0.485 \frac{\text{mrad}}{\text{sec}^2}\right) (30 \text{ kg m}^2) = 0.0146 \text{ N m} \quad (9.30)$$

The torques required for turn-around in the various cases are summarized in Table 9-5. This is also easily accommodated by the reaction wheel.

9.5 Analysis and Simulation Results

Because it was assumed that the stepping and scanning rotation axes are orthogonal and are both principal axes of the system and of the payload, the stepping and scanning actions are uncoupled. Thus, they can be considered separately in this section. Also, as indicated earlier, the analysis is restricted to the scan frames located at nadir. The stepping and scanning analyses are discussed in Subsections 9.5.1 and 9.5.2, and cases where the above assumption are not valid are discussed briefly in Subsection 9.5.3. The simulation results were obtained using the nonlinear model of Equations (9.12) and (9.18) with small angle approximations for θ and α . This model is valid for all 12 cases shown in Figure 9-2.

The approaches presented in Section 9.4 with T_c as in Equation (9.24) would theoretically move the payload without rotating the spacecraft. This will not happen because the nonlinear terms will cause slight disturbances to the spacecraft, the 0.025 second wheel motion time constant will cause a torque mismatch, and the system parameters will not be matched precisely. Note that the additional control torque T_c given by Equation (9.24) depends on T_m , where T_m is the hinge torque applied to the vehicle. Due to friction and similar phenomena this may not be proportional in the electrical signal driving the payload motor. It may be necessary in practice to get a better estimate, for instance, with accelerometers, etc. The parameter variations which will be considered here are motor torque constant variations of $\pm 5\%$, 1 sigma. The motor is assumed to be a DC motor with negligible time constant.

Table 9-5. Control Torque Needed to Reverse the MASR Scan

Turn-Around Time (sec)	Torque (N m)	
	Parabolic Reflector	Mirror
7.2	0.0058	0.0116
11.2	0.0025	0.0049
18.0	0.0073	0.0146

It is assumed that the control torque given by (9.24) is added to the normal wheel torque at the input to the motor drive amplifier in order to avoid the 0.4 second sampling delay when feeding it through the on-board computer. The objective of the analysis is to determine how well the stepping and scanning can be accomplished with the simple control schemes of Section 9.4. As long as the stepping or scan reversal is completed within the allowable turn-around time, the control capability will be judged by comparing the peak spacecraft rotation with the maximum permissible value of $2 \mu\text{rad}$.

9.5.1 MASR Stepping

The six stepping cases can be reduced to form cases by eliminating the 18° frame as a separate case. The 18° frame nominally requires a 1.3 mrad step in 18 seconds but this is certainly possible if the 1.3 mrad step can be completed in 11.25 seconds for the 1500 km frame. Since the 18° frame is not needed as an isolated case, there is no need to consider the longer turn-around time. Additionally, an attempt will be made to use the 7.2 second settling time of the 0.8 mrad step size for the 1.3 mrad step so the same control parameters can be used in all three cases.

As indicated in Table 9-3 the moving mirror is easier to control, so that is considered first; the parameters are given in Table 9-6. The first approach used is to let the continuous payload controller act alone-- $T_0 = 0$ in Figure 9-7. When this is done the resulting response is shown in Figure 9-10 for the 1.3 mrad step size with $\xi = 0.7$ and $\omega_n = 0.5 \text{ rad/sec}$ for the payload controller. The spacecraft rotation is nonzero due to the motor time constant, because there are no nonlinear terms--with $\epsilon_2 = 0$ --and no errors were introduced.

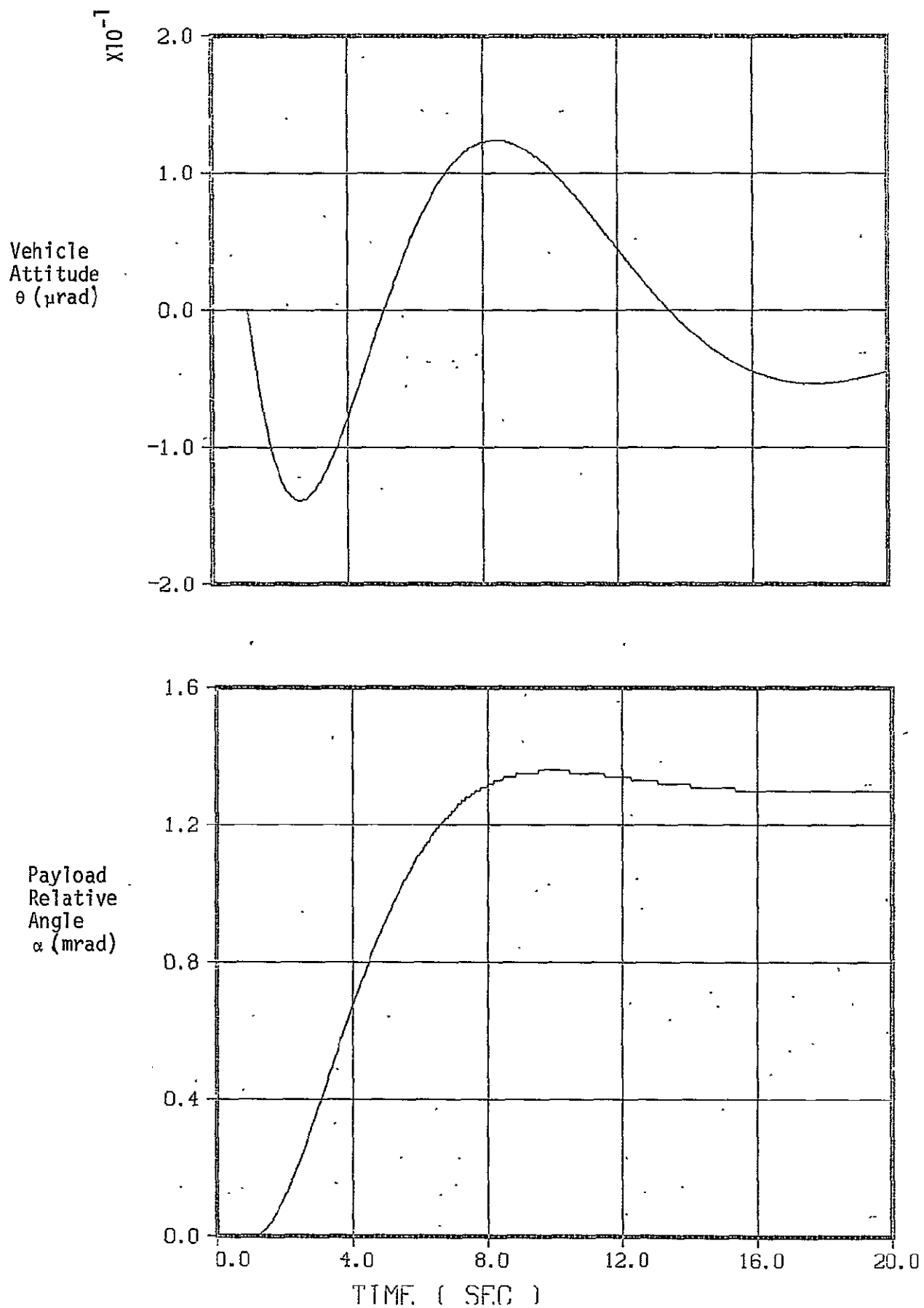


Figure 9-10. Continuous Stepping Control of Mirror With $T_0 = 0$, $\xi = 0.7$ and $\omega_n = 0.5$ rad/sec

Table 9-6. Nominal Parameters for Stepping the Mirror

PARAMETER	NOMINAL VALUE
m_1	800 kg
m_2	64 kg
I_1	325 kg m ²
I_2	30 kg m ²
l_1	3.75 m
l_2	0
I_{11}	1188 kg m ²
$I_{12} = I_{21}$	30 kg m
I_{22}	30 kg m ²
I_0	3.47×10^4 kg ² m ⁴

The response shown in Figure 9-10 has a settling time of about 14 seconds--the peak overshoot of 4 per cent at 7 seconds is too large--which is too slow. If the payload controller parameters are modified to achieve $\xi = 1.0$ and $\omega_n = 1.0$ rad/sec, the step response in Figure 9-11 is obtained. This has a settling time of less than 7 seconds--the error is reduced to 0.03 mrad in 5.6 seconds--which meets the criterion for either step size. If the payload motor torque constant is increased by five per cent, the response in Figure 9-12 is obtained. The peak spacecraft rotation of 0.86 μ rad is well within the allowable range. The peak spacecraft rotation angles for the four basic torque constant variations are summarized in Table 9-7. The expected

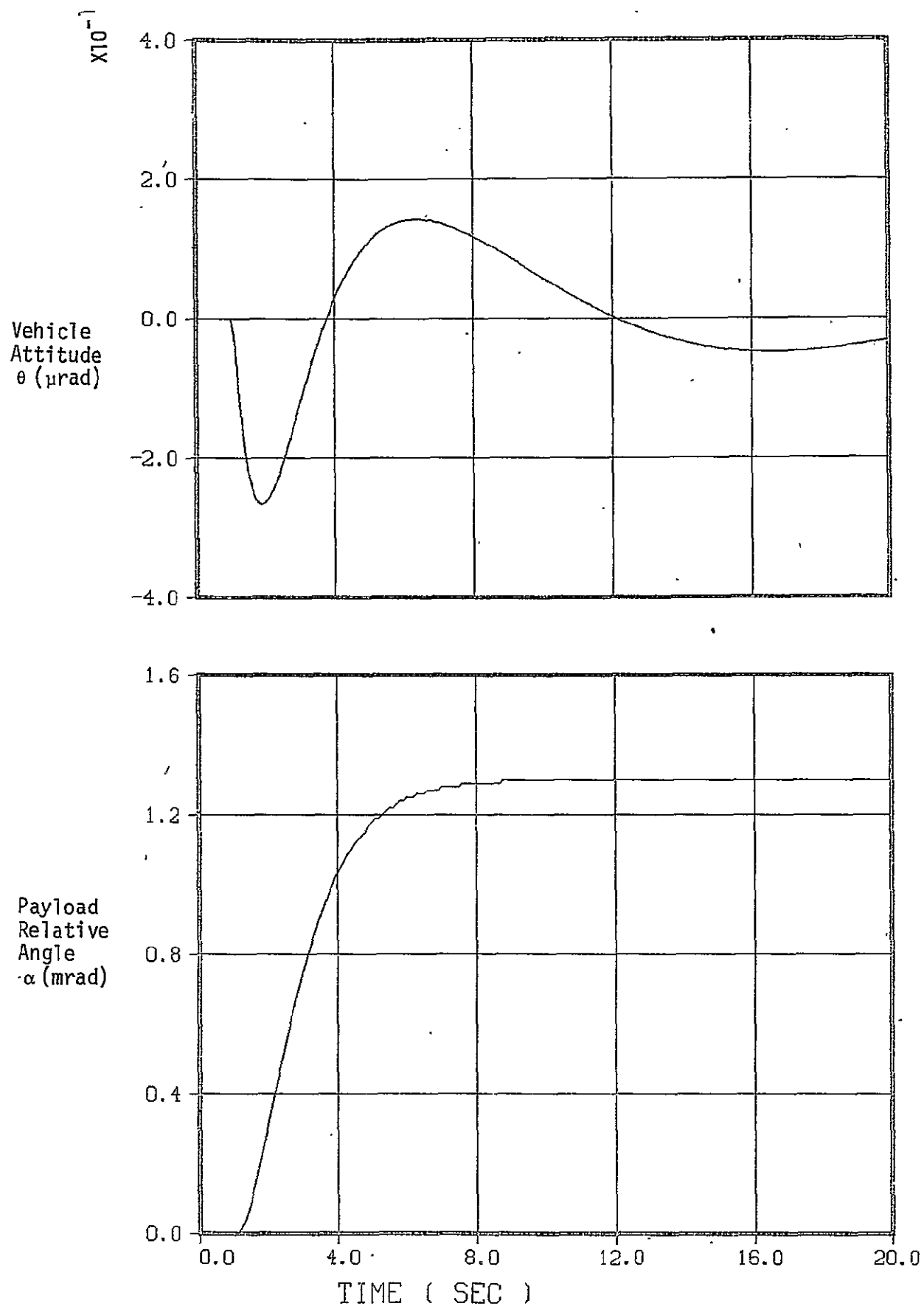


Figure 9-11. Continuous Stepping Control of Mirror With $T_0 = 0$, $\xi = 1.0$ and $\omega_n = 1.0$ rad/sec

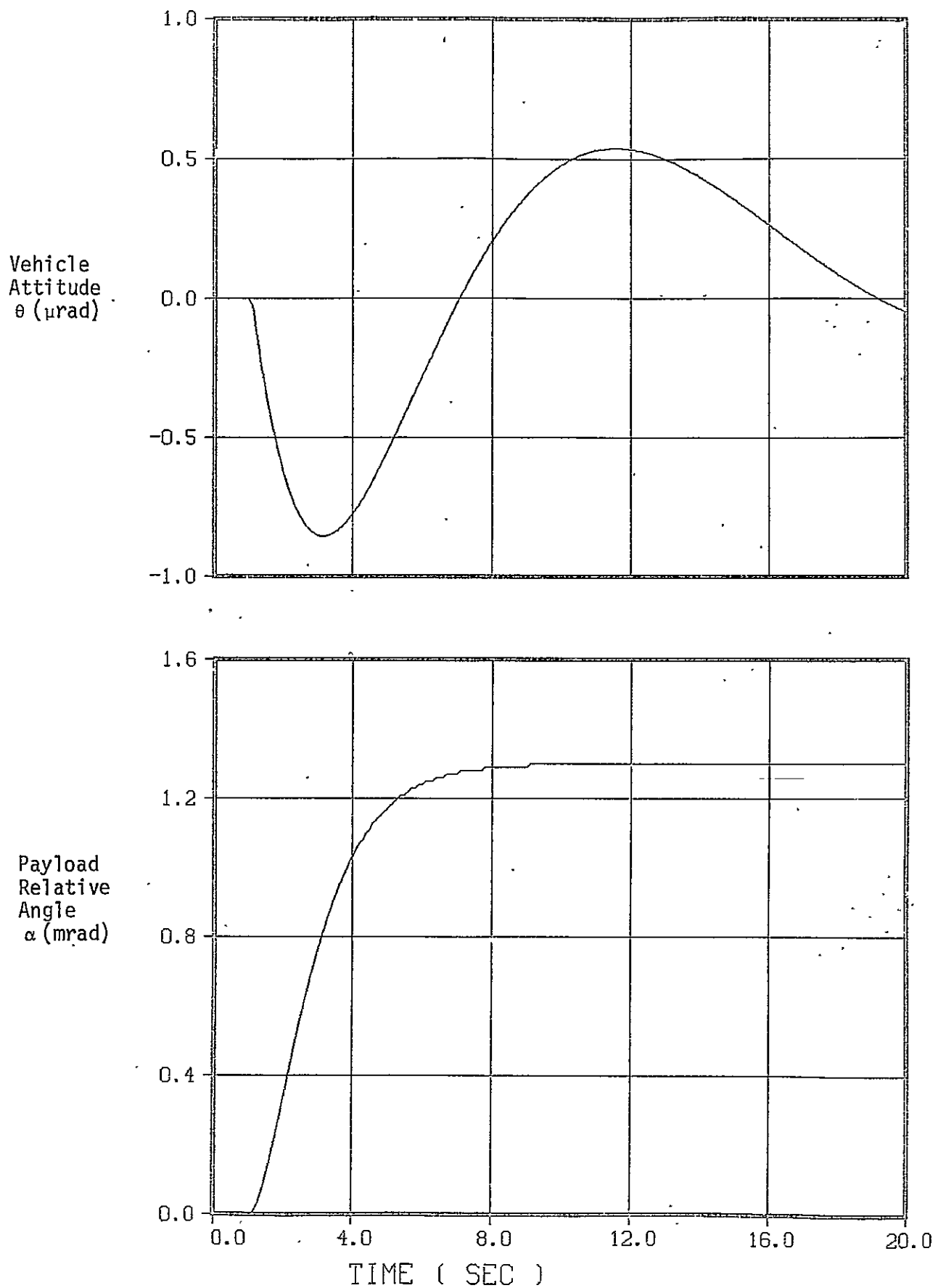


Figure 9-12. Continuous Stepping Control of Mirror With $\xi = 1.0$,
 $\omega_n = 1.0$ rad/sec and the Motor Torque Constant Increased by 5%

Table 9-7. Peak Spacecraft Rotation Due to Stepping the Mirror 1.3 mrad Within 7.2 Seconds (Payload Controller: $\xi = 1.$, $\omega_n = 1.$ rad/sec)

Parameter	% Change In Parameter Value		θ_{\max} (μrad) (0.27 Nominal)	
	+5	-5		
Wheel Motor Torque Constant	+5	-5	0.87	0.91
Payload Motor Torque Constant	+5	-5	0.86	0.93
RSS Expected Value			1.30	

Table 9-8. Nominal Parameters for Stepping the Reflector

Parameter	Nominal Value
m_1	800 kg
m_2	18 kg
I_1	325 kg m ²
I_2	15 kg m ²
l_1	1.5 m
l_2	2.25 m
I'_{11}	588 kg m ²
$I_{12} = I'_{21}$	164 kg m ²
I_{22}	104 kg m ²
I_o	3.43×10^4 kg m ²

value is obtained by combining the expected responses due to variations in the two torque constants, and it is this number which should be less than about 2 μ rad. Note that each of the four individual cases has approximately the same response. This is true for all of the cases analyzed, so the results presented in the sequel will be restricted to a five per cent-high payload motor torque constant:

The parameters for stepping the reflector are given in Table 9-8. Again use of the payload controller alone will be studied first--with $\xi = 1.0$ and $\omega_n = 1.0$ rad/sec. The vehicle response to a 1.3 mrad step with RW motor time constant $\tau_c = 0.025$ seconds is 4.05 μ rad--see Figure 9-13. This is too large to be acceptable and does not even include errors. The vehicle attitude error is due almost entirely to the motor time constant and can be completely eliminated by the addition of a simple lag filter with a 0.025 second time constant in series with the payload motor--this removes the phase shift between the two torques. That filter is now considered part of the reflector controller. The response of this new nominal system to a 1.3 mrad step input with the payload motor torque constant increased by five percent is shown in Figure 9-14. The spacecraft response, $\theta_{\max} = 8.93$ μ rad, is too large to be acceptable, and increasing the ACS natural frequency ω_{ACS} to 1.0 rad/sec only reduces θ_{\max} to 5.08 μ rad. So this particular design is not acceptable. The spacecraft reaction is less for the 0.8 mrad step or for the 1.3 mrad step in 11.2 seconds as shown in Table 9-9. The 11.2 settling time is obtained by reducing the payload controller natural frequency to $\omega_n = 0.7$ rad/sec. This gives the ACS system a better chance to react to the disturbance while it builds up. But even with $\omega_{\text{ACS}} = 1$ rad/sec, the results are not acceptable. The settling times are actually somewhat faster than the nominal values shown, but they cannot be lengthened sufficiently--by reducing ω_n --to make the spacecraft response acceptable.

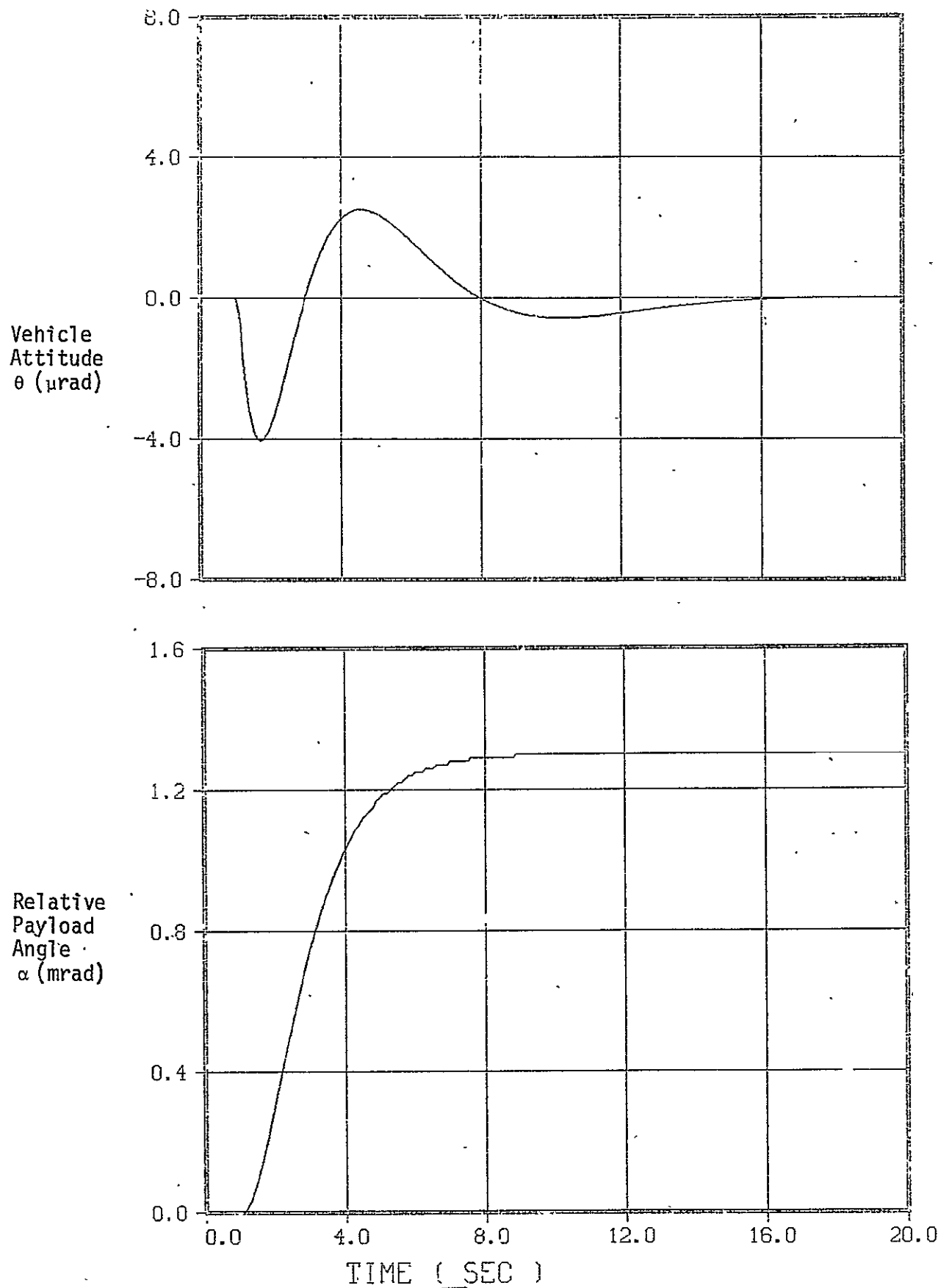


Figure 9-13. Continuous Stepping Control of Parabolic Reflector With $T_0 = 0$, $\xi = 1.0$ and $\omega_n = 1 \text{ rad/sec}$

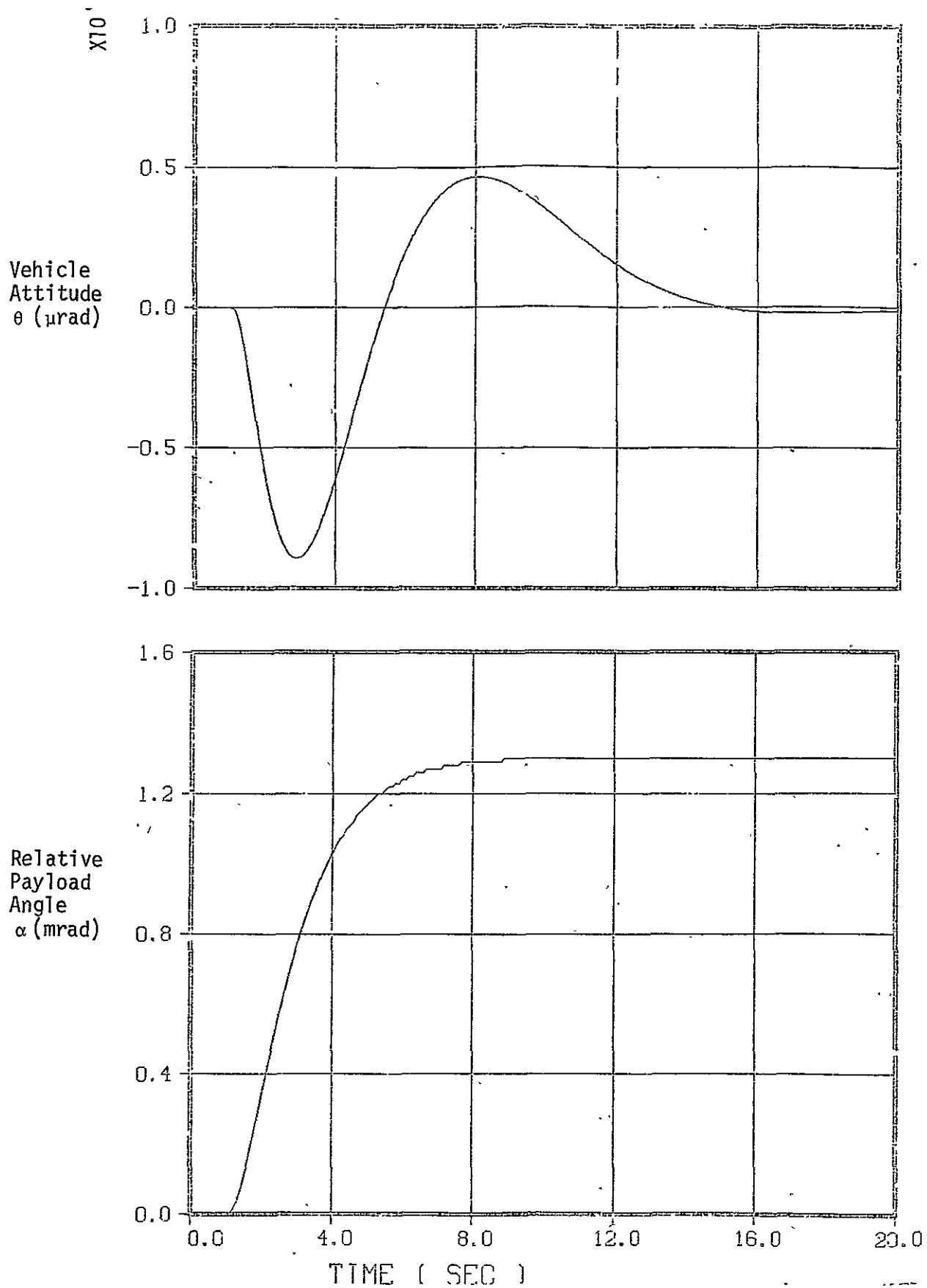


Figure 9-14. Continuous Stepping Control of Reflector With τ_m Added and 5% Torque Constant Error ($\xi = 1.0$ and $\omega_n = 1.0$ rad/sec)

Table 9-9. Spacecraft Response in μrad to Reflector Stepping with a Continuous Linear Controller and 5% Torque Constant Error

STEP SIZE (mrad)	1.3	1.3	0.8
SETTLING TIME (Sec)	7.2	11.2	7.2
ω_{ACS} (Rad/Sec)			
0.5	8.93	6.77	5.5
1.0	5.08	3.52	3.13

The other approach that was tried was the addition of a feed forward torque T_0 as shown in Figure 9-7. Unless an input $\alpha_c(t)$ is generated and matched to the resulting $\alpha(t)$ during the turn-around period, the payload controller will work against the torque T_0 . One solution to this problem is to step $\alpha_c(t)$ at any time during the turn-around period but open the controller loop until the torque profile T_0 is completed. This approach does not work because a five per cent torque constant error causes about a 5 per cent error at the end of the torque T_0 , and the controller then has to remove that error.

The other possibility is to actually generate an appropriate $\alpha_c(t)$ and let the payload controller remove any small errors from this throughout the stepping period. Specifically, the torque profile that was used had the form shown in Figure 9-15. The input $\alpha_c(t)$ was formed by filtering the motor input signal which generates T_0 with the transfer function (K/S^2) where K is appropriately chosen. Of course this input signal must be further modified by the transfer function $(1 + K_2 S/K_1)$ as can be seen in Figure 9-7. Using this controller, the results shown in Table 9-10 were obtained. The payload controller parameters $\xi = 0.7$ and $\omega_n = 0.5$ rad/sec were used.

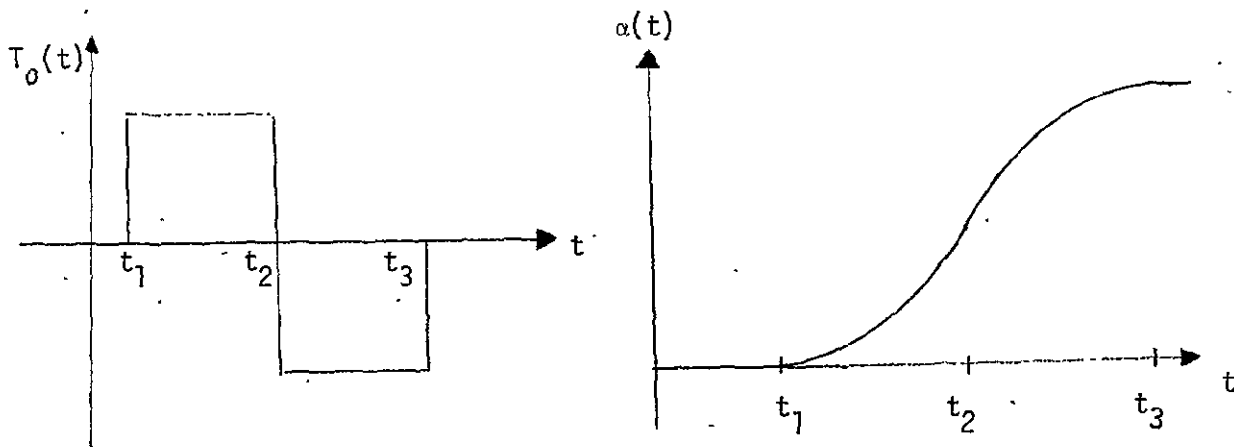


Figure 9-15. Torque Profile T_o and Resulting Payload Response

Table 9-10. Spacecraft Response in μrad to Reflection Stepping With a Torque Profile Input and Five Percent Torque Constant Error

Step Size (mrad)	1.3	1.3	0.8
Settling Time (sec)	7.2	11.2	7.2
ω_{ACS} (rad/sec)			
0.5	6.45	3.63	3.98
1.0	2.47	1.06	1.53

These results show that it is still not acceptable to complete the 1.3 mrad step within 7.2 seconds, and since a separate T_0 must be used anyway, there would be no advantage to that response even if it were possible. The two step sizes can be achieved as long as $\omega_{ACS} = 1$ rad/sec. The expected value of θ_{max} for the 0.8 mrad step is 2.2 μ rad which should be acceptable. The response for the 0.8 mrad step with $\omega_{ACS} = 1$ rad/sec is shown in Figure 9-16.

9.5.2 MASR Scan Reversal

As pointed out in Section 9.5, the scan reversal case that requires the largest torque is for the mirror in the 18 degree frame. Because this case requires the largest torque, it is also the one that will have the largest spacecraft response due to torque constant errors. Using the controller shown in Figure 9-8, the spacecraft peak responses for the various cases are shown in Table 9-11. With the ACS bandwidth set at 1.0 rad/sec all of the responses are acceptable except the moving mirror--MASR configuration 2--on the 18 degree frame. And even that case is close enough that it can probably be made to work. For an ACS bandwidth of 0.5 rad/sec, the only response that is very small is for the 1.3 mrad FOV and the 1500 km frame. Thus it is concluded that the scan reversal is feasible in all cases as long as the high bandwidth ACS is used. A typical response is shown in Figure 9-17.

9.5.3 Additional Topics

Two additional topics are considered in this subsection. The first is the effect of the AASIR on the MASR. The AASIR scanning and stepping were discussed in Reference 2, where it was shown that the spacecraft response during AASIR stepping can be limited to 18 μ rad. Again noting that the vehicle is a platform which transmits motion from one payload to the other, the AASIR stepping does not present a problem for the MASR control because the transmitted motion, 18 μ rad, is only 25 per cent of the allowable MASR error of 0.08 mrad.

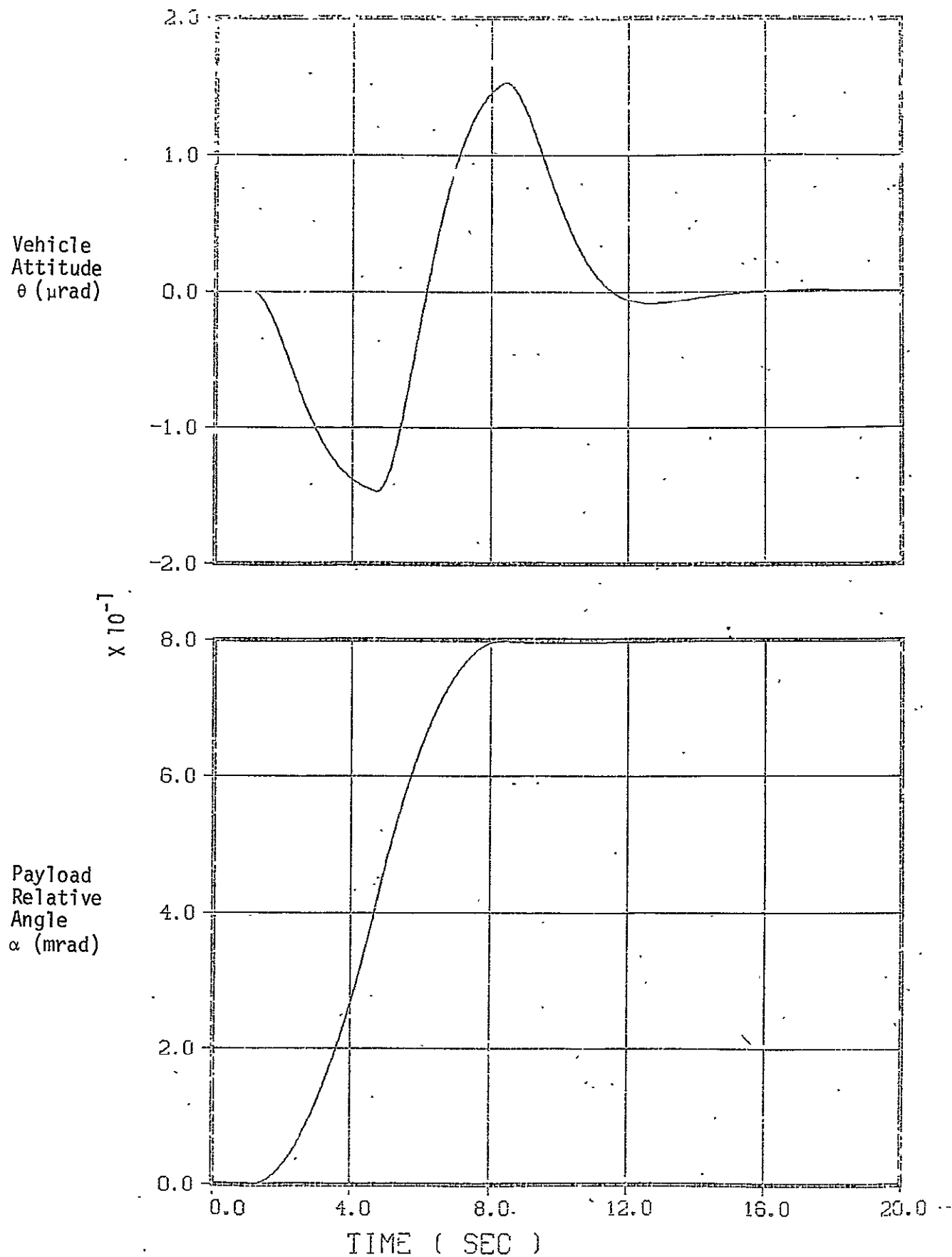


Figure 9-16. Continuous Stepping Control of Reflector With 5% Torque Constant Error and Vehicle ACS Bandwidth $\omega_{ACS} = 1.0 \text{ rad/sec}$

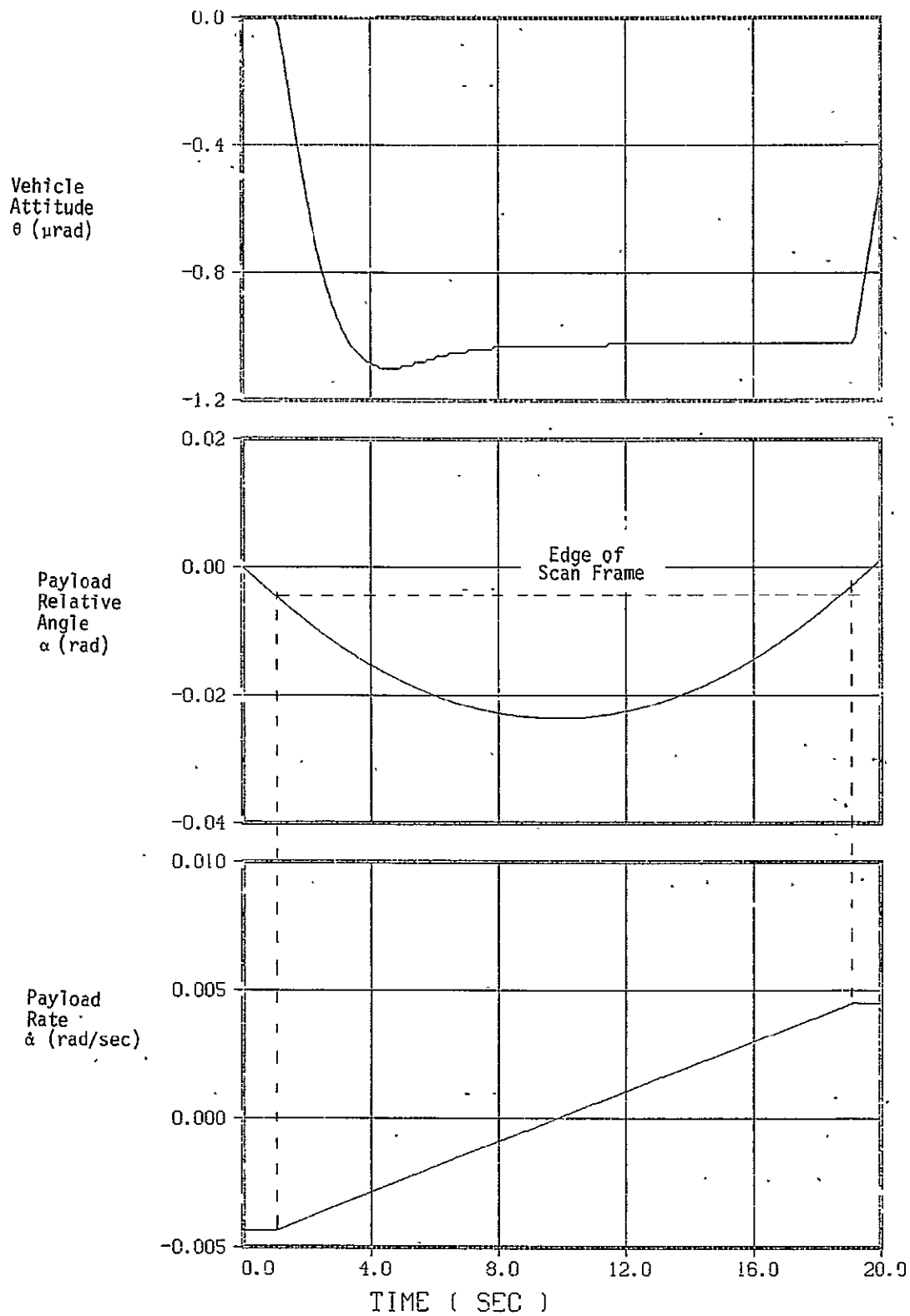


Figure 9-17. Scan Reversal for 18° Frame With 5% Torque Constant Error and Vehicle ACS Bandwidth $\omega_{ACS} = 1.0$ rad/sec .

Table 9-11. Scan Reversal With the Payload Motor Torque
Constant High by Five Per Cent

	Case		θ_{\max} (μrad)	
			ω_{ACS} (rad/sec)	
	Step Size (mrad)	Turn-Around (sec)	0.5	1.0
Mirror	0.8	7.2	6.34	1.62
	1.3	11.2	2.72	0.69
	1.3	18.0	8.05	2.05
Parabolic Reflector	0.8	7.2	3.39	0.87
	1.3	11.2	1.46	0.37
	1.3	18.0	4.31	1.10

The model of the MASR and vehicle developed in this chapter is equally valid for the AASIR and vehicle. So (9.26) can be used to estimate the vehicle response to AASIR scanning: The AASIR scan motion is approximately a sinusoid with amplitude of 12.36 degrees and frequency of 0.03876 Hz, or

$$\text{AASIR SCAN} = 12.36^\circ \sin 2.44 t. \quad (9.31)$$

The AASIR scan mirror inertia is $0.43 \text{ slug ft}^2 = 0.58 \text{ kg m}^2$, and the spacecraft inertia depends on whether GSMR configuration 1 or 2 is used. To be conservative, assume configuration 1 is used; the spacecraft inertia is $I_{\text{sc}} = 325 \text{ kg m}^2 + 15 \text{ kg m}^2 = 340 \text{ kg m}^2$. So, the spacecraft reaction to the AASIR scan is sinusoidal of the form:

$$\text{SC REACTION} = (0.37 \text{ mrad}) \sin 2.44 t. \quad (9.32)$$

This motion is transmitted to the MASR and is larger than the total allowable error of 0.08 mrad by about 2.3 times. This applies, however, only to the 20 degree AASIR imaging/sounding frame. For the 4 degree and 1.2 degree frames the effects of AASIR scan mirror motion on the MASR become almost insignificant.

The above response assumes that the ACS does nothing to reduce the reaction. And in fact the ACS does very little to reduce the amplitude of that sinusoid because its frequency, 2.44 rad/sec, is too far beyond the ACS bandwidth of 0.5 rad/sec. This means that to meet the MASR error requirement the momentum due to the AASIR scanning must be absorbed within the AASIR--requiring an AASIR redesign--or the AASIR effect must be compensated in the spacecraft or MASR. For this latter approach, AASIR scanning information could be obtained from within the AASIR scan mechanism and used to modify the MASR control function; or that information could be utilized by the data taking equipment to filter the high frequency disturbance out of the data. Regardless of the approach, more work needs to be done on the solution to this problem.

The other topic to be considered is the effect of cross-products of inertia on the MASR stepping and scanning. If the spacecraft or payload axes defined in the earlier parts of this chapter are not principal axes, the resulting cross products of inertia will cause cross-coupling between axes. First, this means that both stepping and scanning will affect the spacecraft in both pitch and roll (yaw also, but that is not considered here). Since these inertia terms should be known, the cross-coupling can be minimized by feeding the dynamic compensation signals derived from the payload motor drive voltages into both the pitch and roll reaction wheels. Secondly, due to payload cross-products of inertia the scanning will affect stepping and vice versa. Most of this will occur during turn-around where there is no accuracy requirement. This leaves only the rotation about the stepping axis during line scan to be considered. Appropriate design of the stepping servo, i.e., an integral controller, would prevent the cross-coupling torque from disturbing the orthogonal gimbal position.

9.6 Summary and Conclusions

This section studied the dynamic interaction between a scanning MASR and the AASIR. When imaging a frame on the earth's surface, the MASR scans back and forth and steps 1 line in an orthogonal direction at the end of the each scan. The disturbances entailed in its stepping motion and in its scan reversal cause the spacecraft to rotate which in turn causes motion in the AASIR. In order to meet the AASIR short-term pointing stability requirement of $4.2 \mu\text{rad}$, the criterion was established that the MASR should not cause more than $2 \mu\text{rad}$ peak spacecraft response in roll and pitch. The remainder of the AASIR error budget is taken up by errors from other sources, namely the attitude reference system, the attitude control system, the AASIR gimbal drive and the AASIR line step dynamic compensator.

Two MASR configurations were addressed in this study and they are identified as the parabolic reflector configuration and the flat mirror reflector configuration. The results obtained are shown in Tables 9-12 and 9-13. In all cases the MASR gimbal drive input, minus the friction torque, was fed forward to the respective ACS wheel motor inputs. If the uncertainty in the friction torque of the MASR gimbal drive is large, then an accelerometer must be used to derive this compensating feed-forward signal for the ACS. The spacecraft attitude error responses given in Table 9-12 and 9-13 are therefore entirely caused by compensating-torque mismatches. It has been assumed that acceleration torques obtained from electrical signals introduced to the MASR gimbal drives and the reaction wheels exhibit a 1σ modeling error of 5% for either of the actuators. It was found that mirror reflector stepping could be accomplished with a single second-order continuous linear controller using rate plus position feedback, with the expected peak spacecraft rotation being less than $1.3 \mu\text{rad}$. Parabolic reflector stepping on the other hand caused a spacecraft rotation of $5.6 \mu\text{rad}$ even when done with a slightly more sophisticated controller, where the step is primarily accomplished with an externally

generated torque profile and the linear controller is used to remove the small residual errors. The reason the results are poorer when stepping the parabolic reflector is that its effective inertia is more than three times larger than the of the mirror-- 106 kg m^2 versus 30 kg m^2 --due to its moment arm about the hinge point.

In the case of scan reversal, the mirror has twice as much inertia as the parabolic reflector because it is twice as heavy with the same basic size/shape, so it causes more spacecraft reaction. None of the results shown in Table 9-12 are sufficiently near the $2 \text{ } \mu\text{rad}$ goal except the mirror stepping, but they do show that more sophisticated schemes may be sufficient to meet the error criterion. If the ACS bandwidth is increased from the nominal value of 0.5 rad/sec to 1.0 rad/sec , the results shown in Table 9-13 are obtained. These results are acceptable-- $2.2 - 2.3 \text{ } \mu\text{rad}$ should be close enough--with the exception of the mirror scan reversal for the 18 degree full earth coverage frame. Previous studies have shown, however, that with an ACS bandwidth of 1 rad/sec , gyro noise will cause spacecraft jitter that is unacceptable under the present specification. Increasing the ACS bandwidth may, therefore, not be a solution to the MASR/AASIR interaction problem.

The above results are directly related to the requirements on the system. They could be improved if more time were allowed to scan out a frame or if a different ratio of scan time to turn-around time were used (lower scan efficiency). The effect of the AASIR line scan on the MASR is not negligible either, and without internal momentum compensation of the AASIR resonant scan mirror, the MASR cannot meet a 10% pixel size accuracy. An additional problem with the MASR is spatial interference of the MASR antenna with the solar array. This problem can be solved by relocating the solar array shaft from the mission adaptor of the MMS more toward the propulsion module. A less conventional array layout may also solve the problem. In summary, the investigations have shown that flying the MASR in addition to the AASIR on StormSat, does create a number of significant payload functional problems. The obtained study results indicate, however, that the desire to add the MASR is not a hopeless case if one is willing to make some compromises with respect to pointing accuracy and overall system complexity.

Table 9-12. Peak Expected Spacecraft Attitude Error for Nominal ACS*

		Assuming 5% Torque Mismatches			
		RSS θ_{\max} (μrad)			
		Parabolic Reflector		Mirror	
Frame Size	Beam Width (μrad)	Stepping	Scan Reversal	Stepping	Scan Reversal
1500 km	0.8	5.6	4.8	<1.3	9.0
1500 km	1.3	5.1	2.1	<1.3	3.9
18°	1.3	<5.1	6.1	<1.3	11.4

* Nominal ACS has equivalent parameters: $\xi = 0.7$, $\omega_n = 0.5$ rad/sec

Table 9-13. Peak Expected Spacecraft Attitude Error for High Bandwidth ACS*

		Assuming 5% Torque Mismatches			
		RSS θ_{\max} (μrad)			
		Parabolic Reflector		Mirror	
Frame Size	Beam Width (μrad)	Stepping	Scan Reversal	Stepping	Scan Reversal
1500 km	0.8	2.2	1.2	<1.3	2.3
1500 km	1.3	1.5	0.5	<1.3	1.0
18°	1.3	<1.5	1.6	<1.3	2.9

* High Bandwidth ACS has Equivalent parameters: $\xi = 0.7$, $\omega_n = 1.0$ rad/sec

REFERENCES

1. "StormSat ACS Tradeoff Study," Interim Technical Report, Severe Storms Observing Satellite Study, prepared by TRW Systems for NASA/GSFC, TRW Report Number 26818-6001-RU-00, 14 April 1975.
2. "StormSat ACS Design Study," Interim Technical Report, Severe Storms Observing Satellite Study, prepared by TRW Systems for NASA/GSFC, TRW Report Number 26818-6002-RU-00, 20 February 1976.
3. "Low Cost Modular Spacecraft Description," NASA/GSFC Report Number X-700-75-140, May 1975.
4. Rodger Doxsey, "SAS-C Tracker (BBRC CT-401) Analysis," MIT Center for Space Research, Memo Number 37-595, Cambridge, Mass., 13 May 1974.
5. James C. Shiue, "AAFE Proposal for Geosynchronous Sounding Microwave Radiometer (GSMR)," NASA/GSFC Document Number A.O. Number QA-75-3, November 1975.
6. "Design Review Report, Advanced Atmospheric Sounder and Imaging Radiometer (AASIR)," Report Prepared by Santa Barbara Research Center for NASA/GSFC, November 1975.
7. D. B. Beard, "The Effect of an Interplanetary Magnetic Field on the Solar Wind," Journal of Geophysical Research (JGR), 1 April 1964, pages 1159-1168.
8. G. D. Mead and D. B. Beard, "Shape of the Geomagnetic Field Solar Wind Boundary," JGR, 1 April 1964, pages 1169-1179.
9. G. D. Mead, "Deformation of the Geomagnetic Field by the Solar Wind," JGR, 1 April 1964, pages 1181-1195.
10. J. E. Midgley, "Perturbation of the Geomagnetic Field--A Spherical Harmonic Expansion," JGR, 1 April 1964, pages 1197-1200.
11. W. D. Cummings, J. N. Barfield, and P. J. Coleman, "Magnetospheric Substorms Observed at the Synchronous Orbit," JGR, 1 November 1968, pages 6687-6698.
12. M. P. Aubry, C. T. Russell, and M. G. Kivelson, "Inward Motion of the Magnetopause before a Substorm," JGR, 1 December 1970, pages 7018-7031.
13. W. P. Olson and W. D. Cummings, "Comparison of the Predicted and Observed Magnetic Field at ATS-1," JGR, 1 December 1970, pages 7117-7121.

REFERENCES.
(Continued)

14. T. L. Skillman and M. Sagiura, "Magnetopause Crossing of the Geostationary Satellite ATS-5 at 6.6 R_E ," JGR, 1 January 1971, pages 44-50.
15. P. J. Coleman and W. D. Cummings, "Stormtime Disturbance Fields at ATS-1," JGR, 1 January 1971, pages 51-62.
16. R. L. McPherron, et al. "Satellite Studies for Magnetospheric Substorms on 15 August 1968--2. Solar Wind and Outer Magnetosphere," JGR, 1 June 1973, pages 3054-3061.